Axisymmetric Buoyant Jets in a Cross Flow with Shear

Transition and Mixing

Thesis by

Regina E. Dugan

In Partial Fulfillment of the Requirements

for the Degree of

Doctor of Philosophy

California Institute of Technology

Pasadena, CA

1993

(submitted January 22, 1993)

To Quincey,

my faithful companion

Acknowledgments

I hope that this is not the first time I have said thank you to all the people who have helped me. I learned early that a PhD is much closer to original than it is to independent. I share the credit for this work with the following people:

My advisor, Professor E.John List. He showed keen insight into a complex problem and taught me a great deal about interpreting data.

Professor Norman Brooks. For "nudging" me in the right direction at key points during this work. Dr. Brooks invested a considerable amount of time in my work; he was always patient and encouraging.

Professor Fred Raichlen. For some tough questions that improved the quality of this research and for having a sense of humor about some "dog things" in the lab.

The members of my examining committee - Professors Brennen, Hunt, and Zukoski. I am grateful for their input.

My mentor and friend, Professor J.B. Jones. He and Jane have been my private rooting section – always providing gentle reassurance to strengthen my resolve. I consider myself lucky to have them amongst the people I consider family.

Professor Rolf Sabersky. For welcoming me to Caltech and for welcoming me into his office, always.

Professor Jim Knowles. For coaching me through my first semester at Caltech and for being the kind of teacher who inspires learning.

Professor Ares Rosakis. He saw something unique and valuable in my style.

The staff of the W.M.Keck Laboratories. Rich Eastvedt, Joe Fontana, and Hai Vu. These men dazzled me with their ingenuity. There are no unsolvable problems in the sub-basement of Keck.

Cecilia Lin. Cheerfully, she turned rough sketches into virtual works of art.

The women who kept me paid and in the clear administratively. Jackie Beard, Dana Young, Evelina Cui, and Fran Matzen. That alone would have made me classify them as friends – add the warm smiles and I had the best administrative help possible.

My colleagues and friends. Catherine Petroff, who always allowed me the extra week to "finish up" my experiments; Talal Balaa, for being my sounding board and for never being too busy to lend a hand; Keith Langer, my SURF student, who worked diligently even through tedious experiments.

My friends. Kelly Goodwin, for helping me to realize my karma, and for recognizing the small turning points and marking them with celebration; Adiel Guinzburg, for always listening, and for finishing first to show me the way; Terry DeDominicis, the twin sister that I keep bumping into on my journey through life; Nancy Gallagher Corliss, my pseudo-therapist; Laurie Wood, for getting me to my candidacy: "Study, study, study;" and Linda Salzhauer, for teaching me about comfort foods.

The community of women at Caltech. Mary Kennedy, Joan Goverman, Phyllis Brewster, Sheila Spiro, Gina Morea and many more. These women showed me the greatness of womanhood, the depth of injustice, and the satisfaction of participating in change. Whatever I invested in the "cause" at Caltech was given back to me tenfold.

My family. They taught me courage and self-reliance. During the final days of this thesis preparation, my parents provided more than emotional support. They pasted figure captions, ran errands, and made sure that I was fed. Thus, not only are they responsible for preparing me to start this, they are responsible for helping me to finish it.

My second family. The Vielmetters. Susanne, Jost, David, Eva, and Ariane. We experienced L.A. together: broken-down cars, camping trips, late nights drinking wine on the porch, big-screen movies, and *dinner*. We have shared a rare friendship. It has become so much a part of my life that I can't seem to remember the time before it, or conceive of a time without it.

Brad. For riding out the storm. And a storm it was. I firmly believe that supporting someone through a PhD is often more demanding than doing it. When I neglected him – he didn't neglect me. When I faltered – his faith in me didn't. I am fortunate to have this gentle, giving, loving man in my life.

And lastly - Quincey. He was with me in the lab, in the computer room, on the best days and on the worst. And he always wagged his tail.

This work was supported by the U.S. National Science Foundation through Award number CTS-8819584, by the U.S. Department of the Interior, Geological Survey through Grant number 14-08001-G1628, and through the State Water Resources Research Institute, Project number G1550, and by the University of California Water Resources Center, Project UCAL-WRC-W-735. The contents of this publication do not necessarily represent the views or policies of the U.S. Department of the Interior, nor does the mention of commercial companies or brand names suggest endorsement by the U.S. Government.

Abstract

It has been proposed that axisymmetric buoyant jets discharged vertically into a horizontal turbulent boundary layer flow undergo a transition from self-induced mixing to an ultimate state where mixing is dominated by the shear-flow turbulence. Both plume mixing and ambient shear-flow mixing have been separately well characterized by many previous studies and can be thought of as asymptotic mixing regimes. This investigation focuses on the transition between the two asymptotic regimes that is not well understood and that is often of particular engineering interest.

In this work, we present the results of a detailed experimental analysis of buoyant jet mixing in a turbulent shear flow. Our purpose is to obtain a detailed picture of the turbulent velocity field and the concentration distributions throughout the various mixing regimes in order to discern the effects of changes in various flow parameters on the predominant mixing mechanisms. The experimental technique employs buoyant jets whose fluid is optically homogeneous with that of the ambient shear flow. This enables the combined use of laser-Doppler velocimetry and laser-induced fluorescence to measure the velocity and concentration profiles, respectively.

Dimensional analysis indicates that the cross-flow shear velocity and the plume specific buoyancy flux are the parameters controlling the transition from plume mixing to diffusion mixing. Quantitative analysis of the experimental results indicates that the mixing is dominated entirely by diffusion, or shear-flow mixing, even close to the point of discharge. Further, we observe that within the diffusive mixing regime, a transition occurs from a region where the turbulent mixing coefficient is proportional to the local elevation to a region where the turbulent mixing coefficient is proportional to the boundary layer thickness. Detailed instantaneous spatial concentration distributions indicate that regions of dilution far below mean values persist well into the mixing regime

dominated by shear-flow turbulence. This indicates that both plume mixing and diffusion-type mixing models may provide a false sense of security with regard to the absolute minimum dilutions observed in actual flow situations since both methods focus on the minimum average dilution.

Table of Contents

List of Figures

List of Tables

Nomenclature

A	constant used in log-law velocity relation for open-channel flow
	constant used in LDV system calibration
A	cross-sectional area of channel flow, Wh, [L^2], cm^2
A'	modified constant for expanded log-law velocity relation
a_j, a_{bj}	constants for *j*et and *b*ouyant *j*et regions
A_j	cross-sectional area of buoyant jet discharge orifice, [L^2], cm^2
b	aspect ratio, h/W
	"puff" strength, B/U, [L^3/T^2]
B	constant used in LDV system calibration
B	specific buoyancy flux, $g'Q$, [L^4/T^3], cm^4/s^3
c	speed of light in a vacuum, [L/T]
$\overline{C}(z)$	time-averaged concentration of tracer material at location y, [M/L^3], M (gm/mole)
$C(z,t)$	concentration of tracer material, [M/L^3], M (gm/mole)
C_1, C_2, C_3	constants
C_i	concentration of tracer material at *i*th pixel, [M/L^3], M (gm/mole)
C_o	concentration of tracer material in unmixed source fluid, [M/L^3], M (gm/mole)
C_{tf}	concentration of tracer material in transfer function fluid, [M/L^3], M (gm/mole)
d	diameter of buoyant jet discharge orifice, [L], cm
D	turbulent diffusion coefficient, [L^2/T], cm^2/s
D_i	dark noise for laser-induced fluorescence calibration

f	Darcy-Weisbach friction factor
	frequency
f_o	frequency of light as seen by stationary observer
f_p	frequency of light reflected by moving particles
f_s	frequency of source emission light
F_d	densimetric Froude number
g	gravitational acceleration, [L/t^2], cm^2/s
g'	apparent gravitational acceleration, $(\Delta\rho/\rho)g$, [L/T^2], cm/s^2
G_i	intermediate LIF calibration function
h	depth of cross flow, [L], cm
H_i	optical transfer function for laser-induced fluorescence calibration
$\vec{i}$	unit vector, perpendicular bisector between $\vec{x}_s$ and $\vec{x}_o$
i_f	number of first high-intensity pixel reading for magnification ratio
i_l	number of last high-intensity pixel reading for magnification ratio
I_o	laser beam intensity as it enters the test section
I_e	laser beam intensity as it exits the test section
I_{tf}	laser beam intensity as it enters the test section during calibration procedure
$\vec{j}$	unit vector, perpendicular to source emission direction $\vec{x}_s$
l_b	buoyancy length scale, B/U^3, [L], cm
l_b	length scale describing where a plume will bend under the action of the cross flow, B/U^3, [L], cm
L_c	length of calibration vessel, [L], cm
l_j	length scale describing where a jet will bend under the action of the cross flow, $M^{1/2}/U$, [L], cm
l_j	momentum length scale, $M^{1/2}/U$, [L], cm

l_m length scale describing where momentum generated by buoyancy becomes equivalent to initial momentum, $M^{3/4}/B^{1/2}$, [L], cm

l_q length scale describing where initial geometry effects are no longer important, $A_j^{1/2}$, [L], cm

m mass

m momentum impulse, M/U, [L^3/T], cm^3/s

mass per unit area [M/L^2]

mf_a mole fraction of alcohol

mr magnification ratio

M molar, (gm/mole)

M specific momentum flux, [L^4/T^2], cm^4/s^2

$\dot{M}$ rate of mass discharge, [M/T]

n index of refraction

O observation point

p particle

P wetted perimeter of channel flow, $2h + w$, [L], cm

q total rate of mass transport of a tracer [ML/T]

Q volumetric flow rate, [L^3/T], cm^3/s

r correlation coefficient for linear fit using least-squares

R_h hydraulic radius, A/P, [L], cm

R_o source Richardson number, $QB^{1/2}/M^{5/4}$

s channel slope

s_{cf} cross-flow surface slope

s_p center-to-center spacing between diodes in photo diode array, [L], cm

S dilution

source

S_d non-dimensionalized dilution in the shear-flow (diffusion) mixing regime

S_p	non-dimensionalized dilution in the plume mixing regime
T	temperature
t	time, [T], s
U	magnitude of spatially averaged cross-flow velocity (averaged across vertical cross-section), [L/T], cm/s
u	magnitude of time-averaged cross-flow velocity in x-direction(averaged at one vertical location over time), [L/T], cm/s
	speed of particle
u'	magnitude of fluctuating component of cross-flow velocity in x-direction, [L/T], cm/s
u_p	speed of wavefronts as observed by particle p, [L/T], cm/s
u_*	shear velocity, [L/T], cm/s
u^+	non-dimensionalized velocity U/u_*
V	volume, [L^3], cm^3
	voltage output from LDV signal processor
V_i	voltage output from the ith element of the photo diode array
W	magnitude of averaged velocity of buoyant jet at orifice, [L/T], cm/s
	width of channel, [L], cm
w'	magnitude of fluctuating component of cross-flow velocity in z-direction, [L/T], cm/s
w_m	magnitude of centerline velocity in an axisymmetric flow, [L/T], cm/s
w_A, w_B	weight of picnometer A, B
$w_{A,sw}$, $w_{B,sw}$	weight of salt-water filled picnometer A, B
x	coordinate measuring horizontal distance from buoyant jet release point, [L], cm
x^+	non-dimensionalized horizontal coordinate, $B^{2/3}x^{1/3}/u_*Uh$
x_{fm}	flow meter percentage reading

$\vec{x}_o$	unit vector from particle to point of observation, O
$\vec{x}_p$	unit vector in direction of particle trajectory
$\vec{x}_s$	unit vector in direction of source emission
y	coordinate measuring spanwise distance from flume center, [L], cm
z	coordinate measuring vertical distance from flume bottom, [L], cm
z^+	non-dimensionalized vertical coordinate, zu_*/ν
z_c	vertical coordinate measuring location of bent-jet to bent-plume behavior, [L], cm

Greek

α	angle from vertical for index of refraction calculation
	angle of particle path with $\vec{i}$
β	angle of particle path with $\vec{j}$
ε	attenuation parameter for Rhodamine 6G, [1/L], 1/cm
ε_t	transverse mixing coefficient, [L^2/T], cm^2/s
Φ	dimensionless transverse mixing coefficient
κ	von Karman constant used in log-law formulation of open-channel flow
λ_o	apparent wavelength of light as seen by observer, [L]
λ_p	apparent wavelength of light emitted by particle, [L]
λ_s	wavelength of light emitted by source, [L]
λ_v	wavelength of light in a vacuum, [L]
ν	kinematic viscosity, [L^2/T^2], cm^2/s^2
θ_{op}	angle between particle trajectory and observation point, O
θ_{os}	angle between source direction and observation point, O
ρ_a	ambient, cross-flow fluid density, [M/L^3], kg/m^3
ρ_{aw}	density of ethanol(alcohol)-water mixture, [M/L^3], kg/m^3

ρ_O	buoyant jet fluid density, [M/L^3], kg/m^3
ρ_{sw}	density of salt-water mixture, [M/L^3], kg/m^3
$\Delta\rho/\rho$	relative density difference
$\Delta\rho_O$	density difference of buoyant jet unmixed fluid and ambient fluid, [M/L^3], kg/m^3
τ_O	shear-stress at boundary, [M/LT^2], kg/m^3
ξ_i	distance to *i*th pixel location
ζ	arbitrary flow variable

Chapter 1. Introduction

As human beings, we generate materials that require disposal. In some cases, the materials are toxic in high concentrations but relatively harmless in low concentrations; in other cases, the materials appear naturally in the environment at low concentration levels and disposal into the environment is an appropriate method of recycling. Environmental engineers are faced with the task of discharging such materials into the environment in a responsible and knowledgeable manner. Often, the primary concern is to get the waste material diluted with other materials as rapidly as possible, and to predict this initial dilution accurately enough to circumvent harm.

Since waste fluids frequently have a density different from the receiving fluid, buoyant jets are common in the release of the waste materials. If the buoyant jet discharges into a receiving fluid that is flowing and is turbulent, then this receiving fluid has turbulent mixing characteristics of its own. This study focuses precisely on such a case; specifically, that of buoyant jets discharged into a cross flow with shear as shown in Fig. 1.1.

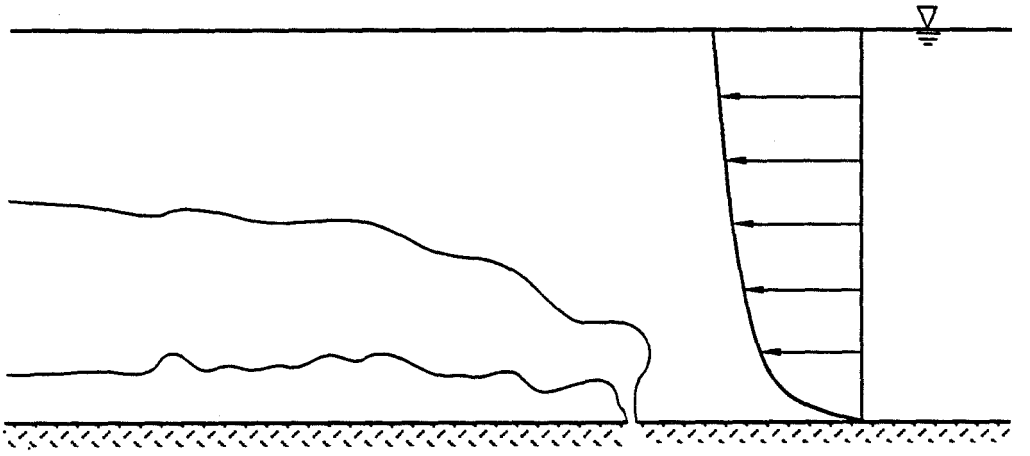

Figure 1.1 Buoyant jet discharged into a cross flow with shear

Many of the models in use by regulatory agencies to describe the dilution of wastes and toxic materials released to the environment depend upon one or the other of two basic approaches:

1. Buoyant jet and plume models that define the dilution of emitted materials in a zone near the point of discharge.
2. Diffusion models that use knowledge of ambient turbulence to define the dilution in regions removed from the point of discharge.

It is often argued that models which ignore ambient turbulence in consideration of buoyant jet mixing are conservative since ambient turbulence should only enhance dilution. Similarly, when diffusion models are considered, the effect of initial buoyant jet mixing can be viewed simply as a shift in origin of the discharged tracer. However, in many situations it is the transition region of the flow field for which reasonably accurate estimates of the dilution are required.

There have been extensive research studies on turbulent buoyant jets and plumes (*e.g.*, see List (1982ab), Papanicolaou and List (1987,1988), and Papantoniou and List (1989) for comprehensive reviews). Much of this prior work has resulted in the development of computer models of jet and plume dilution that are widely used in industry and by regulatory agencies (Muellenhof *et al.*, 1985; Hanna *et al.*, 1982; Schatzmann, 1979).

Turbulent diffusion in turbulent flows has received a large amount of attention since the first, and probably the most widely referenced, paper by Taylor (1921). Subsequent work by hundreds of others has resulted in three basic approaches for predicting the dilution caused by turbulent diffusion:

(a) Simulation models based on statistical methods (Lamb, 1978; Sawford, 1985ab; Legg and Raupach, 1982)

(b) Diffusion equation models (Raupach and Legg, 1983; Nokes *et al.*, 1984)

(c) Langevin equation models (Raupach, 1983; Pearson *et al.*, 1983)

These models have been combined in many variations of "puff" and "Gaussian plume" models. In addition, there are numerous field studies (*e.g.*, Sawford *et al.*, 1985; Gudiksen *et al.*, 1984), and laboratory work (*e.g.*, Deardorff and Willis, 1984; Nokes and Wood, 1988). It is interesting that despite all of this work on both jets and plumes and on ambient turbulent mixing, there is apparently little work that relates the two mixing processes to each other.

1.1 Analysis

In chapter 2 we will show that a buoyant source with volume flow, Q, and specific buoyancy flux, $B=gQ\Delta\rho/\rho$, released in a steady uniform ambient flow with an average velocity, U, will attain a dilution

$$S \sim \frac{B^{2/3}x^{1/3}}{UQ}, \qquad x >> \frac{B}{U^3} \tag{1.1}$$

where x is the horizontal distance from the release point (Fischer *et al.*, 1979). This implies that the dilution at a fixed distance from the source decreases with increasing mean flow velocity. However, the minimum dilution of a continuous source that results from mixing induced by turbulent diffusion is estimated to be (Fischer *et al.*, 1979)

$$S \sim \frac{4\pi Dx}{Q} \tag{1.2}$$

where D is a turbulent diffusion coefficient. The use of a constant diffusion coefficient can be justified using Taylor's (1921) argument, provided that a fluid particle has had the opportunity to sample from all possible scales of the turbulence. In general, D is proportional to the flow depth, h, and shear velocity, u_*, which are measures of the turbulence scales. In this case,

$$S \sim \frac{u_* hx}{Q} \tag{1.3}$$

In other words, the rate of dilution is defined by the shear velocity and the size of the largest eddies. Since u_* increases with U, the dilution will increase with mean cross-flow velocity at a fixed distance downstream from the source point. (It is noted in passing that for normal channel flow

$$\left(\frac{f}{8}\right)^{\frac{1}{2}} = \frac{u_*}{U} \tag{1.4}$$

where f is the Darcy-Weisbach friction factor and for a channel

$$f = 4\left[\frac{2ghsU}{U^3}\right] \tag{1.5}$$

where s is the channel slope. In this case, f is four times the ratio of the turbulent kinetic energy dissipation rate, $\rho ghsU$, to the mean flow kinetic energy flux, $(\rho U^3)/2$. Thus for constant f, u_* increases with U, the average cross-flow velocity).

As stated above, Eq. 1.1 indicates that at constant x the dilution must ***decrease*** with increasing mean cross-flow velocity. It is useful to imagine that in this regime, mixing is affected by plume-generated vortical interactions with the cross-flow. These interactions require time to mix the source fluid with the cross-flow fluid. Therefore, when the mean cross-flow velocity increases, source fluid reaches the point of observation, x, faster. The effective amount of time for mixing diminishes and the dilution goes down. In essence, the source fluid is swept past the point of observation before it has time to dilute.

Equations 1.2 and 1.3, on the other hand, indicate that at a constant distance, x, the dilution must ***increase*** with increasing mean cross-flow velocity. In the diffusive regime, a larger turbulent diffusion coefficient enhances mixing and the diffusion coefficient increases with the mean cross-flow velocity. Essentially, in this regime, a higher mean cross-flow velocity implies a more turbulent, or "churning" flow, and dilution improves. This explanation of the effect of increasing cross-flow velocity on the dilution

in the diffusion regime is somewhat incomplete. However, it is adequate for this introduction wherein we are trying to gain insight to the problem. A more complete discussion appears in chapter 2.

Since both these regimes exist asymptotically, there must be a point at which a transition occurs from plume turbulence-induced mixing to mean-flow turbulence-induced (or shear-flow) mixing. This simplistic argument is the basis of the analysis.

1.2 Objective

The purpose of this investigation is to determine the nature of transition between the plume-mixing regime and the shear-flow mixing regime of a buoyant jet in a cross flow.

The research is primarily experimental. A series of turbulent buoyant jets were discharged into a turbulent cross flow within a laboratory water channel. The concentration of a tracer material was measured along a line within the discharged fluid using the laser-induced fluorescence method developed by Koochesfahani (1984), and modified and refined by Papantoniou and List (1989). This method relies on the ability of certain organic dyes, in this case Rhodamine 6-G, to fluoresce under the action of laser light. The fluoresced light is at a wavelength different from the wavelength of the excitation light. Fluid velocities were measured using laser-Doppler velocimetry developed by Gartrell (1979) and modified by Skjelbreia (1987). These optical techniques were made possible by the use of fluids differing in density but rendered optically homogeneous by the methods developed by McDougall (1979) and modified by Hannoun (1985).

Chapter 2. Theory

The intellectual exercise necessary for understanding the flow of a buoyant jet in a cross flow with shear is one of building, little by little, a progressively more solid understanding of this complex flow from a fundamental understanding of simpler flows. In the brief analysis of chapter 1, we presented equations describing the asymptotic rate of dilution in the plume and shear-flow mixing regimes. Both of these asymptotic results have been previously developed and well-characterized. Several other transitions, that are also well understood, precede the plume to shear-flow mixing transition. A discussion of these earlier transitions as well as the asymptotic mixing regimes is an aid to understanding the transition from plume mixing to shear-flow mixing that is the focus of this study.

In this chapter, we recapitulate the previous work done in simpler flows and then discuss the work unique to this study. Therefore, we first discuss buoyant jets released into a quiescent medium, then discuss buoyant jets released into a cross flow without shear before beginning the dimensional argument which leads to the equation describing the dilution of a plume in a uniform cross-flow, Eq. 1.1. In the same spirit, we discuss the dilution of a point source release into a diffusive environment to obtain Eq. 1.2. At that

point, we will be poised to build the hypotheses regarding the transition from plume to shear-flow mixing.

2.1 Buoyant jet discharged into a quiescent medium

A buoyant jet is distinguished from a simple jet by an initial density difference. Namely, a buoyant jet has a density difference, $\Delta\rho_o = (\rho_a - \rho_o)$, from the ambient fluid that makes it either positively, or negatively buoyant. The orientation of the buoyant jet with respect to the gravitational field is important in these flows because of the body force introduced by the density difference. Fundamentally, a positively buoyant jet discharged vertically upward is the same as a negatively buoyant jet discharged vertically downward. Since in this experimental work, the configuration was exclusively that of a positively buoyant jet discharged vertically upward, we will use the geometry of Fig. 2.1 to discuss the development of the governing equations.

A buoyant jet can be thought of locally as either a jet or a plume, depending upon the ratio of the local momentum flux to the initial momentum flux. Of course, plume-like characteristics will always eventually dominate the flow. This can be argued as follows. If the receiving fluid is stagnant, in other words, has no inherent flow-mixing character of its own, then, the only parameters that can affect the flow are the initial volume flux, Q, the initial specific momentum flux, M, the initial specific buoyancy flux, B, and the vertical distance from the point of release, z. It is worthy of note that the viscosity might also be of significance in such flows. However, we have assumed here that the initial jet Reynolds number, $M^{1/2}/\nu$ is sufficiently large that the flow is fully turbulent, and hence, that viscosity is unimportant in determining the flow. This assumption is valid provided the initial jet Reynolds number exceeds 4000 as discussed by Labus and Symons (1972). Additionally, we have made the Boussinesq assumption, i.e., that with regard to the basic

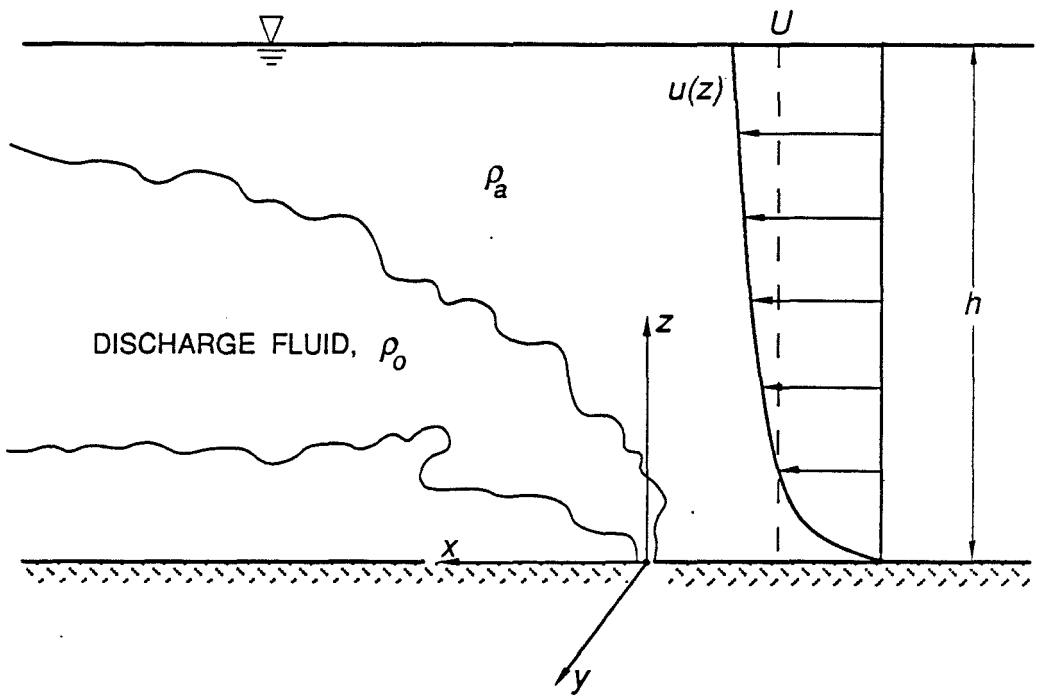

Figure 2.1 Geometry of buoyant jet discharged vertically into a horizontal turbulent boundary layer

inertial aspects of flow, $\rho_o \approx \rho_a \approx \rho$. We can therefore form, by dimensional analysis, two dimensionless quantities:

$$\frac{M^{1/2}z}{Q}, \quad \text{and} \quad \frac{B^{1/2}z}{M^{3/4}}$$

Since z has the dimensions of length, these dimensionless quantities define two length scales, l_q, and l_m, respectively:

$$\frac{z}{l_q} = \frac{M^{1/2}z}{Q}, \quad \text{and} \quad \frac{z}{l_m} = \frac{B^{1/2}z}{M^{3/4}}$$

where (2.1)

$$l_q = \frac{Q}{M^{1/2}}, \quad \text{and} \quad l_m = \frac{M^{3/4}}{B^{1/2}}$$

It is recognized that the first length scale is influenced only by parameters that effect the behavior of a jet. The second length scale, on the other hand, has parameters that are a measure of the relative initial momentum-dominated to buoyancy-dominated characteristics of the buoyant jet. Any other dimensionless flow variable, ζ, must, therefore, be a function of these two dimensionless quantities, z/l_q, and z/l_m.

$$\zeta = f\left(\frac{z}{l_q}, \frac{z}{l_m}\right)$$

It can be argued that for $z/l_q >> 1$, equivalent conditions are:

1. $z \to \infty$ with l_q fixed $(M, Q \text{ fixed})$

or

2. $l_q \to 0$ with z fixed
   a. $l_q \to 0$, is equivalent to $M \to \infty$ or
   b. $l_q \to 0$, is equivalent to $Q \to 0$

In 2a and 2b above, we might question how it is possible to reason that $M \to \infty$, is equivalent to $Q \to 0$, since Q and M are coupled. If we examine the equations describing Q and M, the explanation is clear. Since,

$$Q \propto Wd^2 \quad \text{and} \quad M \propto W^2 d^2$$

where W is the average velocity of the buoyant jet discharge, and d is the diameter of the discharge, if Q is to remain finite, the only way that M can simultaneously approach infinity is for $d \to 0$. Thus, $l_q \to 0$, is equivalent to the orifice diameter approaching zero. In other words, as z is increased (condition 1, above) it is as if the initial volume flux, Q, drops from the list of variables defining the flow. This is exactly analogous to dropping the viscosity, ν, from the list of relevant variables when the Reynolds number exceeds a given threshold value. Therefore,

$$\zeta = f\left(\frac{z}{l_m}\right) \text{ for } \frac{z}{l_q} >> 1$$

This is of course provided that the initial jet Reynolds number exceeds 4000 as mentioned above and the Boussinesq assumption is valid.

Many previous studies (Crow and Champagne (1971), Corrsin and Uberoi (1950), Rosler and Bankoff (1963), Sami *et al.* (1967)) have shown that l_q is an indicator of the distance from the point of discharge where a steady decay of turbulence along the axis of a jet begins to occur. These studies have shown that at a distance from the point of discharge equivalent to ten times this length scale, the turbulence within the jet is fully developed. This region of flow development is referred to as the *zone of flow*

establishment (ZFE). Past this region, the velocity and concentration profiles of the flow are self-similar and therefore this region is referred to as the *zone of established flow (ZEF)*. Therefore, the first length scale, l_q, can be regarded as a measure of the distance over which initial geometry effects the flow. Precisely, we can write:

$$\zeta = f\left(\frac{z}{l_m}\right) \text{ for } \frac{z}{l_q} > 10$$

and since, $l_q = Q/M^{1/2} = A^{1/2} = (\pi/4)^{1/2}d$, this is approximately equivalent to assuming that beyond ten diameters downstream, the initial volumetric flux is no longer important in defining the flow.

What about the second length scale, l_m, in Eq 2.1 above?

We reasoned in forming, z/l_q and z/l_m that all dimensionless flow variables of a buoyant jet must be functions of these two non-dimensional parameters. Thus, if we consider some limiting cases of the flow, we will elucidate the significance of l_m.

Consider a buoyant jet with initial momentum flux, M, and initial specific buoyancy flux, B, at a location where $z/l_q > 10$. The only characteristic length scale of importance to the flow then, is l_m. All flow variables must be some function of z/l_m alone.

As an example, consider the centerline velocity, w_m. If we are interested in examining the functional dependence of w_m on z/l_m we must first make w_m non-dimensional. The velocity, w_m, has dimensions, [L/T]. Therefore, we need some combination of B and M to use for the non-dimensionalization:

$$B^n M^p = \left[\frac{\mathrm{L}^4}{\mathrm{T}^3}\right]^n \left[\frac{\mathrm{L}^4}{\mathrm{T}^2}\right]^p \text{ then, we have}$$

$4n + 4p = 1$ and

$3n + 2p = 1$ which gives,

$n = 1/2$, and $p = -1/4$ thus,

$$\frac{B^{1/2}}{M^{1/4}} = \left[\frac{\mathrm{L}}{\mathrm{T}}\right] \text{ and } w_m \frac{M^{1/4}}{B^{1/2}} \text{ is dimensionless}$$

Then, since z/l_m is the only parameter that the flow variables can depend on, it must be true that:

$$w_m \frac{M^{1/4}}{B^{1/2}} = f\left(\frac{z}{l_m}\right) = f\left(\frac{zB^{1/2}}{M^{3/4}}\right) \tag{2.2}$$

Now suppose we consider cases as we did above for l_q. First, consider $z/l_m \ll 1$. This is equivalent to:

1. $z \to 0$ with l_m fixed $(M, B$ fixed$)$

or

2. $l_m \to \infty$ with z fixed
   a. $l_m \to \infty$, is equivalent to $B \to 0$ or
   b. $l_m \to \infty$, is equivalent to $M \to \infty$

For case 2a, where the initial specific buoyancy flux goes to zero, flow variables must not depend on B, and thus the functional dependence of Eq. 2.2 must be such that the specific buoyancy flux no longer appears. This is satisfied as follows:

$$w_m \frac{M^{1/4}}{B^{1/2}} = f\left(\frac{z}{l_m}\right) = f\left(\frac{zB^{1/2}}{M^{3/4}}\right)$$

$$w_m \frac{M^{1/4}}{B^{1/2}} \propto \left(\frac{zB^{1/2}}{M^{3/4}}\right)^{-1} = \left(\frac{M^{3/4}}{zB^{1/2}}\right)$$

$$w_m = a_j \frac{M^{1/2}}{z} \tag{2.3}$$

which is the centerline velocity equation for a jet in a quiescent medium.

Second, if we consider cases for which $z/l_m \gg 1$. This is equivalent to either

1. $z \to \infty$ with l_m fixed $(M, B$ fixed$)$

or

2. $l_m \to 0$ with z fixed
   a. $l_m \to 0$, is equivalent to $B \to \infty$ or
   b. $l_m \to 0$, is equivalent to $M \to 0$

and if there is to be no dependence on the initial momentum flux, M, as is the case for 2b, then, we find that

$$w_m \frac{M^{1/4}}{B^{1/2}} = f\left(\frac{z}{l_m}\right) = f\left(\frac{zB^{1/2}}{M^{3/4}}\right)$$

$$w_m \frac{M^{1/4}}{B^{1/2}} \propto \left(\frac{zB^{1/2}}{M^{3/4}}\right)^{-1/3} = \left(\frac{M^{1/4}}{z^{1/3}B^{1/6}}\right)$$

$$w_m = a_p \frac{B^{1/3}}{z^{1/3}} = a_p\left(\frac{B}{z}\right)^{1/3}$$

which is the equation governing the centerline velocity for a plume. Thus, z/l_m, can be thought of as the ratio that determines whether the flow is jet-like or plume-like.

Finally, then, we have determined the flow can be thought of as first going through a transition to the zone of fully established flow and becoming jet-like, this is for $z>>l_q$ but $z<<l_m$, then transitioning from jet-like behavior to plume-like behavior, and this occurs after $z>>l_m$. What, however, about the case when l_q and l_m are of the same order? This is equivalent to the Richardson number, $R_O = l_q/l_m = 1$, or the densimetric Froude number, $F_d = (\pi/4)^{1/4} \approx 1$ since $R_O = (\pi/4)^{1/4}(1/F_d)$. In this case, there would be no jet-like region of the flow. Instead, the flow would be immediately plume-like except for the region close to the discharge where initial geometry effects are important.

2.2 Buoyant jet discharged into a uniform ambient cross flow without shear

In many practical applications, buoyant jets are released into environments where there exists a cross flow with shear. It is precisely for this reason that the present work focuses on such flow conditions. Large numbers of the earlier experimental investigations of jets or buoyant jets under cross flow conditions were conducted such that no shear existed in the cross flow. As an example, consider Wright's (1977) experiments which employed a negatively buoyant jet discharged vertically downward and dragged across the surface of a quiescent medium to create an effective cross-flow condition. The introduction of a cross flow complicates the flow behavior by introducing another driving force for the system, namely, the momentum flux of the cross flow itself. Thus, the next logical step in building our understanding of buoyant jets in a cross flow *with* shear is to examine the release of a buoyant jet into a cross flow *without* shear.

As mentioned above, we will look only at a positively buoyant jet discharged vertically upward. In this flow situation, we can consider two distinct geometric regions of the flow. First, when the buoyant jet has not yet been significantly influenced by the cross flow, and therefore, is essentially rising vertically, and second, after the buoyant jet has succumbed to the force of the cross flow and is horizontal. This is sketched in Fig. 2.2. Wright (1977) referred to these two configurations as the near-field and the far-field flows and reasoned that the fundamental flow behavior was different in these two regions. Flows in the near-field, Wright suggested, behave as if they were released into a quiescent medium but advected at the average velocity of the flow. It is as if the buoyant jet is being "sheared" by the action of the cross-flow as depicted in Fig. 2.3. (Note: This is an important assumption which will be referred to later in chapter 5.) As Wright mentions, this is true beyond the region of acceleration only. A buoyant jet enters the cross flow with zero horizontal velocity and must be accelerated up to the velocity of the cross flow. This is accomplished by the entrainment of horizontal momentum and by a pressure force

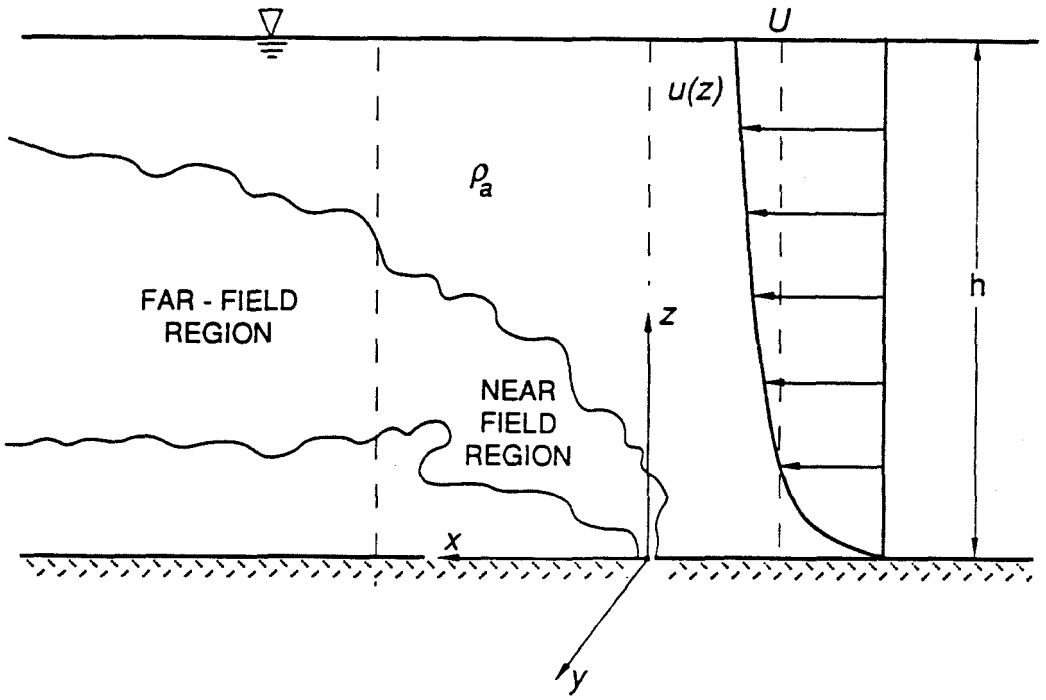

Figure 2.2 Near-field and far-field regimes of a buoyant jet in a uniform cross-flow

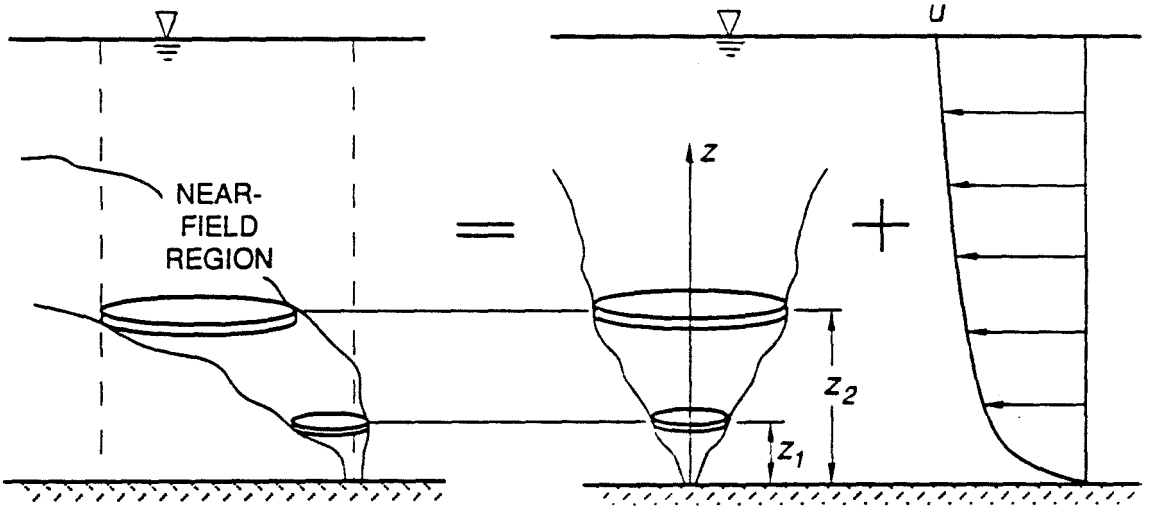

Figure 2.3 Effect of cross-flow shearing action on geometry of buoyant jet flow

exerted on the buoyant jet by the cross flow. Hirst (1971a), Chu and Goldberg (1974) suggested that this acceleration occurs within the first few diameters downstream of the point of release. Beyond these first few diameters the vertical velocity of the buoyant jet so dominates the flow that the influence of the cross flow is not yet sufficiently important to influence the flow and hence the cross flow effect is minimal. Therefore, it is assumed that beyond this initial acceleration region, while the acceleration forces may skew the shape of the buoyant jet and hence its concentration and velocity profiles, they do not otherwise affect the flow. The work of Priestley (1956) confirms that buoyant jets even very near the source are advected horizontally at the cross-flow velocity. (The present work also verifies this result as will be seen later.)

When the cross-flow velocity is considered as an additional variable, more length scales are possible. If we neglect the initial volume flux, Q (this is reasonable provided we are not close to the point of discharge) then the new length scales are:

$$l_j = \frac{M^{1/2}}{U} \text{ and } l_b = \frac{B}{U^3} \tag{2.4}$$

l_j can be thought of as the ratio of the buoyant jet momentum to the momentum of the cross flow, and thus, a measure of when a momentum-dominated buoyant jet would bend under the influence of the ambient velocity. l_b, similarly, can be regarded as a measure of when a buoyancy-dominated buoyant jet would bend under the action of the ambient velocity. In other words, these length scales refer to the point at which the vertical velocity of the buoyant jet (whether it be in the momentum-dominated or the buoyancy-dominated regime) decays to the cross-flow velocity. Thus, for $z/l_j \ll 1$, no appreciable bending over of a momentum-dominated buoyant jet would be apparent, while at $z/l_j \sim O(1)$ the jet would begin to bend. Further into the flow, when $z/l_j \gg 1$, the buoyant jet would be nearly horizontal. An analogous argument follows for a buoyancy-dominated buoyant jet, where l_b is the governing characteristic length scale.

If we recall the two length scales that were determined in the preceeding analysis of buoyant jets in a quiescent medium, namely, l_q and l_m, and assume that the flow rapidly achieves a state wherein l_q is no longer relevant, then the three length scales, l_m, l_j, and l_b, remain. These length scales are not independent of one another, rather only two independent length scales are possible. Notice for example that $l_m = l_j^{3/2} l_b^{-1/2}$. Hence, any combination of two of these three length scales makes possible two flow regimes: the jet→plume→bent plume regime, or the jet→bent jet→bent plume regime.

The next logical question is, of course, how is it possible to determine, *a priori* which of these flow regimes will be achieved? The relative magnitude of l_b with regard to l_j determines the flow regime. As an example, consider a buoyant jet that has length scales, l_j and l_b such that $l_j < l_b$. In this case, we reason that if the buoyant jet were in the momentum-dominated, or pure jet regime, then it would bend under the action of the cross flow before the same buoyant jet, in the buoyancy-dominated, or pure plume regime would bend. Thus, since the actual flow possesses both initial momentum flux and initial specific buoyancy flux, we reason that it will transition to plume-like behavior before it bends. The momentum flux induced by the buoyancy so far exceeds the initial momentum flux that it controls the flow. This induced momentum flux is more powerful in resisting the influence of the cross-flow velocity than is the initial momentum flux. Therefore, the flow regime is that of a jet, plume, bent plume. Further, as we discussed above, since the jet region occurs before the bend in the flow, it can be viewed as if it were a jet in a quiescent medium, but advected with the ambient cross flow. The characteristic length scale, l_m, would thus determine the transition from jet to plume behavior. Clearly, in this case, l_m and l_b, are the length scales governing the flow.

If, on the other hand, $l_j > l_b$ then the initial specific momentum flux is more important than the momentum generated by the specific buoyancy flux in withstanding the influence of the ambient velocity, and the flow will be that of a jet, bent jet, bent plume. In this case, we cannot assume that the flow behaves as if it were in a quiescent medium and

simply advected with the cross-flow velocity and the transition from jet-like to plume-like behavior will not occur at l_m. In fact, precisely because the vertical velocity of the buoyant jet has decayed to the level of the cross-flow velocity, we cannot assume that the cross flow has no effect on the flow behavior. We must model the flow and the transition from jet-like to plume-like behavior differently.

We have already found length scales that we can use in the development of equations for a jet-like or a plume-like flow in the far-field. There are no more unique length scales possible. However, we have more information regarding the flow that we have not used to this point. Namely, the flow itself, in transitioning from bent jet to bent plume behavior, cannot be discontinuous. Therefore, if we match one of the flow variables, for example the centerline velocity, between the jet and the bent jet, or between the bent jet and the bent plume cases, we should be able to estimate these transitions. Before it is possible to match the centerline velocity between these cases, however, we must develop the equations describing the centerline velocity in the far-field regimes. (Note: The relevance of defining transition as the point of centerline velocity equivalence is discussed in more detail in chapter 5.)

As we did in the previous arguments for the centerline velocity in the near-field jet, we can derive equations for the centerline velocity in the far-field. We are able to do this only for the limiting cases of momentum-dominated, pure jet-like flow, or buoyancy-dominated, pure plume-like flow.

In the bent-jet or bent-plume regime, precisely because the cross-flow has affected the flow sufficiently to bend it, the influence of the cross-flow velocity cannot be ignored. Therefore, in the bent-jet regime, we liken the flow to that of a cylindrical momentum puff. Again relying on dimensional analysis, we determine that the flow can depend only on the momentum impulse, m, and on the vertical distance from the point of release; thus, $w_m = f(m,z)$. Dimensionally, this implies that:

$$w_m = a_{bj}\frac{m}{z^2}$$

If we write the momentum impulse as $m=M/U$, then:

$$w_m = a_{bj}\frac{M}{Uz^2} \tag{2.5}$$

Similarly, in the buoyancy-dominated region of the flow, the bent plume flow resembles a bouyant thermal. In this case, the vertical velocity depends on the buoyant impulse or the "puff" strength, b, and the vertical distance from the point of release. Therefore, $w_m = f(b,z)$. Dimensionally, then:

$$w_m = a_{bp}\left(\frac{b}{z}\right)^{1/2}$$

If we write the buoyant impulse, $b=B/U$, then:

$$w_m = a_{bp}\left(\frac{B}{Uz}\right)^{1/2} \tag{2.6}$$

The equations governing the centerline velocity in these two limiting cases are summarized below:

$$\begin{aligned} \frac{w_m}{U} &\propto \left(\frac{M^{1/2}}{Uz}\right)^2 = \left(\frac{l_j}{z}\right)^2 \quad \text{for } \frac{z}{l_j} >> 1 \\ \frac{w_m}{U} &\propto \left(\frac{B}{U^3 z}\right)^{1/2} = \left(\frac{l_b}{z}\right) \quad \text{for } \frac{z}{l_b} >> 1 \end{aligned} \tag{2.7}$$

where z refers to the vertical coordinate of the buoyant jet axis. The transition from jet to bent-jet behavior is found by finding the value of z where the centerline velocities are equal (assuming that the virtual origin for bent jet flow occurs at $z = 0$):

$$a_j \frac{M^{1/2}}{z} = a_{bj} \frac{M}{Uz^2}$$

$$z_{j-bj} = \left(\frac{a_{bj}}{a_j}\right) \frac{M^{1/2}}{U}$$

$$z_{j-bj} = \left(\frac{a_{bj}}{a_j}\right) l_j \tag{2.8}$$

We similarly find the point at which transition from far-field jet-like flow to far-field plume-like flow. The location of this transition is referred to as $z_{bj\text{-}bp}$:

$$a_{bj}\left(\frac{M}{Uz^2}\right) = a_{bp}\left(\frac{B}{Uz}\right)^{1/2}$$

$$z^3 = \left(\frac{a_{bj}}{a_{bp}}\right)^2 \left(\frac{M}{U}\right)^2 \left(\frac{U}{B}\right)$$

therefore:

$$z_{bj-bp} = \left(\frac{a_{bj}}{a_{bp}}\right)^{2/3} \left(\frac{M^2}{UB}\right)^{1/3} \tag{2.9}$$

Table 2.1 summarizes the two possible flow conditions along with the characteristic vertical length scales that determine the transitions for each regime.

Table 2.1 Summary of flow variables for two different flow regimes

Condition	Flow regime	First Transition	Second Transition
$l_j<l_b$	jet, plume, bent plume	jet - plume, l_m	plume - bent plume, l_b
$l_b<l_j$	jet, bent jet, bent plume	jet - bent jet, lj	bent jet - bent plume

Table 2.2 summarizes the definitions of each of the characteristic length scales. Figures 2.4 and 2.5 show the centerline velocity as a function of the buoyant jet vertical coordinate in each of these flow regimes.

Table 2.2 Summary of characteristic length scales

Transition	Characteristic length	Equation
→ zone of fully established flow	l_q	$\frac{Q}{M^{1/2}}$
jet → plume (near-field)	l_m	$\frac{M^{3/4}}{B^{1/2}}$
jet → bent jet	l_j	$\frac{M^{1/2}}{U}$
plume → bent plume	l_b	$\frac{B}{U^3}$
	Elevation	
jet → bent jet	$z_{j\text{-}bj}$	$\left(\frac{a_{bj}}{a_j}\right) l_j$
bent jet → bent plume (far-field)	$z_{bj\text{-}bp}$	$\left(\frac{a_{bj}}{a_{bp}}\right)^{2/3}\left(\frac{M^2}{UB}\right)^{1/3}$

We do not formulate the transition from jet→plume behavior since in all the experiments conducted for this investigation, the flow regime was that of a jet→bent jet→bent plume. However, the derivation is exactly analogous.

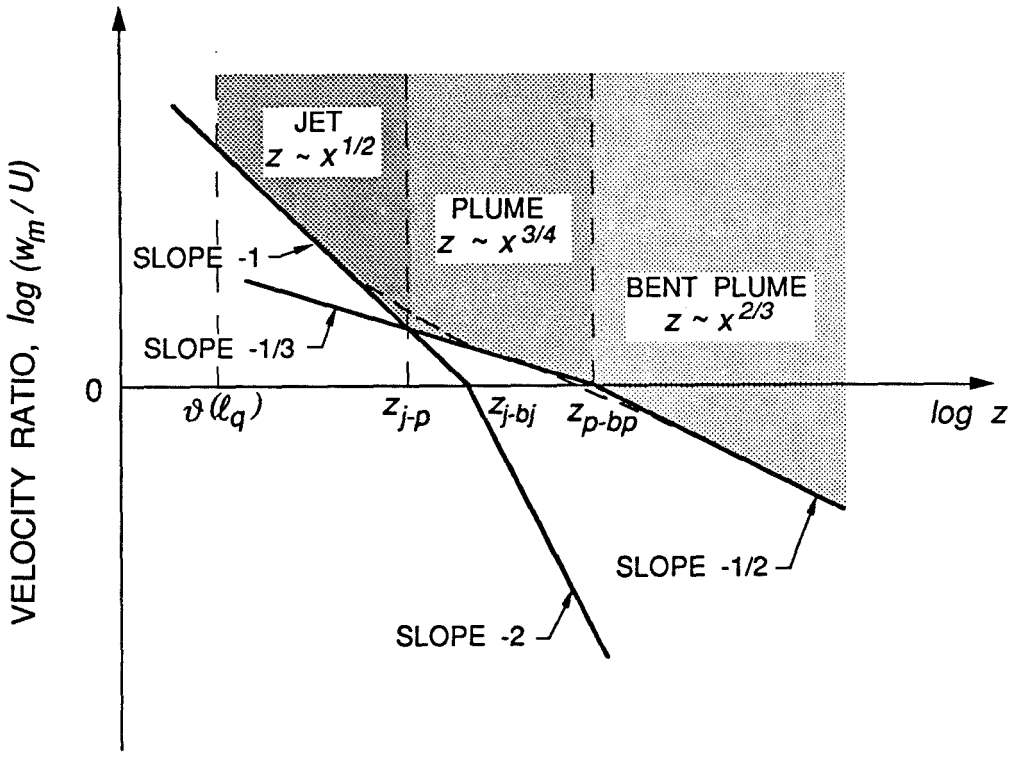

Figure 2.4 Centerline velocity as a function of vertical distance, jet-plume-bent plume regime (adopted from Fischer (1979))

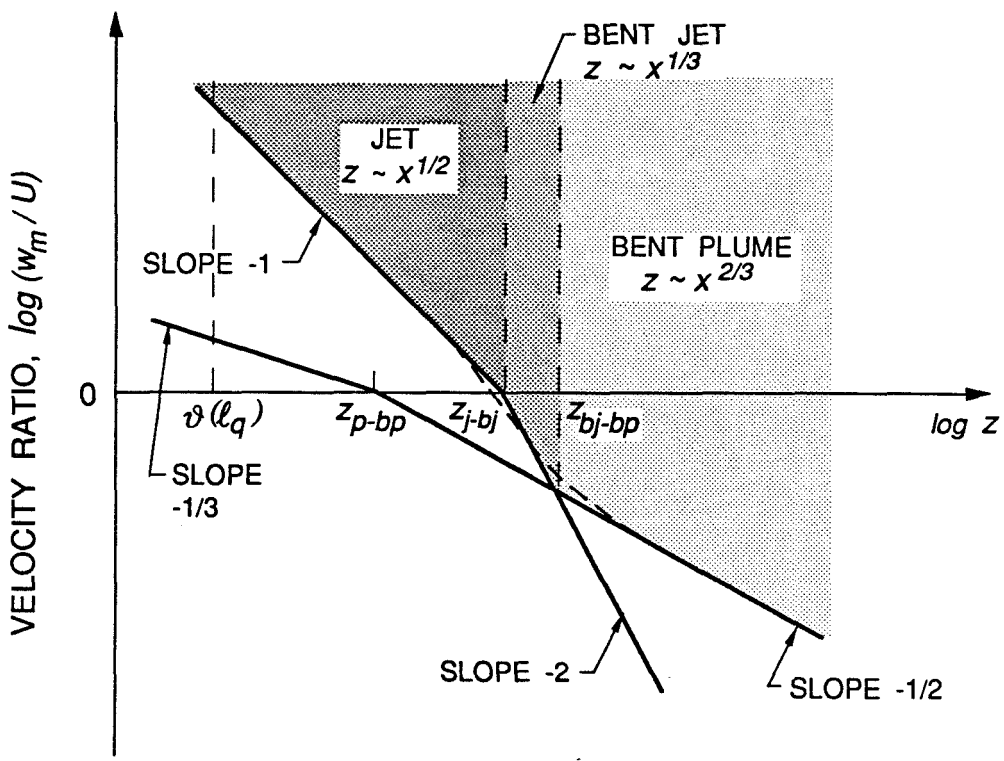

Figure 2.5 Centerline velocity as a function of vertical distance, jet-bent jet-bent plume regime (adopted from Fischer (1979))

2.3 Dilution equation for a buoyant jet released into a cross flow without shear

We are concerned in this investigation with the transition from buoyant jet induced mixing to shear-flow induced mixing. We assume that the transition from bent jet to bent plume behavior has passed before the onset of shear-flow mixing. Therefore, in the argument that follows, we assume that the transition to far-field buoyancy-dominated mixing has already occurred.

In the far-field buoyancy-dominated regime, a vertical cross section of the flow resembles that of a cylindrical momentum puff or a buoyant thermal at the same elevation as shown in Fig. 2.6. Given that we accept the analogy of a far-field buoyancy-dominated flow (or plume-like flow) to a buoyant thermal, we can use dimensional analysis to formulate an equation to describe the rate of dilution in this flow regime. To begin this analysis, we ask which flow variables can influence the dilution?

In this far-field regime, the dilution can depend only on the "puff" strength, b, defined as

$$b = \frac{g_o' Q}{U} = \frac{B}{U}$$

where g_o' is the initial apparent gravitational acceleration $g\Delta\rho_o/\rho$, the local relative density, $g'(x)$, and the time from release, t. Using these three parameters, it is possible to obtain a dimensionless quantity as follows:

$$\frac{\left(\frac{g_o' Q}{U}\right)}{(g')^3 t^4} = \frac{\left(\frac{\left[\frac{L}{T^2}\right]\left[\frac{L^3}{T}\right]}{\left[\frac{L}{T}\right]}\right)}{\left[\frac{L}{T^2}\right]^3 [T]^4} = \frac{\left[\frac{L^3}{T^2}\right]}{\left[\frac{L^3}{T^2}\right]} = \text{constant}$$

But, we can represent t as x/U, therefore, we have:

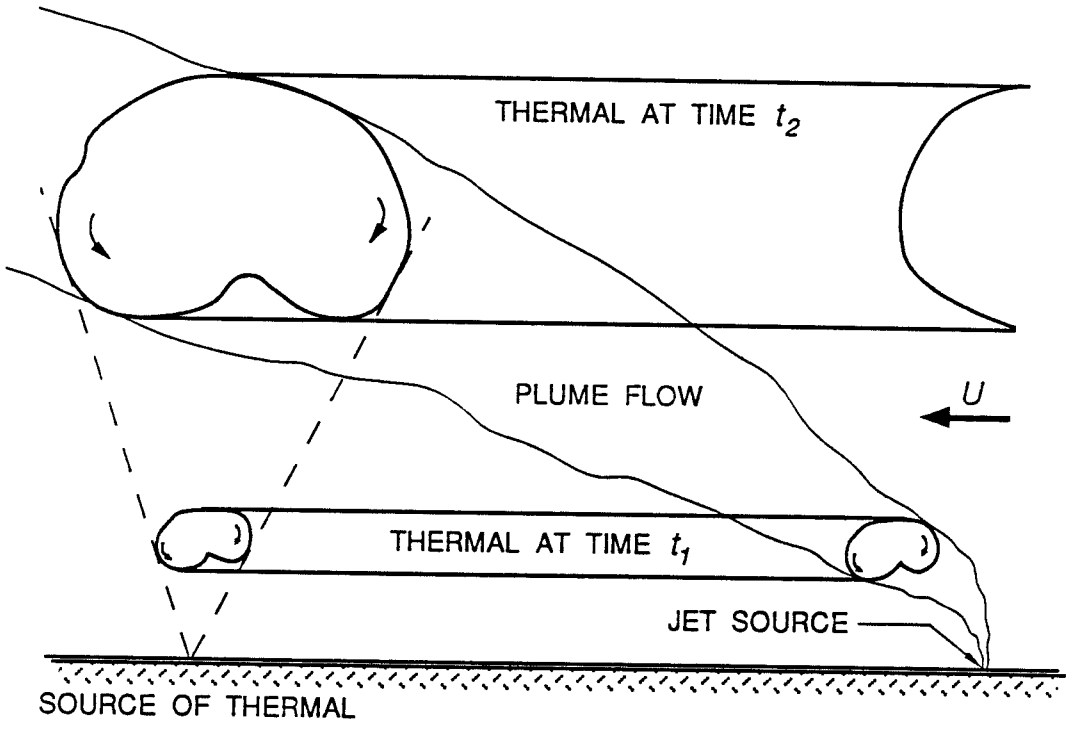

Figure 2.6 Far-field and cylindrical puff or buoyant thermal analogy

(adopted from Wright(1977))

$$\frac{\left(\frac{g_o'Q}{U}\right)}{(g')^3 t^4} = \frac{\left(\frac{g_o'Q}{U}\right)}{(g')^3\left(\frac{x}{U}\right)^4} = \frac{\left(\frac{g_o'Q}{U}\right)}{(g')^3}\left(\frac{U}{x}\right)^4$$

$$= \left(\frac{g_o'QU^3}{(g')^3 x^4}\right) = \text{constant}$$

and thus, the dilution, S:

$$g' \sim \left(\frac{g_o'QU^3}{x^4}\right)^{1/3}$$

$$\frac{g_o'}{g'} \sim \frac{g_o'}{\left(\frac{g_o'QU^3}{x^4}\right)^{1/3}} = \frac{g_o' x^{4/3}}{(g_o'Q)^{1/3}U} = \frac{Q}{Q}\frac{g_o' x^{4/3}}{(g_o'Q)^{1/3}U}$$

$$S \sim \frac{B^{2/3}x^{1/3}}{UQ}$$

which is exactly Eq. 1.1. It is important to keep in mind that this equation is valid only for $x>>B/U^3 = l_b$.

2.4 Point source release into a diffusive environment

The development of Eq. 1.2 is based on a theory that applies to advective diffusion. The premise of the analysis is that mass transport occurs by virtue of the mean motion of the fluid and by turbulent diffusion. Further, it assumes that these two effects can be treated as if they were linear, i.e., that they can be added without higher-order effects. If the diffusion is due to turbulence, then the diffusion coefficient can simply be adjusted accordingly from the laminar case.

The three-dimensional "advective diffusion" equation is:

$$\frac{\partial C}{\partial t} + \nabla\cdot\left(C\vec{U}\right) = \nabla^2 DC$$

If the fluid is incompressible, then this equation reduces to the following:

$$\frac{\partial C}{\partial t} + \vec{U} \cdot \nabla C = \nabla^2 DC \tag{2.10}$$

where C is the concentration of the tracer mass, U is the average cross-flow velocity, and D is the turbulent diffusion coefficient which we have not assumed is equal in all three directions.

In this investigation, the relevant geometry is that of a continuous point discharge released into a diffusive environment. The problem is inherently three dimensional. If we consider a point source discharge of mass at rate $\dot{M}$, at the origin of an x,y,z coordinate system, Eq. 2.10 becomes:

$$\frac{\partial C}{\partial t} + U\frac{\partial C}{\partial x} = \left(D_x \frac{\partial^2 C}{\partial^2 x} + D_y \frac{\partial^2 C}{\partial^2 y} + D_z \frac{\partial^2 C}{\partial^2 z} \right)$$

To simplify the solution, we neglect diffusion in the direction of the flow. (Diffusion in the flow direction occurs at a length scale equal to $\sqrt{2Dt}$, and the distance from the source is $x = Ut$. Therefore, flow-direction diffusion can be neglected if $x >> \sqrt{2Dt}$, or $t >> 2D/U^2$. In most flow situations, this condition is easily satisfied.) If we assume that flow-direction diffusion is negligible, then we can reduce the three-dimensional problem to a two-dimensional one, i.e., the instantaneous spread of a point source in two dimensions. The flow can be visualized as a series of parallel disks as shown in Fig. 2.7. The disks are advected past the source and as they pass they pick up a slug of fluid $\dot{M}\delta t$ where $\delta t = \delta x / U$. If we substitute this into the diffusion equation in two-dimensions, the mass per unit area, m, in the slice is:

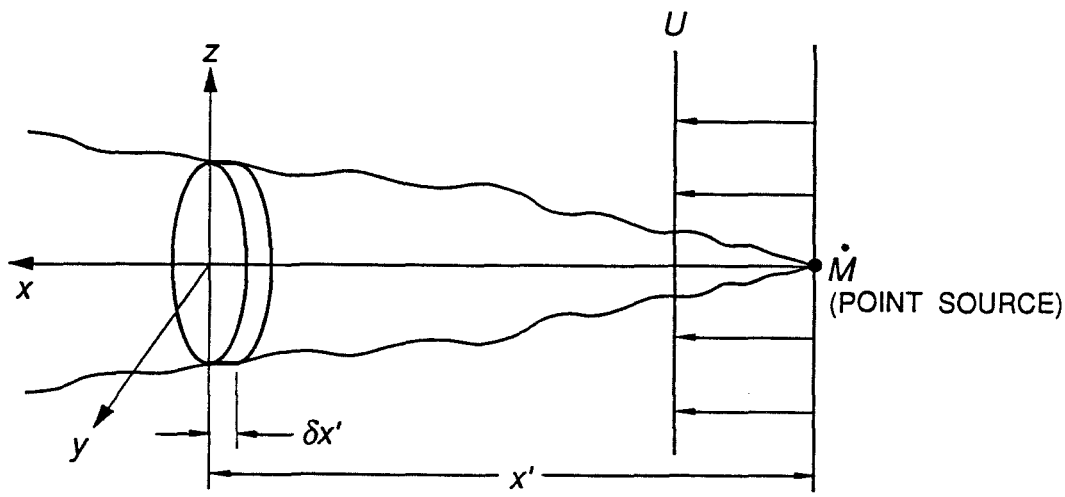

Figure 2.7 Parallel disks analogy for diffusion regime

$$m = \frac{\dot{M}\delta x}{4\pi\sqrt{D_y D_z}\,tU}\exp^{-\left(\frac{y^2}{4D_y t}+\frac{z^2}{4D_z t}\right)}$$

The location of the slice in the flow direction, x, is Ut, thus the above equation is equivalent to:

$$C(x,y,z) = \frac{\dot{M}}{4\pi\sqrt{D_y D_z}\,x}\exp^{-\left(\frac{y^2 U}{4D_y x}+\frac{z^2 U}{4D_z x}\right)}$$

where it is also recognized that, in the limit, the mass per unit area, m, divided by the width of the slice, δx, is the concentration, C.

Finally, if we put the above equation in terms of the dilution, we find:

$$\frac{1}{S} = \frac{C(x,y,z)}{C_o} = \frac{\dot{M}}{4\pi\sqrt{D_y D_z}\,xC_o}\exp^{-\left(\frac{y^2 U}{4D_y x}+\frac{z^2 U}{4D_z x}\right)}$$

$$S = \frac{4\pi\sqrt{D_y D_z}\,x}{(\dot{M}/C_o)}\exp^{\left(\frac{y^2 U}{4D_y x}+\frac{z^2 U}{4D_z x}\right)}$$

$$= \frac{4\pi\sqrt{D_y D_z}\,x}{Q}\exp^{\left(\frac{y^2 U}{4D_y x}+\frac{z^2 U}{4D_z x}\right)}$$

and along the centerline, $y = 0$, $z = 0$, with $\sqrt{D_y D_z}$ replaced by an equivalent diffusion coefficient, D, we have:

$$S = \frac{4\pi D x}{Q}$$

which is exactly Eq. 1.2.

In turbulent shear flows, the coefficient of diffusion is obtained using the Reynolds analogy which equates the diffusion of momentum and mass. The well-known result for the average vertical mixing coefficient in logarithmic shear flows (see Fischer (1979)) is:

$$\bar{\varepsilon}_v = \frac{\kappa}{6} h u_* = 0.067 h u_*$$

The average transverse mixing coefficient has been studied extensively (see Lau and Krishnappan (1977)) and an average value of $\varepsilon_t \cong 0.15 h u_*$ was found, which, unfortunately, can be considered valid only to ±50%. This is approximately 2-3 times the vertical mixing coefficient. The work of Okoye (1970) (see Fig. 2.8) showed that the transverse mixing coefficient in open-channel flow is a function of the aspect ratio, $b = h/W$, where h is the depth of flow and W is the width of the channel. The aspect ratio dependence can be rationalized by recognizing that the presence of secondary flows is a function of the aspect ratio and further that secondary flows effect the transverse mixing coefficient. The aspect ratio typical of this study is outside the range of values reported by Okoye, therefore, the best estimation we can make of the non-dimensionalized transverse mixing coefficient, Φ, is 0.1. Where:

$$\Phi(b) = \frac{\varepsilon_t}{u_* h}$$

and ε_t is the transverse mixing coefficient. Others have shown experimental results that disputed Okoye's results. (See Lau and Krishnappan (1977).)

Therefore, following the development presented in the previous section, the diffusion coefficient should be the geometric mean of the vertical and transverse components and is therefore found to be:

$$D = \sqrt{D_y D_z} = u_* h \sqrt{\varepsilon_v \varepsilon_t}$$
$$\cong u_* h \sqrt{0.067(0.1)} = 0.082 u_* h$$

Substitution into Eq. 1.2 yields the dilution equation for a continous point source release into a homogeneously diffusive turbulent shear-flow environment, where diffusion in the flow-direction can be neglected relative to advection:

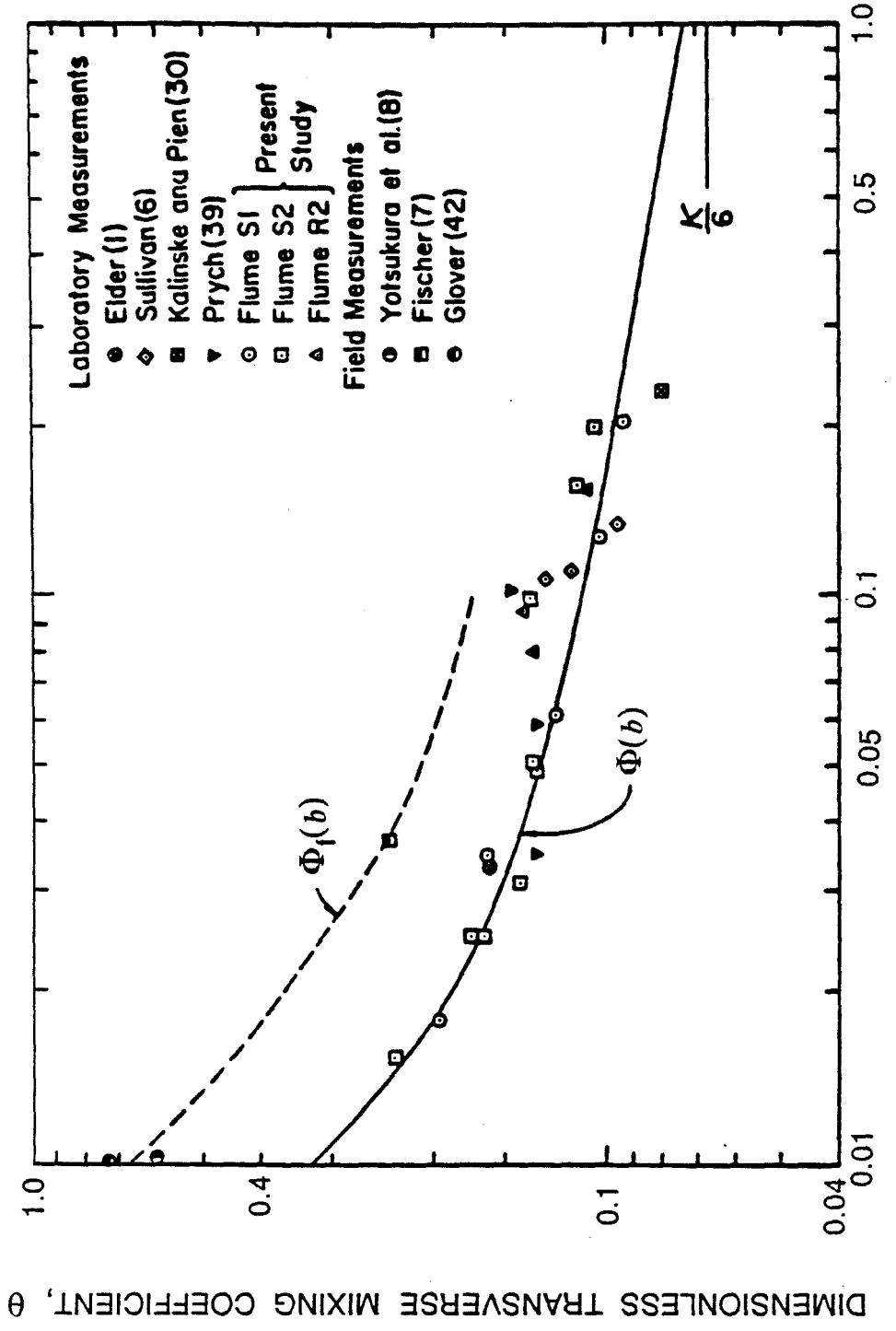

Figure 2.8 Dimensionless transverse mixing coefficient as a function of the aspect ratio (from Okoye (1970))

$$S \sim \frac{u_* hx}{Q}$$

which is, of course, Eq. 1.3.

In the Analysis of chapter 1 we interpreted this equation with regard to the effect of increasing cross-flow velocity on the dilution in the diffusive mixing regime. This result may be counterintuitive in the following sense. There are three effects of an increasing cross-flow velocity on the dilution in a diffusive regime. First, as the cross-flow velocity increases, the amount of tracer material released into any block of passing fluid goes down. This would increase the dilution. Nothing has actually changed in the mixing characteristics of the flow, rather, less tracer is emitted per unit of passing fluid. Second, at a fixed location, x, as the cross-flow velocity increases, the amount of time available for mixing goes down. These two effects directly cancel one another and the remaining effect, the third effect, of an increasing cross-flow velocity is on the diffusive mixing coefficient, D. The mixing coefficient scales directly with the cross-flow shear velocity and hence the average cross-flow velocity. Therefore, as was stated earlier in the analysis of chapter 1, increasing cross-flow velocity makes the cross-flow a more "churning" environment and improves the dilution.

2.5 Transition from plume mixing to shear-flow mixing

We reasoned in the Analysis section of chapter 1 that a transition from plume mixing to shear-flow mixing *will* occur, but can we hypothesize as to *where* this transition will occur?

To predict the transition from plume mixing to shear-flow mixing, it seems reasonable to argue that the transition will occur when the turbulent kinetic energy of the plume decays to the level of the turbulent kinetic energy of the shear flow. In actuality, transition might be a complicated function of many parameters, including for example, the

shear velocity, the boundary layer depth or the flow depth, the initial buoyancy flux, etc. However, a transition length scale predicated on the equivalence of the turbulence kinetic energy is possibly an adequate first estimate.

It is necessary, therefore, to determine the point at which the turbulent kinetic energy level of a plume becomes equivalent to the turbulent kinetic energy of the cross-flow. This is accomplished below.

The recent work by Papanicolaou and List (1988) shows that the rms velocity in a plume decays with elevation, z, according to

$$\sqrt{\overline{w'^2}} = 0.88\left(\frac{B}{z}\right)^{1/3} \tag{2.11}$$

From its functional form, we can immediately discern that the Equation 2.8 refers to the vertical rms decay in a plume that has not yet bent under the action of the cross-flow. In chapter 5, Transition Phenomena, we will show how this equation can be translated into an equivalent equation for a bent plume. This gives the following equation describing the vertical rms velocity for flow in the bent plume regime:

$$\sqrt{\overline{w'^2}} = 0.62\left(\frac{B}{Uz}\right)^{1/2} \tag{2.12}$$

For channel flow, Nezu and Rodi (1986) provided detailed measurements of the distribution of $\sqrt{\overline{u'^2}}$ and $\sqrt{\overline{w'^2}}$, and thus, an estimate of the turbulent kinetic energy distribution. They found that away from the bottom, the rms velocity scales with the shear velocity, u_*, and the channel depth, h. (Near the bottom, the appropriate scaling parameters are $z^+ = zu_*/\nu$ and $u^+ = U/u_*$, as determined by Clauser(1956).) Furthermore, Nezu and Rodi (1986) showed that in a channel, $\sqrt{\overline{u'^2}}/u_*$ is of order one.

[As will be shown later, we found that for the geometry and boundary conditions in this experimental investigation:

$$\frac{\sqrt{\overline{u'^2}}_{avg}}{u_*} = 0.75$$

Since the relevant ratio is $\sqrt{\overline{w'^2}}/u_*$, it is important to determine this ratio and we found that:

$$\frac{\sqrt{\overline{w'^2}}_{avg}}{\sqrt{\overline{u'^2}}_{avg}} = 0.88$$

therefore,

$$\frac{\sqrt{\overline{w'^2}}_{avg}}{u_*} = 0.66 \text{]}$$

Thus, the ambient turbulence and plume turbulence will be of the same order when $\sqrt{\overline{w'^2}}$ of the plume is approximately equal to $\sqrt{\overline{w'^2}}$ in the cross flow. This will occur when the plume has risen to a height

$$z_{bp-d} = \left(\frac{0.62}{\sqrt{\overline{w'^2}}_{avg}}\right)^2 \left(\frac{B}{U}\right)$$

$$= \frac{(0.62)^2}{\left(u_*\left(\frac{\sqrt{\overline{w'^2}}_{avg}}{u_*}\right)\right)^2}\left(\frac{B}{U}\right)$$

$$= \left(\frac{0.62}{u_*(0.66)}\right)^2 \left(\frac{B}{U}\right)$$

$$z_{bp-d} = 0.88\left(\frac{B}{u_*^2 U}\right) \qquad (2.13)$$

Clearly, if the buoyant jet has significant initial momentum flux, this will introduce a further parameter, the source Richardson number, $R_O = QB^{1/2}/M^{5/4}$, where M is the specific momentum flux of the buoyant jet (Fischer *et al.*, 1979).

In what follows, we apply the above arguments to the results of the experimental program.

Chapter 3. Experimental Facility and Procedures

3.1 Flow facilities

All experiments were conducted in the sub-basement of the W. M. Keck Hydraulics Laboratory. The following sections describe in detail the various equipment relevant to this investigation.

3.1.1 Flume and cross-flow generation

The 40-meter precision-tilting flume was used in its recirculating mode to create the cross flow for this investigation. The flume is 40 meters long with a cross-section that is 110 cm wide and 61 cm deep. Details regarding the flume geometry can be found in Vanoni *et al.* (1967). For this investigation, the flume was positioned at zero slope for all experiments. To accommodate experiments performed for another experimental investigation, the flume was modified with a 10.7 cm high false bottom. Thus, the available working depth was approximately 50 cm. (Note: Hereafter, "flume bottom" refers to the top of the false bottom.) To minimize adverse flow affects caused by

interaction with an abrupt step, a fitted cubic spline ramp was used at the upstream end of the flume. Details of the ramp design are included in Appendix A. The test-section is located approximately 40 flow-depths and 15 flow-widths from the ramp to allow the boundary layer to develop. Figure 3.1 shows the general geometry of the flume and the location of the test section. The flow passed through a series of wood baffles and screens to eliminate secondary flow effects as indicated in Fig. 3.2.

Two pumps, a 10-hp and a 30-hp, were available to generate a continuously-circulating cross flow in the 40-m flume. For the purposes of this experimental investigation, only the 30-hp pump was used and the orifice plate that Gartrell (1979) inserted into the 30-hp line was removed to allow higher cross-flow velocities to be achieved. The 30-hp return line contains a Venturi meter that is connected to a water manometer. All cross-flow parameters were calibrated to this manometer to facilitate efficiency in experiment runs. Obviously, some cross-flow parameters are functions of not only the bulk volumetric flow (the quantity measured by the Venturi), but also of the depth of the flow, i.e., at a constant volumetric flow, and hence at a constant manometer reading, the average velocity would increase if the depth of flow decreased. Thus, a constant-level overflow set at a given height for the duration of the experimental study was used to ensure a constant and repeatable depth of flow. The depth of the flow was monitored using a point gauge accurate to within 0.5 mm since evaporation changes the depth slightly over time.

3.1.2 Buoyant jet flow generation

The buoyant jet flow was generated using the configuration show in Fig. 3.3. A 1300 L tank that contained a bubble air supply to facilitate mixing was used to mix the buoyant jet (source) fluid. The source fluid was pumped up to a constant head tank using a 1/3 hp pump. (In the initial process of mixing fluids, the pump and head tank configuration was used to enhance the mixing process.) During an experiment, the source fluid flowed

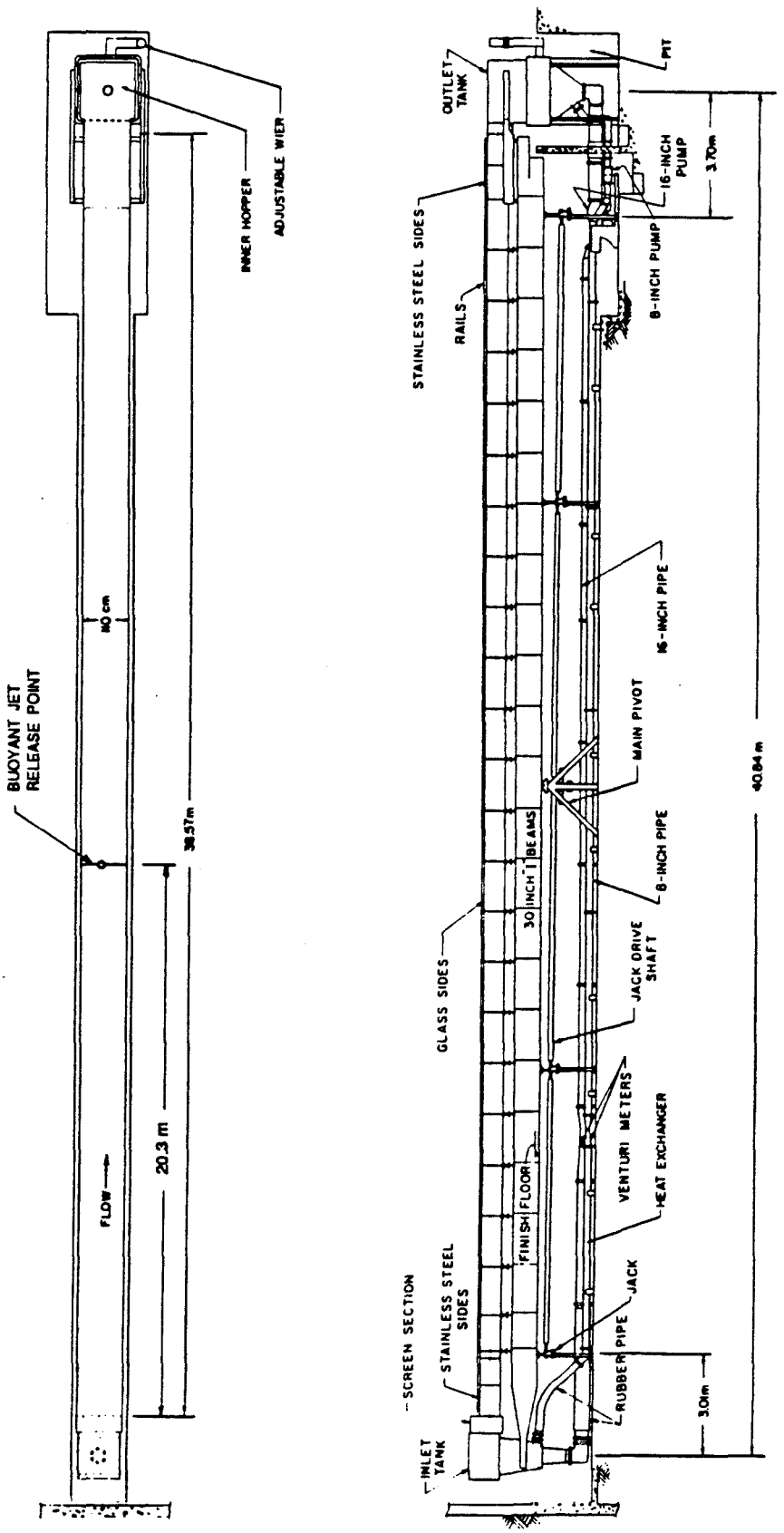

Figure 3.1 General flume geometry and location of test section

(from Gartrell (1977))

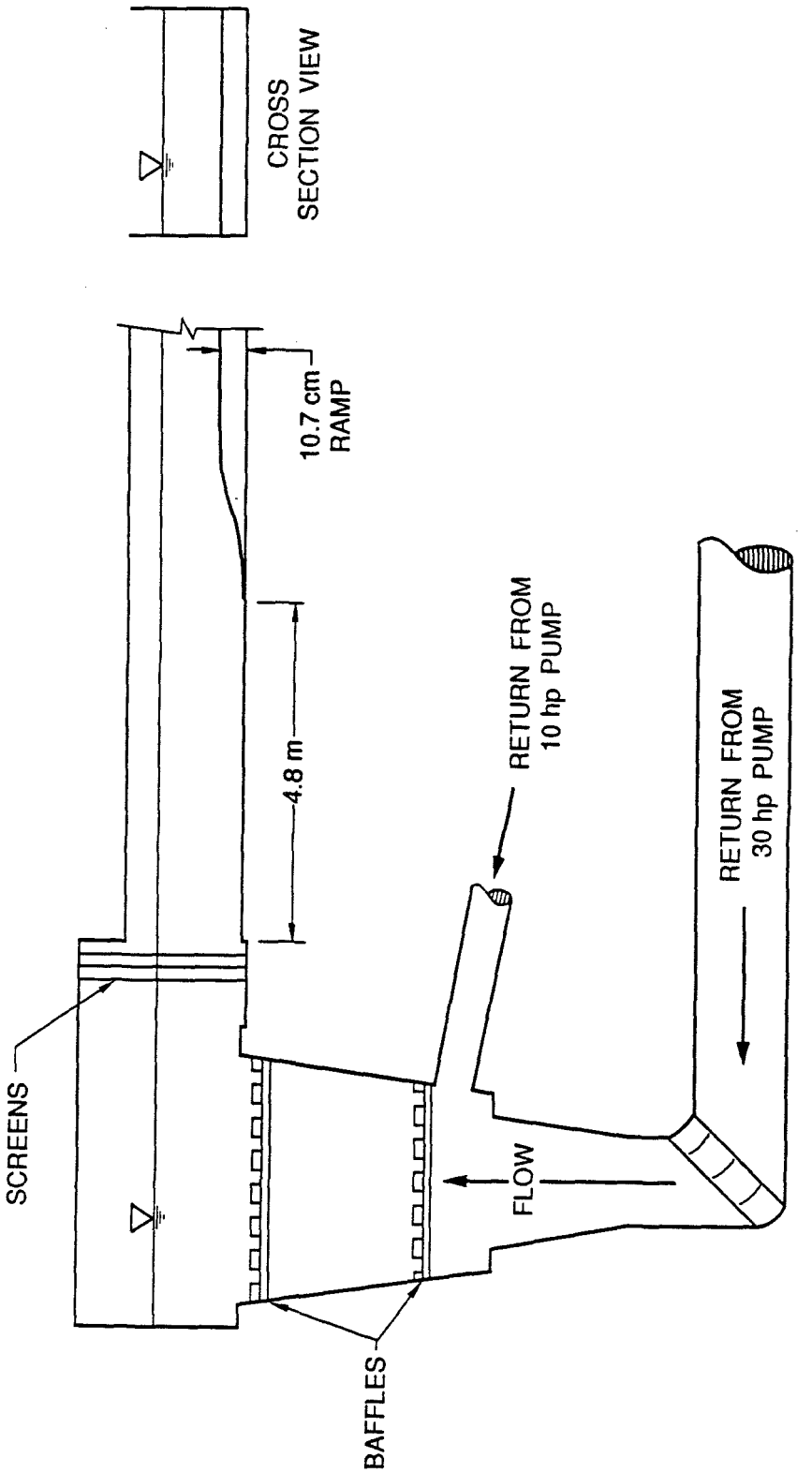

Figure 3.2 Flume flow management (modified from Gartrell (1979))

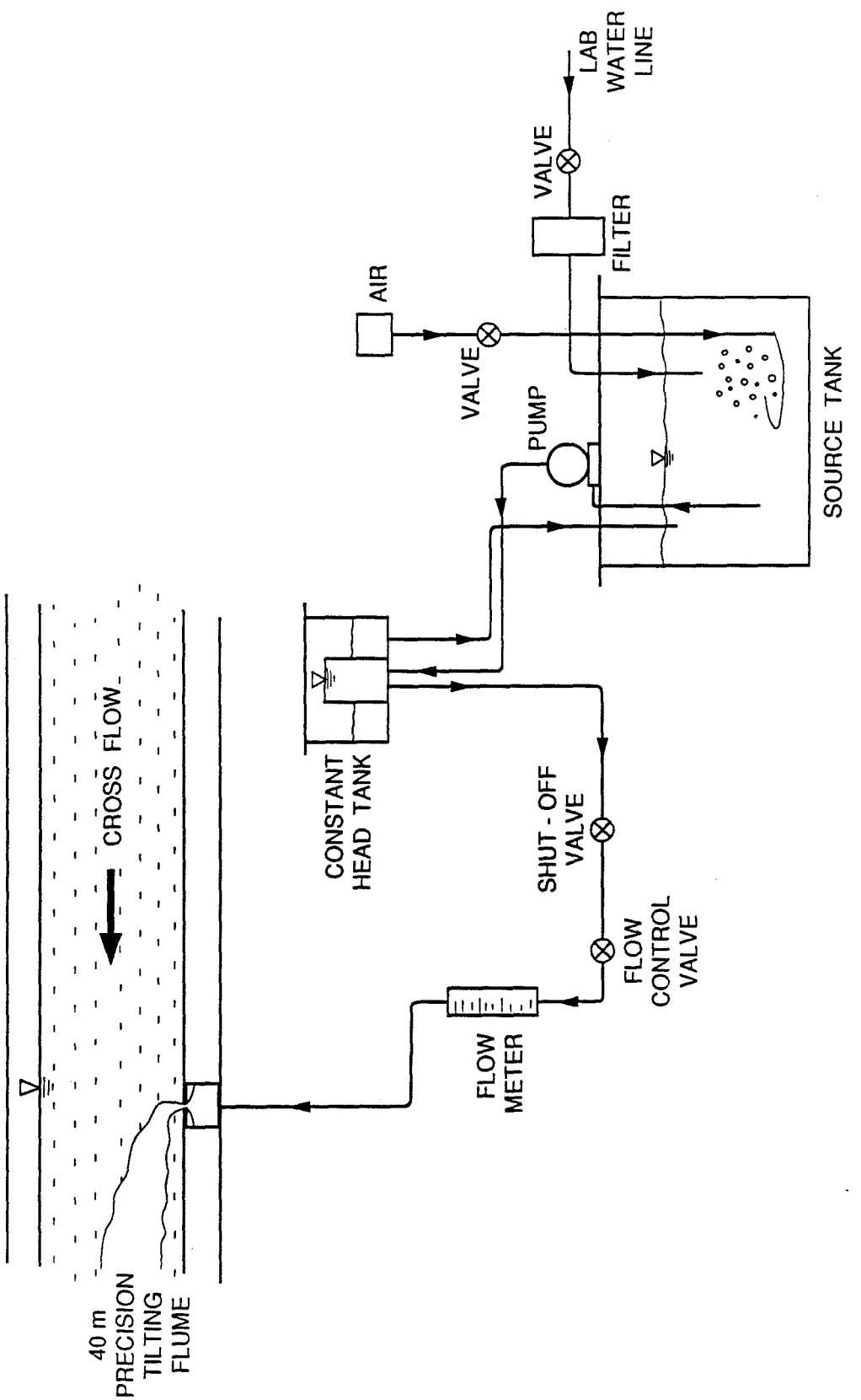

Figure 3.3 Buoyant jet flow generation apparatus

through 1.9 cm Tygon tubing from the constant-head tank through cut-off and flow-regulation valves, and an F&P Company precision bore flowmeter, before ultimately reaching the test section. The flow meter was calibrated *in situ* and was found to behave linearly. The calibration curve appears in Appendix C. At the test section, the source fluid passed through a flow-settling chamber located under the false bottom to allow the exit flow to become uniform. This settling chamber is flush with the top of the false bottom of the flume as shown in Fig. 3.4. The settling chamber was designed using the guidelines described in Andrews (1988) which briefly explains many of the parameters developed by other researchers to assure a uniform exit flow.

3.2 Fluid preparation

To obtain two fluids with differing densities, salt-water and ethanol-water mixtures were used. The ethanol-water mixture was premixed with Rhodamine 6G to create a positively buoyant jet with dye. The buoyant jet was then released into the higher density salt-water cross flow. Although these mixtures had different densities, they could nevertheless be rendered optically homogeneous. Thus, there were no changes in the index of refraction between the two fluids to interfere with the laser diagnostics. (This requirement limits the magnitude of the relative density. For this study, the relative density difference between the source and the ambient fluids ranged between 0.96 and 1.6%.)

The density of the cross-flow fluid was increased by adding food quality sodium chloride directly to the flume at the pump inlet hopper (north end hopper) so that mixing was affected by recirculation. The flume contained roughly 20,000 L of water, thus the concern over whether the salt-water solution was adequately mixed prompted a conductivity probe test of the salinity over time. To check the sensitivity and the time constant of the probe, it was first calibrated with fluids of known salinity. The calibration procedure and subsequent mixing results are discussed in Appendix B. These tests

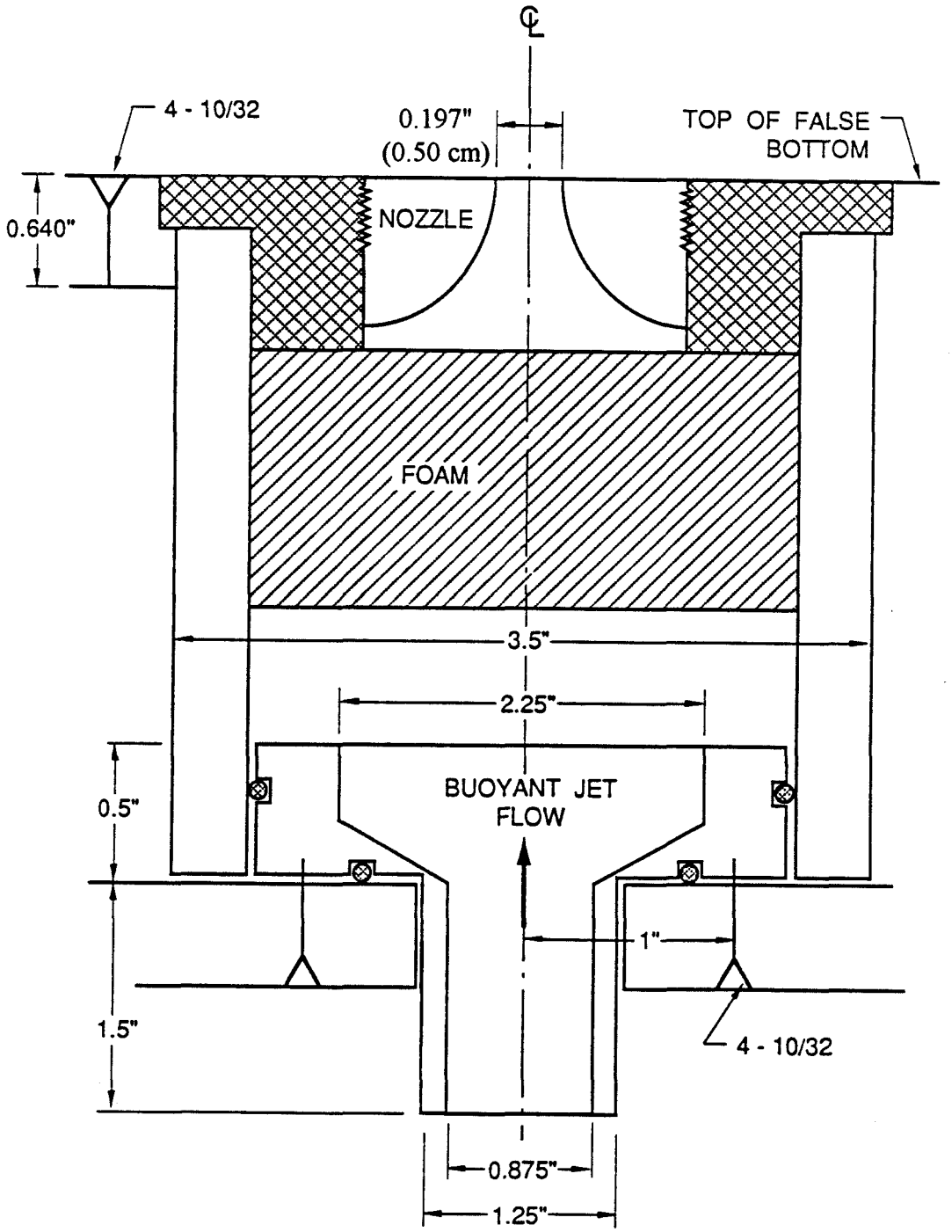

Figure 3.4 Buoyant jet settling chamber

showed that 27 kg of salt added was well-mixed after 10 min of recirculation with the 30 hp and the 10 hp pumps operating at about 30%. (Note: This test was conducted with the orifice plate (Gartrell (1979)) still in the 30 hp return line. This orifice plate was removed in subsequent experiments; therefore, mixing would be more rapid since the cross-flow velocity was higher at the same pump operating speed. This would be true even when the 10 hp pump was not used.) Further experimental observations indicated that the fluids were thoroughly mixed when index of refraction variations were no longer visible across the cross-section of the flume for a period of time not less than 30 minutes.

To decrease the density of the buoyant jet fluid, ethanol was added to the source tank. The reaction of ethanol with water is exothermic; therefore, some increase in temperature results. Even after allowing several days to pass, the temperatures of the ethanol-water mixture and the salt-water mixture differed by a maximum of 3.0°C. In other studies, ice was added to the source tank until the source fluid and the receiving fluid were in thermal equilibrium. However, to change the temperature of the source fluid by 3.0°C, 53 kg of ice would be required. Since we determined that the temperature difference was not due to the ethanol addition but to the different heat transfer characteristics of the source tank and the flume, it was decided that even if ice were added, the temperature differential would reappear. Thus, the temperature differential was tolerated and a discussion of the error introduced in the index of refraction and the density appears below.

3.2.1 Measuring the indices of refraction

The two fluid mixtures were rendered optically homogeneous using a temperature-correcting refractometer (AO Scientific Instruments, Model 10419, Temperature-correcting Refractometer). The temperatures of the mixtures were also measured at the start of each set of experiments and were found not to vary relative to each other, although some variation in the absolute temperatures on various experiment days was

observed. As mentioned above, the temperatures of the fluids did not differ by more than 3.0°C for any experiment, with the ethanol-water mixture always being the warmer of the two. Since the refractometer corrects for the temperature effects, it measures the index of refraction of the two fluid mixtures at the same temperature. Obviously, when the ethanol-water mixture was released into the salt-water, the temperatures were slightly unequal.

The index of refraction of water is a weak function of temperature. If we assume that the effect of temperature on the mixture is captured by examining the effect on pure water (this does not seem unreasonable, as each mixture is predominantly pure water), a temperature difference of 3.0°C corresponds to a 0.05-0.1% variation in the index of refraction of an ethanol-water mixture. (See Appendix D.) The refractometer is accurate to within 0.01% of index of refraction; therefore, this error was initially of some concern. However, experimental observation confirms that the index of refraction variation is negligible. No visual indications were apparent, nor did there appear to be any laser beam wobble even very close to the point of release where the temperature difference was likely to be the largest.

3.2.2 Measuring the fluid densities

The fluid densities were measured using two pycnometers, A and B, 25 ml each, and a precision scale. The pycnometer flasks and stoppers were first well rinsed, dried, and weighed. Then, both flasks were filled with either the ethanol-water mixture, or the salt-water mixture. The exterior of each flask was dried and the weights of full flasks recorded. The density of the salt-water was calculated as follows:

$$\rho_{sw} = \frac{\left(w_{sw,A} - w_A\right)}{\text{Volume of pycnometer}}$$

where w is the weight, the subscript, sw, indicates salt-water and, A, indicates pycnometer A. The same procedure was used to determine the density of the salt-water from the

measurements made on pycnometer B. This process would then be repeated for the ethanol-water mixture and the relative density difference between the two fluids was calculated as follows:

$$\left.\frac{\Delta\rho}{\rho}\right|_A = \frac{\left(\rho_{sw,A} - \rho_{aw,A}\right)}{\rho_{sw,A}}$$

for pycnometer A and the same calculation was made for pycnometer B. If the two results yielded relative densities that differed by more than 0.0002 (for typical values of approximately 0.01) the entire process was repeated.

As was mentioned above, the two fluid mixtures were at slightly different temperatures. For water, the density at 292 K is 998.4301 kg/m^3 and at 295 K is 997.8332 kg/m^3 (Mills (1992)). This amounts to a relative density of 0.06% due to a 3°C temperature differential. Therefore, for a measured relative density of 1.2%, approximately 5% of the relative density is due to the effect of temperature.

The remaining concern regarding the temperature difference was, of course, the effect on the rate of diffusive mixing. For this experimental investigation, diffusive effects that would blur the interfaces of the flow were considered negligible over the time periods used for any experimentally-sampled portion of the flow. Although molecular diffusion effects due to heat are an order of magnitude higher than similar effects due to concentration gradient, because of the small temperature gradient it was assumed that the diffusive effect of heating was also negligible. For all intents and purposes, the two fluids were treated as if they were at the same temperature.

3.3 Velocity and concentration measurement equipment

There were two primary measurements required in this experimental investigation: velocity and concentration. The velocity profile in the cross-flow fluid was necessary to quantify the shear velocity. Concentration measurements provide valuable information about the dilution rates in various flow regimes and both instantaneous and average

concentration values are important. Further, concentration data for the buoyant jet in a cross flow allowed a characterization of the turbulent kinetics of the flow.

3.3.1 Velocity measurements

A two-component, reference beam based, forward-scattering laser-Doppler system developed by Skjelbreia (1987) was used for these experiments. The signal processing system was developed by Gartrell (1979). Skjelbreia (1987) discusses in detail the layout of the current system, its operation, and capability. Details of the system pertinent to this particular experimental investigation are discussed here and the basic principles of laser-Doppler velocimetry (LDV) are treated only briefly since sources such as Durst *et al.* (1981) or Drain (1979) provide complete discussions.

3.3.1.1 Basic laser-Doppler velocimetry principles and error assessment

Laser-Doppler velocimetry is based on a principle observable in everyday occurrences, namely, the Doppler shift. As a train passes a fixed observation point, the frequency of the sound changes. This change in frequency is evidence of a Doppler shift.

In a laser-Doppler velocimeter, the same principle is in effect. Only it is the frequency of light that is shifted by the passage of an illuminated moving particle. Consider, for example, a source, S, emitting monochromatic light in direction $\bar{x}_s$, where $\bar{x}_s$ is a unit vector, at frequency, f_S, as shown in Figure 3.5a. Wavefronts travel at the speed of light in a vacuum, c. We are interested in three cases. First, a stationary particle, P, on vector $\bar{x}_s$ observes the light emitted from source S. This is shown in Figure 3.5b. In this case, the particle observes wavefronts passing at speed, c. Second, if the particle P is moving at velocity $\bar{u}$ away from the source along direction $\bar{x}_s$, then the particle will observe wavefronts passing at a speed lower than c by amount u as is shown in Figure 3.5c. The most general case is shown in Figure 3.5d wherein the particle traveling at velocity, $\bar{u}$, passes at angle θ_{ps} to the direction $\bar{x}_s$ through the wavefronts. In this case

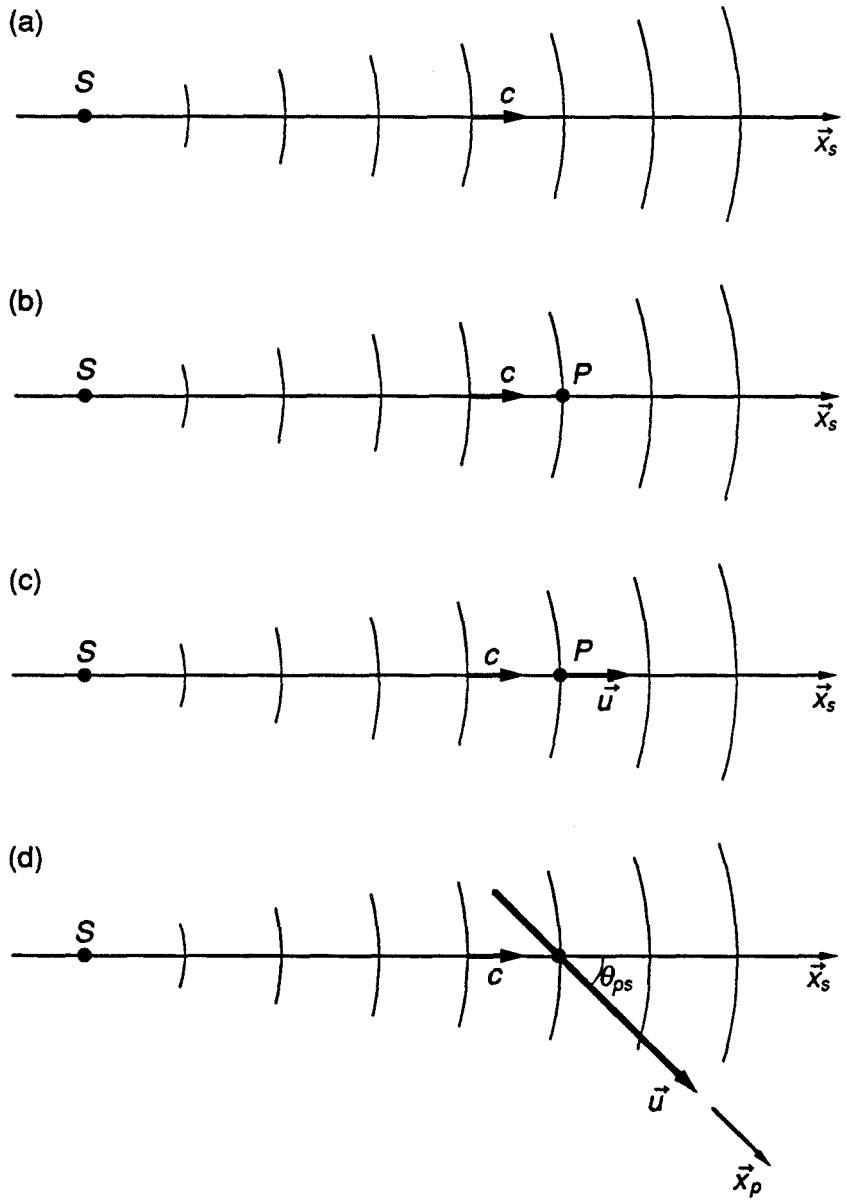

Figure 3.5 Laser-Doppler velocimetry basics: a) source and particle geometry, b) stationary particle, c) particle moving with speed u, away from source, d) particle moving with velocity $\vec{u}$ at an angle to source direction

the particle will observe wavefronts arriving at speed, u_p, defined as $(c\text{-}\vec{u}\cdot\vec{x}_s)$ and therefore sees light at an apparent wavelength:

$$\lambda_p = \frac{c}{f_p} = \frac{c}{\left((c-\vec{u}\cdot\vec{x}_s)/\lambda_s\right)} = \frac{c\lambda_s}{c-\vec{u}\cdot\vec{x}_s}$$

Now, suppose we are observing this particle from a fixed point, O, along direction of unit vector $\vec{x}_o$, at angle θ_{op} to the direction of the particle trajectory which follows the unit direction, $\vec{x}_p$. In other words, to the stationary observer the particle appears as a moving source. Figure 3.6 shows the geometry. By an argument similar to the one raised above, an observer at point O sees an effective wavelength, λ_o, defined as:

$$\lambda_o = \frac{c-\vec{u}\cdot\vec{x}_o}{f_p}$$

The frequency of light observed from O is therefore:

$$f_o = \frac{c}{\lambda_o} = \frac{cf_p}{(c-\vec{u}\cdot\vec{x}_o)} = \frac{c(c-\vec{u}\cdot\vec{x}_p)}{\lambda_s(c-\vec{u}\cdot\vec{x}_o)}$$

The difference between the source frequency and the observed frequency, is:

$$\begin{aligned} f_s - f_o &= \frac{c}{\lambda_s} - \frac{c(c-\vec{u}\cdot\vec{x}_s)}{\lambda_s(c-\vec{u}\cdot\vec{x}_o)} \\ &= \frac{c}{\lambda_s}\left[1 - \frac{(c-\vec{u}\cdot\vec{x}_s)}{(c-\vec{u}\cdot\vec{x}_o)}\right] \\ &= \frac{c}{\lambda_s}\left[\frac{(\vec{u}\cdot\vec{x}_s)-(\vec{u}\cdot\vec{x}_o)}{(c-\vec{u}\cdot\vec{x}_o)}\right] \end{aligned}$$

Since: $c >> |\vec{u}|$, $\quad c-\vec{u}\cdot\vec{x}_o \approx c$, and the resulting frequency shift is:

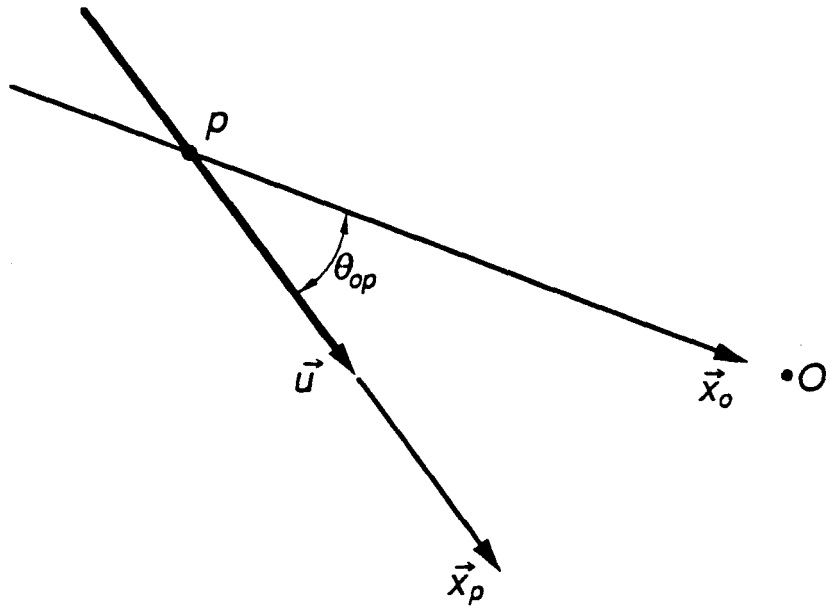

Figure 3.6 Laser-Doppler velocimetry basics: particle and observer geometry

$$\Delta f = \frac{1}{\lambda_s}\left[(\vec{u}\cdot\vec{x}_s)-(\vec{u}\cdot\vec{x}_o)\right]$$
$$= \frac{1}{\lambda_s}\left[\vec{u}\cdot(\vec{x}_s-\vec{x}_o)\right]$$

If we next looked in the plane of the source and observation directions, we would find a geometrical arrangement as shown in Figure 3.7. In this case, $(\vec{x}_o - \vec{x}_s) = 2\sin\frac{\theta_{os}}{2}\vec{i}$, where $\vec{i}$ is the perpendicular bisector of $\vec{x}_o$ and $\vec{x}_s$. If we further account for source light traveling through a medium rather than through a vacuum, then, the wavelength λ_s is adjusted to n/λ_v, where λ_v is the wavelength of light in a vacuum and n is the index of refraction of the actual medium. In this case, we have:

$$\Delta f = \frac{n}{\lambda_v}\left[(\vec{u}\cdot\vec{i})\left(2\sin\frac{\theta_{os}}{2}\right)\right]$$

For a small angle θ_{os}, the component of $\vec{u}$ in the direction of $\vec{i}$ is close to the component of $\vec{u}$ in a direction perpendicular to the source direction $\vec{x}_s$, call it $\vec{j}$. (The error associated with this assumption is discussed further in 3.3.1.5 Error Assessment.)

Therefore, if light that is shifted in frequency by the amount shown above is mixed with the original light, the resultant signal has "bursts," called Doppler bursts, as indicated in Fig. 3.8. By counting the number of zero crossings over time, the shift in frequency and hence the velocity of the particle can be determined.

3.3.1.2 Laser-Doppler system equipment

The LDV system developed by Skjelbreia (1987) and used for this study is a slightly non-conventional reference beam based LDV system. In the traditional reference beam LDV

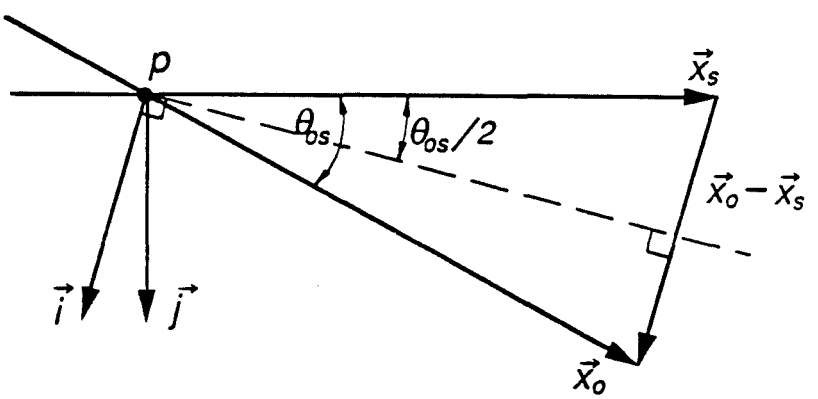

Figure 3.7 Laser-Doppler velocimetry basics: velocity projection geometry

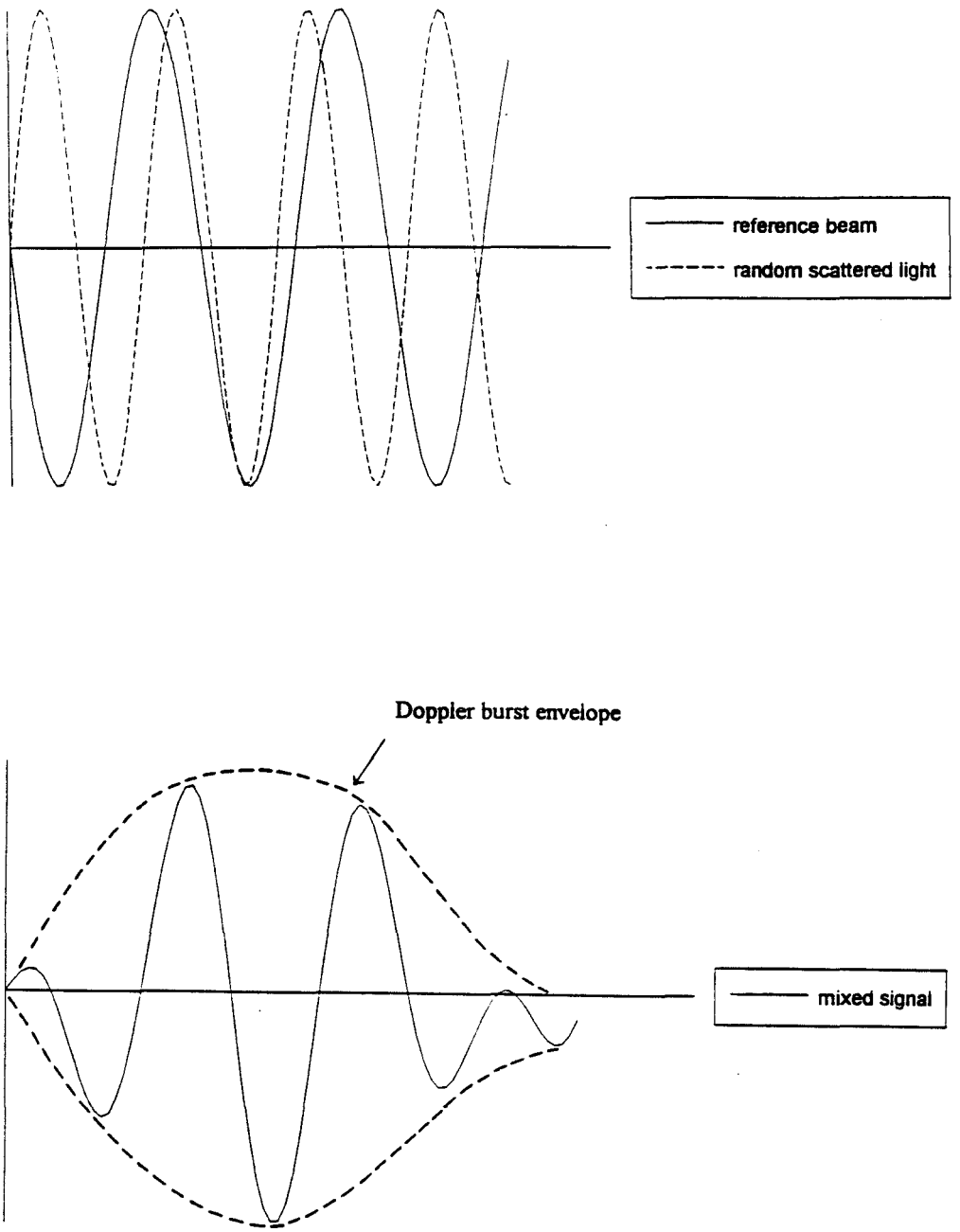

Figure 3.8 Laser-Doppler bursts

system, the reference beam intersects the scattering beam within the flow control volume under study. Instead, Skjelbreia's system uses an alignment beam arrangement to free the system of the geometrical restrictions imposed by the conventional reference beam arrangement. In the conventional system, the reference beam is directed onto the photodector and since it passes through the control volume, the scattered light from a particle must be mixed with the reference beam in the direction of its transmission. This restricts the geometrical arrangement of the system since the reference beam must pass through the control volume at some angle to the scattering beam and be detected on the receiving side of the facility. Skjelbreia's system avoids this restriction by utilizing alignment beams to arrange the optics such that light from a particle passing through the control volume is detected in two known directions, the directions of the alignment beams. This light is then mixed with light from the reference beam which passes through the fluid at a location separate from the control volume. Since the alignment beams are required only for the focusing of the optics, they can be turned off and therefore need not pass through the control volume during the actual experiment.

Skjelbreia's LDV system operates in two modes: the upward-looking and the downward-looking. Figure 3.9 is repeated from Skjelbreia and shows the configuration of the reference beam with respect to the scattering beam in each of the two modes. It is possible with this configuration to obtain measurements within 1 mm of the bottom surface in the downward-looking mode and within 1 mm of the free surface in the upward-looking mode. For the purposes of this study, measurements very near the free surface were not required. However, to obtain an accurate measure of the shear velocity, measurements near the bottom of the flume were valuable. Furthermore, for all subsequent experiments, wherein the velocity profiles of a buoyant jet in cross flow were measured, it was found that the area of interest was near the flume floor. Thus, the LDV was operated exclusively in the downward-looking mode. In the subsequent discussions only the downward-looking mode will be discussed.

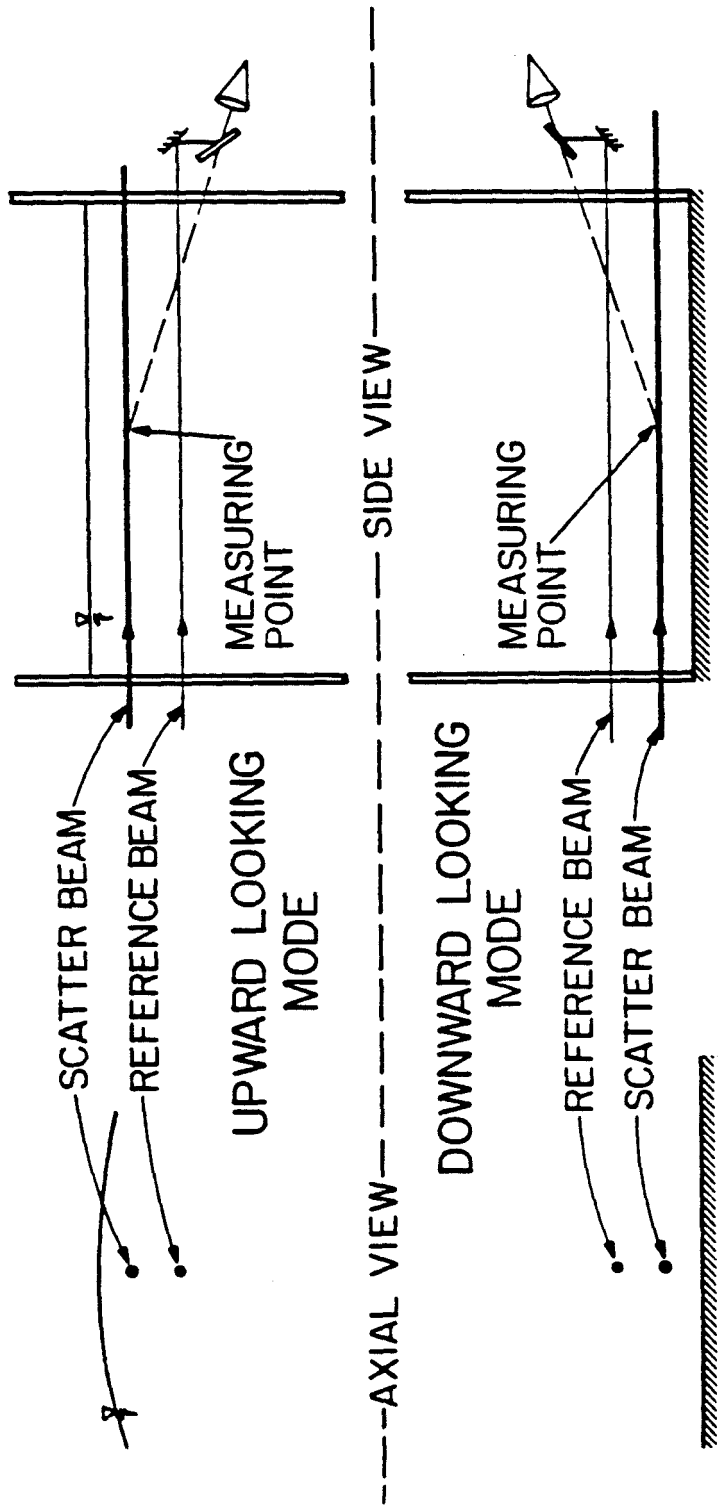

Figure 3.9 Configuration of laser beams for upward and downward looking modes of LDV system (from Skelbreia (1987))

The LDV system consists of three essential parts: the transmitting optics, the receiving optics, and the signal processing system. Skjelbreia (1987) provides detailed schematics of the transmitting and receiving optics. These schematics are repeated here as Figures 3.10 and 3.11.

Transmitting optics

Briefly, the transmitting optics employ two He-Ne lasers (one 5mW laser used for alignment and a 10mW laser used for the reference and scattering beams - the 10mW laser is an upgrade from Skjelbreia's system and provides a more robust signal), a polarizing beamsplitter, Bragg cells (Coherent Model 305), a focusing lens, a 1 to 4 beamsplitter (various splitters and lenses), right angle prisms, and mirrors. The 10mW laser was split using the polarizing beamsplitter into the reference beam (~10%) and the scattering beam (~90%). Each of these beams were then passed through Bragg Cells and finally directed into the flow. RF power amplifiers (EIN Model 300L) fed with signals from two oscillators (one operating at 40.0 MHz and the other at 40.5 MHz) were used to drive the Bragg cells and thus created a frequency shift of 500 kHz between the reference and scattering beams. This allowed the system to discern both positive and negative particle velocities.

Receiving optics

The receiving optics consist of mirrors, beamsplitters, lenses, and photo-detectors. In the downward-looking mode, the scattered light was brought to the level of the reference beam after the first reflection. (This is also true for the upward-looking mode; thus, most of the components on the receiving side are not specific to one configuration.) The reference beam was split evenly between the two alignment directions.

The reference beam is mixed with light from the scattering beam in the directions of the alignment beams by focusing each signal separately onto an aperture placed on the

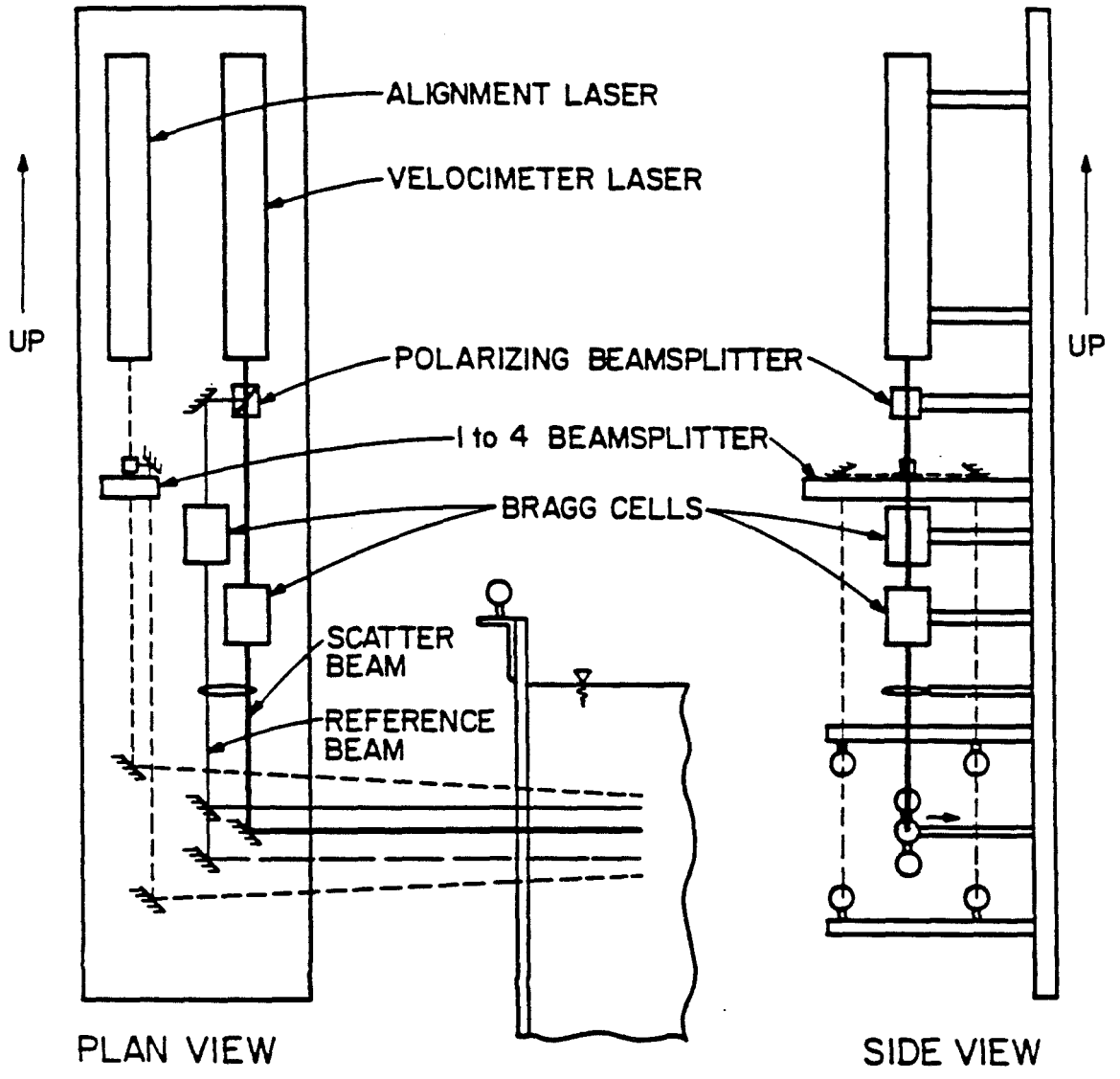

Figure 3.10 Schematic of transmitting optics for LDV system

(from Skelbreia (1987))

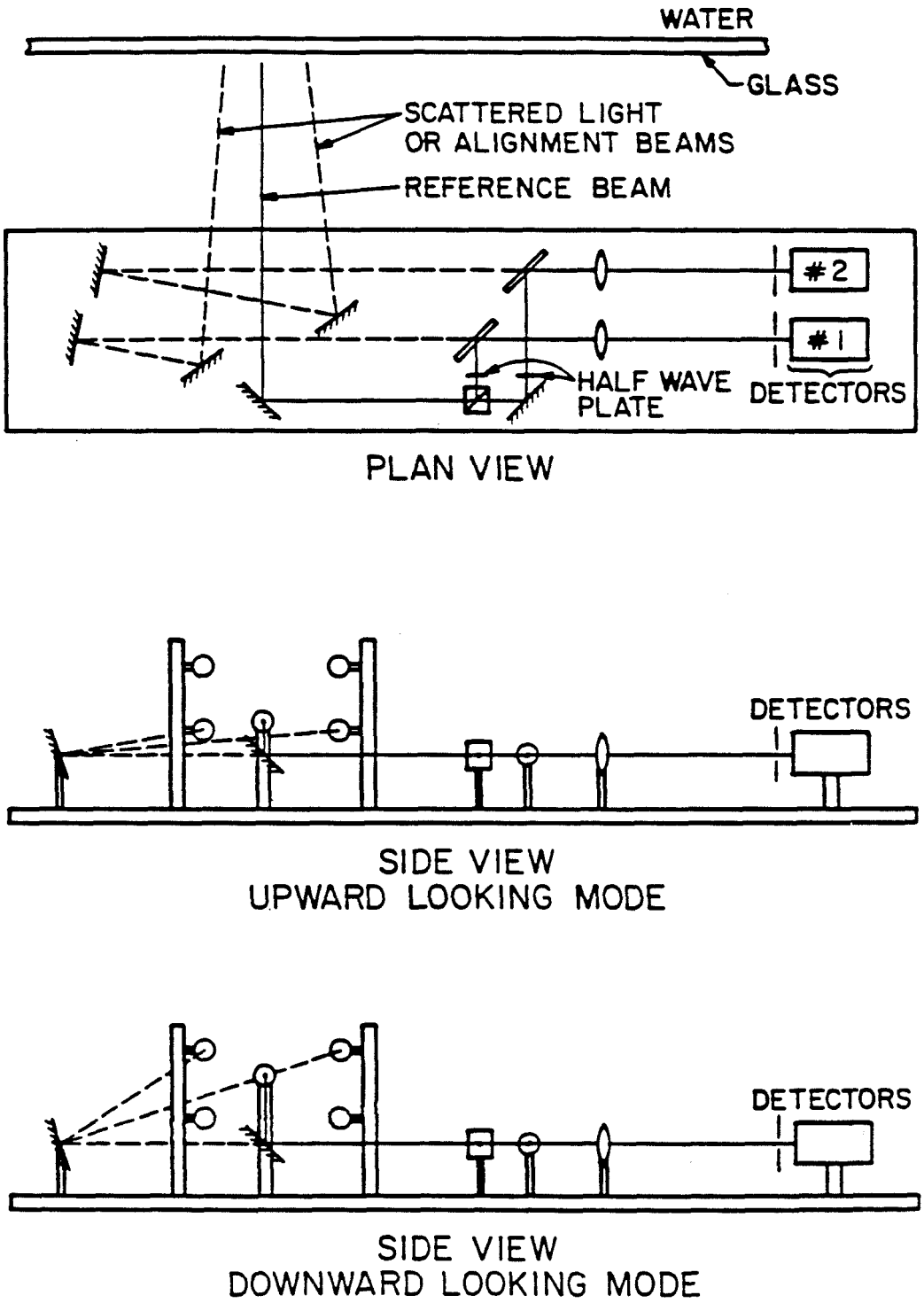

Figure 3.11 Schematic of receiving optics for LDV system

(from Skelbreia (1987))

front of each of the photo-detectors. The signal strength from the reference and alignment beams was maximized separately for each photo-detector using an oscilloscope. In order to mix the signals appropriately, it was necessary that the beams be linearly coincident. This was ensured by using a "lollipop"-like device with a pin hole centered in the disk, located at the height of the photo-detector aperture. The beams were then adjusted such that they all passed through the "lollipop" pin hole along the axis of transmission past the last focusing lens. This ensured that each beam was transmitted horizontally into the photo-detector and as such was coincident with the others. The output of each photo-detector was sent to the signal processor.

Signal processor

Each signal from the photo-detectors was first bandpassed (Krohn-Hite Model 3202R Filter) and then processed using a counter system developed by Gartrell (1978). Briefly, the signal processor first amplifies the bandpassed signal and then uses a level-detection and count scheme to determine when a Doppler burst occurs. When the system detects a burst, it uses a 20 MHz clock to time a counted number of zero crossings that exceed a threshold level strength. The system then provides a voltage output that corresponds to the frequency of the signal. Figure 3.12 shows a schematic for the signal processor. For further details, refer to Gartrell (1978).

LDV instrument carriage

The LDV system resides on an instrument carriage that is vibrationally decoupled from the flume. With the pumps operating, a low-frequency vibration is created making it necessary to decouple the experimental measurement apparatus from the flume itself. The instrument carriage straddles the flume and hangs from I-beam tracks on the ceiling of the laboratory. The carriage can be moved along the length of the flume by hand. An inner

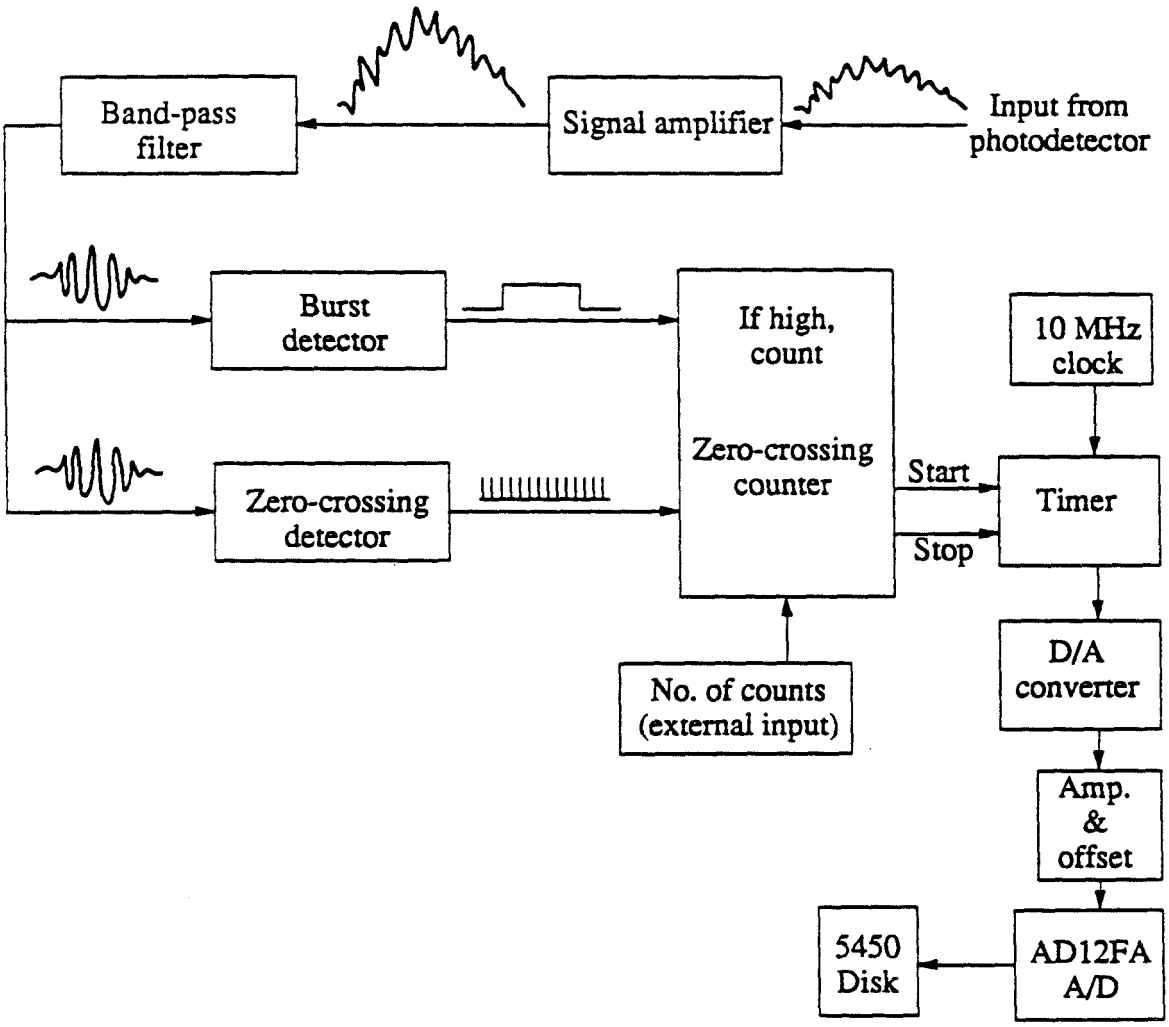

Figure 3.12 Schematic of signal processing system (from Gartrell (1978))

portion of the carriage rides on three vertical precision rails connected to the main frame. This inner carriage is supported by two twin-screw jacks which are driven by an electric motor with variable speed control. This inner carriage movement permits the LDV system to traverse the flume vertically.

Hand positioning of the carriage allows x-direction adjustments and the inner carriage permits y-direction positioning. The x-location can be measured to within 0.5 cm using a tape that runs the length of the flume. For the purposes of this investigation, an additional tape was attached to the exterior of the flume wall just below the flume bottom on the receiving optics side. The scattering beam was then aligned such that it passed spanwise through the flume across the point of release of the buoyant jet and just above the measuring tape. This reading became the zero x-location and a similar procedure was used to determine the x-location of various other experiments relative to the point of release. The x-position could therefore be determined to within 1 mm.

The instrument carriage uses a Vernier scale (accurate to within 0.1 mm) attached to the main frame to measure the change in the z-location of the inner carriage relative to the main frame. Therefore, as above, the scattering beam was positioned on the bottom of the flume and a Vernier scale reading taken. This became the z-coordinate zero point. To determine the z-location for all subsequent measurements, the Vernier scale reading was subtracted from the zero-point reading and hence the elevation, z, was determined relative to the flume bottom.

3.3.1.3 Calibration procedure for velocity measurements

The output voltage from the signal processor must be calibrated to a known frequency in order to determine the frequency shift of the particle-scattered light and hence the particle's velocity. This was accomplished using a sine-wave signal generator and a digital frequency counter to provide signals of known frequency to the processor. The output voltage was related to the frequency as follows:

$$V = \mathrm{A} + \frac{\mathrm{B}}{f}$$

where V refers to the output voltage, f refers to the frequency, and A and B are calibration coefficients. The system was calibrated before each set of experiments over a range of frequencies between 400 kHz and 600 kHz. (A 500 kHz signal corresponds to zero velocity.) Typically seven data points were taken using the Masscomp data acquisition system. The output voltage was sampled at the experimental frequency setting of 140 Hz and averaged over a 60-second period. The correlation of the data to the above equation was always better than 0.99. Calibration coefficients were found to drift a maximum of 0.3% and most often less than 0.1% over the course of a two-week period provided the electronics were always permitted a one hour warm-up period. Therefore, it was felt that a system calibration at the beginning of a set of experiments was sufficient. Appendix E shows the results of a typical calibration.

3.3.1.4 Determination of LDV geometric variables

In the LDV system described above, measurements of the velocity were taken in a reference frame that is not the *x-z* reference frame associated with the flume coordinates. To relate the actual measurements to flume coordinates, it is necessary to rotate the coordinate system. This required measurements of the system geometry.

In order to decrease labor, the geometry of the LDV system was fixed in the following way. A plate as shown in Figure 3.13 was leveled and attached to the outside of the flume wall on the transmitting side of the LDV system. A brass plate with a pin hole was then placed at some elevation z above the centerline of the flume and the scattering beam, and both alignment beams forced to pass through the pin hole. This fixed the geometry of the system. Index of refraction changes cannot therefore effect this geometry. (The effect of index of refraction on the geometry of the LDV signals is

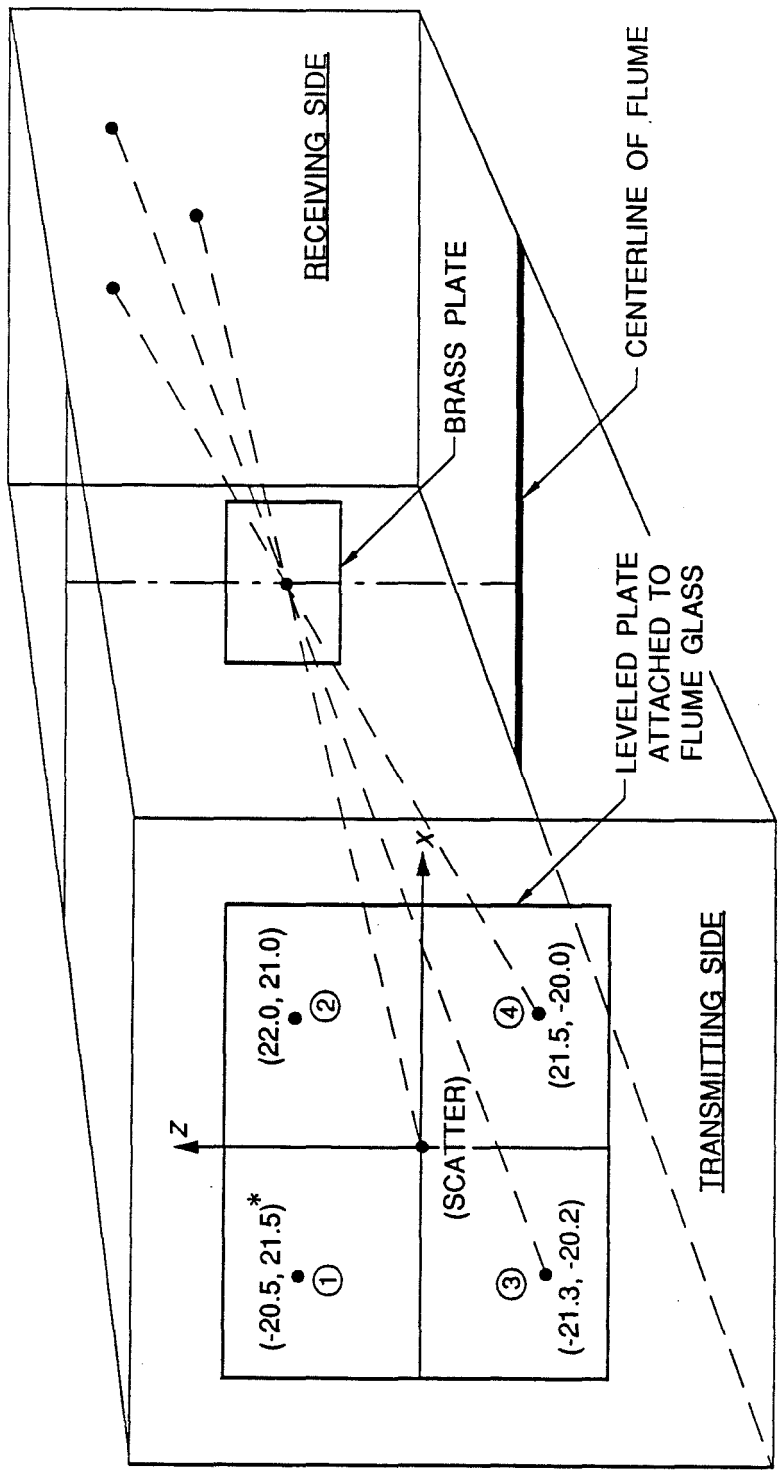

*Note: Numbers in parenthesis refer to (x,z) coordinates (in mm) from location of scattering beam, (0,0).

Figure 3.13 System for fixing geometry of LDV system

evaluated in Appendix F. Appendix F also contains the details of the coordinate transformation.)

3.3.1.5 Error assessment

To assess the error associated by approximation of the velocity component in direction $\vec{j}$ by the component in direction $\vec{i}$, refer to Figure 3.14. In Fig. 3.14 angles α and β refer to the angle of the particle path, $\vec{x}_o$, with $\vec{i}$ and $\vec{j}$ respectively. The distance Δu is equal to $u(\cos\alpha-\cos\beta)$. This difference is at a maximum when $\vec{u}$ is in the plane of $\vec{i}$ and $\vec{j}$ and lies outside of the angle $\theta_{os}/2$ as shown in Figure 3.15. In this case, $\beta=\alpha+(\theta_{os}/2)$. Therefore, Δu is defined by the following equation:

$$\Delta u = |\vec{u}|\left(\cos\alpha - \cos(\alpha + \frac{\theta_{os}}{2})\right)$$

Using the angle addition theorem, and $\theta_{os}=3°$ for the geometry of the system, the maximum possible error is 5%. In most cases, the error would be substantially less. Note: Much of the above discussion on LDV basics, geometry, and error assessment made use of personal communications with Petroff (1990).

3.3.2 Concentration measurements

Concentration measurements were made using the laser-induced fluorescence method developed by Koochesfahani (1984) and modified by Papantoniou and List (1989). This technique is based on the ability of certain organic dyes to fluoresce under the action of light. In particular, the molecules of such dyes absorb photons and reradiate some of the absorbed energy. This reradiation, or fluoresence, occurs at a wavelength different from the wavelength of the excitation light, and is essentially instantaneous (on the order of nanoseconds). The beauty of this technique lies in its inherently non-intrusive nature and in spatial and temporal resolutions significantly higher than those achievable with conventional techniques.

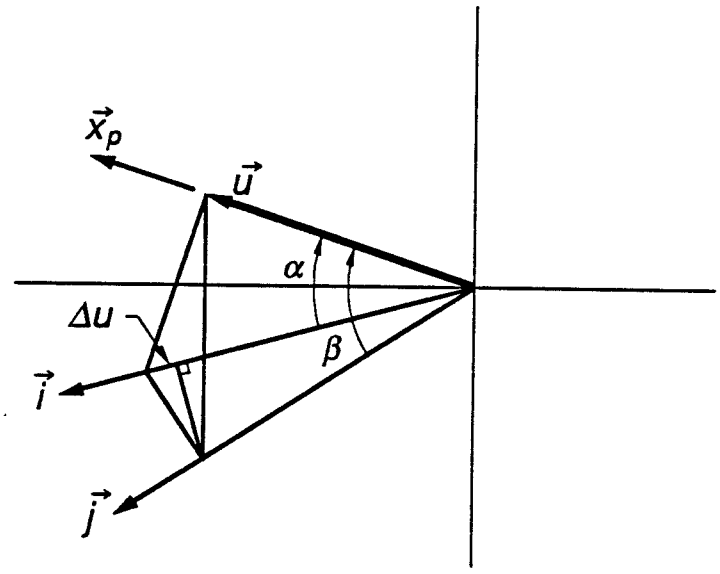

Figure 3.14 Geometric layout of error in assuming LDV signal perpendicular to scattering beam

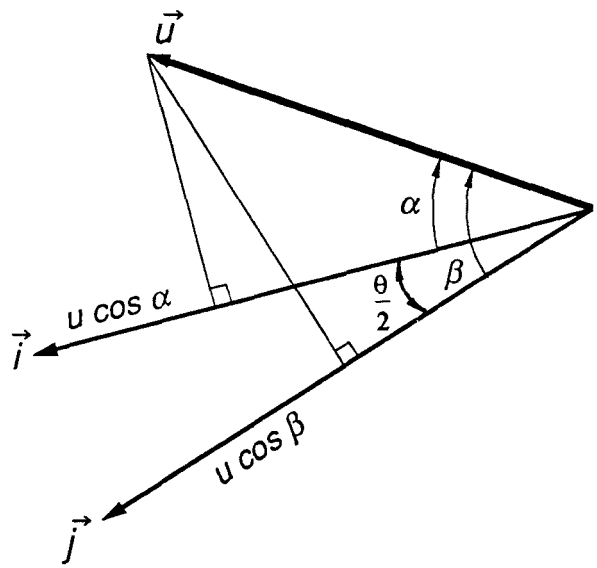

Figure 3.15 Geometric layout for maximum error in assuming LDV signal perpendicular to scattering beam

For this experimental investigation, Rhodamine 6G was used as the tracer for the source fluid. A 2W Argon-Ion laser (Spectra Physics Model 265) operated in single wavelength mode at 514.5 nm (green) was used to excite the dye which fluoresces at a wavelength of 570 nm (yellow). The laser beam was then positioned vertically along the centerline of the flow in the z-direction and at a given location, x, from the point of release. The beam was then focused onto an array of light-sensitive photo diodes (Reticon RL-1024 G) using a 50 mm f1.8 Nikon lens. An orange filter was used on the lens to eliminate incident light of wavelengths less than 530 nm while permitting the higher-wavelength fluoresced light to pass. The array consists of 1024 elements arranged vertically with a center-to-center spacing of 25μm and an aperture width of 26μm which are housed in a camera (EG&G Reticon LC 300A). The camera circuitry is described in the Reticon LC 300A manual (1981) and relevant aspects of the circuitry are described below in section 3.3.3 Data acquisition system. The elements were sampled rapidly to provide detailed information regarding the flow characteristics. In the sampling, two things are important. First, the sampling frequency, pixel-to-pixel, which determines the dynamic and temporal resolution of the experiment. Second, the number of scans sampled, or the total duration of the sample, which must be sufficient to converge all the appropriate flow parameters. High sampling rates are necessary since the entire array must be sampled before the first pixel can be sampled again. This means that the frequency at which each individual pixel is sampled is approximately three orders of magnitude lower than the pixel-to-pixel sampling frequency. For example, a sampling frequency of 200 kHz provides for a pixel-to-pixel sampling rate of 200 kHz, however, each individual pixel is sampled at a rate roughly equal to 200 Hz. This is sufficient to freeze the flow since we do not expect turbulent fluctuations in a plume to exceed 70 Hz (Papanicolaou(1988)).

Aligning the vertical laser beam with the vertical photo diode array was no small feat. An assembly consisting of a gimbal mirror mount (Newport model 6520-6) and a

precision rotation stage (Newport model 471-A) was custom constructed to facilitate this process. This assembly, in conjunction with the lens focus, provided all the necessary degrees of freedom required to focus the laser beam accurately onto the photo diode array. (For details regarding the camera assembly, see Sullivan (1992)). Thus, the array records an Eulerian "picture" of the buoyant jet as it passes location x.

The location x was determined by using the scattering beam of the LDV system to "mark" a line along the bottom of the flume at x and the argon laser beam was aligned so as to intersect the scattering beam at the centerline of the flume. This method was sufficient to determine x to within 0.5 cm.

Measurements were obtained along the centerline of the flume only. This raises questions as to whether these measurements capture the peak concentration given that the location of the maximum concentration might be skewed spanwise (i.e., in the y-direction), due to secondary flows in the cross flow, or may occur to either side of the centerline due to bifurcation events. Dye injections in the cross flow along with Prandtl tube measurements off centerline (Figure 3.16) indicated no measurable secondary flow within the accuracy of the instruments. Further, laser-sheet (x-y plane) examinations of the buoyant jet in cross flow over the range of experimental parameters showed that the buoyant jet was not skewed to one side of the flume, and that under certain experimental conditions visible bifurcations existed, but were not perceptible in the flow past approximately 5 flow diameters, or 2.5 cm. Furthermore, Fric (1989) showed that a jet in cross flow does *not* behave like a cylinder in cross flow, thus suggesting that these short-lived bifurcation events should not be viewed as the extended arms of horse-shoe vortices. This is in contrast to the suggestion of many researchers, *e.g.*, Wright (1977), Fan (1967), who have observed a resemblance between the far-field regimes and counter-rotating vortices described as the trailing arms of horse-shoe vortices formed at the buoyant jet - cross flow interaction point. The work of Fan (1967) showed that absolute minimum dilutions occur to either side of the centerline, which supports the concept of counter-

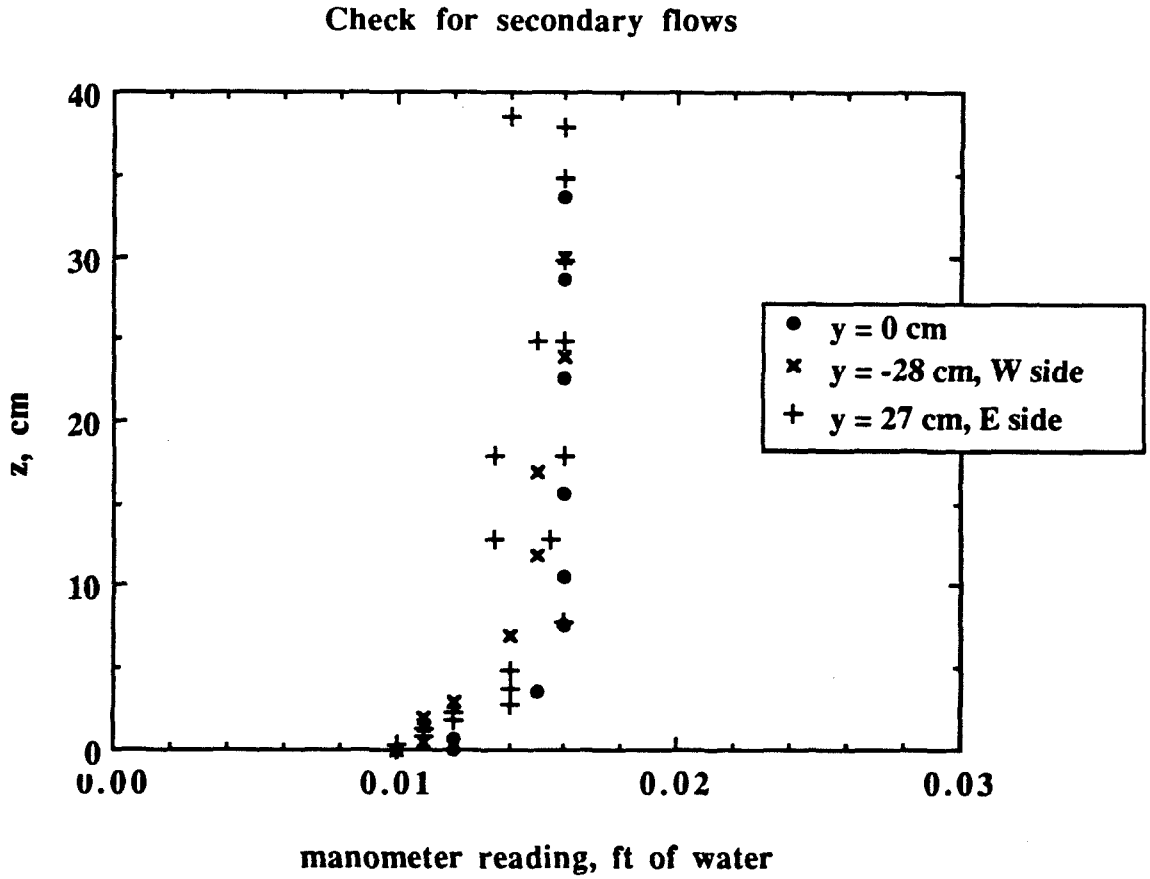

Figure 3.16 Assessment of cross flow secondary flow using Prandtl tube and water manometer

rotating vortices, or bifurcation in the flow. The difference between these off-centerline values and the centerline would not necessarily be visible in the laser-sheet experiments conducted above. While certainly the location and value of the maximum concentration is of interest in determining the physics of the flow, to determine transition we need only be concerned with relative changes in the dilution as influenced by other flow parameters.

Figure 3.17 shows the optical layout. The Spectra Physics laser was used for several experimental investigations within the W.M.Keck Laboratory. Thus, the laser location, while convenient for the other experimental investigations, was inconvenient for use in the 40 m flume. Since it was necessary to transmit the laser beam across the laboratory, safety considerations required the use of a fiber optic system. The laser beam exited the laser with a diameter of 1.25 mm and a divergence of 0.69 mrad. The beam was then focused into a fiber optic (Newport model FC-FA-15, single mode (488nm, 514.5nm), 3.2μm core,15 m length, cabled) using a precision fiber optic coupler (Newport model F1015) attached to a custom constructed mount that allowed the optical axis of the coupler to be aligned with the optical axis of the laser. Laser light that exits the terminal end of the fiber is highly divergent. Therefore, an identical coupler was used in reverse at the terminal end to recollimate the laser beam. Because some adjustment in the z-direction (the direction of transmission) of the microscope objective contained in the coupler was possible, the beam could be focused in the test section. In fact, the beam that results from the fiber optic arrangement is much cleaner than that obtained using conventional lensing systems. This must however be traded against the reduction in power that results from losses in the fiber. The most significant losses are end losses which result from imperfect fiber cuts and from imperfect coupling of the laser beam to the fiber optic. Typical power transmissions were on the order of 70-80%. This still provided adequate power to conduct the experiments.

The terminal end of the fiber, along with the coupler, was mounted on a specially constructed addition to the LDV instrument carriage. This support structure was capable

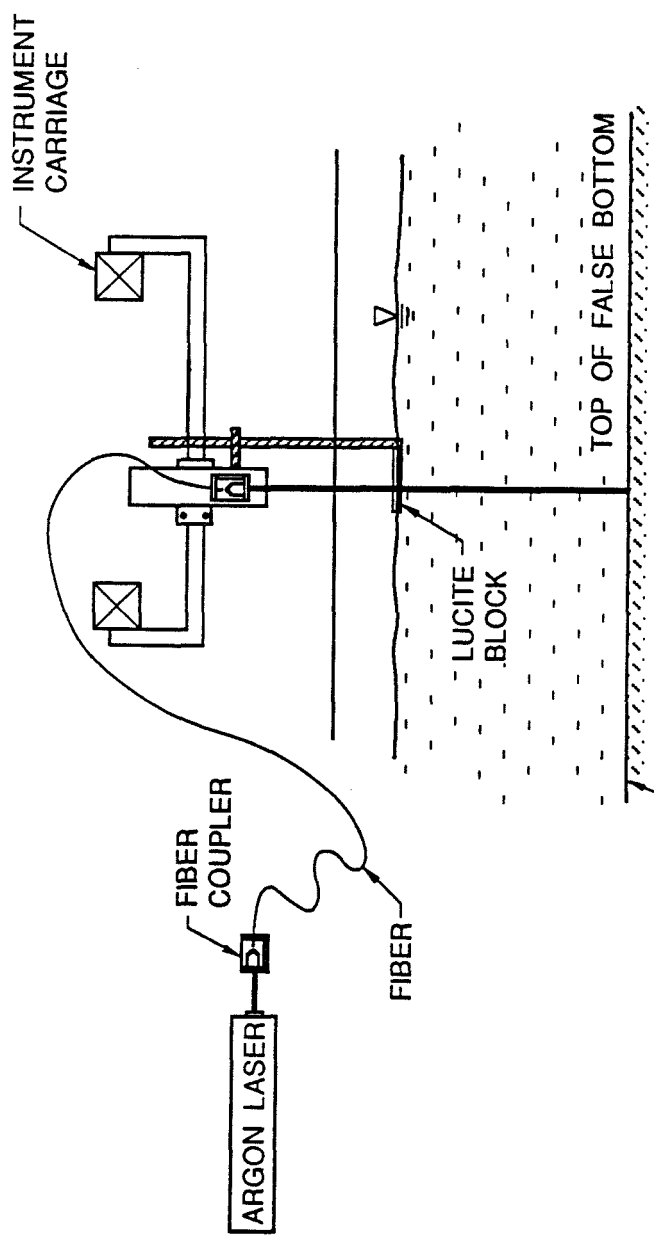

Figure 3.17 LIF optical layout

of adjustments in the x, y, and z directions so as to allow the argon beam of the LIF system and the He-Ne beams of the LDV system to be coincident at a point. This is necessary to obtain a measurement of the turbulent tracer flux which requires knowledge of the instantaneous velocity and the instantaneous tracer concentration at a point. The specially designed box described in 3.3.3 Data acquisition would also facilitate the measurement of this quantity. However, for this experimental investigation, such measurements were not obtained. It was left to future investigators.

3.3.2.1 Calibration procedure for concentration measurements

To relate the voltages recorded from the photo diode array to actual values of the concentration, a calibration procedure that corrects for laser beam attenuation by the dye as well as variations in the optical system was used. These variations include variable beam width, pixel response non-uniformity, inaccuracy in the alignment of the array. For a discussion on the development of the calibration procedure, see Koochesfahani (1984). Briefly, the photo diode output may be written approximately as

$$V_i = C_i H_i \left(I_o e^{-\varepsilon \int_0^{\xi_i} C(z,t)dz} \right) + D_i \qquad (3.1)$$

where V_i is the voltage output from the ith element, or pixel, of the photo diode array, I_O is the intensity of the laser beam as it enters the test section ($\xi = 0$), H_i is the optical transfer function and D_i is the dark noise, both of which must be determined during the calibration procedure.

The determination of the dark noise, D_i, was simple. After the laser beam had been focused onto the array, the laser beam was blocked and the array sampled for 128

scans. The voltages were then averaged over the number of samples to determine the average voltage at each pixel and hence, the dark noise.

The determination of the optical transfer function, H_i, was more complicated. The calibration vessel was filled with a diluted mixture of the source fluid and placed in the path of the laser beam. This was necessary because of the high dilutions observed in this investigation. If the system was calibrated with undiluted source fluid, the intensity of the fluorescence at the test section was indistinguishable from the noise. Furthermore, at high concentrations of dye, attenuation effects rapidly decrease the intensity of the fluoresced light over the test section, and photo-bleaching of the dye prevents accurate calibration. The source fluid was diluted with cross-flow fluid to a known concentration, C_{tf}, where *tf* refers to the *t*ransfer *f*unction fluid. Diluting the source fluid with the cross-flow fluid ensured that the indices of refraction were matched between the mixed transfer function fluid, and the cross-flow fluid which surrounded the calibration vessel. The averaged value of the voltage for each pixel then has the following meaning:

$$V_{tf} = C_{tf} H_i \left(I_{tf} e^{-\varepsilon C_{tf} \xi_i} \right) + D_i \tag{3.2}$$

where V_{tf} is the *i*th pixel voltage averaged over the number of scans (in this case 256 scans) taken for this part of the calibration, and H_i, is the desired transfer function at the *i*th pixel. Upon rearrangement, we find:

$$H_i = \frac{\left(V_{tf} - D_i\right)}{C_{tf} I_{tf} e^{-\varepsilon C_{tf} \xi_i}} \tag{3.3}$$

To avoid adverse effects due to photo-bleaching (which occured even for the diluted calibration fluid), the fluid was mixed by gently rotating the calibration vessel by hand during data collection. This seemed to eliminate such effects.

Further, if we then let

$$G_i = H_i \cdot C_{tf} I_{tf} \tag{3.4}$$

and this equation is then substituted into Eq. 3.1, the result is:

$$V_i = \frac{C_i}{C_{tf}} \frac{I_o}{I_{tf}} \frac{1}{G_i} \left(\exp^{-\varepsilon \int_0^{\xi_i} C(z,t)dz} \right) + D_i \tag{3.5}$$

thus

$$\frac{C_i}{C_o} = \frac{I_o}{I_{tf}} \frac{C_{tf}}{C_o} (V_i - D_i) \cdot \left(\exp^{\varepsilon C_o \int_0^{\xi_i} \frac{C(z,t)}{C_o} dz} \right) \tag{3.6}$$

The integral in brackets above can be approximated as

$$\Delta z \sum_{j=1}^{n} \left(\frac{C_j}{C_o} \right) \tag{3.7}$$

where n is the number of pixels valid for the calibrated region. Making this substitution, we have

$$\frac{C_i}{C_o} = \frac{I_o}{I_{tf}} \frac{C_{tf}}{C_o} (V_i - D_i) \cdot \left(\exp^{\varepsilon C_o \Delta z \sum_{j=1}^{n} \left(\frac{C_j}{C_o} \right)} \right) \tag{3.8}$$

There are four interesting points to be made regarding this equation.

1. The attenuation parameter, ε, appears exclusively in the equation paired with C_O. Therefore, it is necessary to determine εC_O only. The above development assumes a constant value for ε, in other words, that ε is not a function of the concentration. Over relatively small ranges of the concentration, roughly one order of magnitude of a molar solution, this is true, as was verified by several other researchers (Koochesfahani (1984), Papantoniou and List (1989)), and confirmed in this study.. However, over the range of concentrations observed in this experimental investigation, ε is not constant. Rather, it is a function of the concentration. It was found that εC is not a linear function of the concentration, rather it is quadratic with concentration. This functional relationship is explained further in Appendix G.

   The above equation must therefore actually be written

$$\frac{C_i}{C_o} = \frac{I_o}{I_{tf}} \frac{C_{tf}}{C_o} (V_i - D_i) \cdot \left\{ \exp^{\Delta z \sum_{j=1}^{n} \left[\varepsilon C_j \right] \frac{C_o}{C_j} \left(\frac{C_j}{C_o} \right)} \right\}$$

$$\frac{C_i}{C_o} = \frac{I_o}{I_{tf}} \frac{C_{tf}}{C_o} (V_i - D_i) \cdot \left\{ \exp^{\Delta z \sum_{j=1}^{n} \varepsilon C_j} \right\} \tag{3.9}$$

which, if looked at simply, accounts for the attenuation through the previous sections of fluid by adjusting the attenuation parameter according to the concentration of the dye *in that section.* This second equation is the more general case.

2. The attenuation parameter, paired with a concentration as it appears in these equations, has units of concentration and inverse length. Therefore, while most of the parameters in the equation relate directly to a pixel, it is necessary that the attenuation calculations use a length scale. This requires the determination of the magnification ratio for each experiment, which is described next.

In the calibration process, when the optical transfer function was determined using the calibration vessel, the camera was located such that the image of the vessel did not extend past the first or the last pixels of the array. Then, when the signal from the transfer function was first analyzed, no attenuation was taken into account, and the averaged pixel voltage versus the pixel number was examined. The location of the first, i_f, and last, i_l, high intensity pixels were recorded and then, knowing the length of the calibration vessel, L_c, and the center-to-center spacing of the pixel array, s_p, a magnification ratio, mr, could be calculated

$$mr = \frac{L_c}{s_p (i_l - i_f)}$$

This process is illustrated in Fig. 3.18. The magnification ratio determines the static resolution of the concentration experiments. The dynamic resolution is determined by the sampling frequency and is discussed later.

3. I_O in the equation refers to the intensity of the laser light *as it enters the test section*. In these experiments, part of the cross flow depth is outside of the calibrated region of the flow. The calibration vessel is 29.6 cm tall and always rested on the bottom of the flume. Thus, in most cases, nearly 11 cm of the flow was outside of the calibrated region of the flow, and hence not "visible" by the camera. This was not a problem as long as the cross-flow fluid did not contain any dye, since, in that case, the laser beam would not be noticeably attenuated. However, because the experimental facility was recirculating, the cross-flow fluid becomes contaminated with dye from the buoyant jet over the course of several experiments. In this case, the additional attenuation caused in the first 11 cm must be accounted for. Figure 3.19 gives a pictorial representation of this scenario. To determine the attenuation, two parameters were required. First, the distance over which the beam was attenuation, $\Delta\xi$, and the concentration of the dye in that region. The flow depth and the height of the calibration vessel determine $\Delta\xi$ and the only parameter that remained to be determined was the concentration of dye in the cross flow. This was accomplished by recording the volume of source fluid released into the flume over the course of each experiment, and by measuring the concentration of dye at the conclusion of the experimental runs. It was then possible to approximate the concentration of dye in the cross-flow fluid for each experiment. The real limitation with this technique was the determination of the concentration of dye. This was accomplished by filling the

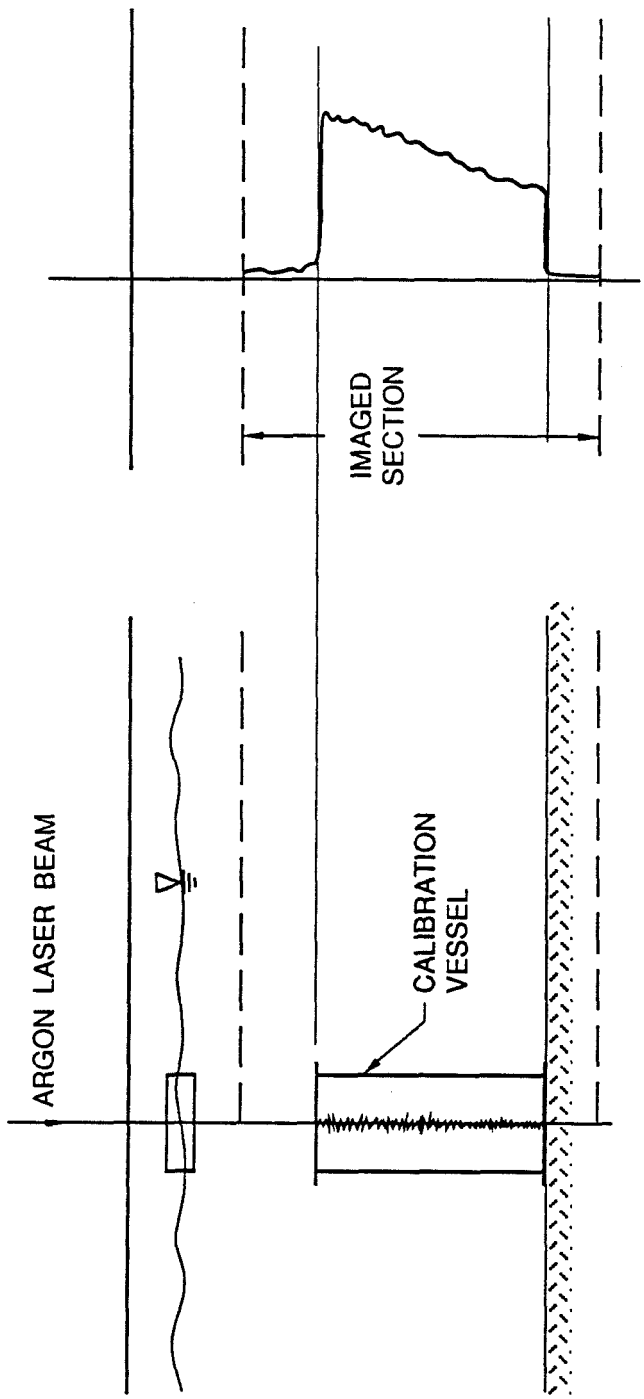

Figure 3.18 Determination of the magnification ratio for LIF experiments

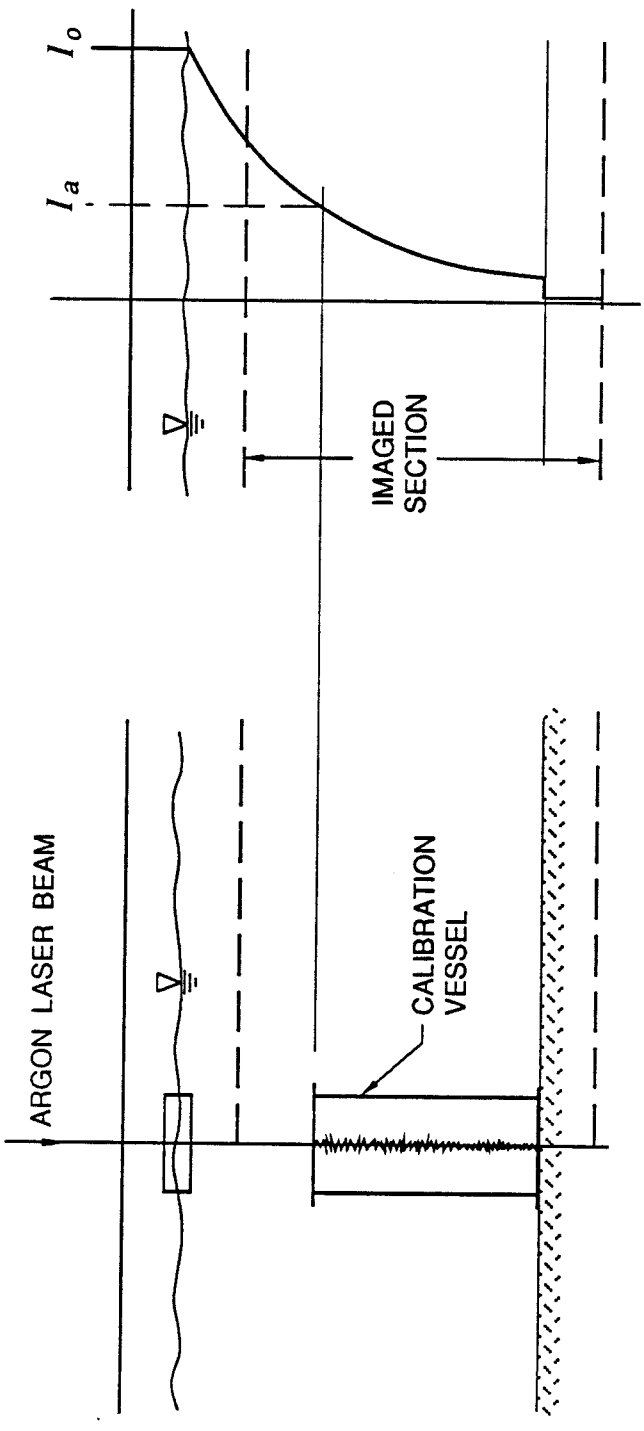

Figure 3.19 Determination of the additional attenuation in uncalibrated region of the flow

calibration vessel with fluid and measuring the attenuation through the vessel in the same way described in Appendix G. The concentration was computed from the observed attenuation using the inverted relationship between εC and C. Between *sets* of experiments, the flume was rechlorinated to bleach out any residual dye in the cross-flow fluid and sodium sulfite was added to dechlorinate the water shortly before the next set of experiments. This procedure had the added benefit of allowing the flume water to remain highly chlorinated during non-experimental periods and thus prevented the growth of bacteria which turned the water a murky white.

4. All parameters, the dark noise, the optical transfer function, the experimental data, must be collected at the same sampling frequency. This is required because the photodiodes in the array are light-integrating. Hence, if the sampling time is doubled, for an experiment, from the sampling time used during the calibration, the concentration values calculated would be double their actual value.

3.3.3 Data acquisition system

The concentration and velocity data were sampled and stored using a Masscomp SLS-5450-01 (Scientific Laboratory) data acquisition system. Laboratory Work Bench (LWB) (software packaged with the hardware) facilitated the use of the system. The system uses a 68020 CPU with a 20 MHz clock and allows burst rate sampling as high as 1 MHz for a single channel. The A/D converter is 12-bit and the disk drive is 142 MB.

The system is limited in two ways. First, the sampling frequency is limited by the system's ability to write information to disk for storage. The maximum sampling frequency we were able to realize for this system was approximately 350 kHz. Second, LWB, while user-friendly, also has some restrictions in sampling capability. Namely, if it is desired to sample more than one channel, both channels must be sampled at the same frequency. For the purposes of these experiments, we hoped to sample three channels, the LIF channel, and two LDV signals. However, the LIF channel must be sampled three orders of magnitude faster than the LDV signals. If data is collected from all three channels at the same rate, a lot of extraneous velocity data would be collected. The LIF experiments are highly data-intensive even without velocity data. Thus, excess data needlessly exacerbates the data management nightmare. Second, the camera does not start sampling until it receives the first positive step pulse from the enable signal. This assures that the first voltage signal sent to the data acquisition system is from the first pixel of the array. However, the data acquisition system records these meaningless values and it is not possible to *a priori* determine the number of data points that must be discarded before the actual signal stream starts. Therefore, we designed the external box to alleviate these two problems.

The external box serves two functions. First, it counts the number of data points received by the system up until the first positive step pulse of the enable signal. Therefore, in the data processing, we are able to delete those points systematically. Second, two more channels can be sampled during the down period of the camera. Two signals must be sent to the Reticon Camera in order for the camera to collect data: a clock signal, and a synchronize (or enable) signal. The camera has dip-switch settings that determine how many counts of the clock to make before starting the next scan. In all experiments, this dip-switch can be set such that the number of down counts can be a variable power of two, but must be a minimum of eight. In all the experiments conducted for this study, the switch was set to the minimum number of down counts, or eight. We thought that since

the camera requires at least eight counts of the clock to clear and reset, we could use these clock down counts to sample the LDV channels. Those channels would then be sampled at the clock frequency during the camera blanking period, but, not sampled again until the next camera blanking period. Therefore, the data sampled on these channels is like additional camera data which replaces the otherwise meaningless down-count data. The signals can then be separated during processing.

The external box operates according to the signal diagram shown in Fig. 3.20. The electrical diagram appears in Appendix H. (The functional aspects of the external box were designed in collaboration with Talal Balaa. The electrical design and physical construction was completed by Hai Vu.)

As discussed previously, in 3.3.2.1 Calibration Procedure for Concentration Measurements, the sampling frequency together with the cross-flow velocity determines the dynamic resolution for the concentration experiments. Appendix I is a discussion of the static and dynamic resolution of the LIF system.

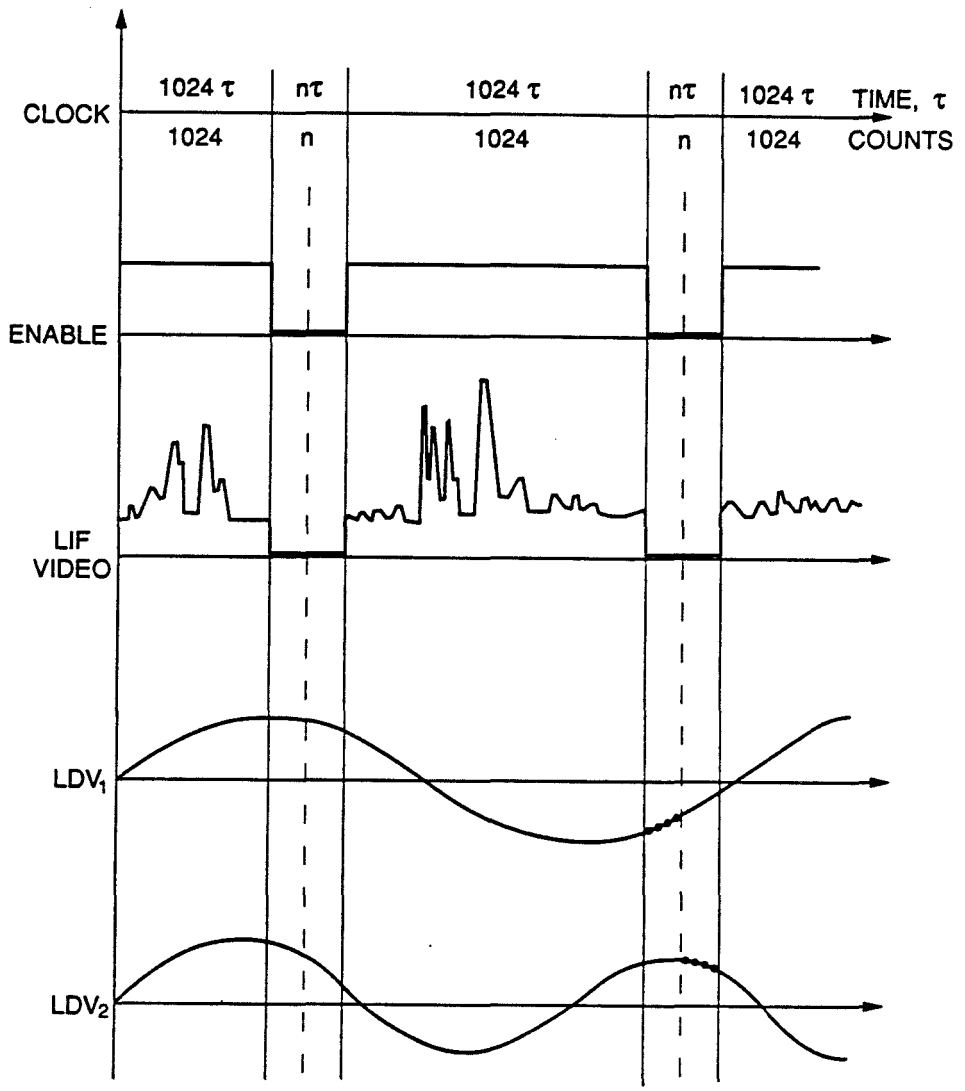

Figure 3.20 Signal diagram for external box of signal processing system

Chapter 4. Characterization of the Cross Flow

The theory outlined in chapter 2 requires knowledge of the mean cross-flow velocity, and the ratio of the cross-flow shear velocity to the root-mean-square (rms) velocity to characterize the cross-flow fully. All velocity data was collected using a sampling frequency of 140 Hz for a duration of 3 minutes. All aspects of the signal were convergent under this sampling scheme.

4.1 Mean cross-flow velocity and rms velocities

Figure 4.1 shows the non-dimensionalized mean cross-flow velocity as a function of distance from the flume bottom for various cross-flow Reynolds numbers, where the Reynolds number is defined as:

$$\mathrm{Re} = \frac{4R_h U}{\nu}$$

The flow is self-similar and the boundary layer occupies roughly 30% of the flow depth. Figures 4.2 and 4.3 show the rms velocities in the flow and vertical directions respectively. The cross-correlated velocity, or Reynolds stress, appears in Figure 4.4. (Note: These

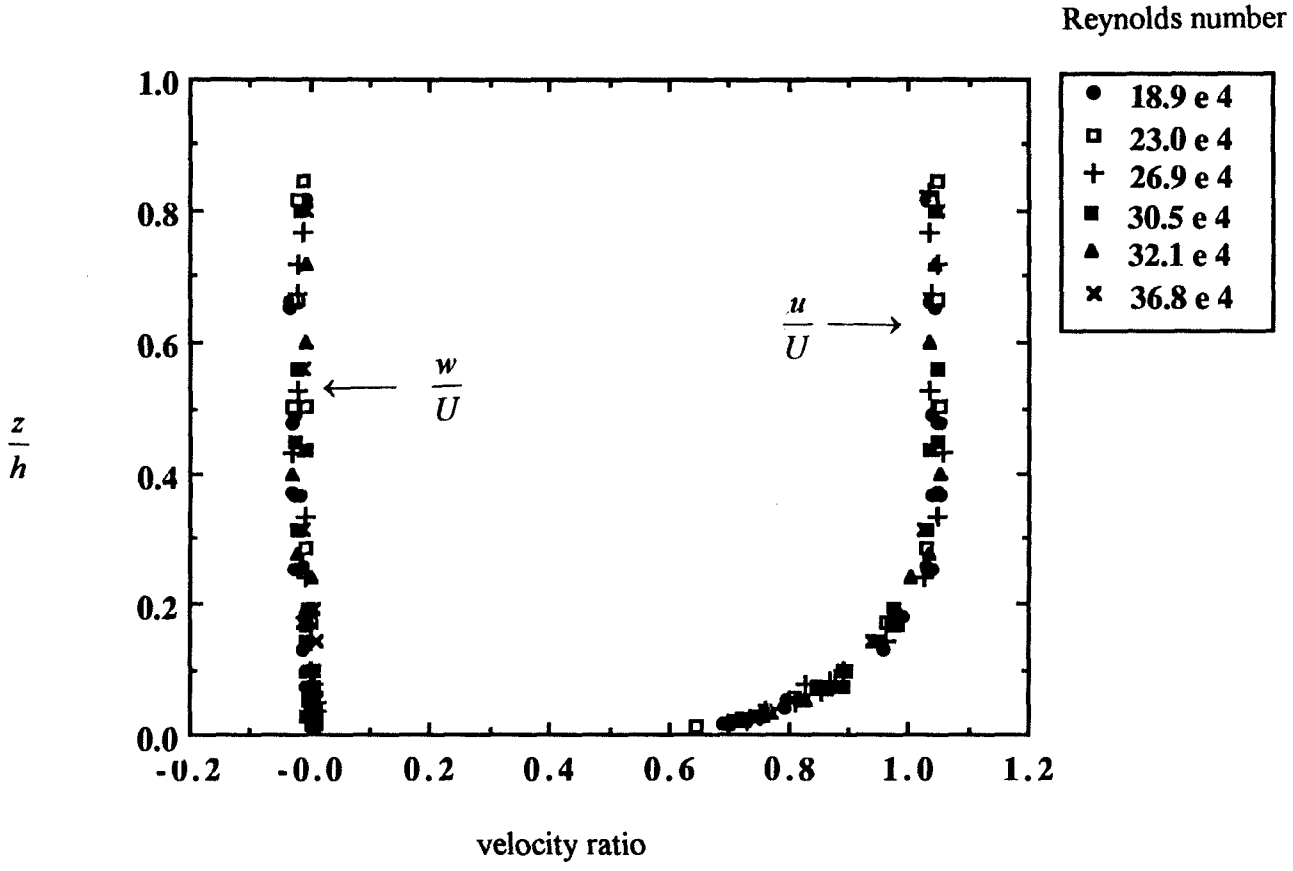

Figure 4.1 Non-dimensionalized cross-flow velocity profile, u/U versus z/h

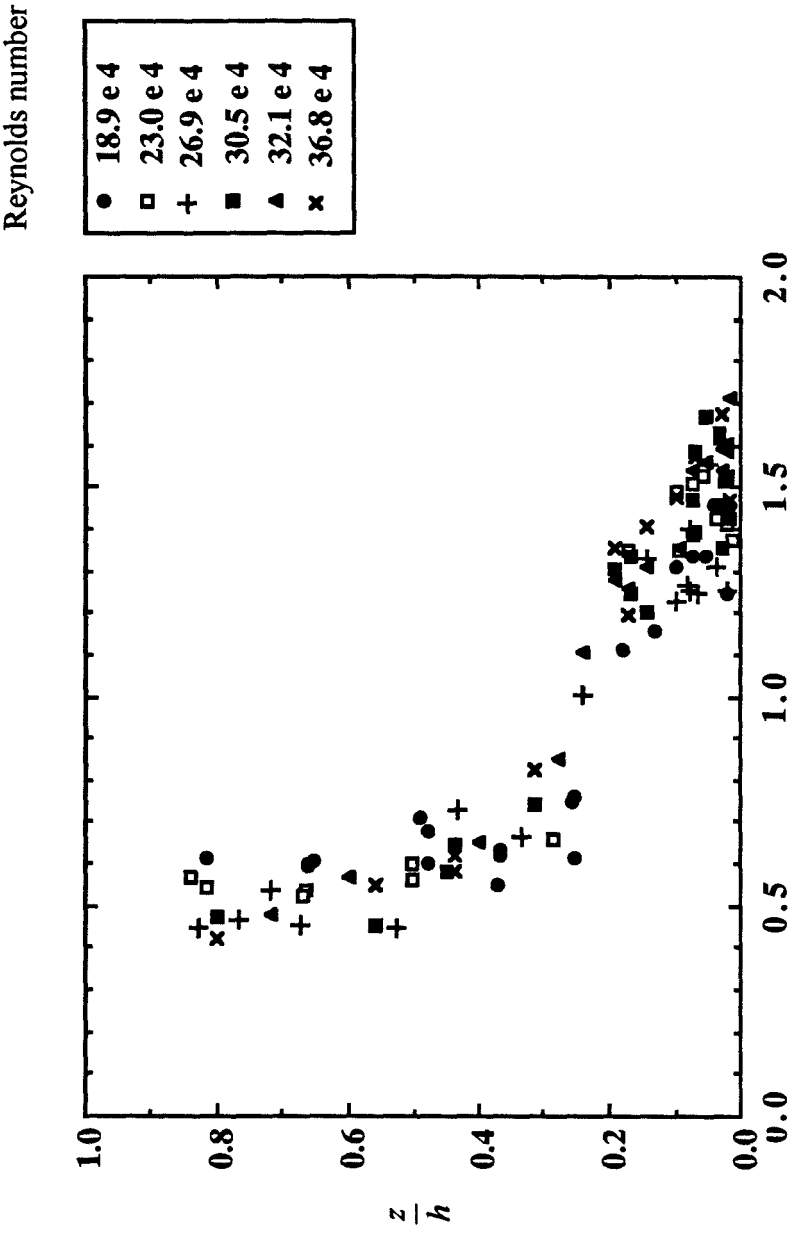

Figure 4.2 Non-dimensionalized flow-direction rms velocity profile, $\sqrt{\overline{u'^2}}/u_*$ versus z/h

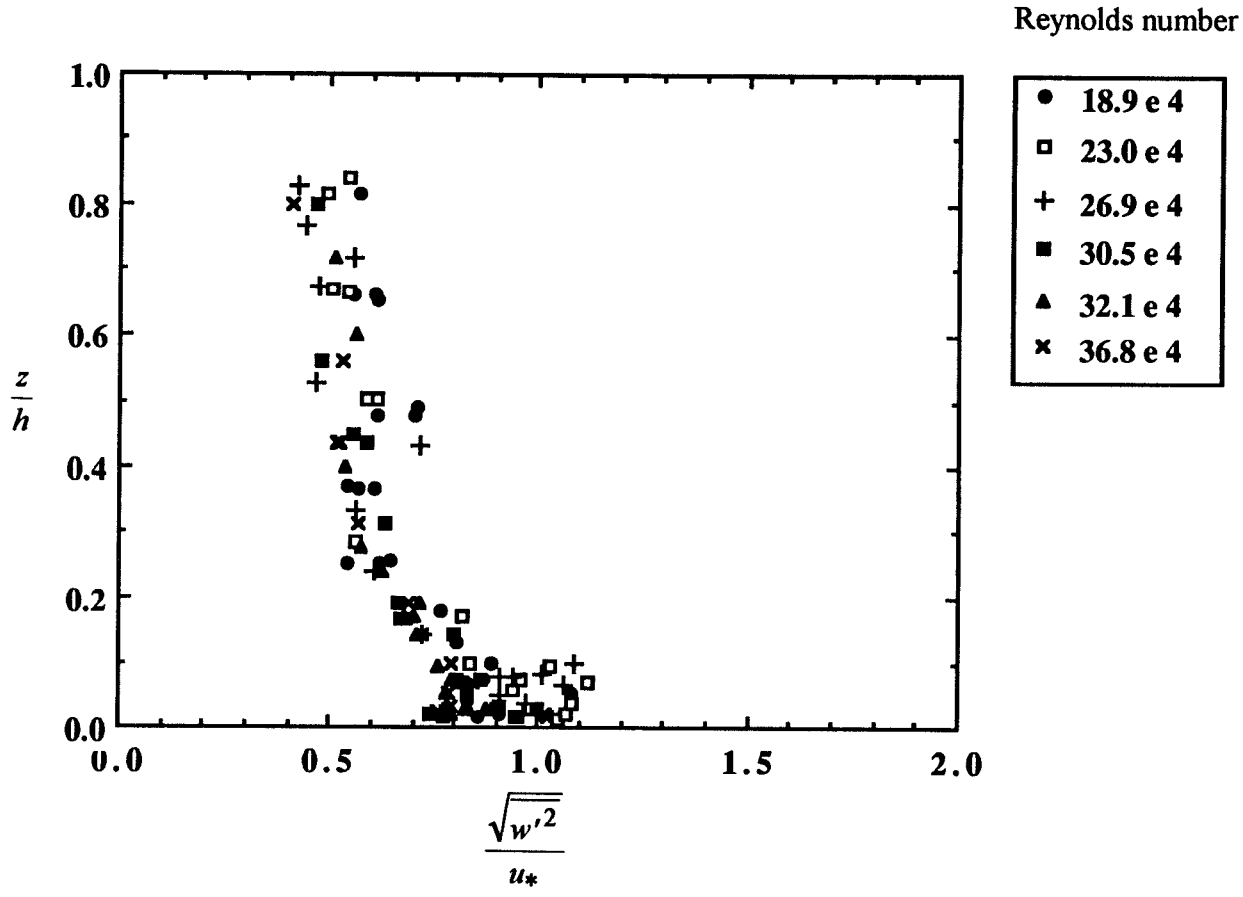

Figure 4.3 Non-dimensionalized vertical-direction rms velocity profile, $\sqrt{\overline{w'^2}}/u_*$ versus z/h

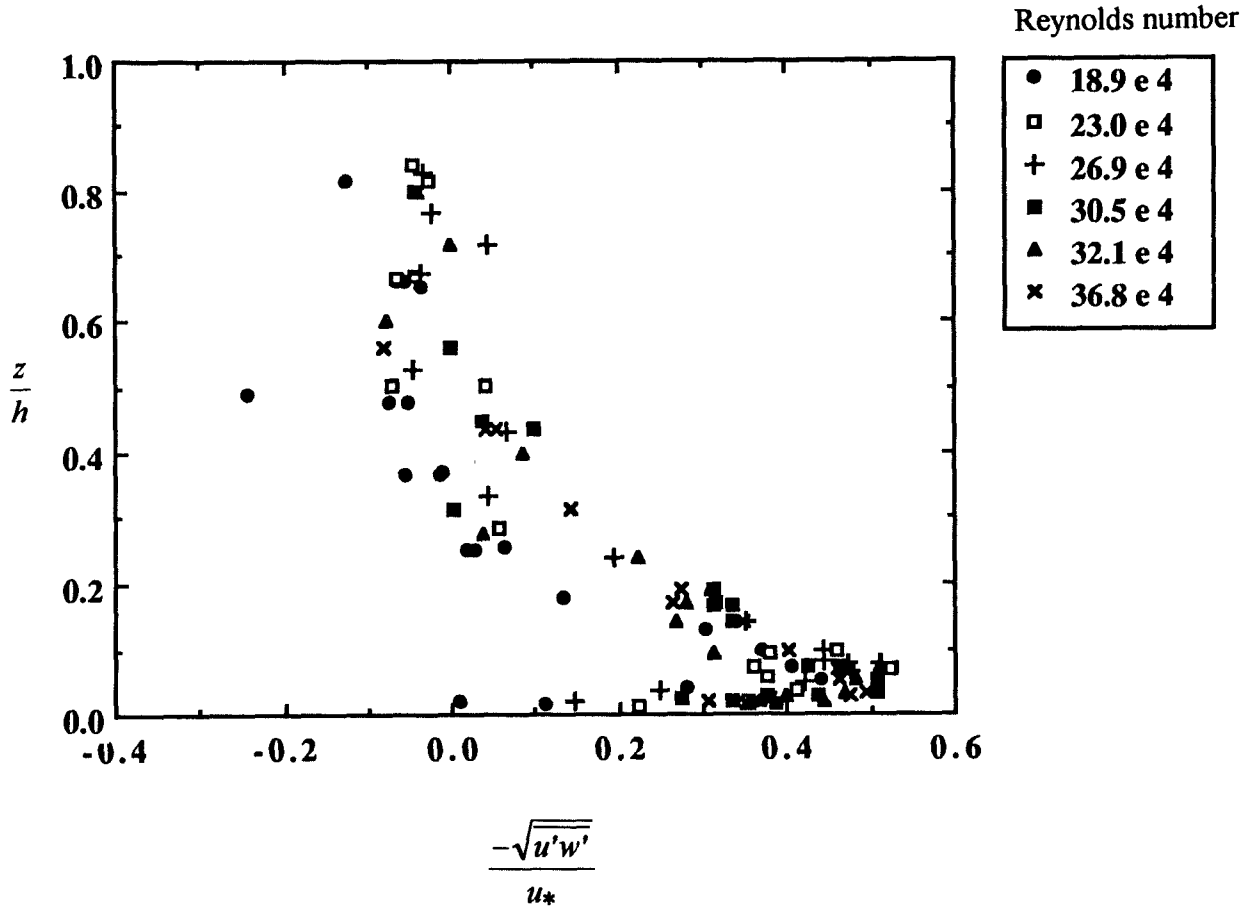

Figure 4.4 Non-dimensionalized cross-correlation profile, $-\sqrt{\overline{u'w'}}/u_*$ versus z/h

velocities are normalized by the shear velocity which is discussed later in section 4.2.) These results agree roughly with the results reported for channel flow in Nezu and Rodi (1986) and Lyn (1986) with the exception of the cross-correlated velocity. The cross-correlated velocity behaves as should be expected for this particular flow, since the cross-correlation should go to zero at the edge of the boundary layer. In this case, that occurs at a z/h of 0.3. We expect that the cross-correlation will approach unity very near the boundary of the flow and then return to a value of zero at the boundary.

Figure 4.4 shows that the cross-correlation does in fact go to zero at the boundary; however, a value of one near the floor of the flume is not observed. This can most likely be explained as follows: The shear stress in a turbulent flow is described by (Sabersky *et al.* (1964)):

$$\frac{\tau}{\rho u_*^2} = -\frac{\left(\overline{u}\,\overline{w} + \overline{u'w'}\right)}{u_*^2} \tag{4.1}$$

Near the wall, where $\tau/\rho = u_*^2$, and we typically assume that $\overline{w} = 0$, Eq. 4.1 implies that:

$$\frac{\overline{u'w'}}{u_*^2} \Rightarrow 1$$

As stated above, we found that this term does not approach one; rather, as shown in Fig. 4.4, it approaches 0.5. If, however, we do not assume that $\overline{w}$ is identically zero, then the first term on the right-hand side of Eq. 4.1 cannot be deleted. In fact, we can estimate, from other experimental results, the magnitude of the vertical velocity needed to account for the observed discrepancy. At an elevation of $0.1h$, Fig. 4.1 shows that $u/U = 0.9$, thus, at $U = 24$ cm/s, $u_* = 1.2$ cm/s, and a magnitude of only 0.03 cm/s in the vertical direction velocity would be needed to bring the right-hand side of Eq. 4.1 to 1.0. Examination of the dimensional velocity data routinely shows vertical velocities of this order.

4.2 Calculation of the shear velocity

Nezu and Rodi (1986) discussed three methods of obtaining the shear velocity in a fully-developed open channel flow. Of the three methods, the log-law was chosen for this investigation because of the inherent reliability of the parameters used. The log-law is defined as follows:

$$\frac{u}{u_*} = \frac{1}{\kappa} ln\left(\frac{zu_*}{\nu}\right) + A \qquad \text{for } \frac{z}{h} < 0.2 \tag{4.2}$$

where u is the average velocity at location z, κ is the von Karman constant, ν the kinematic viscosity, A an arbitrary constant, and u_* is the shear velocity defined as:

$$u_* = \sqrt{\frac{\tau_o}{\rho}}$$

If Eq. 4.1 is expanded, it becomes

$$u = \frac{u_*}{\kappa} ln(z) + A' \tag{4.3}$$

where

$$A' = u_*\left[\frac{1}{\kappa} ln\left(\frac{u_*}{\nu}\right) + A\right]$$

Thus, according to Eq. 4.2, the slope of u vs. $ln(z)$ would yield u_* provided κ is known. Nezu and Rodi report a value of κ equal to 0.412 and A equal to 5.29. Both constants appear to be universal in that there is no observed dependence on either the Reynolds or Froude numbers of the flow. These constant values are in agreement with the results of several other studies (in an open channel, Steffler *et al.* (1983), in boundary layers, Huffman and Bradshaw (1972), and in closed channel flow, Dean (1978)). Figure 4.5 shows the result of plotting u vs. $ln(z)$ over the Reynolds number range used in the open water channel of this study.

As expected, the relationship is linear up to about 15% of the flow depth. This result is consistent with the results reported in Nezu and Rodi and the deviation from the

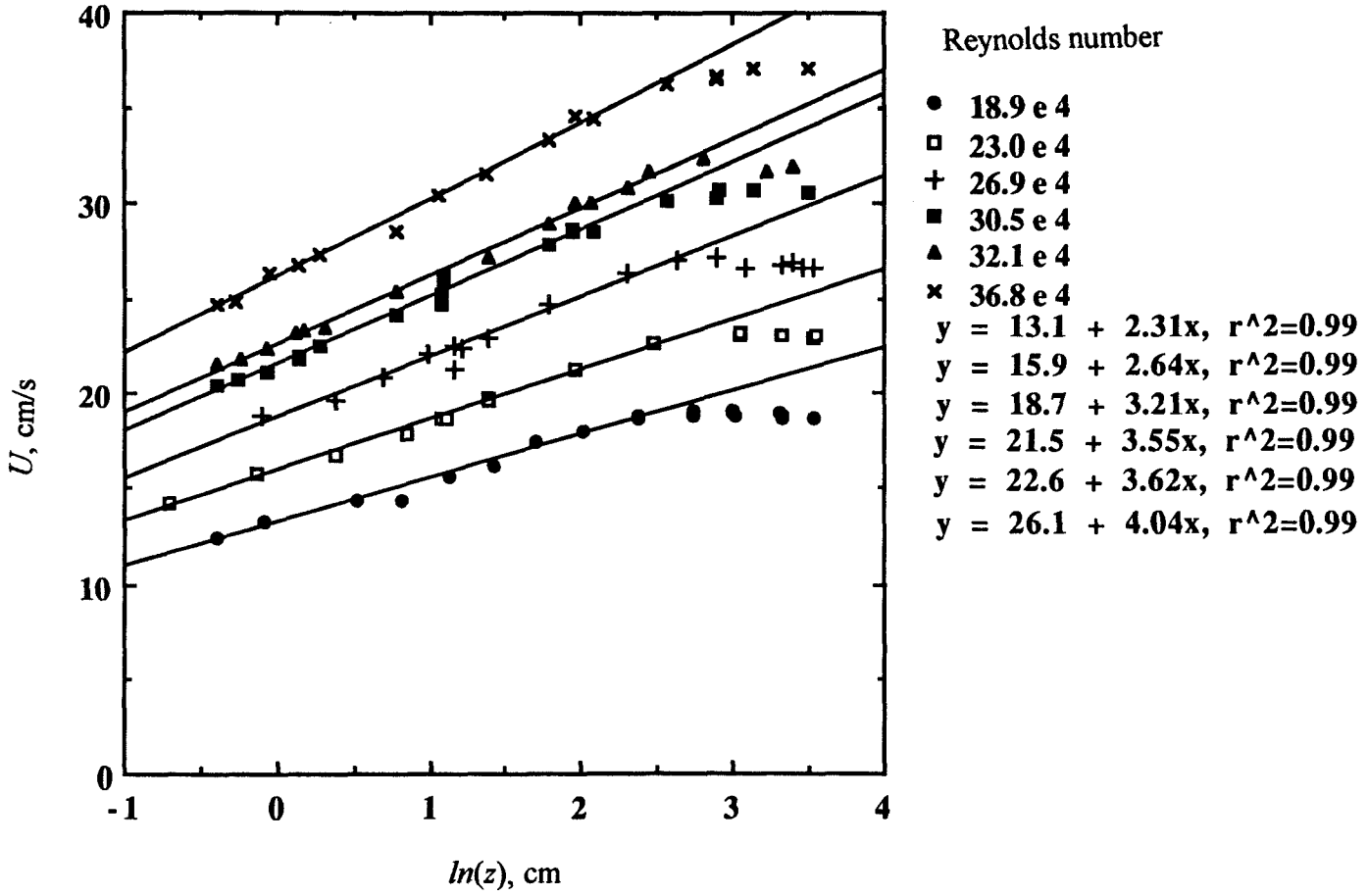

Figure 4.5 Cross-flow velocity versus vertical position, *u* versus *ln(z)*

log-law above 15% can be described by the wake function introduced by Coles (1956). The shear velocity as a function of the average cross-flow velocity can thus be obtained from this plot. The functional relationship between the shear velocity and the average cross-flow velocity is not strictly linear as might be deduced from Eq. 1.4 because the friction factor, f, is also a function of the average cross-flow velocity. The relationship between the friction factor, f, and the Reynolds number for flow in smooth pipes can be defined by the Blasius equation which yields a dependence of the form:

$$f = 0.223\mathrm{Re}^{-1/4} \tag{4.4}$$

Analogous equations for flow in open channels were developed by Keulegan in Corbett *et. al.*(1943). It was found that these results, while not exactly equivalent, were very close to pipe flow results. A plot of the f-Re relationship for flow in smooth channels can be found in Chow (1959) and is shown here as Fig. 4.6. (Note: The Reynolds number that appears in Chow's plot is based on the hydraulic radius, not four times the hydraulic radius.) It can be easily seen that the Blasius equation solution works well for turbulent flow in smooth open channels. Thus, if we recall Eq. 1.4,

$$\left(\frac{f}{8}\right)^{\frac{1}{2}} = \frac{u_*}{U} \tag{1.4}$$

then the following is true:

$$\frac{u_*}{U} \sim \left(\frac{\left(\mathrm{Re}^{-1/4}\right)}{8}\right)^{\frac{1}{2}} \sim \left(U^{-1/4}\right)^{\frac{1}{2}}$$

$$u_* \sim U^{7/8} \tag{4.5}$$

The average velocity, U, in the flume is calculated from the velocity profile by a trapezoidal integration technique. Appendix J contains the program used for the calculation of cross-flow parameters. The above functional relationship between the shear velocity and the average cross-flow velocity is confirmed in Fig. 4.7. Clearly, the flow follows the functional form of the Blasius equation. This is despite the fact that the

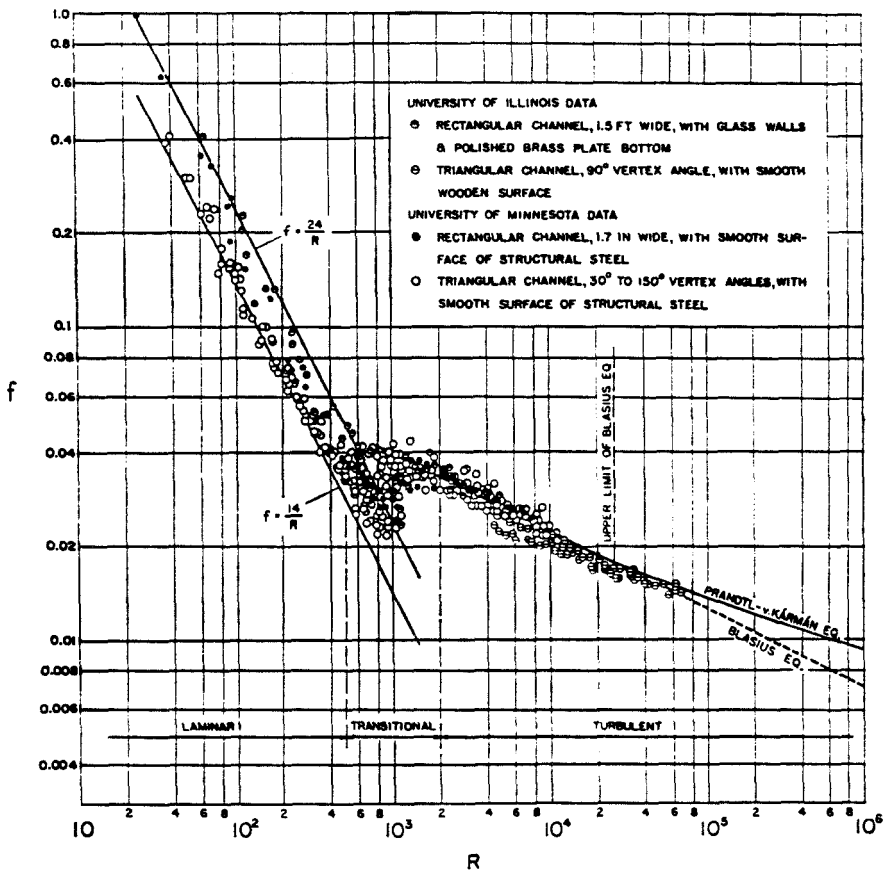

Figure 4.6 Friction factor as a function of Reynolds number for flow in smooth channels (from Chow (1959))

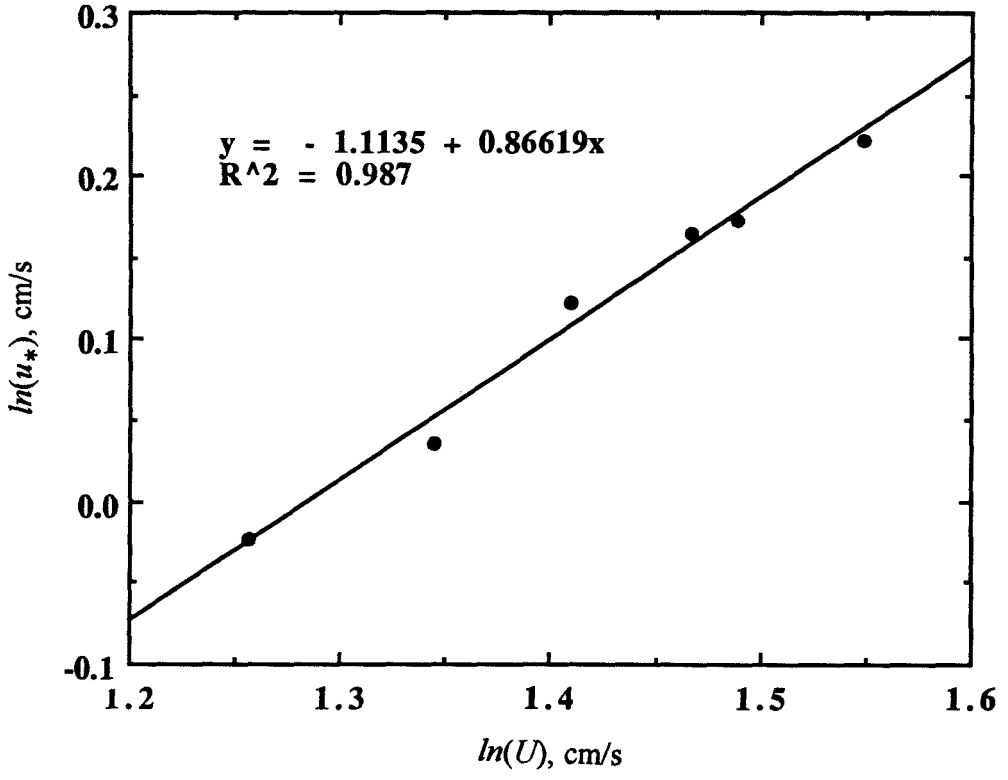

Figure 4.7 Average cross-flow velocity versus shear velocity, U versus u_*

Blasius equation is reported to be applicable only over a Reynolds number range between 3000 and 100,000, which is lower than the typical Reynolds numbers of this study.

Additionally, we can utilize the relationship between the shear velocity and the average velocity to calculate a friction factor for comparison with Chow's data shown in Fig. 4.6. Using a shear velocity of 1.2 cm/s, we calculate, from the numerical fit shown in Fig. 4.7, a value of 23.8 cm/s for the average cross-flow velocity. These numbers can be substituted into Eq. 1.4 to find an approximate value of 0.02 for the friction factor at a Reynolds number of 6.3e4. The value of the friction factor calculated from the Blasius equation, Eq. 4.4, is 0.014 at this Reynolds number, which is a difference of about 30%. Since the flow is not fully developed, we might use the boundary layer thickness as the characteristic length scale for the Reynolds number and calculate a value of 3.3e4. Using this value, the Blasius equation yields a friction factor equal to 0.017, which is about 15% different from the experimentally determined value. This difference may be explained by ridges in the false bottom which increase the roughness of the channel, or may be attributed to the developing nature of the boundary layer since friction factors are higher in developing flows than in fully-developed flows.

4.3 Alternative methods for calculating the shear velocity

Since the shear velocity is a measure of the bottom shear stress, a force balance on a fluid element yields another method of calculating the shear velocity:

$$u_* = \sqrt{g s_{cf} R_h} \tag{4.6}$$

where s_{cf} is the slope of the *c*ross-*f*low water surface, g is the gravitational constant, and R_h is the hydraulic radius. The above equation assumes that the shear is created equally over the entire wetted perimeter of the flow. The value obtained using this method is therefore always low since lower velocities in the corners of the flow channel would

generate less shear. The same equation using the depth of the flow, h, in place of the hydraulic radius

$$u_* = \sqrt{g s_{cf} h} \tag{4.7}$$

assumes a two-dimensional flow case wherein shear is created only on the bottom surface. The value of the shear velocity obtained from this method is always high.

Thus, the value of the shear velocity obtained from these equations serves as a further check on the value of the shear velocity obtained from the log-law method. Values of the shear calculated from Eqs. 4.6 and 4.7 should bracket the actual value of the shear which is more closely approximated by the log-law method. This is shown in Fig. 4.8.

Most often when this method is employed, the flume bottom has been arranged such that the water surface and the flume bottom are parallel. This ensures that the flow is uniform along the entire length of the flume. If the fluid surface has a slope different from the flume bottom slope, then conservation of mass shows that the average cross-flow velocity cannot be constant. In this experimental investigation, where the cross-flow velocity was varied repeatedly in the course of a day's experimental set, the slope of the flume bottom was not changed. Strictly speaking, this means that the cross-flow velocity was not uniform. However, because the slope of the surface was so small, the error introduced was not appreciable over the one meter distance in which experiments were conducted. For the largest cross-flow velocity calibrated, 30.8 cm/s, with a flow depth of approximately 41.5 cm, the slope of the surface was 6.5×10^{-5} m/m The slope quoted here is the difference between the slope at zero velocity and the surface slope at the given velocity. All cross-flow calibration measurements were taken at $x = 0$, i.e., at the point of release of the buoyant jet, and since experiments were conducted at a maximum distance of 100 cm from the point of release, the ratio of the average velocity at the point of release to the average velocity 100 cm downstream is approximately:

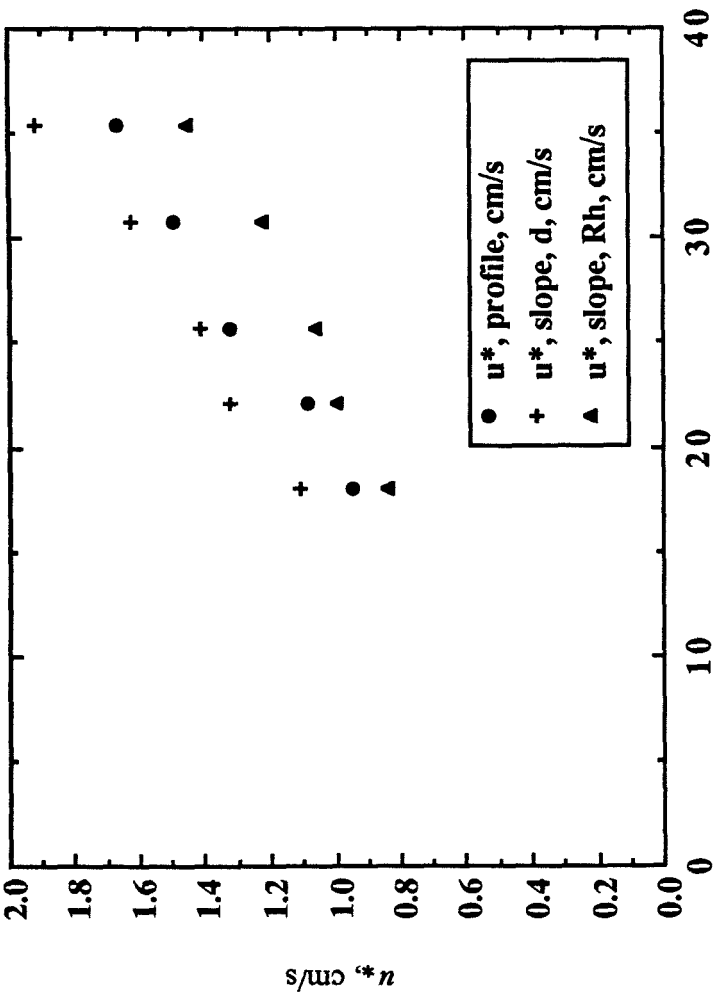

Figure 4.8 Comparison of shear velocity using slope techniques and log-law technique, U versus u_*

$$\rho U_1 A_1 = \rho U_2 A_2$$

$$\frac{U_1}{U_2} = \frac{A_2}{A_1} = \frac{wh_2}{wh_1} = \frac{h_1 - s_{cf}\Delta x}{h_1}$$

$$= \frac{\left(41.5 - (6.456 \times 10^{-3}\,\text{cm/m})(1\text{ m})\right)}{41.5\text{ cm}}$$

$$\cong 1.00$$

Consequently, there is no measurable error in the average cross-flow velocity over this distance due to surface slope.

The growth of the boundary layer, however, introduces more error. Over the 100 cm in which experiments are conducted, the boundary layers on the walls and on the bottom of the flume grow in accordance with the following equation:

$$\frac{\delta}{x} = 0.220\,\mathrm{Re}_x^{-1/6} \qquad 10^6 < \mathrm{Re}_x < 5\cdot 10^8$$

where

$$\mathrm{Re}_x \equiv \frac{Ux}{\nu}$$

Thus, if we assume that the boundary layer thickness is zero at $x = 0$ cm (the buoyant jet release point), then we can calculate the boundary layer growth under average flow conditions as follows:

$$\delta = 0.220\left(\frac{1e-2}{25}\right)^{1/6} 100^{5/6} = 2.8\text{ cm}$$

if we view this boundary layer growth as an effective decrease in the cross-sectional area available for flow, then the average velocity would change as:

$$\frac{U_1}{U_2} = \frac{A_2}{A_1} = \frac{(110-2(2.8))\cdot(41.5-2.8)}{110(41.5)} = 0.89$$

indicating an 11% change in the average cross-flow velocity. This is, of course, an exaggeration, since the boundary layer does not "block" the flow completely, and further, as the flow approaches the fully developed condition, boundary layer growth is inhibited.

Therefore, this amounts to an upper bound on the effect of boundary layer growth on the average cross-flow velocity.

4.4 The ratio of the rms velocity to the shear velocity

To finish the characterization of the cross flow, it was necessary to have some measure of the rms velocity in the cross flow. An integrated average value of the flow-direction rms velocity was used for this purpose. Then, since the average vertical rms is related to the average flow-direction rms by a constant, the ratio of the shear velocity to the vertical rms velocity required for the theory could finally be obtained. Figure 4.9 shows that the ratio of the average flow-direction rms velocity to the shear velocity is a constant for the flow configuration used in these experiments.

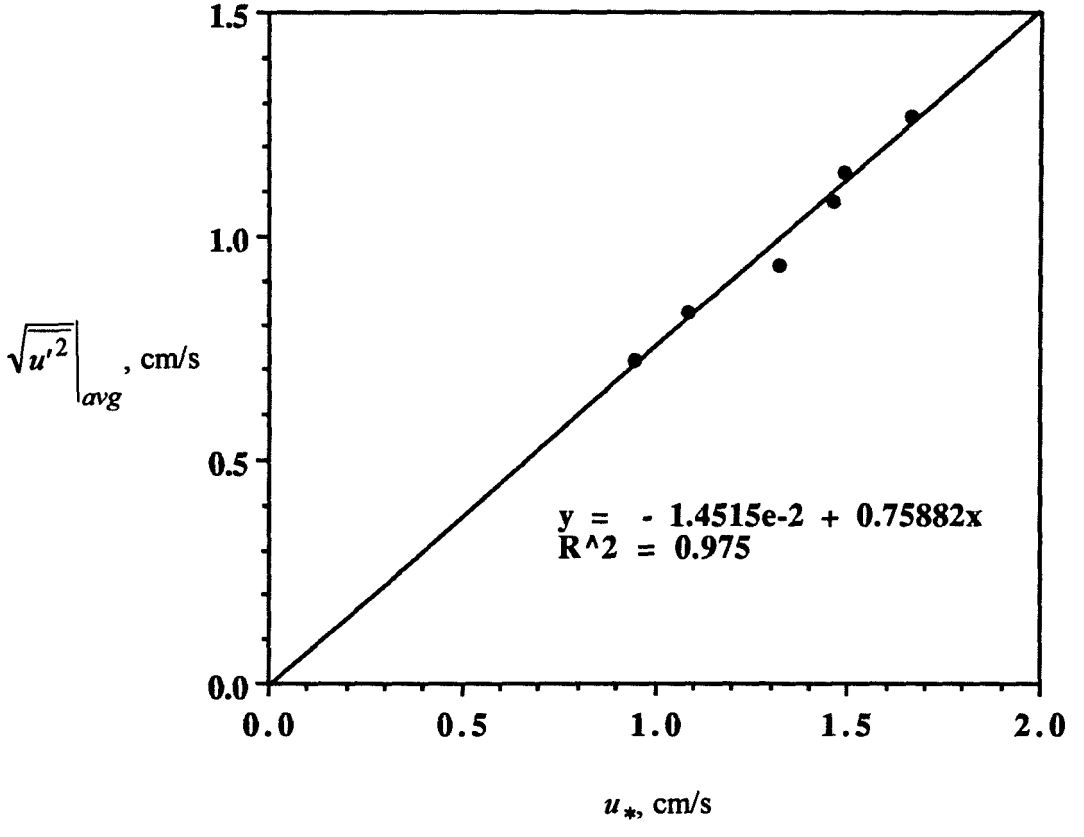

Figure 4.9 Flow direction rms velocity versus average cross-flow velocity

Chapter 5. Transition Phenomena

In this chapter we will address transition as it relates to the vertical and to the horizontal dimensions of a buoyant jet in a cross flow with shear. We will begin by reviewing the discussion of transition in the vertical dimension from chapter 2 and then develop analogous equations describing transition in the horizontal dimension. The trajectory equations describing each regime of the flow are required for this purpose and hence are developed in this chapter. As an aside, we will seek to gain closer estimates of the region of transition using a proposed method for resolving, from other experimental investigations, the leading constants in the above-mentioned equations and for determining the virtual origin for each of the flow regimes. Finally, we will look at some experimental data for the sole purpose of assessing this technique as a method for predicting the location of the region of transition more accurately than dimensional analysis alone permits.

Before we begin, it is important to distinguish between the characteristic length scale governing transition and the physical coordinate of transition.

5.1 The characteristic length scale versus the coordinate of transition

There are many ways to ascertain the relevant characteristic length scales defining a particular transition, and no one way is necessarily superior to the other. We might choose to define transition as the point where the centerline velocities are equivalent, as we did in chapter 2, or as the point where the trajectories of two asymptotic solutions have equivalent x-locations and z-locations, i.e., where the trajectories match, or as the point where the dilutions become equal. Any of these definitions will yield a characteristic length scale that is representative of the *effect various flow parameters have on the location of transition.* This is different from finding the location, or coordinate of transition. Our primary goal in defining characteristic length scales is to be able to non-dimensionalize experimental data correctly and hence to determine empirically the constants that are required to determine transition more accurately. Only when these empirical constants are determined, can we locate the *coordinate of transition.*

In the discussions that follow, a clear distinction is made between the characteristic length scale relevant to a particular transition and the coordinate, or location, of that transition. It should be noted that the discussions regarding the characteristic length scales are not new; in fact, similar discussions can be easily found in several other references (Fischer *et al.*(1979), Wright (1977), Fan (1967)). They are included here for completeness and to assist in later sections. However, the discussions regarding the *physical coordinate* of transition are unique to this work. They are preliminary in nature and should be viewed as such. We are attempting in these later discussions to determine closer estimates for the coordinates of transition by resolving the leading constants and by determining the virtual origins of the various flow regimes.

5.2 Determining the character of the flow using length scales

As a starting point, for any set of flow parameters, it is useful to rank order the characteristic length scales to obtain an estimate of the *order of transitions*. In other words, we can determine, using characteristic length scales, whether the flow will transition from a *jet* to a *bent jet* to a *bent plume* to *diffusion based on the elevation* to *diffusion based on the depth*, or whether it will transition from a *jet* to a *plume* to a *bent plume* to *diffusion based on the depth*. There are of course, many other permutations of the above length scales. Also, there are still other transitions defined by additional length scales that do not appear in the above list, i.e., l_b, the transition from *plume* to *bent plume* behavior, that further complicate the picture. Furthermore, if any two of the length scales are of the same order, we will find it difficult to predict the character of the flow with any certainty. In fact, under such circumstances the actual flow will likely have muddled transition regions that are difficult to decipher.

Nonetheless, characteristic length scale arguments are extremely useful in so much as we are able to determine the effect of changing flow parameters on the region of transition and the order of the asymptotic regimes of flow.

5.3 Transition in the vertical dimension

In chapter 2 we defined transition as the point at which the centerline velocity of one asymptotic form of flow becomes equal to centerline velocity of another asymptotic form. This definition is arbitrary in that there is no overwhelming physical significance for it. We might, however, convince ourselves that such a definition is reasonable by arguing that the centerline velocity is a measure of the local momentum flux. Therefore, while the flow is jet-like, the centerline velocity will go as predicted by jet theory; however, when the flow is dominated by buoyancy-induced momentum, the functional behavior of the centerline velocity would change to that of a plume. The real question is whether or not it is valid to assume that the developments of jet-like and plume-like flow behavior occur

independently, and further if this transition can be assumed to occur where these "independently developed" velocities are equal. After all, the true flow is *not* a plume before the region of transition.

Despite these questions, this definition of transition seems reasonable if viewed as the limit of two asymptotic solutions. Further, if we are to make progress in interpreting experimental results and making better estimates of transition, we must attempt such predictions.

5.3.1 The characteristic length scales in the vertical dimension

With this in mind, recall the results of chapter 2 wherein we developed equations to define the vertical location of transition for the various flow regimes and as a consequence, the vertical characteristic length scales of transition.

In chapter 2 we considered all the transitional length scales previously identified for buoyant jets in a uniform velocity cross flow. In the present work, however, an additional complexity has been added – a boundary layer cross flow rather than a uniform cross flow – and this complexity implies yet another transitional characteristic length scale. We did not include this transition previously, primarily because we assumed that upon reaching the transition from bent-plume mixing to diffusion mixing, the buoyant jet would have spread sufficiently over the depth of the flow that it would be sampling from length scales on the order of the total depth. However, upon examination of the dilution data (see chapter 6) we found the region of diffusive mixing to occur sooner than predictions suggest. This result necessitated the consideration of an additional transition – from diffusion characterized by the elevation in the boundary layer to diffusion characterized by the overall depth. The formulation of this characteristic length scale is straightforward since the turbulent diffusion coefficient, D, will be proportional to the depth when the elevation is of the order of the depth, i.e., when $z \propto h$. Thus, the appropriate characteristic length scale for this transition is quite simply the depth, h. Table 5.1 shows

the characteristic length scales relevant to transition in the vertical dimension along with the additional transition discussed above.

Table 5.1 Summary of vertical characteristic length scales describing transition

Transition	Vertical characteristic length scale
jet - bent jet	$\propto l_{j-bj,z} = l_j$
bent jet - bent plume	$\propto l_{bj-bp,z} = \left(\frac{M^2}{UB}\right)^{1/3}$
bent plume - diffusion	$\propto l_{bp-d,z} = \frac{B}{Uu_*^2}$
boundary layer diffusion - diffusion over depth	$\propto l_{bld-hd,z} = h$

Using these vertical characteristic length scales we are able to predict the effect a change in one flow parameter has on the location of transition. However, we reiterate that characteristic length scale arguments cannot predict the *coordinate of transition*. For that purpose, we must rely on experimental evidence to determine the leading constants and hence fully determine the equations describing transition.

5.3.2 The vertical coordinates of transition

The formulation of equations describing transition in chapter 2 included a leading constant which is a function of the velocity-relation constants. As such, these constants are related to the specific definition of transition that is used. (Section 5.4.3.1 shows the effect of various definitions of transition on the leading constant.) These constants cannot, strictly speaking, be obtained on the basis of the definition of transition and experimental data quantifying other constants. However, in subsequent sections we propose a technique for resolving these constants from other experimental investigations and hence for obtaining estimates of the actual coordinates of transition.

The equations from chapter 2 describing the vertical coordinate of transition are repeated below for convenience. We have also included an equation describing the coordinate of the transition within the diffusive mixing regime, from a region where the diffusion coefficient is based on the elevation, z, to a region where the coefficient is based on the overall depth, h. We have used the constant, a_{hd}, to relate the characteristic length scale to the coordinate.

Table 5.2 Summary of equations describing vertical coordinates* of transition

Transition	z-coordinate of transition
jet - bent jet	$z_{j-bj} = \left(\frac{a_{bj}}{a_j}\right)\frac{M^{1/2}}{U}$
bent jet - bent plume	$z_{bj-bp} = \left(\frac{a_{bj}}{a_{bp}}\right)^{2/3}\left(\frac{M^2}{UB}\right)^{1/3}$
bent plume - diffusion	$z_{bp-d} \propto \left(\frac{B}{Uu_*^2}\right)$
diffusion, z - diffusion, h	$z_{bld-hd} = a_{hd}h$

*(Note: We have not shown the relationship between constants for the leading coefficient in the equation describing the bent plume to diffusion transition. This coefficient is the result of a complex process which results from the definition of transition as the point of vertical rms equivalence. For details, see chapter 2.)

5.4 Transition in the horizontal dimension

Predictions are most useful if they are in terms of measurable experimental parameters. Specifically, in this investigation it is a simple matter to measure the location x at which experiments are conducted. In addition, for regulatory purposes, specifications are typically written in terms of distance from the point of release; therefore, it is the distance, x, from the discharge point that is of regulatory significance. We are thus interested not in the z-location of transition as discussed in chapter 2, but rather in the x-location of transition.

This requires knowledge of the relationship between the vertical coordinate z and horizontal coordinate x, or, the trajectory of the flow in each of the regimes that the buoyant jet follows. Such relationships are superfluous to a pedagogical discussion of the relevant transitions and are therefore not discussed in chapter 2; however, in this chapter they are of prime importance. Therefore, next we will introduce some additional relationships describing the trajectory relations for a buoyant jet in a cross flow.

5.4.1 Trajectory relations

If we assume that a buoyant jet in a cross flow is advected at a constant cross-flow velocity, U, as was suggested in chapter 2, then the kinematic relation, from Wright (1977), describing the flow is:

$$\frac{dx}{U} = \frac{dz}{w_m}$$

In actuality, we do not know that an equality is appropriate in this case. Rather, we should write this equation as:

$$\frac{dx}{U} \propto \frac{dz}{w_m}$$

or alternatively as:

$$\frac{dx}{U} = a_{ke} \frac{dz}{w_m} \tag{5.1}$$

where the constant a_{ke} must be determined from experimental data.

If we substitute the relevant velocity relation into the kinematic equation and integrate, we are able to determine the equation describing the buoyant jet trajectory in each flow regime. For example, recall from chapter 2, that for a nonbuoyant jet in a quiescent medium, we found the centerline velocity to be:

$$w_m = a_j \frac{M^{1/2}}{z}$$

If we substitute into the kinematic equation and prepare to integrate, we have:

$$\int_0^x \frac{dx'}{U} = a_{ke} \int_0^z \frac{z'dz'}{a_j M^{1/2}}$$

where we have assumed that $x = 0$ at $z = 0$, i.e., that the coordinate system has been positioned at the virtual origin. Then, upon integration:

$$\frac{z}{l_j} = \left(\frac{2a_j}{a_{ke}}\right)^{1/2} \left(\frac{x}{l_j}\right)^{1/2} = C_1 \left(\frac{x}{l_j}\right)^{1/2}$$

This provides an equation describing the trajectory of a near-field jet. Note that it is a function of the cross-flow velocity by virtue of the appearance of l_j in the equation.

Wright (1977) performed the same integration, however, failed to recognize the relationship between C_1 and the velocity relation constant. Once this connection is realized, it becomes possible to use the value of Wright's constant and the reported value for a_j to obtain an estimate of a_{ke}. This is discussed in more detail below in section 5.5.1.

It is a simple exercise to derive the other trajectory equations from the velocity relations. The results are provided in Table 5.3.

Table 5.3 Summary of velocity and trajectory relations for a buoyant jet in the various flow regimes

Regime	Centerline velocity	Trajectory relation	Constant
jet	$w_m = a_j \frac{M^{1/2}}{z}$	$\frac{z}{l_j} = C_1 \left(\frac{x}{l_j}\right)^{1/2}$	$C_1 = \left(\frac{2a_j}{a_{ke}}\right)^{1/2}$
bent jet	$w_m = a_{bj} \frac{M}{Uz^2}$	$\frac{z}{l_j} = C_2 \left(\frac{x}{l_j}\right)^{1/3}$	$C_2 = \left(\frac{3a_{bj}}{a_{ke}}\right)^{1/3}$
bent plume	$w_m = a_{bp} \left(\frac{B}{Uz}\right)^{1/2}$	$\frac{z}{l_b} = C_3 \left(\frac{x}{l_b}\right)^{2/3}$	$C_3 = \left(\frac{3a_{bp}}{2a_{ke}}\right)^{2/3}$
plume	$w_m = a_p \left(\frac{B}{z}\right)^{1/3}$	$\frac{z}{l_b} = C_4 \left(\frac{x}{l_b}\right)^{3/4}$	$C_4 = \left(\frac{4a_p}{3a_{ke}}\right)^{3/4}$

The above equations completely describe each part of the trajectory. The last set of relations listed in Table 5.3 (for a near-field plume) are provided for completeness although in this investigation we are concerned with only the jet, bent jet, and bent plume regimes.

5.4.2 The characteristic length scales in the horizontal dimension

Using the trajectory relations, we can define the characteristic length scales for the horizontal dimension. We proceed by substituting the characteristic length scale in the vertical dimension (see Table 5.2) into either of the appropriate trajectory relations as shown below.

For the jet to bent jet transition, we have:

$$\frac{z}{l_j} \propto \left(\frac{x}{l_j}\right)^{1/2}$$

$$\frac{l_{j-bj,z}}{l_j} \propto \left(\frac{l_{j-bj,x}}{l_j}\right)^{1/2}$$

$$\frac{l_j}{l_j} \propto \left(\frac{l_{j-bj,x}}{l_j}\right)^{1/2}$$

$$l_{j-bj,x} \propto l_j$$

In this case, the horizontal characteristic length scale is equivalent to the vertical characteristic length scale. This is not true for the other relevant transitions and it is easy to show that the remaining horizontal characteristic length scales are as in Table 5.4.

The obvious exception is the transition from diffusion based on elevation, z, to diffusion based on the depth, h. The horizontal characteristic length scale for this transition depends on the specific flow regime in which the transition occurs since the relation between z and x is governed by the trajectory for that regime. Therefore, we must form this horizontal characteristic length scale separately for each possible flow regime by

substituting the vertical characteristic length scale, h, into the trajectory equation. These results appear in Table 5.4.

Table 5.4 Summary of horizontal characteristic length scales describing transition

Transition	Horizontal characteristic length scale
jet - bent jet	$\propto l_{j-bj,x} = l_j$
bent jet - bent plume	$\propto l_{bj-bp,x} = \frac{MU}{B}$
bent plume - diffusion, h	$\propto l_{bp-d,x} = \frac{B}{u_*^3}$
diffusion, z - diffusion, h	
jet regime	$\propto l_{bld-hd,x} = \frac{h^2}{l_j}$
bent jet regime	$\propto l_{bld-hd,x} = \frac{h^3}{l_j^2}$
bent plume regime	$\propto l_{bld-hd,x} = \frac{h^{3/2}}{l_b^{1/2}}$

Theoretically, of course, there are several other transitions that might be considered. For example, the transition from bent-plume mixing to diffusive mixing where the coefficient of diffusion is based on the elevation, z; or bent-jet mixing to diffusive mixing where the coefficient of diffusion is based on the depth, h. With this many possible permutations, it seems likely that the best approach is to use the vertical dimension to characterize the *order* of the transitions and to proceed from there with attempts to translate these vertical transitions into the horizontal dimension.

As was true in the case of the vertical characteristic length scales, these horizontal characteristic length scales should be rank ordered to determine the flow's transitional nature. This is the most we can expect from asymptotic dimensional arguments. In the sections that follow, we attempt to relate these characteristic length scales to physical

dimensions by determining the leading constants from empirical data and the kinematic equation.

5.4.3 The horizontal coordinate of transition

The remaining task, then, is to determine the horizontal location, x, at which the transition from one flow regime to the next occurs. As explained above, for the purpose of obtaining the appropriate characteristic length scales, any of several definitions of transition is adequate. However, if we attempt to make estimates of the actual *location* of transition then the value of the leading constant is important. Since the value of this constant depends on the actual definition of transition chosen, we must be careful at this juncture to have a coherent definition of transition for the vertical and horizontal coordinates. Further, if a virtual origin exists, we must know its magnitude in order to estimate the actual x-location of transition. Therefore, in what follows, we suggest a definition for transition that is self-consistent and propose a technique for determining the virtual origins of the various flows. In both cases, we are trying to get a few steps closer to predicting the location of transition more accurately than is possible with length scale arguments alone.

5.4.3.1 Formulating a self-consistent definition of transition

Before proceeding we must decide on a single definition of transition. If we choose to define transition in the vertical dimension as the point of centerline velocity equivalence and then utilize a trajectory matching scheme to find the x-location of transition, then we would have what amounts to different *physical locations* describing the same transition. The same parameters would influence transition in the same ways, i.e., the characteristic length scales would be the same; however, since the leading constant depends on the definition of transition chosen, "mixed" definitions produce "mixed" physical coordinates.

The salient point is that the place of centerline velocity equivalence, for example, need not be the point where the trajectories cross. This can be observed as follows.

If we consider the jet to bent jet transition and match the vertical coordinate, z, to find the x-location of transition, we find:

$$C_1\left(\frac{x}{l_j}\right)^{1/2} = C_2\left(\frac{x}{l_j}\right)^{1/3}$$

$$C_1 x^{\left(\frac{1}{2}-\frac{1}{3}\right)} = C_2 l_j^{\left(\frac{1}{2}-\frac{1}{3}\right)}$$

$$x_{j-bj} = \left(\frac{C_2}{C_1}\right)^6 l_j$$

$$= \left(\frac{3a_{bj}}{2}\right)^2 \left(\frac{1}{a_j}\right)^3 l_j$$

and the corresponding z-value can be taken from either of the trajectory relations:

$$\frac{z}{l_j} = C_1\left(\frac{x}{l_j}\right)^{1/2}$$

$$z_{j-bj} = C_1\left(\frac{C_2}{C_1}\right)^3 l_j$$

$$= \frac{3}{2}\frac{a_{bj}}{a_j} l_j$$

Notice that the leading constant differs from the value of z predicted by the velocity matching technique, by a factor of 3/2 (refer to Table 5.2). This means that the location of centerline velocity matching is not the same as the location where the trajectories match. This observation elucidates the importance of choosing one definition for transition at least for the purpose of determining the *physical transition location* from other experimentally determined constants.

How then shall we proceed? For the purposes of this study we propose to define the point of centerline velocity equality as the point of transition. Then, up to the point of

transition, we will utilize the trajectory equation from *the previous regime* to determine the relationship between the vertical and horizontal coordinates. In other words, for the bent jet to bent plume transition, we will first locate the z-coordinate of transition by matching the centerline velocities and then find the corresponding x-coordinate by using the *bent jet* trajectory equation.

Using this procedure, we still have the requirement that the flow be continuous and it must therefore be continuous not only in centerline velocity, but also in position. This additional requirement allows us to calculate a virtual origin for the regime of flow that exists past the point of transition. Essentially, by calculating a virtual origin, we are forcing the trajectories to match at the z-location determined by the centerline velocity matching and at the x-location determined from the trajectory relation valid in the flow regime preceding the transition.

5.4.3.2 Determining the virtual origins

The procedure for defining the virtual origin of flow for each of the flow regimes is outlined below.

Jet to bent jet transition:

The equations describing the centerline velocity in both the jet (near-field) and bent jet (far-field) regimes are presented above in Table 5.3. In chapter 2 we found that the centerline velocities for the jet and bent jet asymptotic solutions are equal at an elevation:

$$\boxed{z_{j-bj} = \frac{a_{bj}}{a_j} l_j}$$

Following the method described above, we then substitute this value of z into the equation describing the trajectory of a *near-field jet*:

$$\left(\frac{a_{bj}}{a_j}l_j\right)\frac{1}{l_j} = C_1\left(\frac{x}{l_j}\right)^{1/2}$$

$$x_{j-bj} = \left(\frac{a_{bj}}{a_j}\right)^2\left(\frac{1}{C_1}\right)^2 l_j$$

where if we recall that $C_1 = \left(\frac{2a_j}{a_{ke}}\right)^{1/2}$, this reduces to:

$$\boxed{x_{j-bj} = \frac{a_{ke}}{2}\left(\frac{a_{bj}{}^2}{a_j{}^3}\right)l_j} \tag{5.2}$$

This result is as we expect, since l_j was previously identified as the horizontal characteristic length scale governing this transition.

If we proceed with the trajectory equation in the bent-jet regime, we must use a different coordinate, ξ, for the horizontal dimension and this coordinate is different from x by an amount equal to the magnitude of the virtual origin, x_O. Therefore, $\xi = x+x_O$. If we then find the value of ξ that corresponds to the z-coordinate of transition defined above, we have:

$$\frac{z}{l_j} = C_2\left(\frac{\xi}{l_j}\right)^{1/3}$$

$$\xi = \frac{1}{C_2{}^3}\left(\frac{z}{l_j}\right)^3 l_j$$

$$= \left(\frac{a_{ke}}{3a_{bj}}\right)\left(\frac{a_{bj}}{a_j}\right)^3 l_j$$

$$\xi_{j-bj} = \frac{a_{ke}}{3}\left(\frac{a_{bj}{}^2}{a_j{}^3}\right)l_j \tag{5.3}$$

Therefore, the virtual origin for an equivalent bent-jet flow is:

$$
\begin{aligned}
x_o &= \xi_{j-bj} - x_{j-bj} \\
&= a_{ke}\left(\frac{a_{bj}{}^2}{a_j{}^3}\right) l_j \left(\frac{1}{3} - \frac{1}{2}\right) \\
&= -\frac{a_{ke}}{6}\left(\frac{a_{bj}{}^2}{a_j{}^3}\right) l_j
\end{aligned}
\tag{5.4}
$$

Bent jet to bent plume transition:

Matching the centerline velocities yields $z_{bj\text{-}bp}$ as discussed earlier in chapter 2:

$$
\boxed{z_{bj-bp} = \left(\frac{a_{bj}}{a_{bp}}\right)^{2/3}\left(\frac{M^2}{UB}\right)^{1/3}}
$$

If we substitute this value of the vertical coordinate into the equation describing the trajectory of a bent jet (using the adjusted coordinate system, ξ, described above) we find the ξ-location of transition:

$$
\begin{aligned}
\xi_{bj-bp} &= \left(\frac{a_{ke}}{3a_{bj}}\right)\left(\frac{z^3}{l_j^2}\right) \\
&= \frac{a_{ke}}{3}\left(\frac{a_{bj}}{a_{bp}^2}\right)\left(\frac{M^2}{UB}\right)\frac{1}{l_j^2} \\
&= \frac{a_{ke}}{3}\left(\frac{a_{bj}}{a_{bp}^2}\right)\left(\frac{MU}{B}\right)
\end{aligned}
\tag{5.5}
$$

and in terms of the absolute reference frame, the location of transition from bent jet to bent plume behavior is:

$$
\boxed{x_{bj-bp} = \xi_{bj-bp} - x_o} \tag{5.6}
$$

Assigning a new coordinate system for an equivalent bent plume flow allows the calculation of its virtual origin. Namely, $\eta = \xi + \xi_o$, where ξ_o is the virtual origin:

$$\frac{z}{l_b} = C_3\left(\frac{\eta}{l_b}\right)^{2/3}$$

$$\eta = \left(\frac{1}{C_3}\right)^{3/2}\left(\frac{z}{l_b}\right)^{3/2} l_b$$

$$= \frac{2a_{ke}}{3a_{bp}}\left(\frac{z}{l_b}\right)^{3/2} l_b$$

$$= \frac{2a_{ke}}{3}\left(\frac{a_{bj}}{a_{bp}^2}\right)\left(\frac{M^2}{UB}\right)^{1/2}\left(\frac{1}{l_b}\right)^{1/2}$$

$$\eta_{bj-bp} = \frac{2a_{ke}}{3}\left(\frac{a_{bj}}{a_{bp}^2}\right)\left(\frac{MU}{B}\right) \tag{5.7}$$

Then, the virtual origin is calculated as:

$$\xi_o = \eta_{bj-bp} - \xi_{bj-bp}$$

$$= \frac{2a_{ke}}{3}\left(\frac{a_{bj}}{a_{bp}^2}\right)\left(\frac{MU}{B}\right) - \frac{a_{ke}}{3}\left(\frac{a_{bj}}{a_{bp}^2}\right)\left(\frac{MU}{B}\right)$$

$$= \frac{a_{ke}}{3}\left(\frac{a_{bj}}{a_{bp}^2}\right)\left(\frac{MU}{B}\right) \tag{5.8}$$

It is not at all surprising that the virtual origins for these flows are proportional to the horizontal characteristic length scale governing the transition.

Bent plume to shear-flow transition:

Next, we are interested in the x-location of the transition from the bent-plume mixing regime to the shear-flow mixing regime. Recall from chapter 2, we rationalized that this transition occurs when the rms velocity of the plume has decayed to the level of the rms velocity in the shear flow. This is exactly analogous to the matching of the centerline velocities which defined the previous transitions, i.e., we define the point of transition

from bent-plume to shear-flow mixing as the point of equivalent *rms* velocity. Then, as we did above, we substitute the vertical dimension obtained from this matching into the trajectory equation for a bent plume to find the η-location of transition. Knowledge of the magnitude of the virtual origin relative to the original horizontal dimension, x, then allows us to calculate the location of transition in the absolute reference frame.

Recall once again from chapter 2, that the vertical location of transition from bent-plume dominated mixing to shear-flow mixing was defined as:

$$\boxed{z_{bp-d} = 0.88\left(\frac{B}{u_*^2 U}\right)}$$

If we substitute this value into the trajectory relation for a bent plume in the η-coordinate frame, we find:

$$\eta = \frac{2a_{ke}}{3a_{bp}}\left(\frac{z^{3/2}}{l_b^{1/2}}\right)$$

$$= \frac{2a_{ke}}{3a_{bp}}\left(\frac{0.88B}{u_*^2 U}\right)^{3/2}\left(\frac{1}{l_b^{1/2}}\right)$$

$$\eta_{bp-d} = \frac{0.55a_{ke}}{a_{bp}}\left(\frac{B}{u_*^3}\right) \qquad (5.9)$$

Finally, then in terms of the absolute reference frame, the location of transition from bent plume mixing to shear-flow or diffusive mixing is:

$$\boxed{x_{bp-d} = \eta_{bp-d} - \xi_o - x_o} \qquad (5.10)$$

Diffusion based on elevation to diffusion based on depth:

The transition within the diffusive mixing regime from a zone where the mixing coefficient is proportional to the elevation, z, to a zone where the mixing coefficient is

proportional to the depth, h, depends, as we mentioned above, entirely on the trajectory of the flow near the transition. Since we must know the flow regime to know which trajectory equation to use, the coordinate of this transition cannot be written as one equation. Table 5.4 is evidence of this, since three horizontal characteristic length scales are possible, one from each of three trajectories. Therefore, we choose not to write explicitly the equations describing the horizontal *coordinate* of transition. The reasoning for this omission is clear, it is simpler to first determine the order of transition from the vertical characteristic length scales and then translate to the horizontal dimension. The actual procedure is straightforward and is exactly analogous to previous formulations for finding the horizontal coordinate of transition.

5.4.3.3 Summary of transition x-coordinates and virtual origins

Table 5.5 Summary of equations describing horizontal coordinates of transition

Transition	*Absolute* reference frame *x*-coordinate	*Local* reference frame coordinate and virtual origin
jet - bent jet	$x_{j-bj} = \frac{a_{ke}}{2}\left(\frac{a_{bj}^{\,2}}{a_j^{\,3}}\right) l_j$	
bent jet - bent plume	$x_{bj-bp} = \xi_{bj-bp} - x_o$	$\xi_{bj-bp} = \frac{a_{ke}}{3}\left(\frac{a_{bj}}{a_{bp}^{\,2}}\right)\left(\frac{MU}{B}\right)$ $x_o = -\frac{a_{ke}}{6}\left(\frac{a_{bj}^{\,2}}{a_j^{\,3}}\right) l_j$
bent plume - diffusion	$x_{bp-d} = \eta_{bp-d} - \xi_o - x_o$	$\eta_{bp-d} = \frac{0.55 a_{ke}}{a_{bp}}\left(\frac{B}{u_*^3}\right)$ $\xi_o = \frac{a_{ke}}{3}\left(\frac{a_{bj}}{a_{bp}^{\,2}}\right)\left(\frac{MU}{B}\right)$

5.5 Resolving the constants

At this point it is worth investigating a refinement of the length scale arguments by attempting to determine the leading constants in the equations describing the location of transition. A quick calculation using one of the trajectory equations shows the motivation for the work that follows. Namely, an order of magnitude difference in the elevation, z, of transition may result in as much as three orders of magnitude difference in the horizontal position, x, of transition. As an example, consider the bent jet to bent plume transition, if the vertical position varies between one and ten, then the resulting difference in the horizontal position is 10^3 since:

$$\left(\frac{x_2}{x_1}\right) \propto \left(\frac{z_2}{z_1}\right)^3$$

This makes experiments difficult to conduct. Therefore, we would like to be able to estimate the vertical position of transition more accurately. In this regard, it is important whether the leading coefficient is 0.3 or 3.0. Once we have a better estimate of the vertical coordinate we can subsequently form a more precise estimate of the horizontal coordinate of transition. The following is a proposed resolution for the undetermined constants using data available from other investigations.

5.5.1 Using the kinematic equation to relate constants from other experimental investigations

As mentioned above, the constants that appear in the trajectory relations can be related to the velocity relation constants through the kinematic equation – provided the constants appearing in the velocity relations have previously been empirically determined. This is the case for at least two of the velocity relations, namely, the near-field jet and the near-field plume cases.

Fischer *et al.* (1979) and Papanicolaou and List (1988) report values for a_j and a_p as follows:

Constant	Fischer *et al.*	Papanicolaou and List
a_j	7.0 ± 0.1	7.58
a_p	4.7 ± 0.2	3.85

As indicated in Table 5.3, these constants should be consistent with the constants derived using the trajectory relations as in Wright (1977). Wright utilized two methods of obtaining the constants C_1 through C_4: a photographic technique wherein he chose the centerline of the buoyant jet visually and a concentration technique wherein he measured concentration profiles to determine the buoyant jet centerline at various locations. Wright found that the trajectory constants were dependent on the ratio of characteristic length scales, such as l_q/l_j for the constants related to jet trajectories and l_q/l_b and l_m/l_b for the constants related to plume trajectories. There exists considerable scatter in Wright's data and the extrapolated curves drawn in plots might be considered questionable. There might alternatively be some dependence on characteristic length scale ratios that has not been identified in developing the velocity relations. However, the constants a_j and a_p are well-defined (*cf.* Papanicolaou and List (1988)) with little scatter that would be suggestive of another secondary effect.

If we extrapolate Wright's constants, using the drawn curves from the concentration experiments, to their maximum value and then use the relations reported in Table 5.3 to relate them to the velocity-equation constants, we obtain the following values for a_{ke} in the jet and plume cases. (Note: The value of C_1 is confirmed by Hoult *et al.* (1969) who report a value ranging between 1.8 and 2.5.)

Table 5.6 Calculated value of kinematic equation constant

Wright (1977)	Calculated value of constant using Fischer *et al.* data	Calculated value of constant using Papanicolaou and List data
C_1=2.3	a_{ke} = 2.6	a_{ke} = 2.9
C_4=1.8	a_{ke} = 2.9	a_{ke} = 2.3

The most valuable aspect of this exercise is that we can subsequently use this information to calculate constants a_{bj} and a_{bp} from Wright's data for the trajectories. Wright's data for C_2 shows an extrapolated value of about 2.0. This is confirmed by Briggs (1975) who reports a range of values between 1.8 and 2.1, and by Chu and Goldberg who give a value of 1.44. Wright's data shows an average value for C_3 of approximately 1.3 and Fan (1967) shows a maximum value of about 1.8 for C_3. Briggs (1975) reports values ranging from 0.85 to 1.3 and Chu and Goldberg (1974) give an average value of 1.14. Since in determining the constant a_{ke} we used the maximum values from Wright's data, we choose a value for C_2 of 2.3 and for C_3 of 1.3. Then, using these constants and an average value of a_{ke} = 2.7, we are able to resolve, using the relations from Table 5.3, the remaining two velocity-relation constants:

Table 5.7 Calculated value of far-field velocity relation constants

Trajectory relation constant	Velocity relation constant
C_2 = 2.3	a_{bj} = 11.0
C_3 = 1.3	a_{bp} = 2.7

The result of this procedure was used in chapter 2 wherein the above constant was used to fully determine the equation describing the bent plume vertical velocity decay. We further assumed in chapter 2 that the ratio of the vertical rms velocity to the average vertical velocity is the same in the bent plume as it is in the near-field plume case (results for which appear in Papanicolaou and List (1988)), and were able to produce Eq. 2.11 in chapter 2. This equation describes the decay of the vertical rms velocity along the

centerline of a *bent plume* and was required to find the point of transition between the bent plume and diffusive mixing regimes.

5.5.2 The resulting equations describing the location of transition

With the above constants resolved, it then becomes possible to calculate the leading constants describing the z- and x-locations of transition.

5.5.2.1 The z-location of transition

Using the equations for the z-coordinate of transition from Table 5.2 and the resolved constants from the above analysis, we seek an estimate of the physical coordinate of transition. The results are shown below in Table 5.8 where we have used Papanicolaou and List's (1988) constants for a_j and a_p. The only remaining unresolved constant is the coefficient, a_{hd}, which must be empirically determined. We expect it to be less than one, perhaps approximately 0.5 since a buoyant jet has finite width when it reaches an elevation equal to half of the depth, and we suspect that it samples from length scales substantially below and above that elevation. It should be recognized, however, that this is only a rough estimate.

Table 5.8 Equations for vertical coordinate of transition, leading constant resolved

Transition	Equation describing transition z-coordinate, with constant resolved
jet - bent jet	$z_{j-bj} \cong 1.4\dfrac{M^{1/2}}{U}$
bent jet - bent plume	$z_{bj-bp} \cong 2.5\left(\dfrac{M^2}{UB}\right)^{1/3}$
bent plume - diffusion	$z_{bp-d} \cong 0.88\left(\dfrac{B}{Uu_*^2}\right)$
diffusion, z - diffusion, h	$z_{bld-hd} = a_{hd}h$

These estimates for the vertical location of transition then allow us to find the horizontal location of transition with more accuracy than is permitted using length scale arguments alone.

5.5.2.2 The x-location of transition

We are now able to write equations describing the horizontal coordinates of the various transitions by substituting the constant values into the equations from Table 5.5 to find:

Table 5.9 Equations for horizontal coordinate of transition, leading constants resolved

Transition	Equation describing transition x-coordinate	Equation with constant resolved
jet - bent jet		$x_{j-bj} = 0.38 l_j$
bent jet - bent plume	$x_{bj-bp} = \xi_{bj-bp} - x_o$	$\xi_{bj-bp} \cong 1.4\left(\frac{MU}{B}\right)$ $x_o \cong -0.13 l_j$
bent plume - diffusion, h	$x_{bp-d} = \eta_{bp-d} - \xi_o - x_o$	$\eta_{bp-d} \cong 0.55\left(\frac{B}{u_*^3}\right)$ $\xi_o \cong 1.4\left(\frac{MU}{B}\right)$

5.6 Evaluation of transition prediction scheme

The true test of any transition prediction scheme is whether or not it works. In this case, some data are available showing trajectories that might be used to evaluate the technique.

5.6.1 Buoyant jet in a uniform velocity cross flow

Wright (1977) conducted many experiments wherein he photographed a buoyant jet in a uniform cross flow and visually inspected the photographs to estimate the centerline of the flow. We may use some of his data to evaluate the above transition predictions.

If we consider an experiment for which the flow parameters are as follows:

Q, cm^3/s	5.4
M, cm^4/s^2	928.3
B, cm^4/s^3	176.9
U, cm/s	4.57
l_j, cm	6.67
l_b, cm	1.85
l_Q, cm	0.18

we can quickly rank the characteristic length scales to determine the regime of flow. Namely, as we stated in chapter 2, if $l_Q > l_j$, then the flow will reach the zone of established flow before it becomes a bent jet flow. Further, if $l_j > l_b$, then the flow will transition to a bent jet before undergoing the transition to plume behavior. Therefore, the flow will be that of a jet, bent jet, bent plume, which is precisely the type of flow particular to this study.

Figure 5.1 shows Wright's data describing the trajectory of the buoyant jet for these flow parameters. Despite the fact that l_j and l_b are clearly of the same order of magnitude, the flow has a distinct transition from jet to bent jet behavior before plume behavior is observed. If we calculate the characteristic length scale for the bent jet to bent plume transition in the vertical dimension, we have:

$$l_{bj-bp,z} = \left(\frac{M^2}{UB}\right)^{1/3} = 10.2 \text{ cm}$$

This number, again, is of the same order of magnitude as l_j. Our expectations with regard to characteristic length scale theory are such that we cannot be confident that distinct transitions will be identifiable. However, as Figure 5.1 shows, the transition from bent jet to bent plume behavior is, in fact, not muddled with the jet to bent jet transition.

Rank ordering the vertical characteristic length scales determines the order of flow transitions. Next, we will use Wright's data to examine the accuracy of the above outlined theory for estimating the coordinates of the transitions.

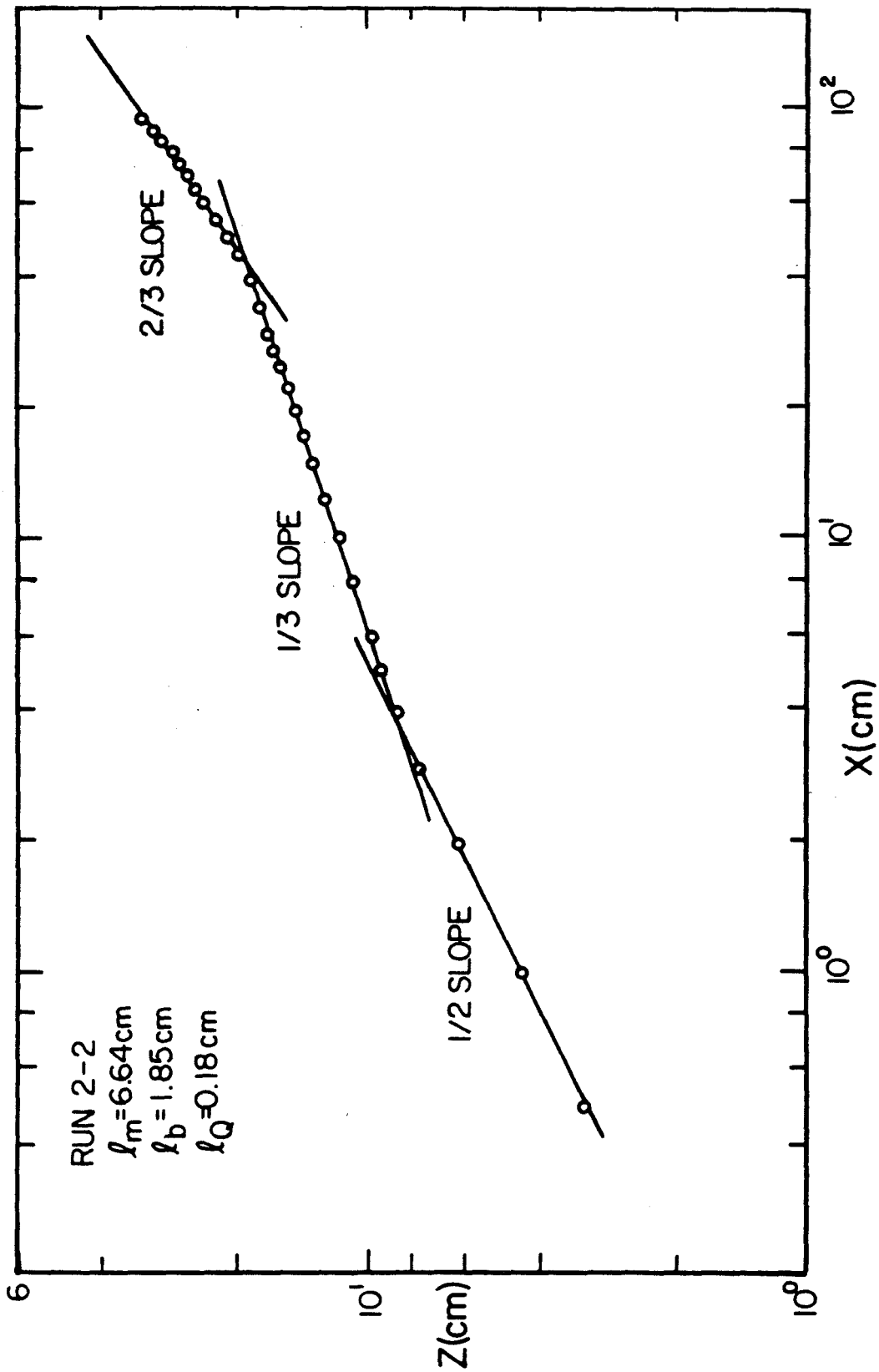

Figure 5.1 Wright's trajectory data for jet, bent jet, bent plume case

Figure 5.2 shows the calculated centerline velocity plots for the jet, bent jet, and bent plume regimes. From this plot we observe that the calculated z-coordinates of transition are close to those found in Wright's experimental data:

Transition	Calculated transition - velocity matching technique	Wright's experimental data
$z_{j\text{-}bj}$	9.3 cm	8 cm
$z_{bj\text{-}bp}$	26 cm	20 cm

Figure 5.3 shows the results of the virtual origin technique used to evaluate the x-location of the transitions corresponding to the calculated z-coordinates. This plot shows the matching of the trajectories at the appropriate z-values as is required by the design of this technique; and the shifting of the local reference frame to force the trajectories to match at the appropriate elevation, z, as calculated from the velocity matching technique. This results in the following values for the x-coordinate of transition:

Transition	Calculated transition - virtual origin technique	Wright's experimental data
$x_{j\text{-}bj}$	2.5 cm	3.2 cm
$x_{bj\text{-}bp}$	34 cm	40 cm

These are indeed promising results since the maximum absolute error is 6 cm which occurs in the vertical and horizontal coordinates for the bent jet to bent plume transition. If we examine the characteristic length scale values for the bent jet to bent plume transition, we find above that the vertical characteristic length scale to be 10.2 cm, and the horizontal characteristic length scale to be 24 cm. This means that this prediction technique works to within between 25 and 60% of the appropriate characteristic length scale for the bent jet to bent plume transition. For the jet to bent jet transition, the error is between 10 and 20% of the characteristic length scale. This is not

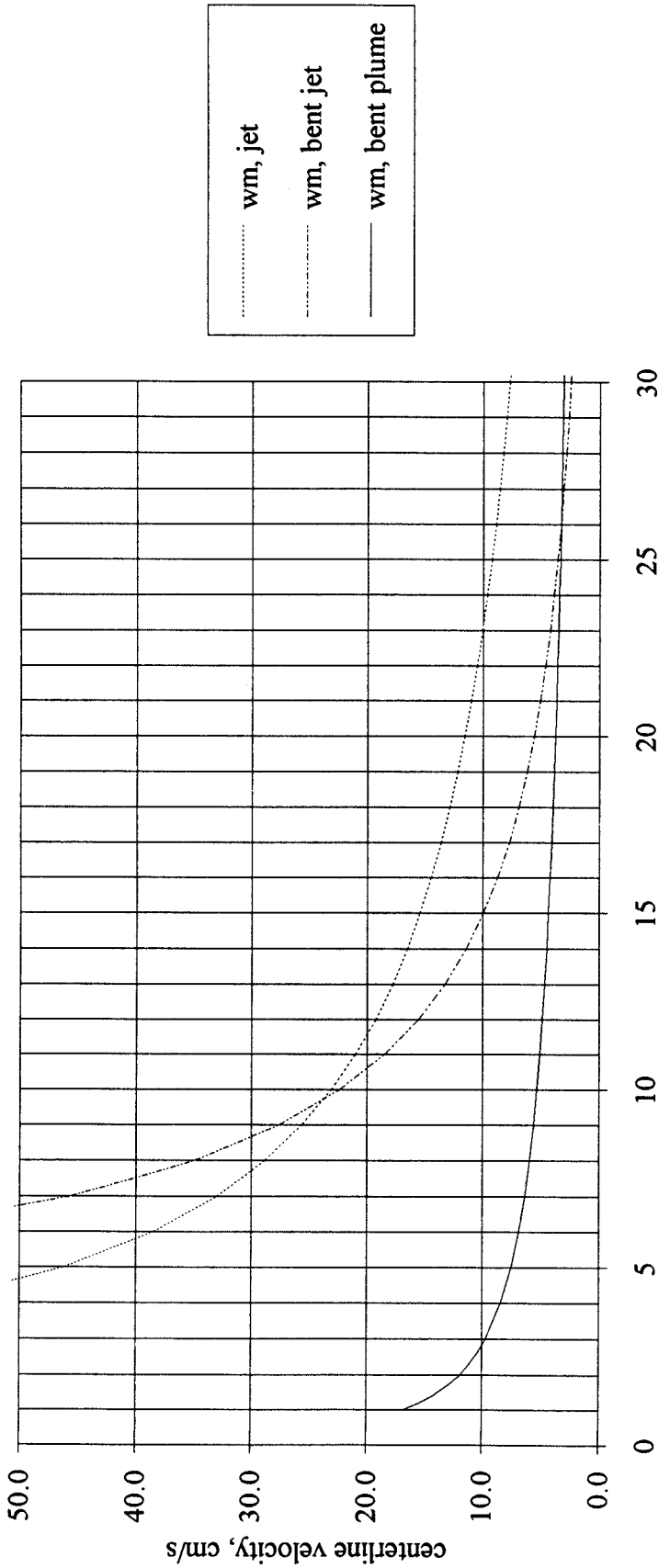

Figure 5.2 Centerline velocity as a function of elevation using prediction scheme and Wright's flow parameters

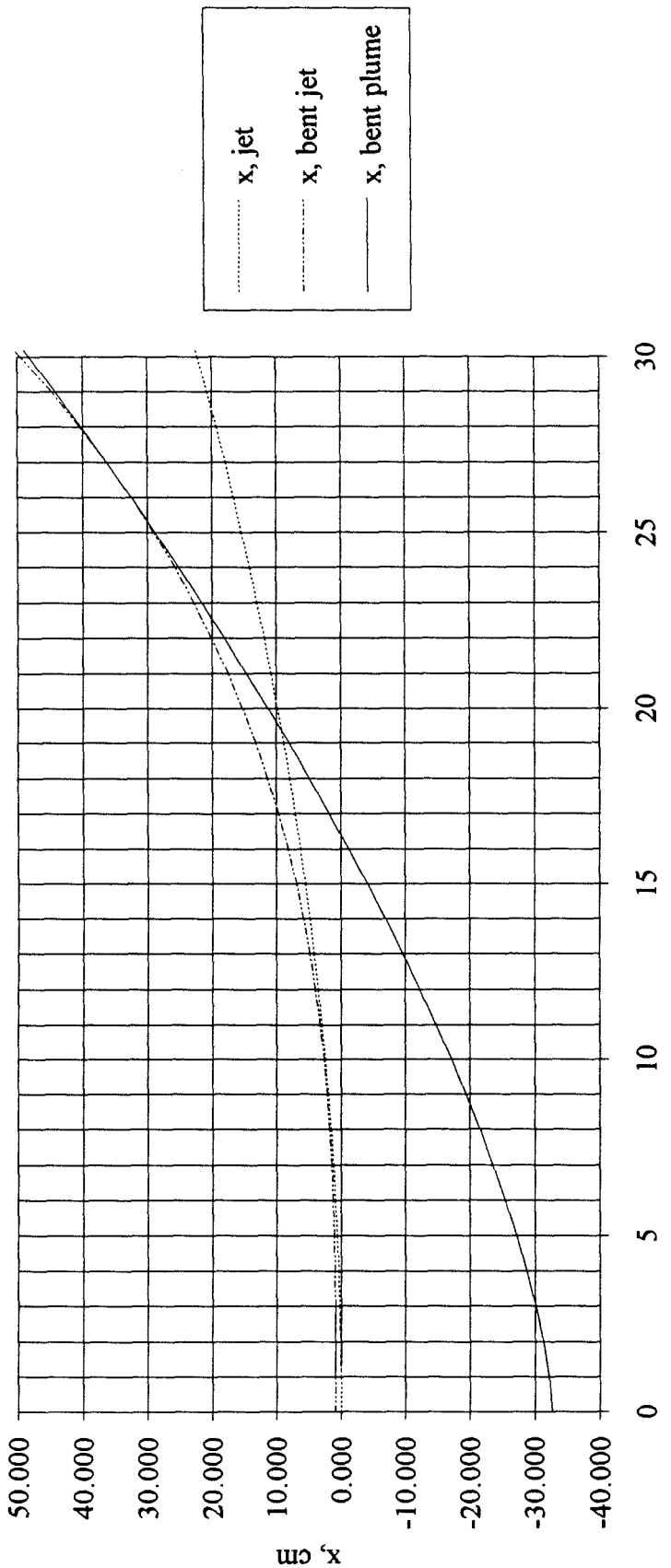

Figure 5.3 Horizontal coordinate versus elevation using prediction scheme and Wright's flow parameters

at all surprising given that the error associated with the prediction scheme will accumulate with each transition since the method relies on experimental data. Additionally, the method is extremely sensitive to the values of the constants used since they often appear to the second or third power. Nonetheless, this scheme is helpful since we are able to predict transition more closely than an order of magnitude range of the characteristic length scale. In this regard, we can with some confidence determine whether each of the leading constants is of order 0.3 or 3.0, which is, in and of itself, a useful result.

5.6.2 Example from the present study ---buoyant jet in a cross flow with shear

Experiments were conducted to investigate the progression of the velocity profile of a buoyant jet in a cross flow with shear. Figures 5.4 - 5.11 show the results of LDV experiments to measure a vertical velocity profile along the buoyant jet centerline at various x-locations for the following experimental conditions:

Q, cm^3/s	16.7
M, cm^4/s^2	1414.8
B, cm^4/s^3	157
U, cm/s	23.6
u^*, cm/s	1.2
l_j, cm	1.6
l_b, cm	0.12
l_Q, cm	2.25

The symbols on the figure are self-explanatory with the exception of the *ucal/U* which is the result of calculating, using the calibration information presented in chapter 4, a cross-flow velocity profile from knowledge of the wall manometer reading during an experiment. *u/U-ucal/U* is the buoyant jet profile with the cross-flow velocity profile subtracted out.

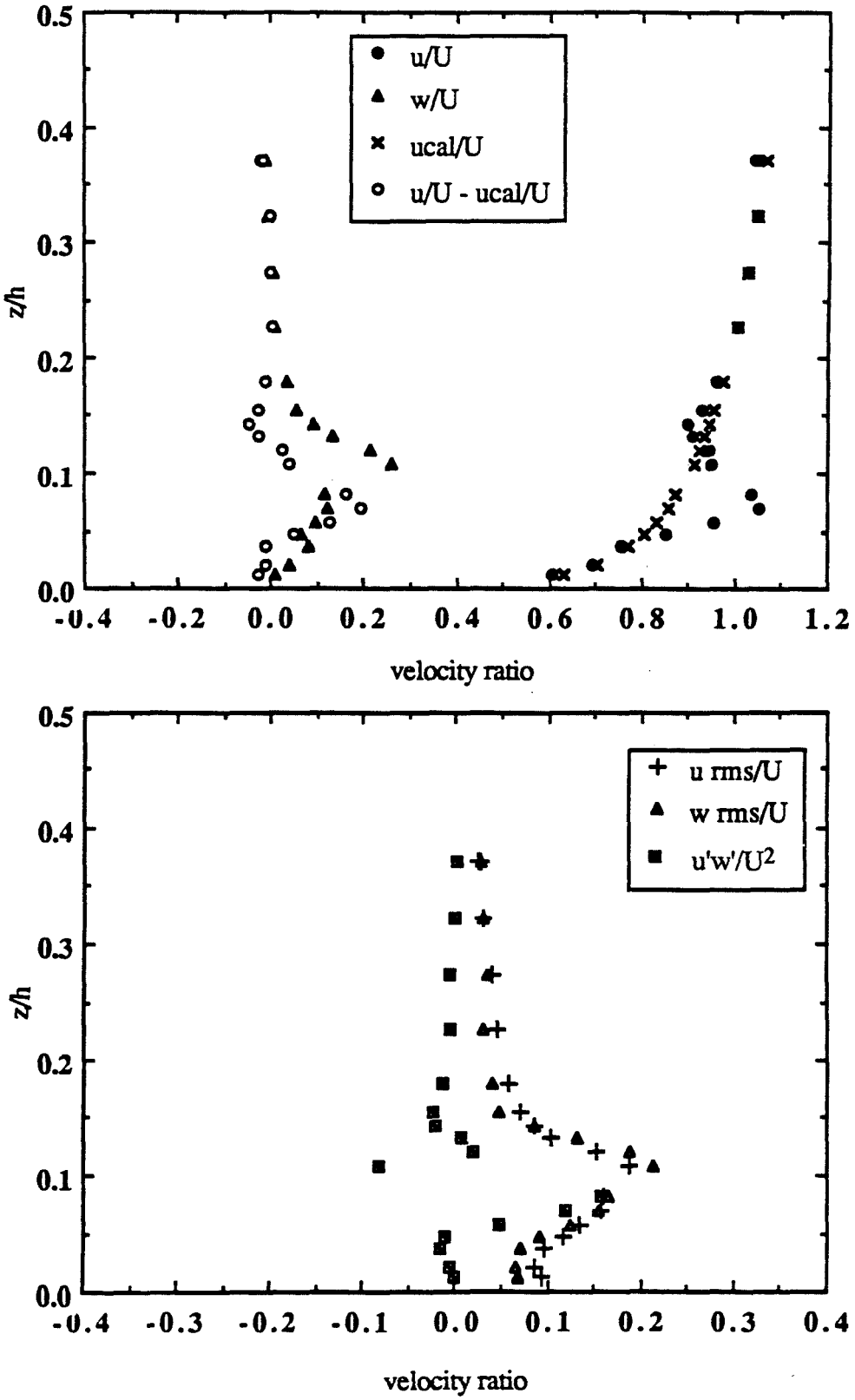

Figure 5.4 Velocity as a function of elevation, x = 3 cm

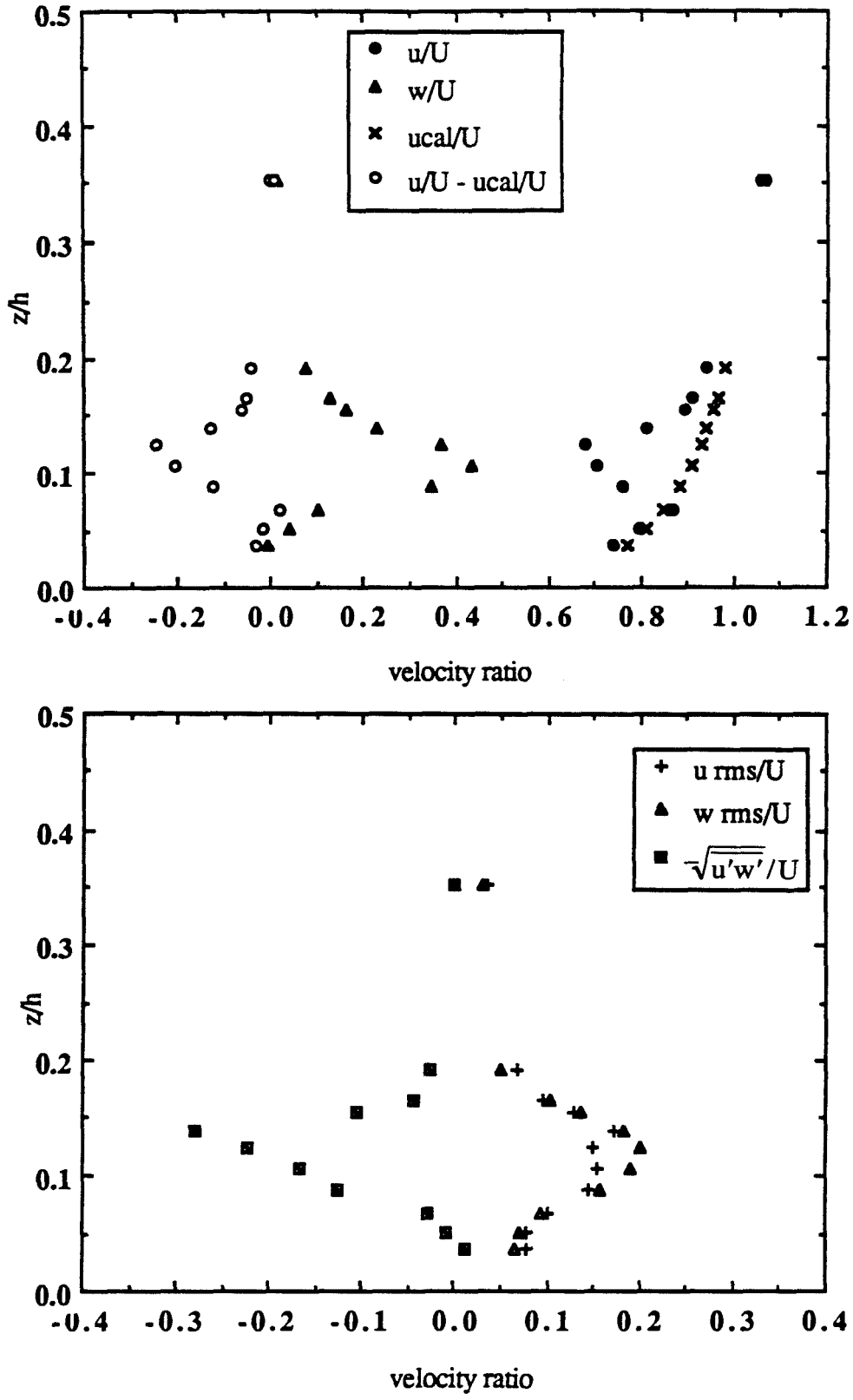

Figure 5.5 Velocity as a function of elevation, x = 6 cm

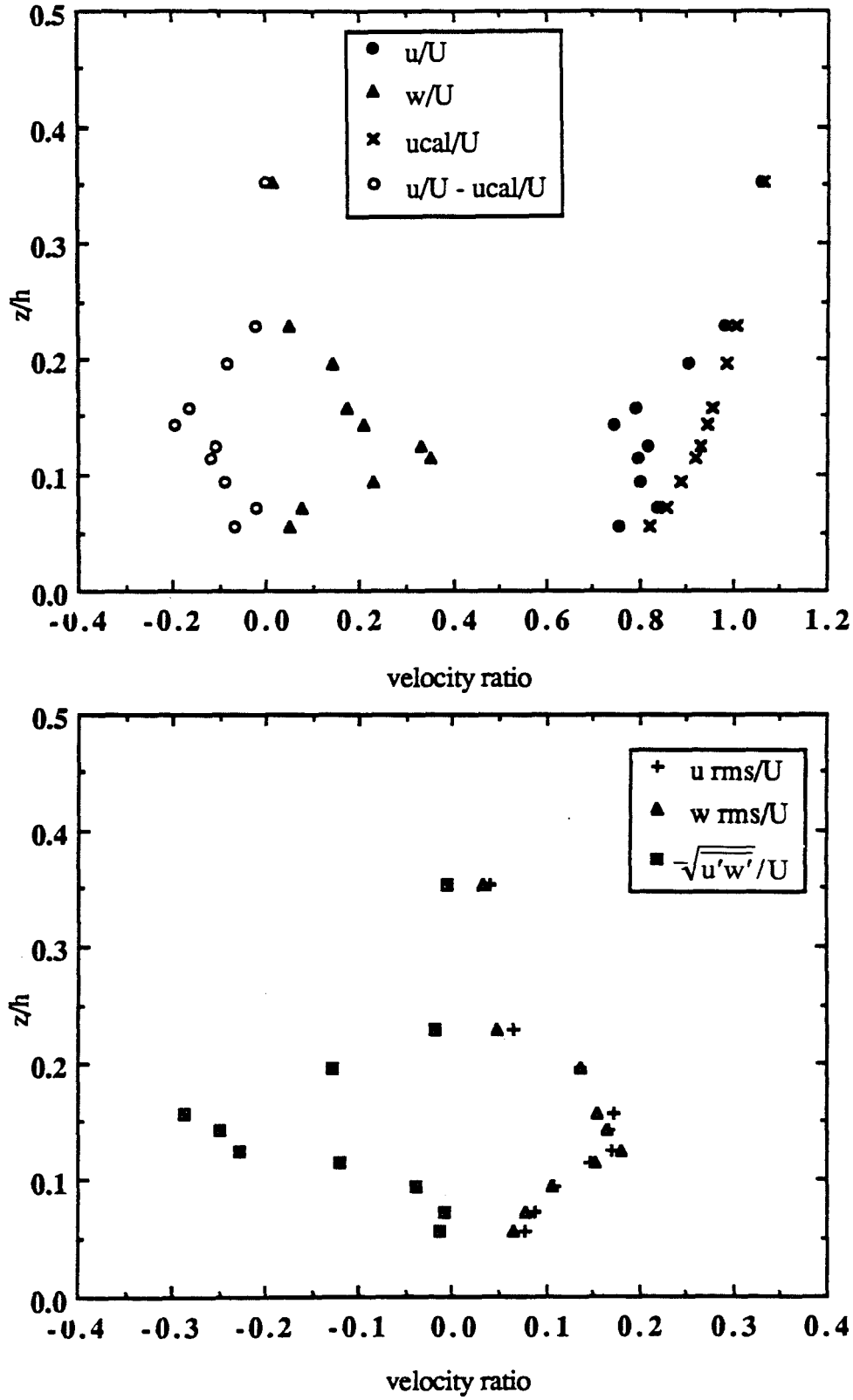

Figure 5.6 Velocity as a function of elevation, x = 9 cm

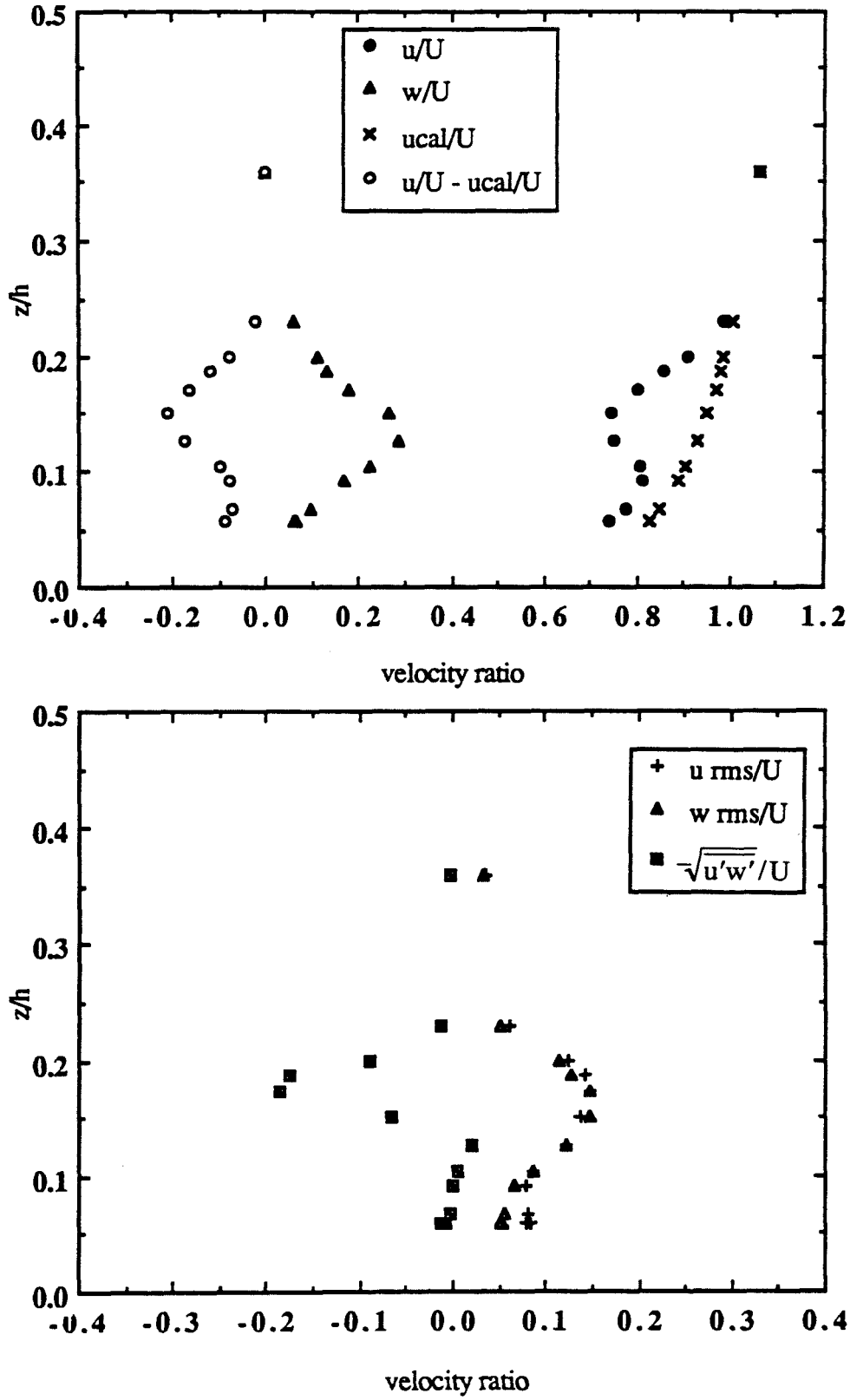

Figure 5.7 Velocity as a function of elevation, x = 12 cm

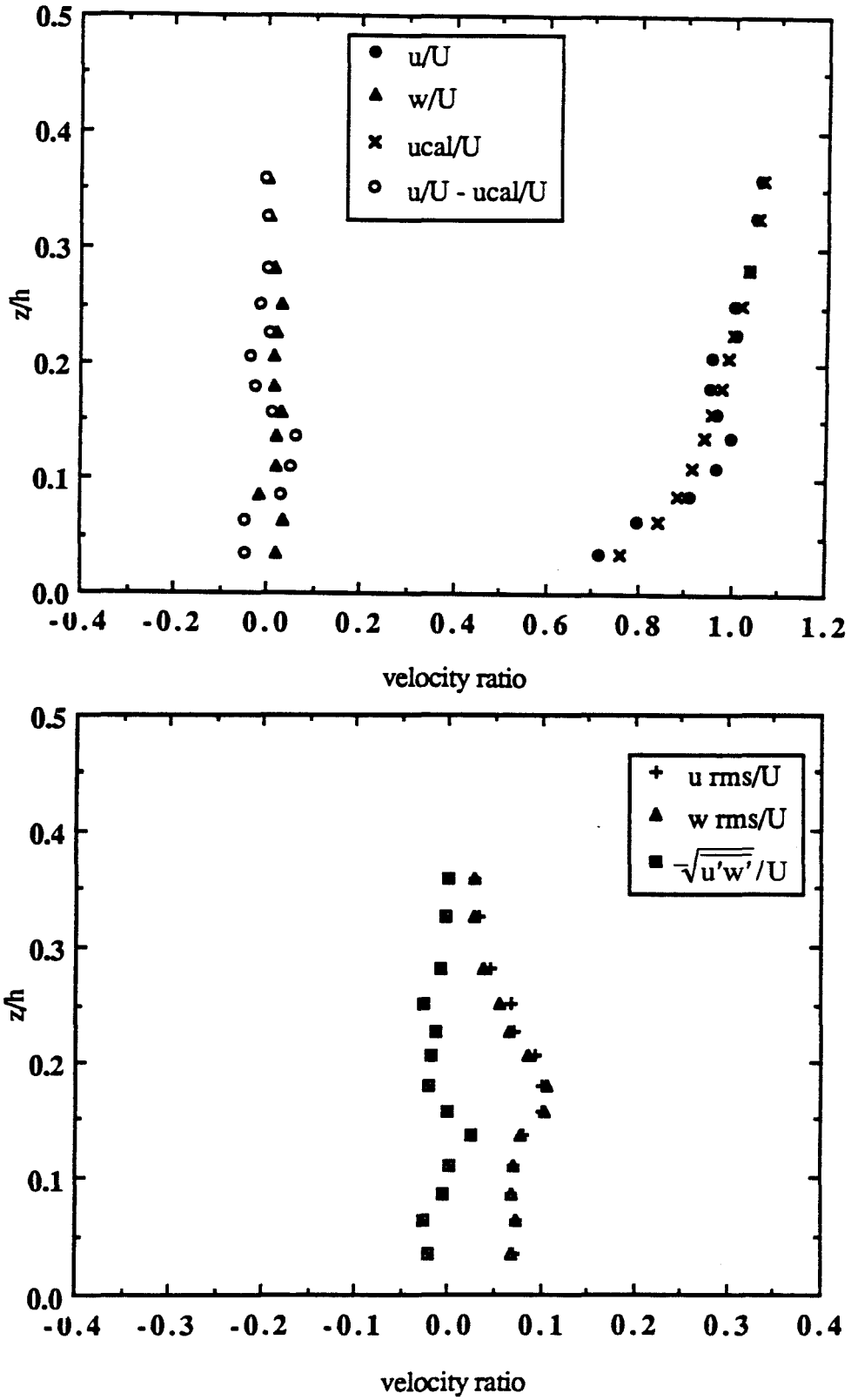

Figure 5.8 Velocity as a function of elevation, x = 20 cm

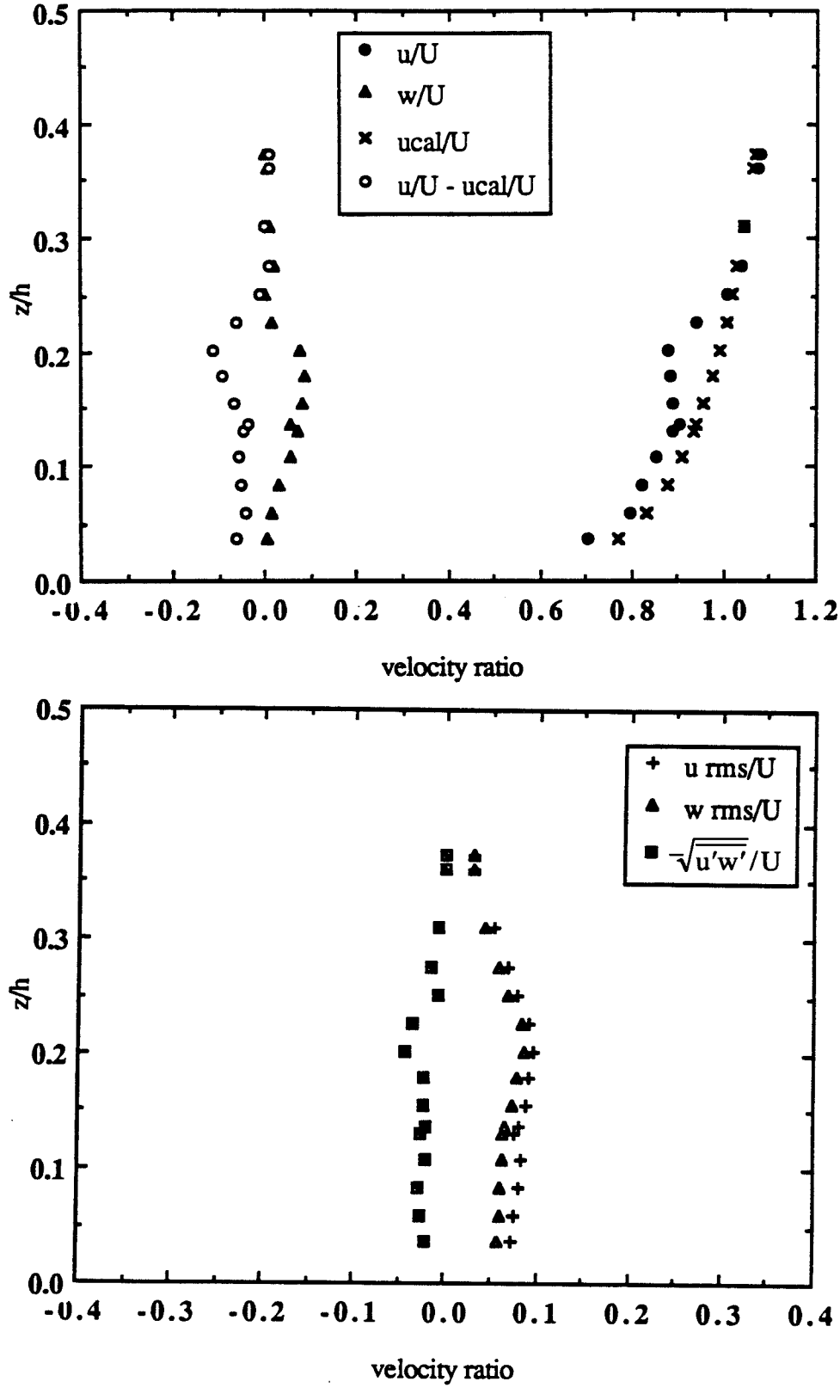

Figure 5.9 Velocity as a function of elevation, x = 40 cm

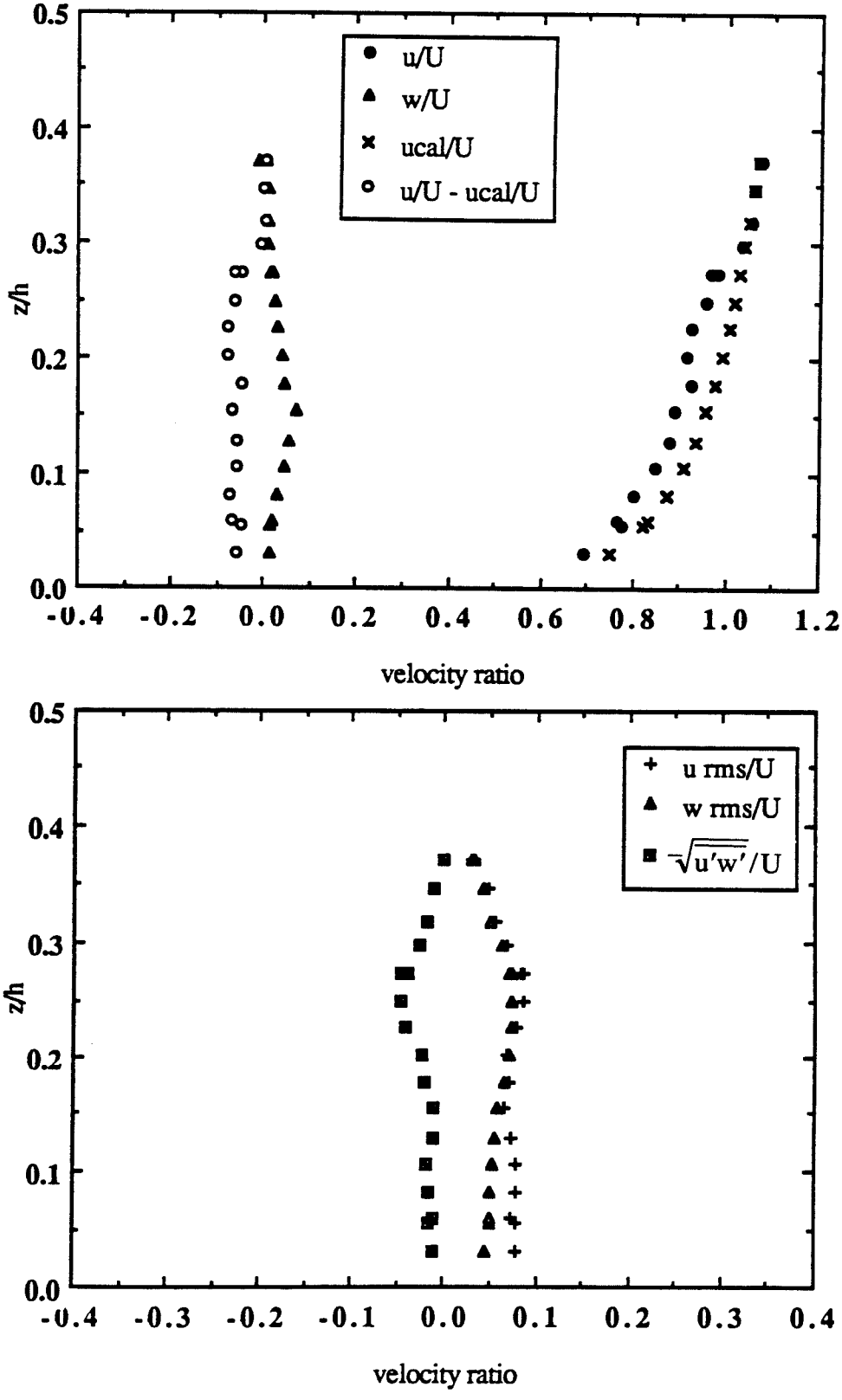

Figure 5.10 Velocity as a function of elevation, x = 60 cm

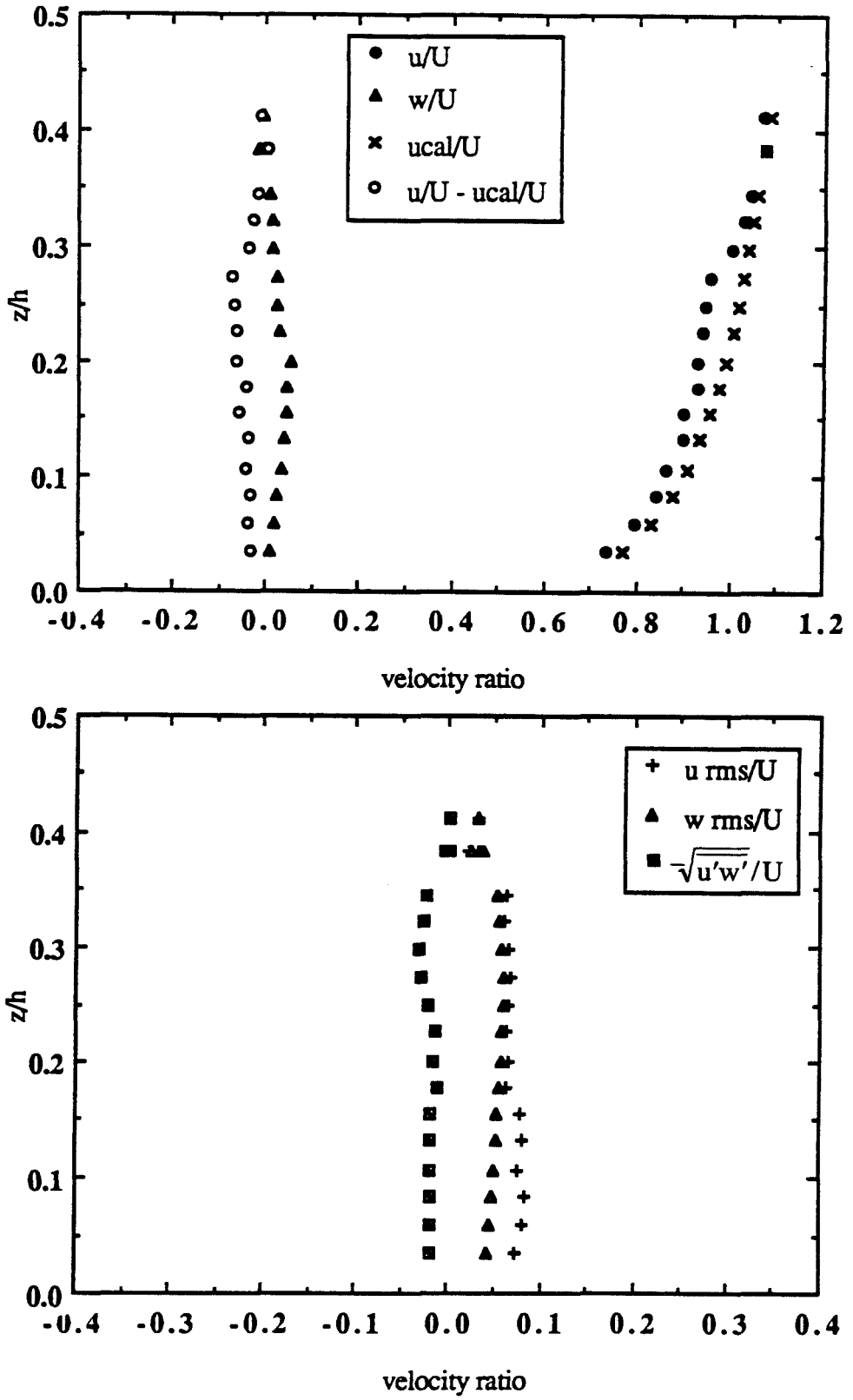

Figure 5.11 Velocity as a function of elevation, x = 100 cm

Several things are of interest in these progressions. First, very close to the point of release, $x = 3$ cm (6 diameters downstream since the orifice is 0.5 cm in diameter), the buoyant jet is seen as a velocity excess in relation to the average cross-flow velocity profile (Fig. 5.4). It is possible to observe from these data the shearing nature of the flow where the buoyant jet meets the cross flow. As early as 6 cm this velocity excess has turned into a velocity deficit, as evidenced in Fig. 5.5, and the vertical velocity has more than doubled at the buoyant jet centerline. (This confirms the assumption that the buoyant jet is advected at the cross-flow velocity, U, as was discussed in chapter 2.) What we observe past this point is a steady decay in the velocity deficit. The overall effect of the buoyant jet is still visible however, even as far as 100 cm from the point of release if we observe parameters such as the average vertical velocity, the rms velocities and the cross-correlated velocity. From this data it is also possible to plot the trajectory of the buoyant jet as shown in Figure 5.12.

Using the above suggested technique for predicting the coordinates of transition, we find:

$$x_{j-bj} = 0.6\text{cm} \qquad z_{j-bj} = 2.2\text{cm}$$
$$x_{bj-bp} = 300\text{cm} \qquad z_{bj-bp} = 20\text{cm}$$

indicating that for these flow parameters, the buoyant jet should be in the bent jet regime throughout the region where experiments were conducted. This is confirmed by the results shown in Figure 5.12 where the trajectory clearly follows the 1/3-rule characteristic of bent jet flow.

The suggested theory also predicts the location of the bent plume mixing to diffusive mixing where transition has been defined as the point of rms velocity equivalence. This prediction assumes that the flow is in the bent plume regime prior to the onset of transition to diffusive mixing. The prediction scheme is valid provided we determine that the onset of diffusive mixing occurs after the transition to bent plume behavior. This is

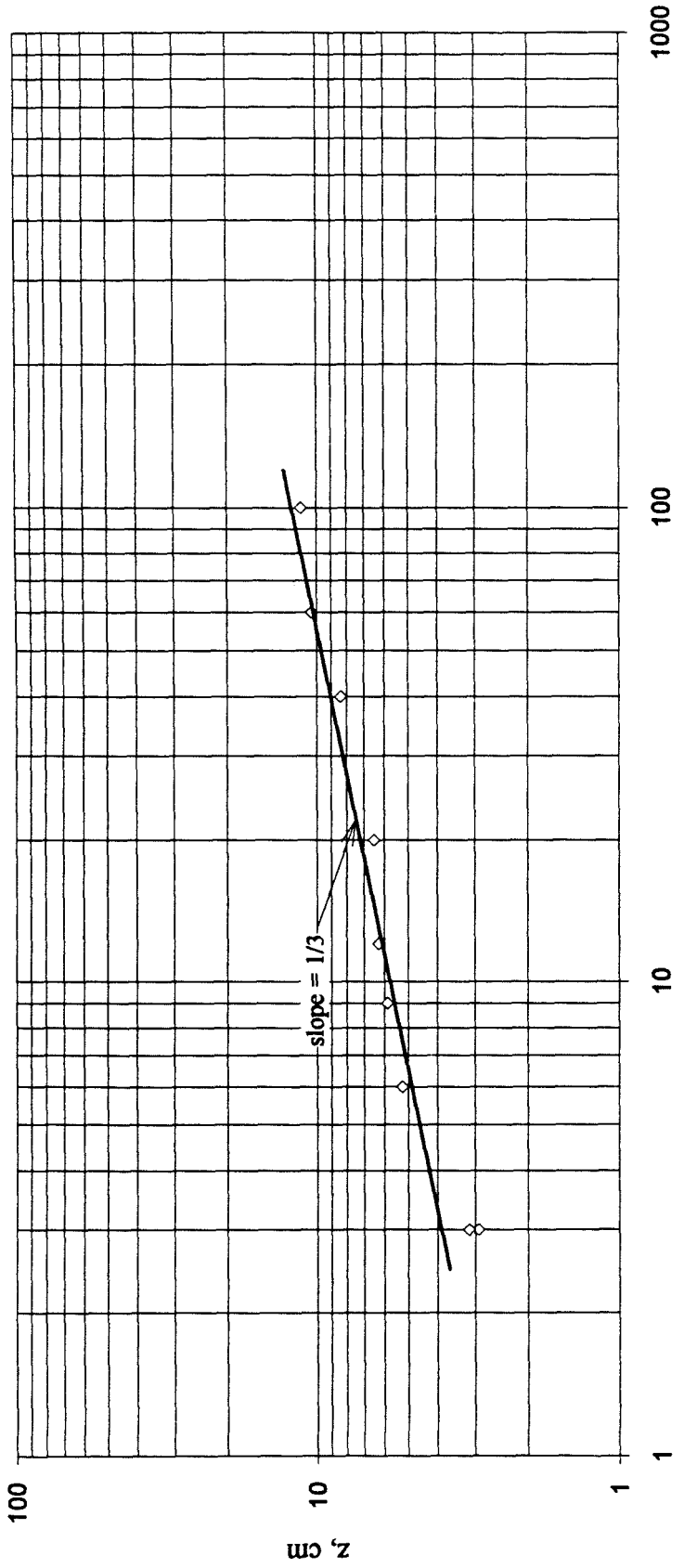

Figure 5.12 Trajectory from velocity progressions

made possible by the use of an "equivalent flow" which is entirely in the bent plume regime and stems from the introduction of a virtual origin. For this purpose, calculation of the z-coordinate of transition is sufficient and $z_{bp\text{-}d} = 4.1$ cm. Clearly, this occurs before the bent jet to bent plume transition.

In this case, we should rather find the location where vertical rms velocity in the bent jet flow reaches the level of the average vertical rms velocity in the cross flow. This is done in the same manner as for the bent plume to diffusive mixing transition. From Papanicolaou and List (1988) we find the equation describing the vertical rms velocity decay in a near-field jet:

$$\sqrt{\overline{w'^2}} = 1.75\frac{M^{1/2}}{z}$$

where the ratio between the rms velocity and the centerline velocity is 0.23 as it was for a plume. Therefore, assuming the ratio of the rms velocity to the centerline velocity is preserved, we find that in the bent jet regime:

$$\sqrt{\overline{w'^2}} = 2.5\frac{M}{Uz^2}$$

and the vertical coordinate defining the transition from bent jet to diffusion is:

$$z_{bj-d} = 2.0\left(\frac{M}{Uu_*}\right)^{1/2} = 14.1 \text{ cm}$$

This suggests that the flow becomes dominated by diffusive mixing before the onset of bent plume behavior.

The x-location of this transition is simply $x_{bj\text{-}d} = \xi_{bj\text{-}d} - x_o$. Where $\xi_{bj\text{-}d}$ is defined by substituting the vertical coordinate of transition, $z_{bj\text{-}d}$ into the trajectory equation for a bent jet. The virtual origin, x_o, remains unchanged. For the flow parameters listed above,

we find that the horizontal coordinate of transition from bent jet to diffusive mixing is:

$$x_{bj\text{-}d} = 90 \text{ cm.}$$

5.7 Summary

The results of the above discussions describing the influence of various flow parameters on transition are valuable in that they provide characteristic length scales vital to any experimental work. The suggested technique for predicting the actual physical coordinate of transition is one of many possible techniques. The preliminary estimates it provides are useful for determining an estimate of the location of transition more closely than length scale arguments alone permit. However, the nature of transition is such that such theories should be carefully tested over a wide range of experimental parameters before they can be used with any great confidence.

In chapter 6, we will find that discussions with regard to the precise location of the early transitions are moot in a cross flow with shear, since it appears that the onset of mixing dominated by turbulent diffusion occurs much earlier than the above predictions suggest.

Chapter 6. Experimental Results and Discussion - Mixing

In chapter 1, we discussed the purpose of this study, namely, to define the dominant mixing mechanisms for a buoyant jet in a cross flow with shear and to investigate the transition between the jet or plume mixing regime and the shear-flow mixing regime. We suggested that in a region near the point of release, the mixing would be dominated by initial jet/plume interactions, and that further downstream, the mixing would be dominated by turbulent diffusion.

In chapter 5, we derived the buoyant jet trajectory equations, and proposed a method for predicting the early transitions characteristic of buoyant jet flows. We required a definition of transition in order to predict the coordinate of transition and we settled upon the point of centerline velocity equivalence between asymptotic regimes as the definition.

For design purposes, however, we have little interest in parameters such as the trajectory or the centerline velocity except as they relate to the predominant mixing mechanisms. That is not to say that such information is not important to our fundamental

understanding of the complex flow, but, from a design perspective, it is the dilution that is of utmost importance. In this chapter, we will focus on the results of a detailed experimental investigation of the dilution for a buoyant jet in a cross flow with shear.

6.1 Dilution data ---the nature of the flow

In chapter 3, Experimental Methods and Procedures, we described the laser-induced fluorescence (LIF) technique used to obtain the spatial concentration distribution as a function of time over the duration of an experiment. In this investigation, we conducted 77 LIF experiments for various flow conditions. Appendix G is a summary of all the experiments conducted. The experimental facility allows the following parameters to be varied: the initial volumetric flow rate, the cross-flow velocity, the x-location of an experiment, the relative density difference, the depth of the cross flow, and the diameter of the orifice. We chose in this study to vary predominantly the first three parameters which are useful in determining transition and hence the specific flow regimes. In addition, we conducted some experiments at slightly different relative density differences. The diameter of the orifice and the depth of flow were not changed.

It is also possible to change the ratio of the shear velocity to the average cross-flow velocity by modifying the flow boundary conditions, for example we could have added sand or rocks on the flume bottom to increase the roughness. We conducted all experiments with the flume bottom unmodified.

Figure 6.1 shows a schematic of how the data is taken. Essentially, as was described in chapter 4, we sample along a line of the flow, to obtain a "picture" of the flow as a function of depth over time. Since the sampling is rapid, this kind of time-and-space picture resembles an actual two-dimensional picture of the flow. The data taken using this technique, while valuable for flow visualization purposes, is quantitative in addition to qualitative, thus, increasing the potential for improving our understanding of the flow.

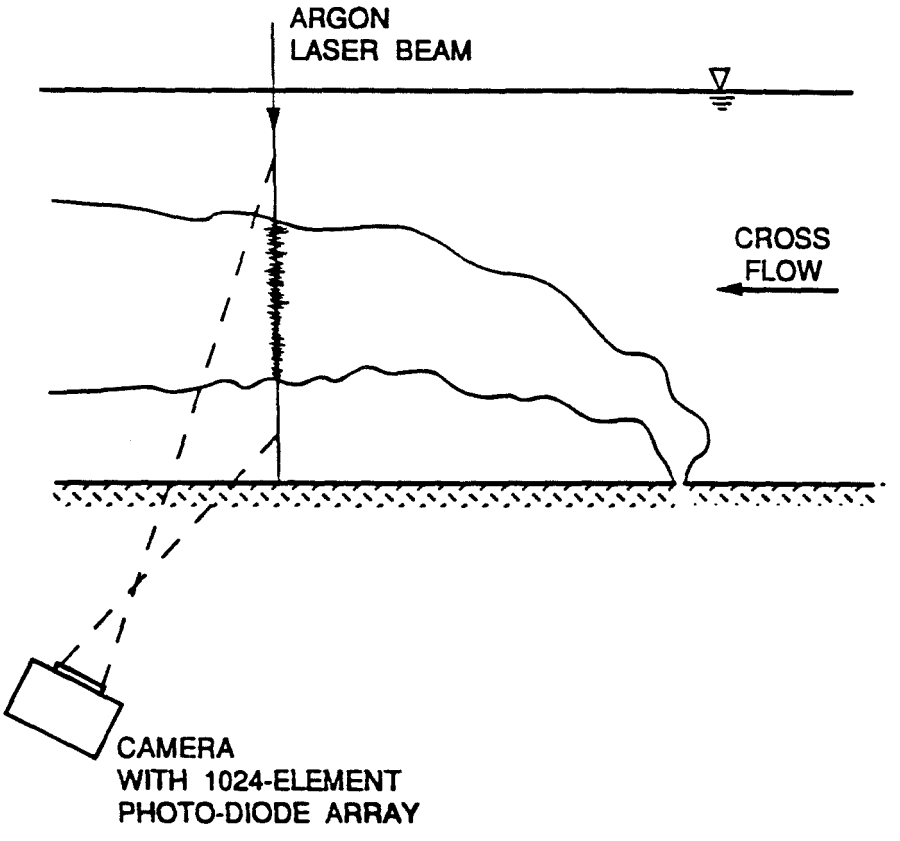

Figure 6.1 Schematic of experimental configuration

6.1.1 The minimum average dilution

The calibration procedure for LIF allows us to relate the instantaneous concentration at a vertical location, z, and time, t, to the original concentration of the tracer fluid to obtain the relative instantaneous concentration, $\frac{C(z,t)}{C_o} = C_{inst}/C_o$, at a fixed location x. (As we mentioned previously, all experiments were conducted along the flume centerline, and therefore all have a y-coordinate equal to zero.) The local instantaneous dilution, then, is the inverse of the relative instantaneous concentration, $S(z,t) = \frac{C_o}{C(z,t)}$.

For regulatory purposes, we are interested in the minimum *average* dilution, where by average, we refer to the *time-averaged* quantity. As shown above, this corresponds to the maximum time-averaged value of the relative concentration ratio and we thus write the minimum average dilution as:

$$S(z) = \frac{1}{t}\int_0^t \frac{C_o}{C(z,t)}dt = \frac{C_o}{\overline{C}(z)}$$

$$\overline{S}_{\min} = \min\left(\frac{C_o}{\overline{C}(z)}\right) \tag{6.1}$$

Additionally, the z-location corresponding to the minimum time-averaged dilution is taken as the buoyant jet centerline elevation. Hereafter, S will be used in place of $\overline{S}_{\min}$.

All experiments were conducted at a pixel-to-pixel sampling rate of 200 kHz which corresponds to a sampling rate of approximately 200 Hz for each individual pixel. Each experiment consists of 53 sec worth of data and as can be seen in Figure 6.2, this is more than sufficient to converge the value of the average relative concentration and the standard deviation. (Note: Only every tenth point of the data series is plotted in Figure 6.2 to facilitate readability.)

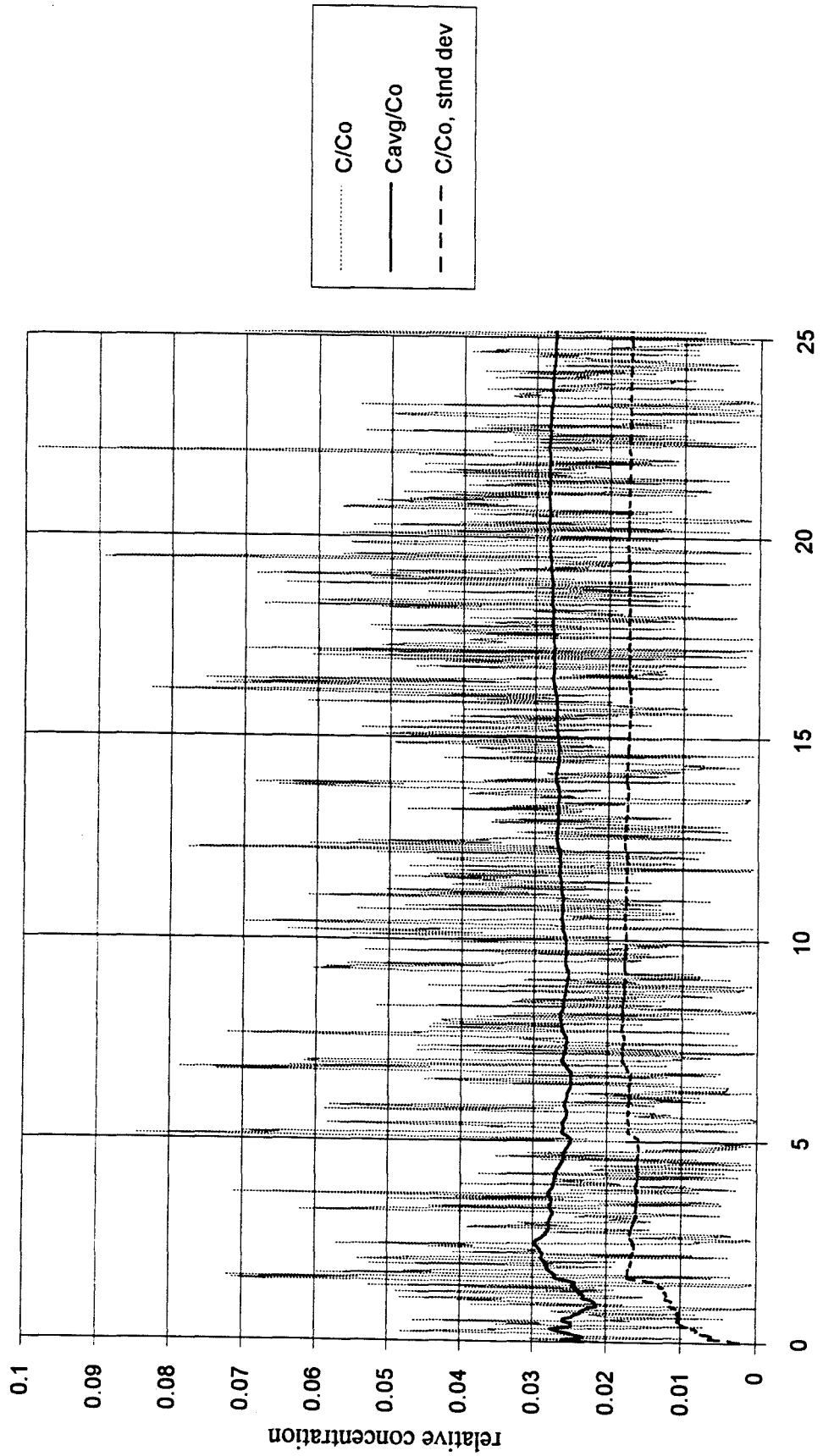

Figure 6.2 Concentration convergence data

6.1.2 A sample flow

Consider a typical flow with the following parameters:

x, cm	40
d, cm	0.5
h, cm	41.68
Q, cm^3/s	16.7
M, cm^4/s^2	1414.8
$\Delta\rho/\rho$	1.2%
B, cm^4/s^3	196.2
U, cm/s	23.8
u^*, cm/s	1.2
exp't reference	1307, a

*Note: We will maintain this system of units for all subsequent parameter values.

Figure 6.3 is a computer-generated, color-enhanced reproduction of a buoyant jet in a cross flow with shear where the experimental conditions are as indicated above. In this reproduction we are observing the flow over time as it passes location $x = 40$ cm, thus we are observing an Eulerian picture of the flow. We have expanded the color-table for Fig. 6.3 such that it is fully utilized over a range of relative concentrations between 0 - 0.1. Figure 6.4 shows the color-table used in Figure 6.3 where there is a one-to-one linear correspondence between the chosen value for the maximum relative concentration and the integer values shown in the color-table. In other words, a relative concentration range between 0 - 0.1 corresponds to the integer range 0 - 242. This permits lower concentration portions of the flow to be more easily visualized; however, since relative concentrations exceeding 0.1 cannot be distinguished, it is not possible to discern from the color-enhanced pictures the maximum relative concentration achieved in the flow. This is not a limitation in the quantitative data, rather only in the color-enhanced pictures. Regions of the flow where the maximum relative concentration exceeds 0.1, appear as regions with a relative concentration equal to 0.1.

Figure 6.5 shows the time-averaged concentration profile for the above buoyant jet. Figs. 6.6*a*, *b*, *c*, and *d* show instantaneous concentration profiles at the times during

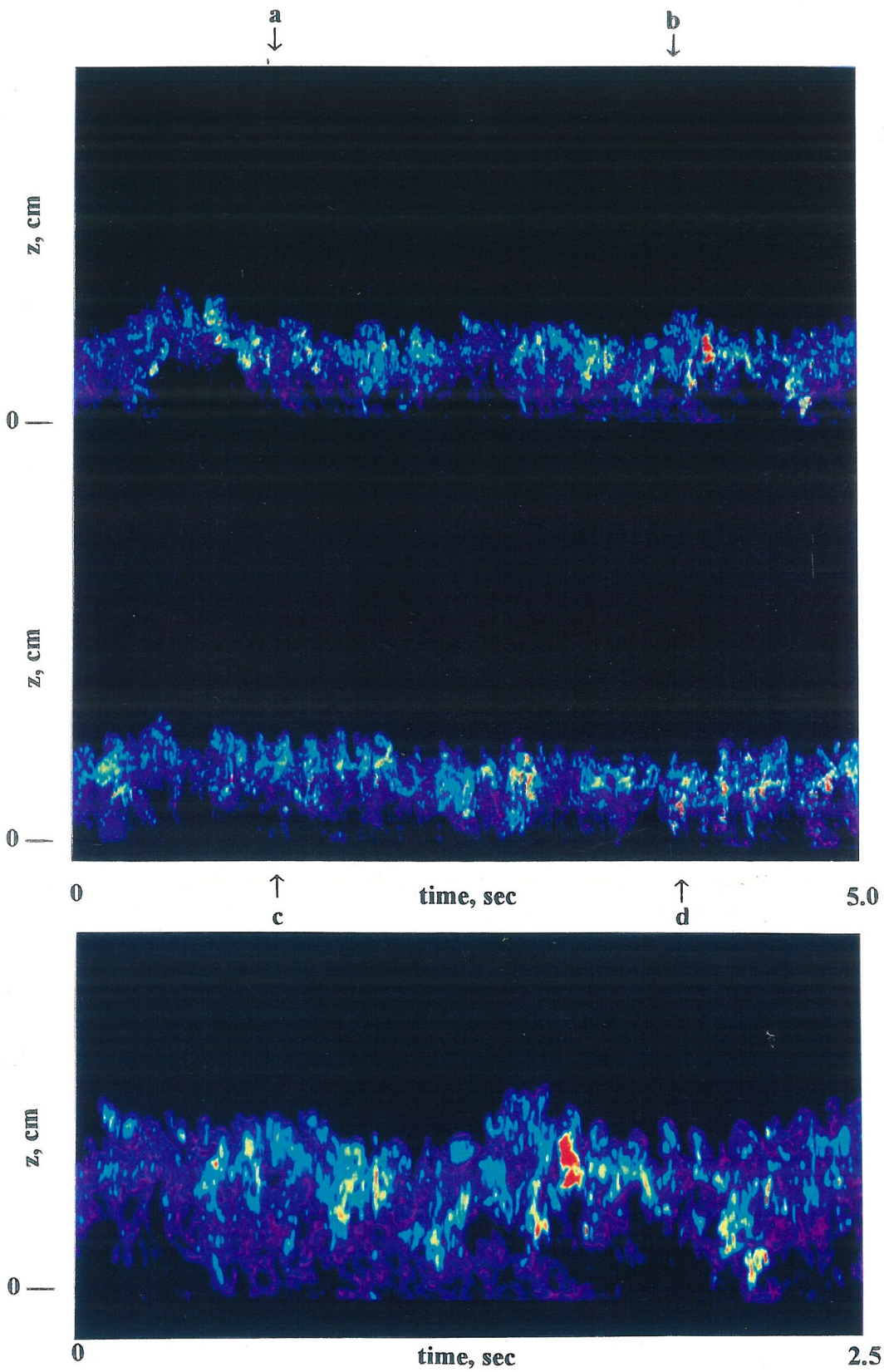

Figure 6.3 Color-enhanced picture of flow at x = 40 cm, C_{max} = 0.1 (Expt 1307a)

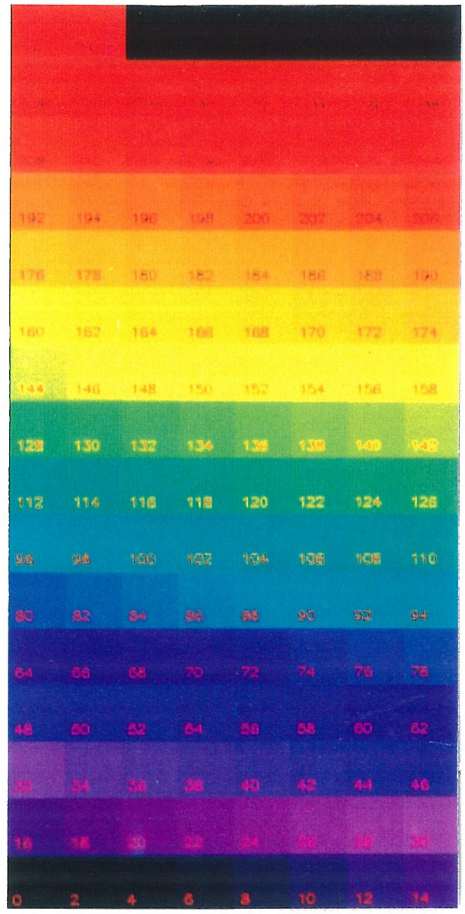

Figure 6.4 Color table for color-enhanced pictures

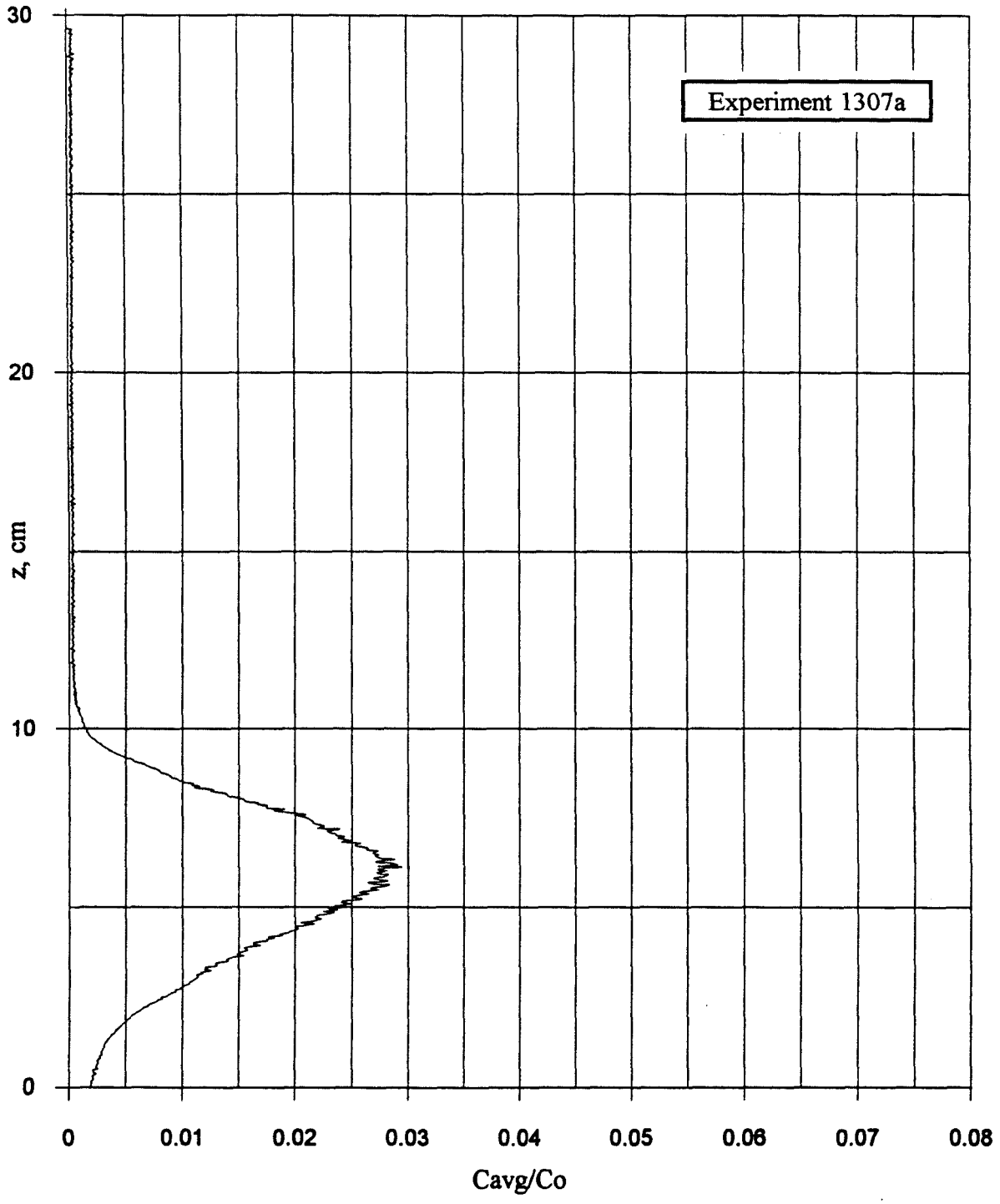

Figure 6.5 Time-averaged relative concentration profile at x = 40 cm

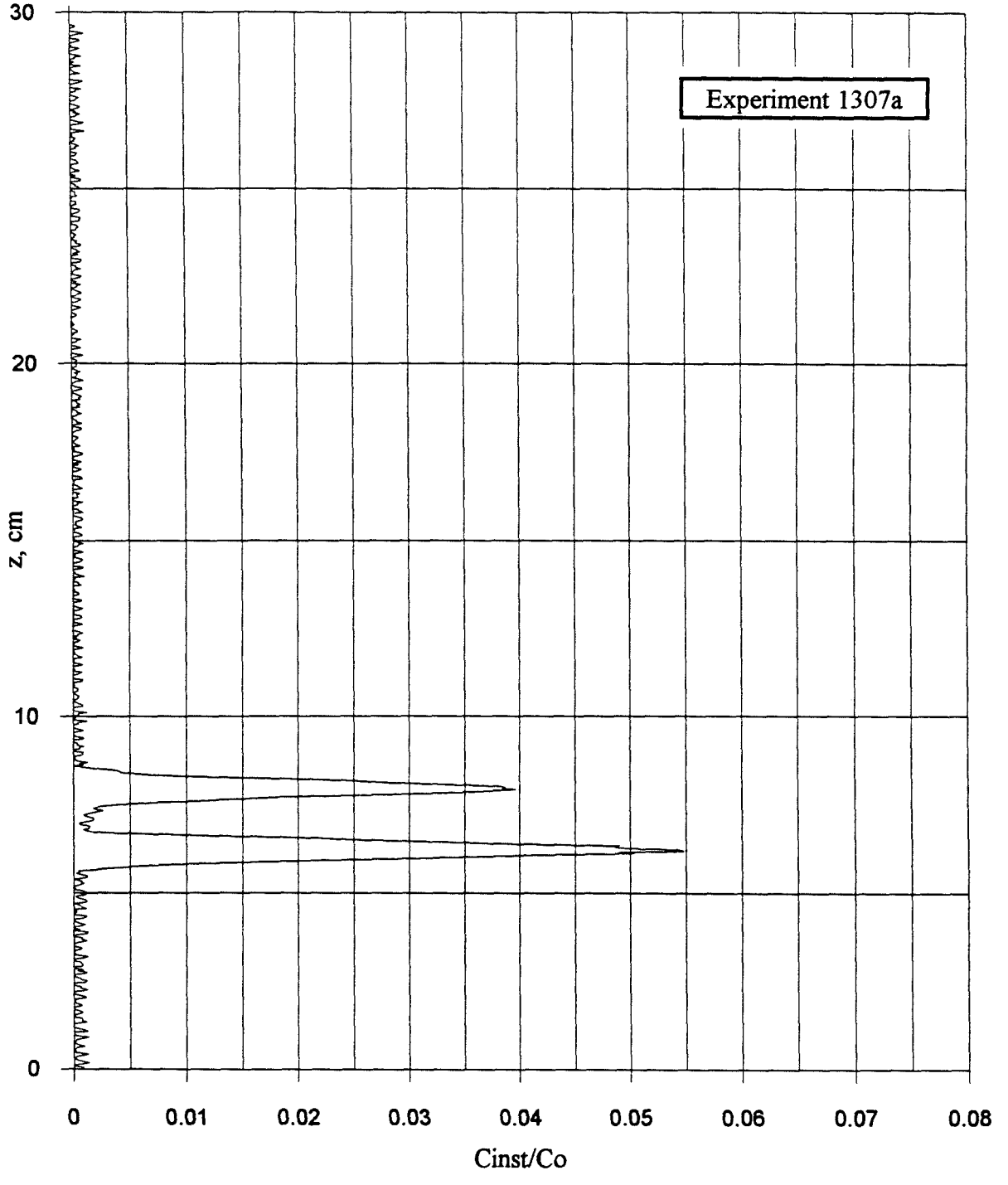

Figure 6.6 Instantaneous relative concentration profile (a) at x = 40 cm

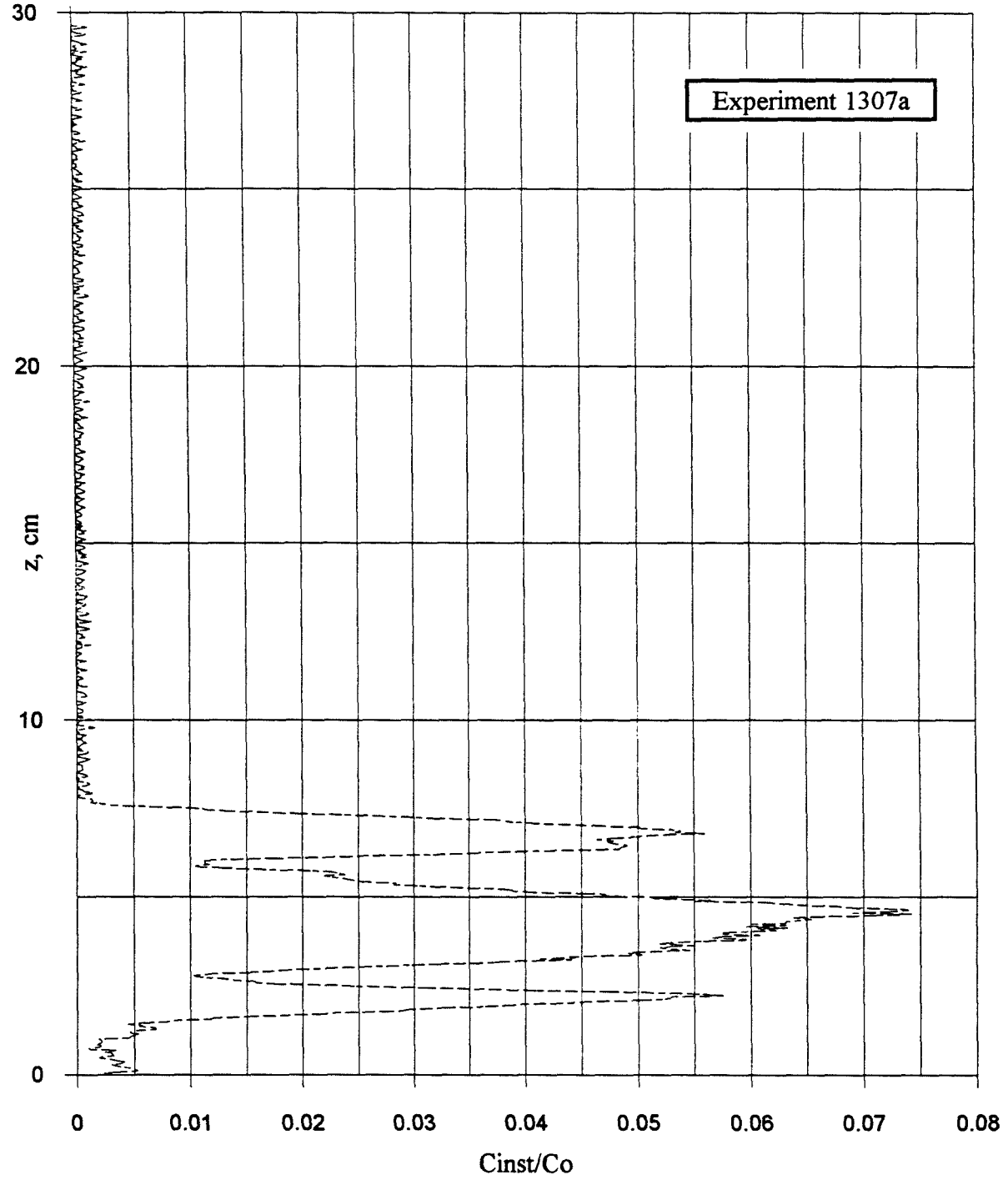

Figure 6.6 Instantaneous relative concentration profile (b) at x = 40 cm

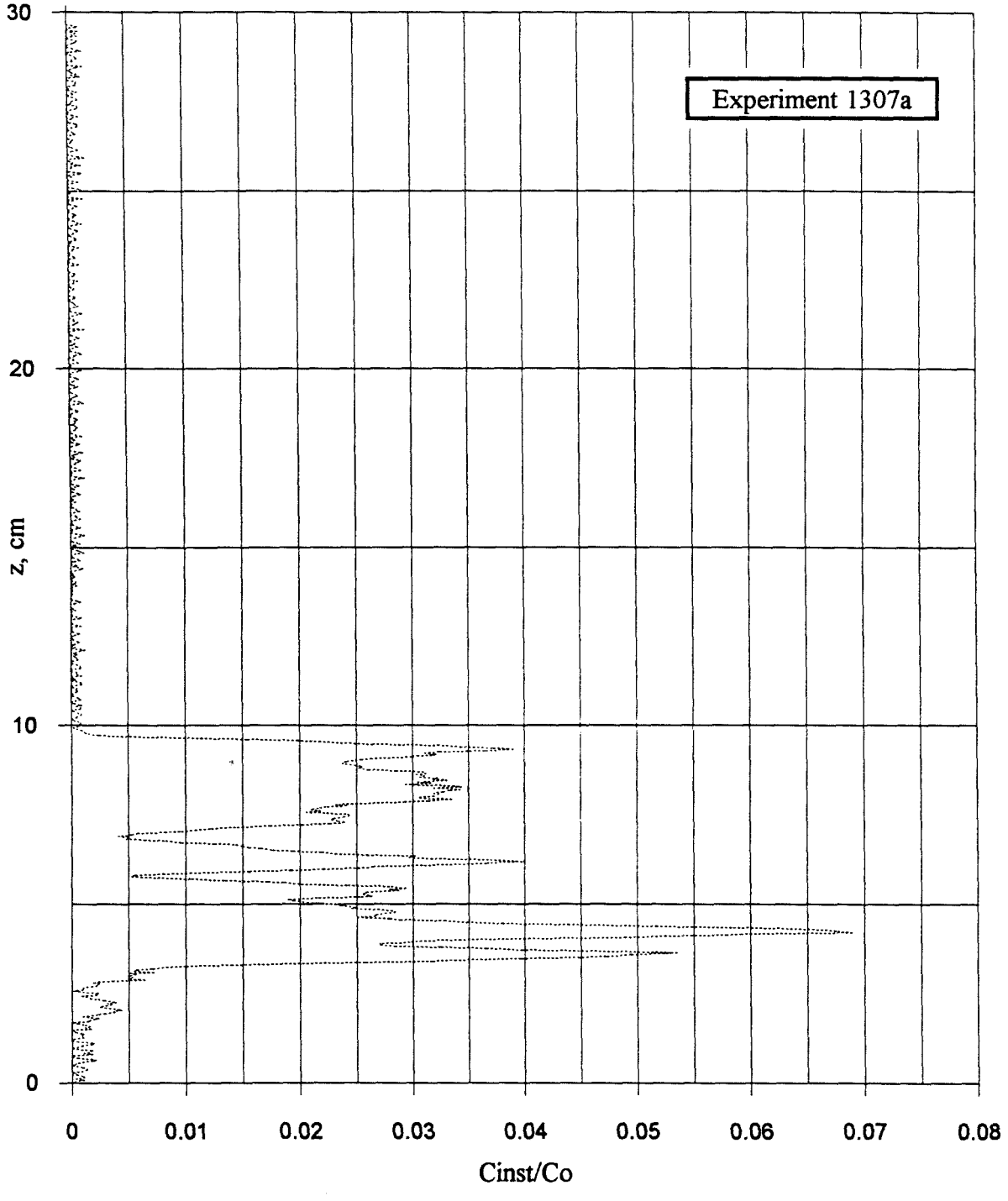

Figure 6.6 Instantaneous relative concentration profile (c) at x = 40 cm

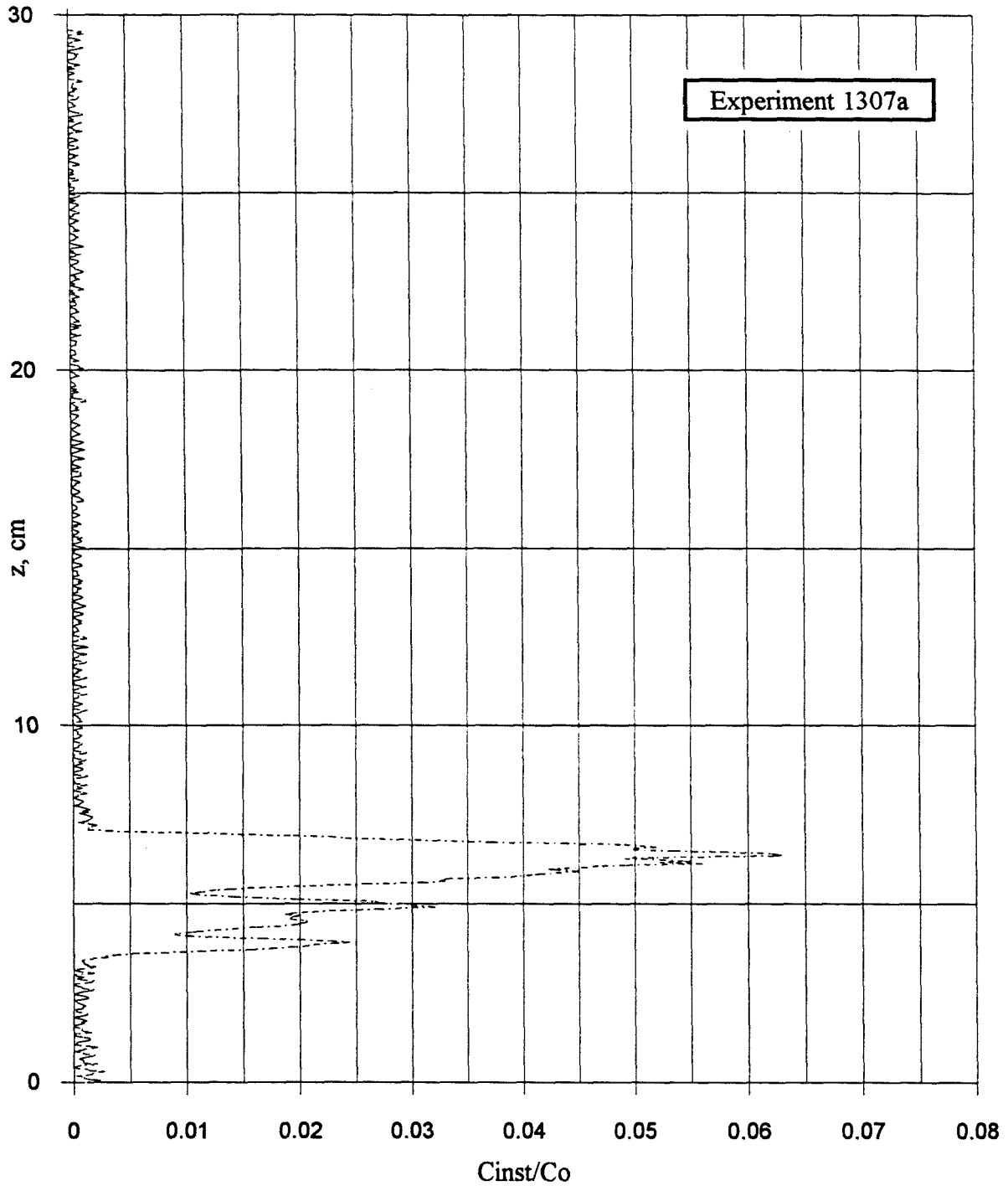

Figure 6.6 Instantaneous relative concentration profile (d) at x = 40 cm

the experiment as indicated in Fig. 6.3. Figure 6.7 is all four of the instantaneous profiles shown in Figs. 6.6*a-d* superimposed. (Notice that the entire buoyant jet flow exists within the boundary layer of the cross flow since, as was shown in chapter 4, roughly 30% of the flow depth is boundary layer flow. Thus, at the depth of 41.3 ± 0.7 cm used for all of the experiments in the present study, the boundary layer exists up to an elevation of 12.4 ± 0.2 cm.) As can be seen from these figures, the instantaneous relative concentration exceeds the value of the maximum time-averaged relative concentration by a factor of up to 2.5. We might expect the maximum instantaneous relative concentration at any location, z, to exceed the average by even larger factors than observed in profiles *a*, *b*, *c*, and *d* since we have chosen these four profiles randomly. This is supported by the value of the relative concentration standard deviation shown together with the average relative concentration as a function of elevation, z, in Fig. 6.8. We can observe from this figure that at a location corresponding to the maximum average relative concentration (C/C_O = 0.03 at h = 6 cm), the standard deviation is approximately 0.018. According to Tchebysheff's theorem then, a fraction of at least $1-(1/k^2)$ of the points will be within k standard deviations of the average. Therefore, the relative concentration will be between 0 - 0.07 approximately 75% of the time. This implies that 25% of the time, the relative concentration will exceed 0.07. Similarly, it will exceed 0.09, 11% of the time, 0.11, 6% of the time, and 0.14, 3% of the time. If we choose to define "often" as 10% of the time, then we should regulate for regions of peak concentration about three times the average. (Figure 6.2 shows every *tenth* value of the relative concentration at h = 6 cm for a period of 25 sec.) Lastly, these instantaneous profiles confirm the result previously reported by Papantoniou and List(1989), namely, that the maximum instantaneous relative concentration profile does not at all resemble the time-averaged Gaussian-type profile.

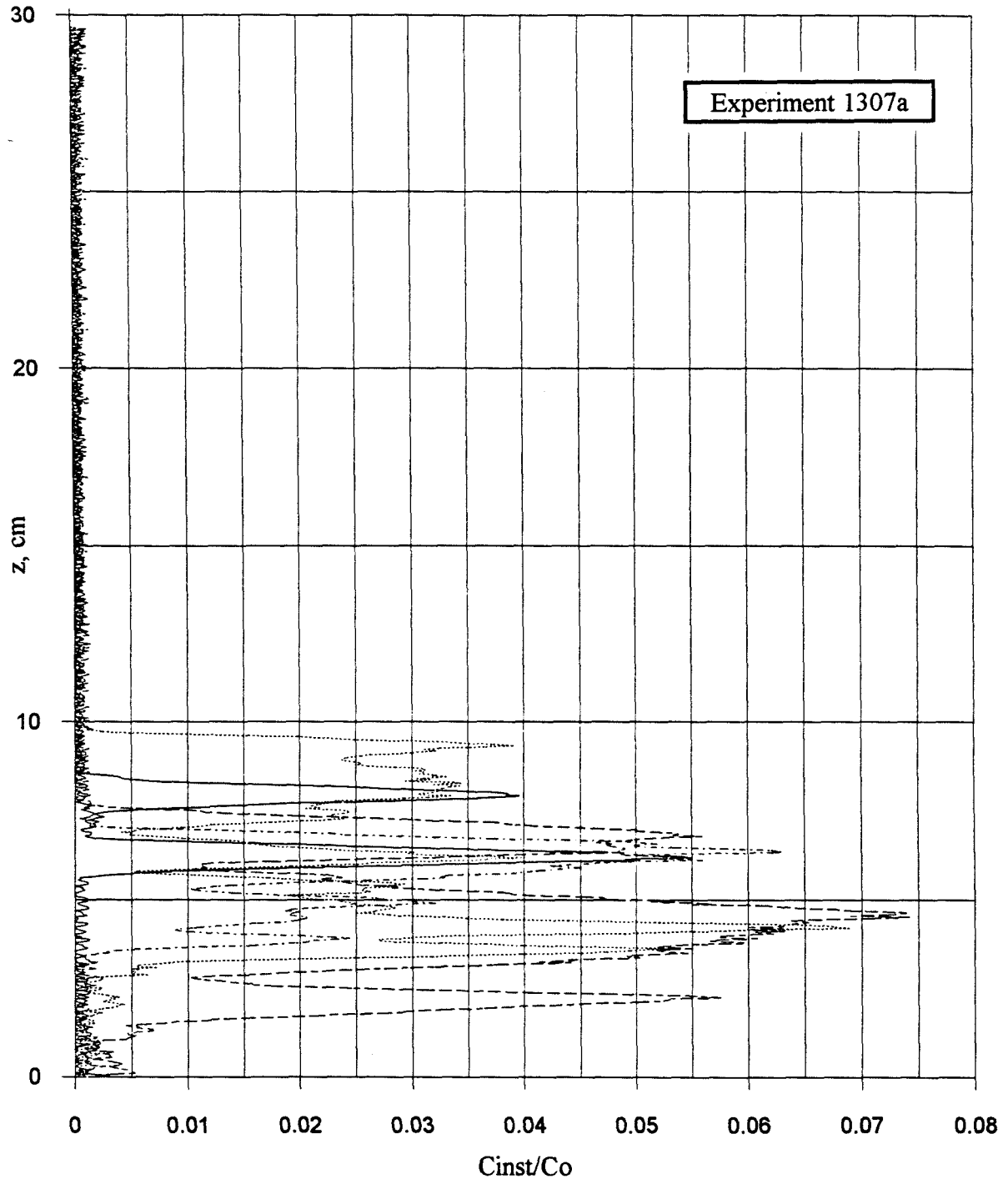

Figure 6.7 Superposition of instantaneous relative concentration profiles at x = 40 cm

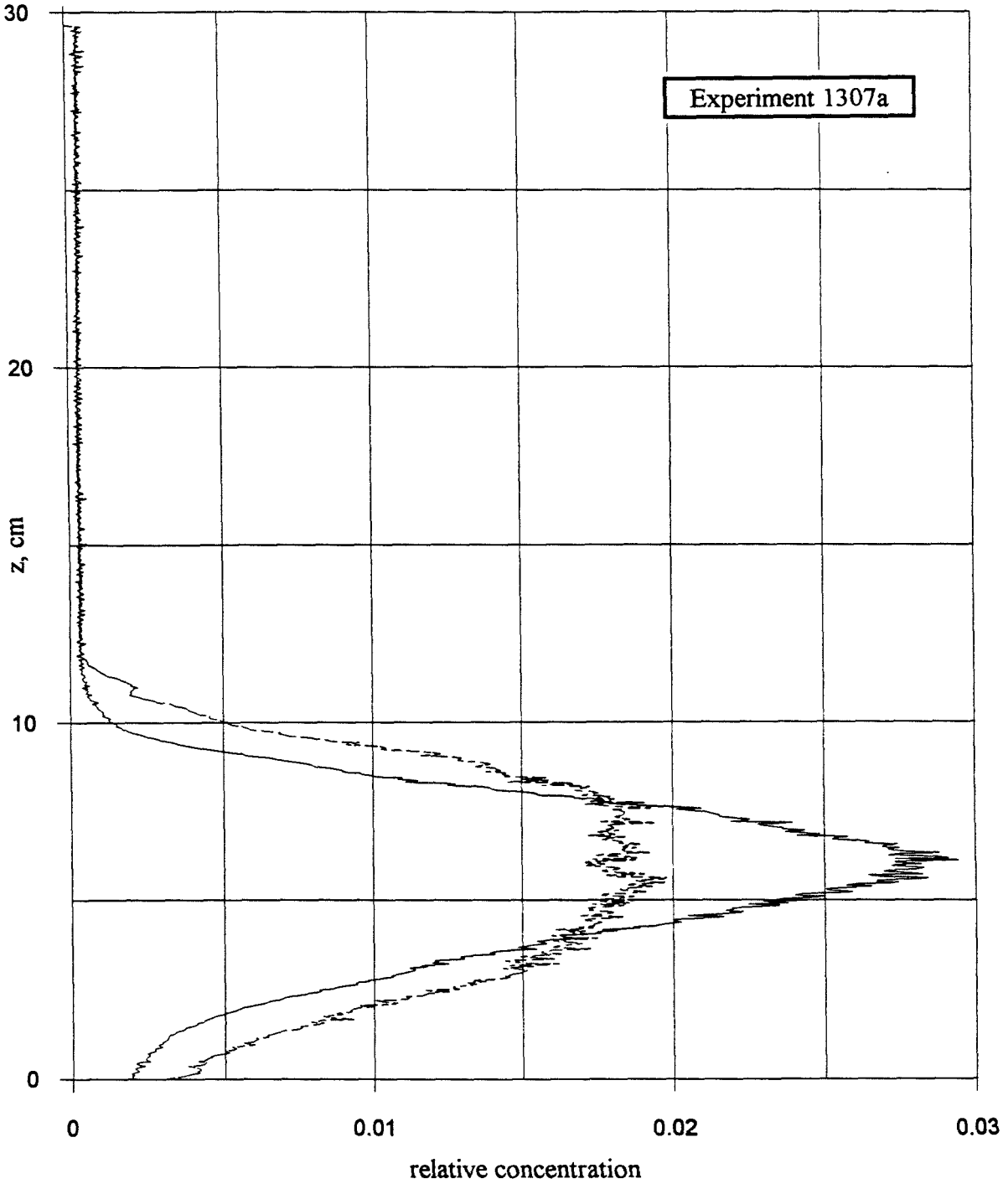

Figure 6.8 Average relative concentration and standard deviation

6.1.3 The power spectrum density

Kolmogorov's (1941a) first hypothesis with regard to isotropic turbulence was that "at sufficiently high Reynolds numbers there is a range of high wavenumbers where the turbulence is statistically in equilibrium and uniquely determined by the parameters ε and ν. This state of equilibrium is universal," where ε is the energy dissipation per unit mass [L^2/T^3] and ν is the kinematic viscosity [L^2/T]. The equilibrium is referred to as "universal" because the relevant length and time scales of turbulence are not influenced by external effects, rather only by changes in ε and ν.

From this hypothesis, it is possible to construct the length and velocity scales of turbulence (Hinze (1959)):

$$l_t = \left(\frac{\nu^3}{\varepsilon}\right)^{1/4}$$
$$u_t = (\nu\varepsilon)^{1/4} \tag{6.2}$$

and from these scales the turbulent Reynolds number can be written as:

$$R_t = \frac{u_t l_t}{\nu} = 1 \tag{6.3}$$

The wavenumber corresponding to very strong viscous effects is defined from the above length scale as:

$$k_d = \frac{1}{l_t}$$

where the subscript d refers to the region of strong dissipation effects. Conversely, we may define a wavenumber corresponding to the range of the energy-containing eddies which is related to the average size of these eddies, l_e.

$$k_e = \frac{1}{l_e}$$

Kolmogorov's (1941b) second hypothesis stated that: "If the Reynolds number is infinitely large, the energy spectrum in the subrange satisfying the condition $k_e << k << k_d$

is independent of ν, and is solely determined by one parameter ε." This hypothesis stems from the realization that in the equilibrium range of turbulence, dissipation occurs at all wavenumbers; however, it strongly increases as the wavenumber increase. Thus, as the turbulent Reynolds number (Eq. 6.3 above) increases, we would expect the dissipation in wavenumbers far below the maximum to become insignificant in comparison to the maximum. This implies that wavenumbers corresponding to the inertial range dominate the dissipation and hence this subregion is referred to as the "inertial subrange."

In this subrange, then, we would expect the effect of the kinematic viscosity to be negligible and therefore the turbulent energy spectrum to be a function of ν alone. Dimensional analysis can then be used to formulate the relationship between the turbulent energy spectrum E and the energy dissipation rate per unit mass, ε, as follows:

$$[E]=\left[\frac{L^3}{T^2}\right],\ [\varepsilon]=\left[\frac{L^2}{T^3}\right],\ [k]=\left[\frac{1}{L}\right]$$

therefore, if E is a function of ε and the wavenumber, k, only, we find:

$$E \propto \varepsilon^{2/3} k^{-5/3} \tag{6.4}$$

which is the familiar Kolmogorov spectrum law.

For the conditions of the experiments shown above, Fig. 6.9 shows a typical power spectrum density at the buoyant jet centerline. The flow behaves in accordance with Kolmogorov's theory in the inertial subrange of flow. Namely, the dissipation of turbulent energy is accomplished primarily through the flux of energy created by inertial effects.

6.1.4 The effect of distance from the point of release

We next examine the behavior of the flow as a function of the distance from the point of release. For the experimental parameters listed above, we examine the flow at one location closer to and at one farther from the release point. Figure 6.10 shows the time-averaged relative concentration profiles at x = 25, 40, and 100 cm (x/d = 50, 80, 200)

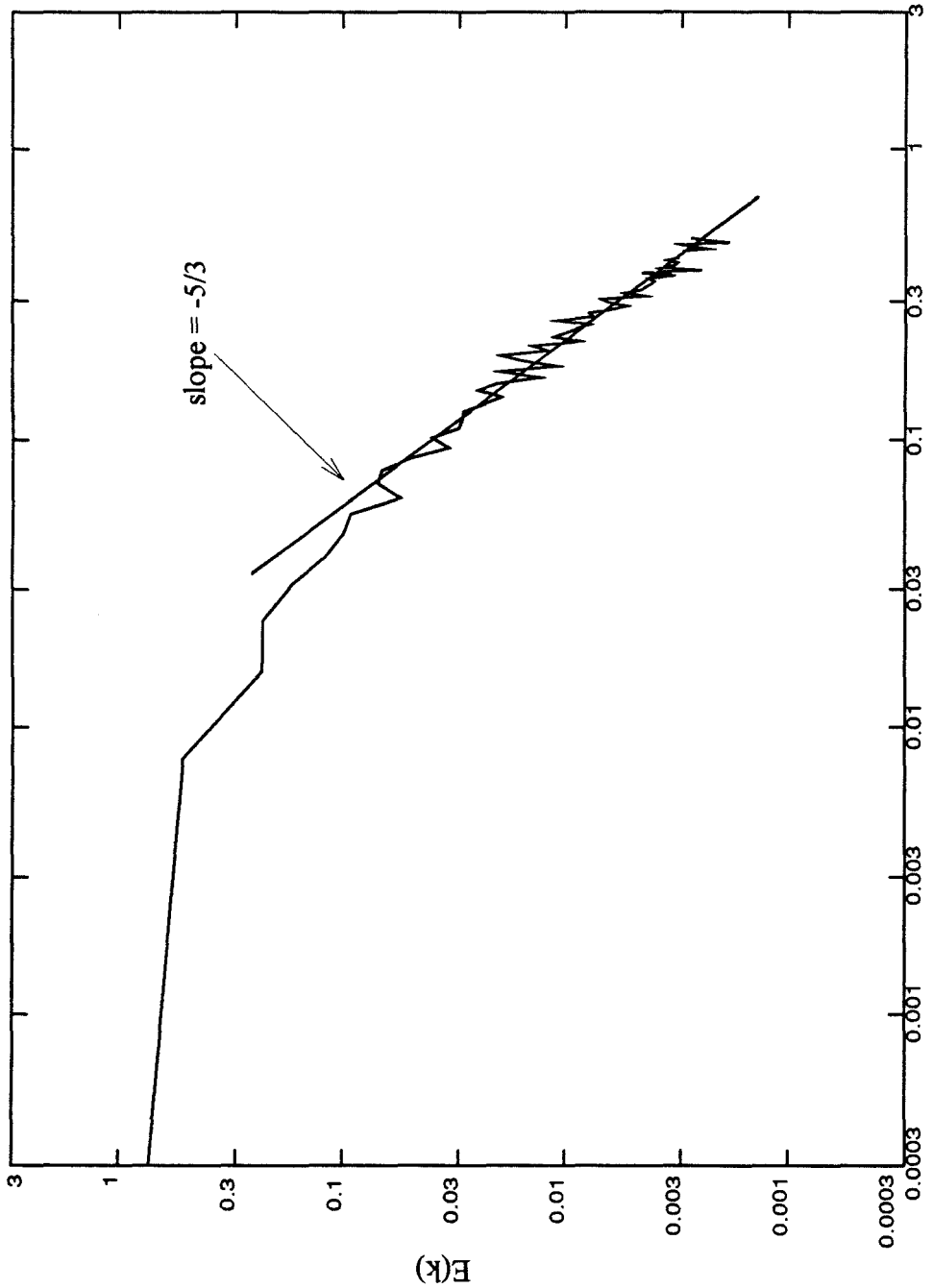

Figure 6.9 Typical power spectrum density at buoyant jet centerline

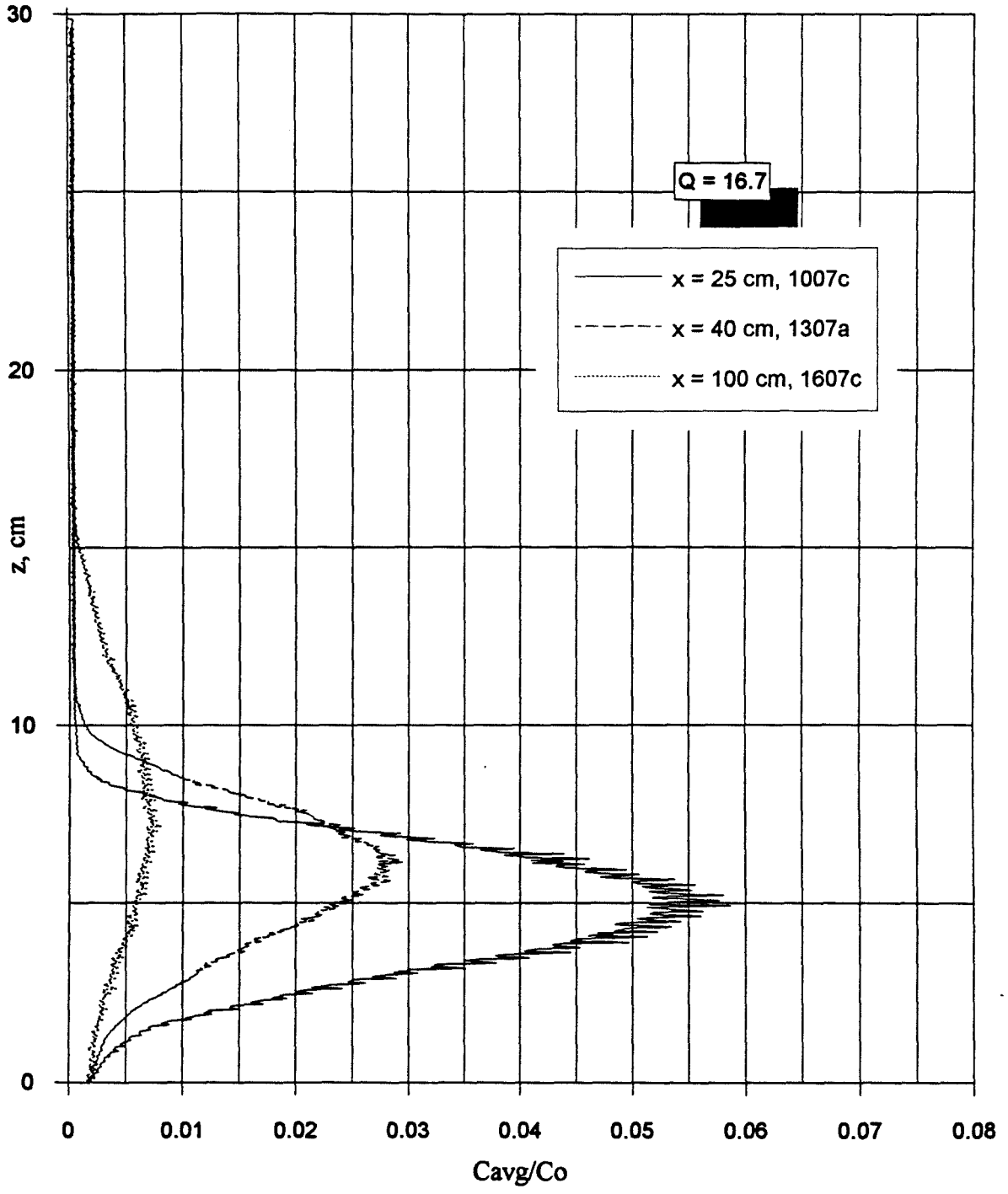

Figure 6.10 Time-averaged relative concentration as a function of distance from point of release

respectively. As can be seen from this figure, the maximum relative concentration decreases with increasing distance, x, as does the elevation of the buoyant jet centerline. These results are consistent with our expectations.

Second, the flow becomes more complex with distance. Figures 6.11, and 6.12 each show four instantaneous relative concentration profiles. Figure 6.11 is data taken at an x-location equal to 25 cm and Fig. 6.12 from a location of 100 cm. (For similar plots at 40 cm, refer to Fig. 6.7) We can discern from these instantaneous profiles that the number of interfaces between the release fluid and the ambient fluid significantly increases as the distance from the point of release increases. Furthermore, as x increases, we observe less ambient fluid (indicated by low relative concentration) along the centerline of the flow as exhibited by typical single instantaneous profiles in Figs. 6.13, and 6.14 corresponding to $x = 25$ and $x = 100$ cm respectively. This implies that ambient fluid that is engulfed early to the centerline of the flow by large-scale structures has begun to mix within the buoyant jet structure by the time the flow reaches a distance of 100 cm. This is confirmed by color-enhanced representations of the flow at 25 and 100 cm shown in Figs. 6.15, and 6.16. Figure 6.17 shows all three of the color-enhanced reproductions from x = 25, 40, and 100 cm.

6.1.5 The effect of increasing initial volumetric flow rate

We can also examine the effect of increasing the buoyant jet initial volumetric flow rate, Q, on the flow behavior at a fixed location x from the point of release. This is especially enlightening for low volumetric flow rate cases where the buoyant jet is suppressed deep within the boundary layer causing high intermittency in the relative concentration within the buoyant jet. Figures 6.18 show the time-averaged relative concentration profiles for initial volumetric flow rates corresponding to 5.5, 16.7, and 27.8 cm^3/s. We note that the effect of increasing volumetric flow rate on the dilution is not monotonic, rather, as discussed above, at very low volumetric flow rates, the buoyant jet is "caught" in the

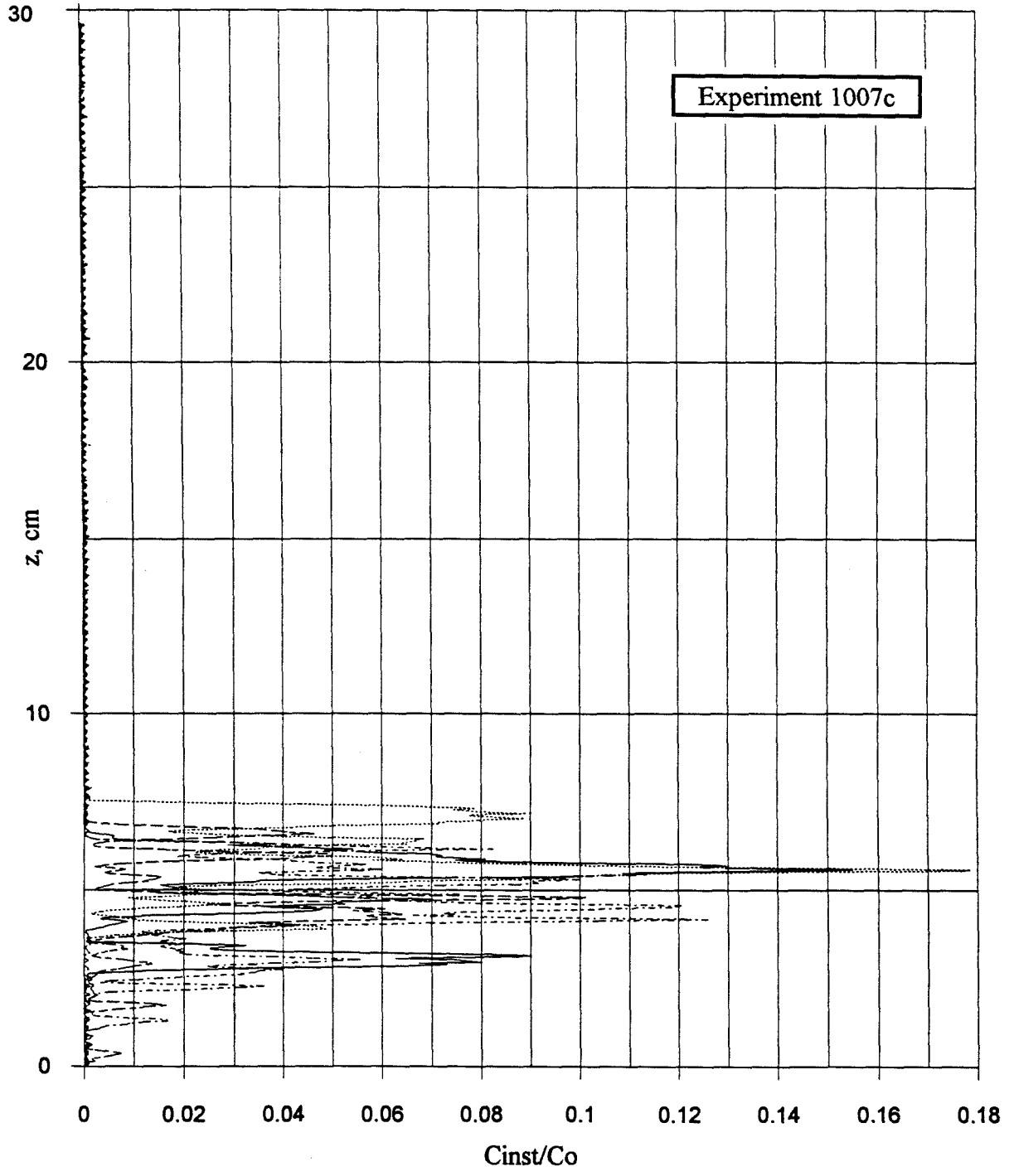

Figure 6.11 Instantaneous relative concentration profiles at x = 25 cm

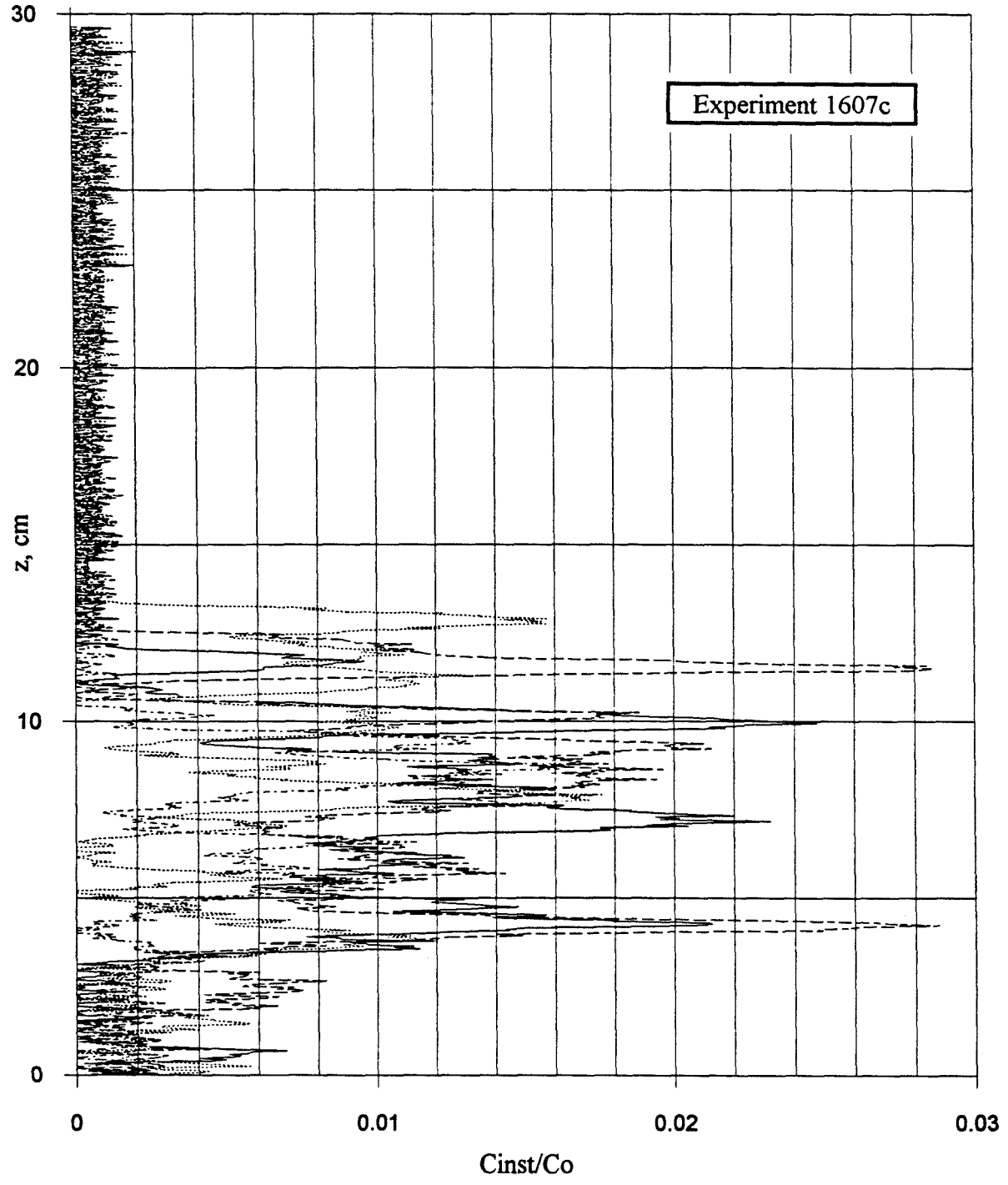

Figure 6.12 Instantaneous relative concentration profiles at x = 100 cm

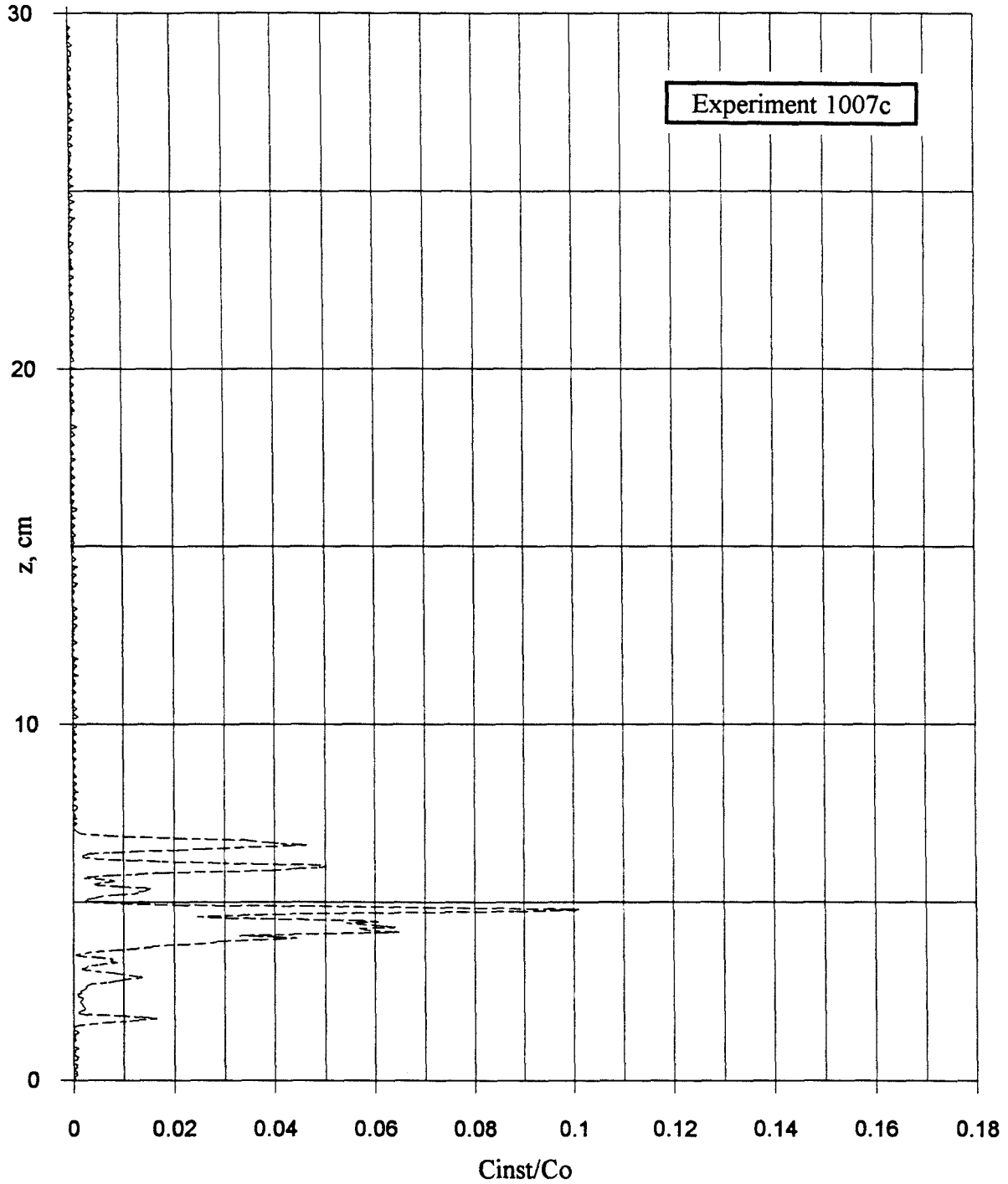

Figure 6.13 Single instantaneous relative concentration profile at x = 25 cm

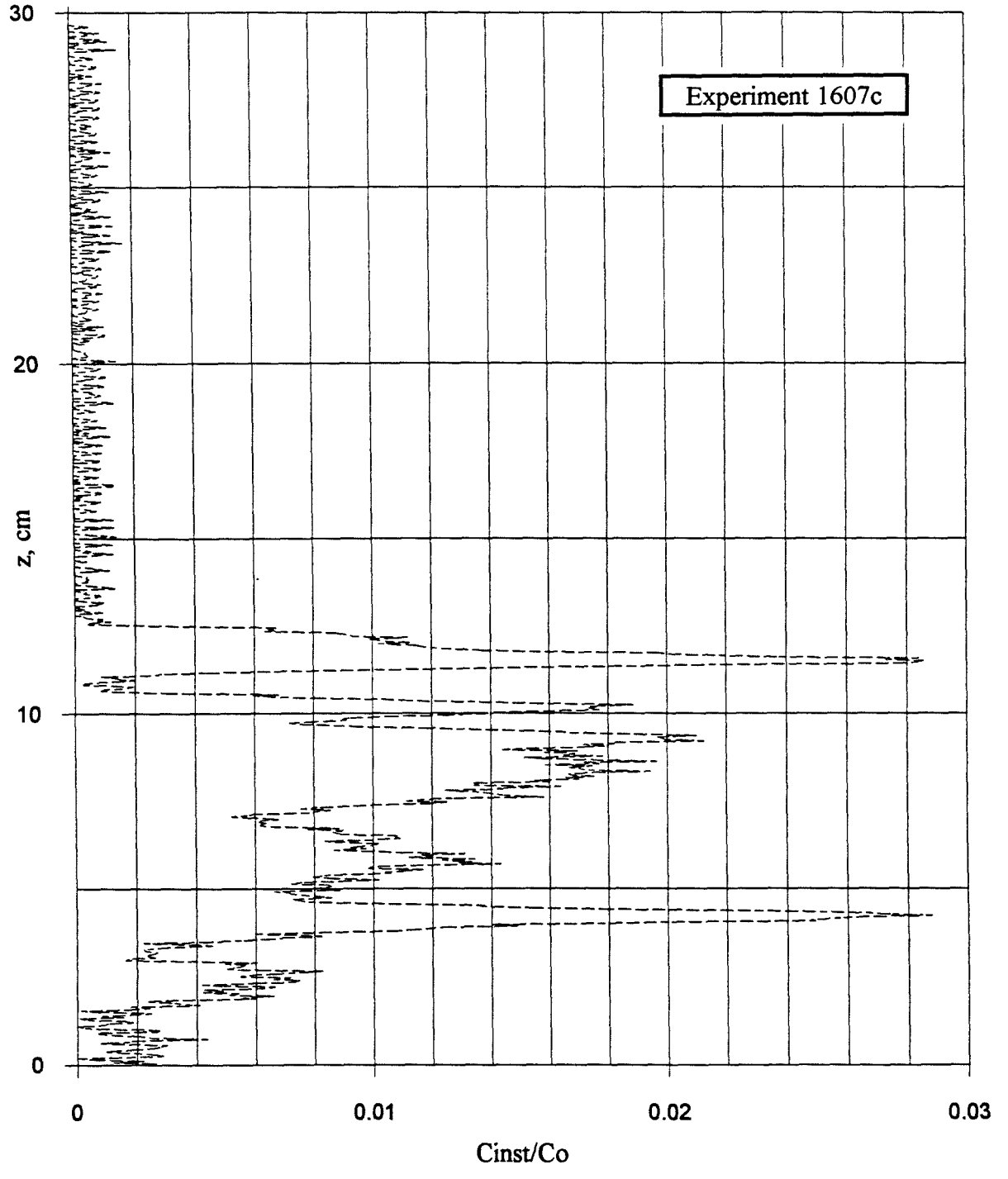

Figure 6.14 Single instantaneous relative concentration profile at x = 100 cm

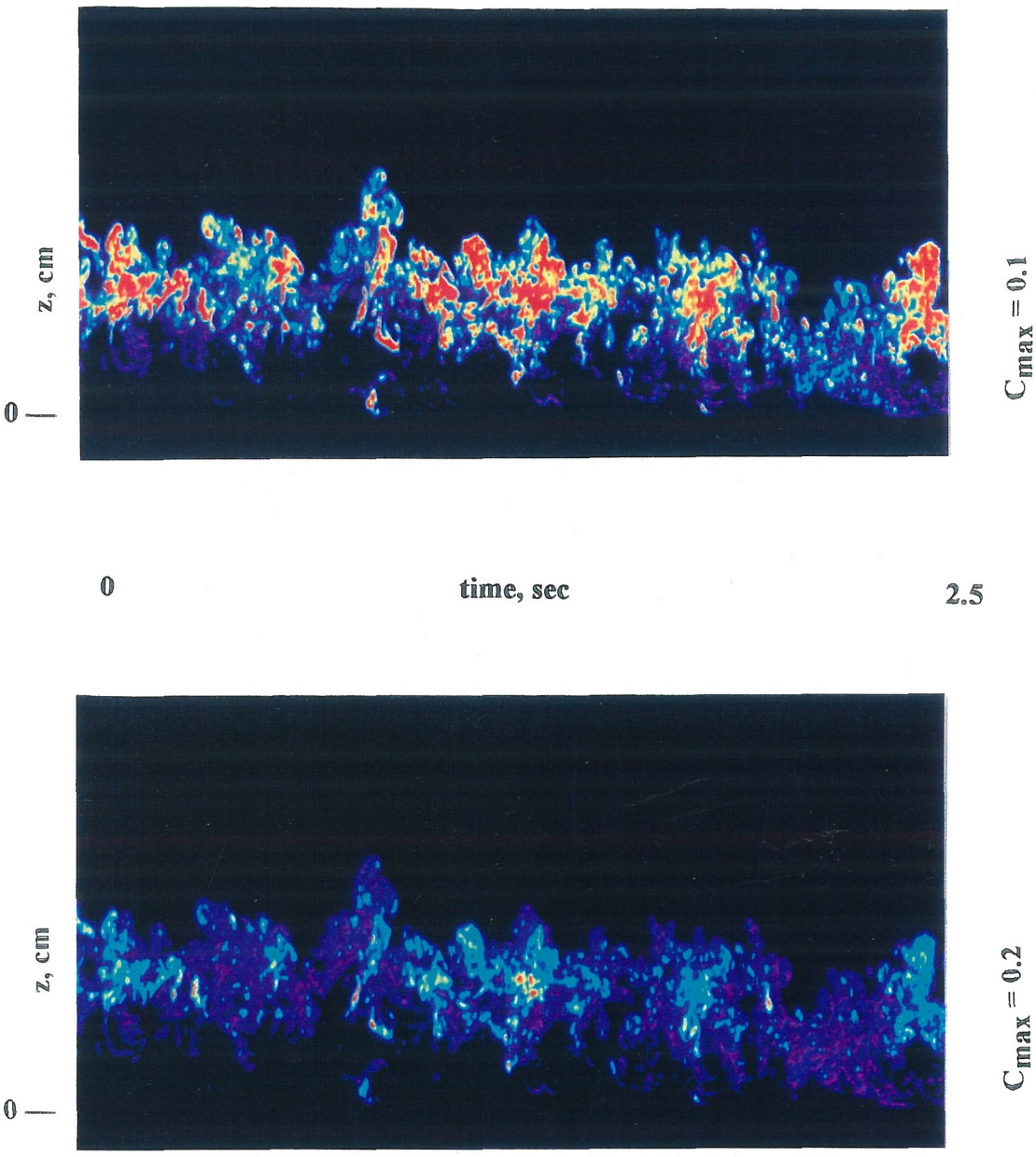

Figure 6.15 Color-enhanced picture of flow at x = 25 cm, C_{max} = 0.1 (Expt 1007c)

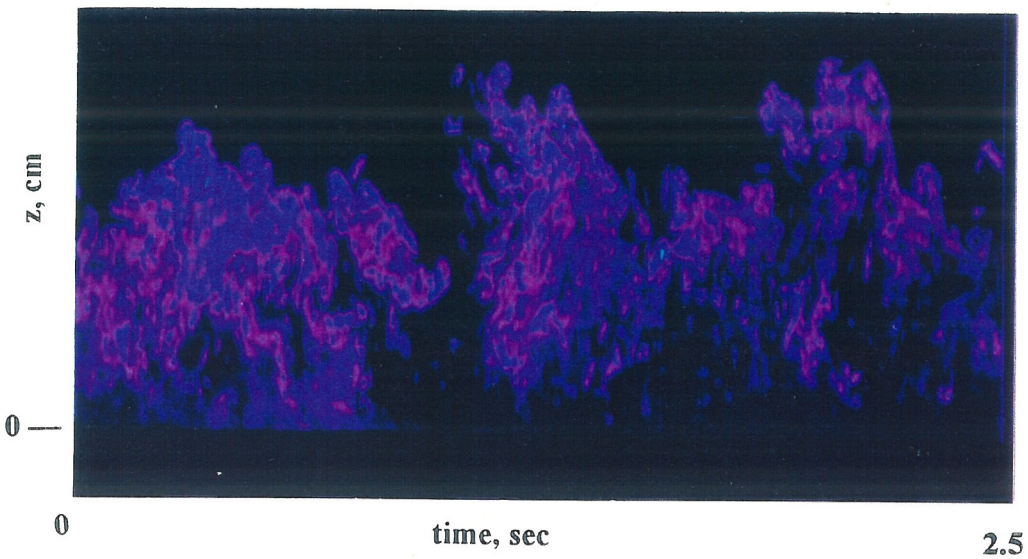

Figure 6.16 Color-enhanced picture of flow at x = 100 cm, C_{max} = 0.1 (Expt 1607c)

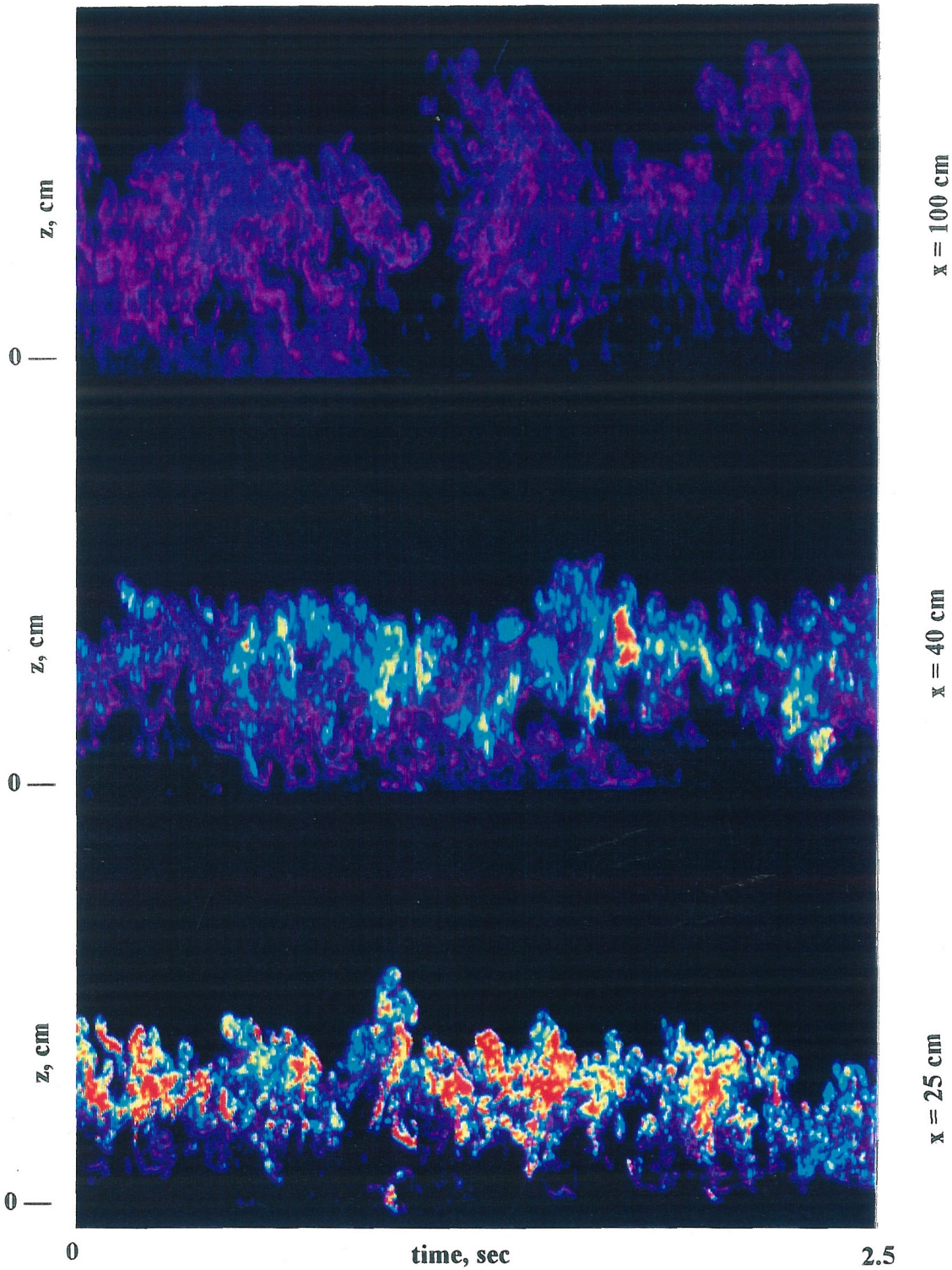

Figure 6.17 Color-enhanced picture of flow at x = 25, 40, and 100 cm, $C_{max} = 0.1$

(Expts 1007c, 1307a, 1607c)

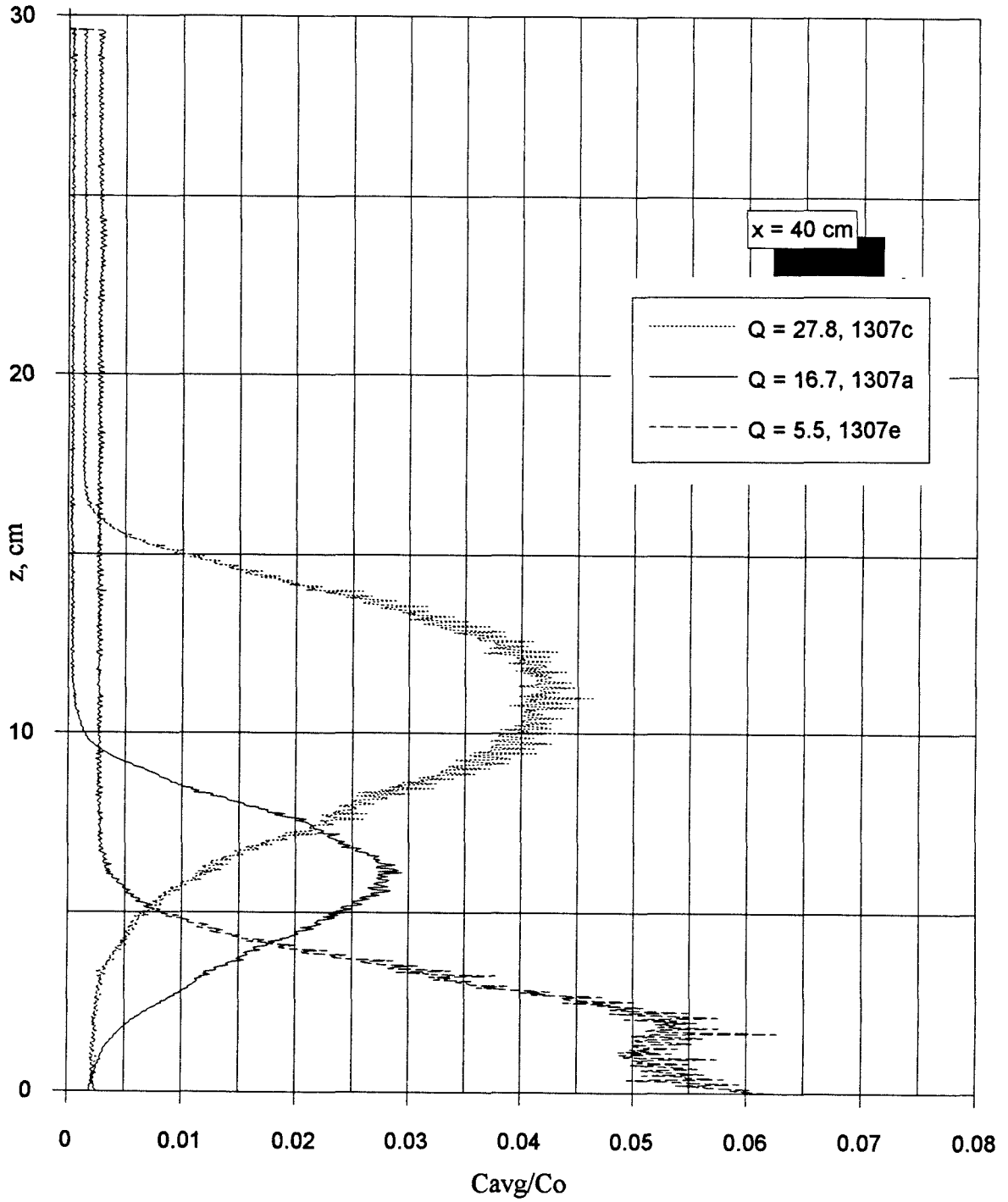

Figure 6.18 Time-averaged relative concentration as a function of initial volumetric flow rate

boundary layer and dilution is inhibited. The effect of increasing the volumetric flow rate on the dilution is not as we might expect until the buoyant jet possesses enough initial momentum to rise in the boundary layer. The intermittency of buoyant jet flows which are suppressed in the boundary layer is exemplified by Figure 6.19 which shows the average relative concentration and the standard deviation for the low volumetric flow rate case, Q = 5.5 cm^3/s. Only in this type of flow situation do we observe that the standard deviation of the relative concentration exceeds the average. This contributes to the inherently higher error seen in data exhibiting this behavior.

6.2 Dimensional data

In chapter 5 we discussed various transition phenomena, the purpose of which was to gain a better understanding of the parameters effecting various transitions. In the end, however, we discovered that for a flow as complex as a buoyant jet in a cross flow with shear, predicting transition with any degree of confidence is difficult. If we know which asymptotic regime the flow is in and which asymptotic regime it is transitioning to, we can easily nondimensionalize the data to elucidate the location of transition. However, if we do not know which asymptotic regime is appropriate, then, nondimensionalization of the data is impossible.

In light of this uncertainty, we thought it would be useful to first examine the data in dimensional form with the hope of verifying the regimes of flow through the determination of the functional relationships between various flow parameters. In the following section, we describe the theoretical relationships between the flow parameters in all of the regimes of flow previously postulated and compare these results with the experimental data. This provides us with keen insight into the flow behavior.

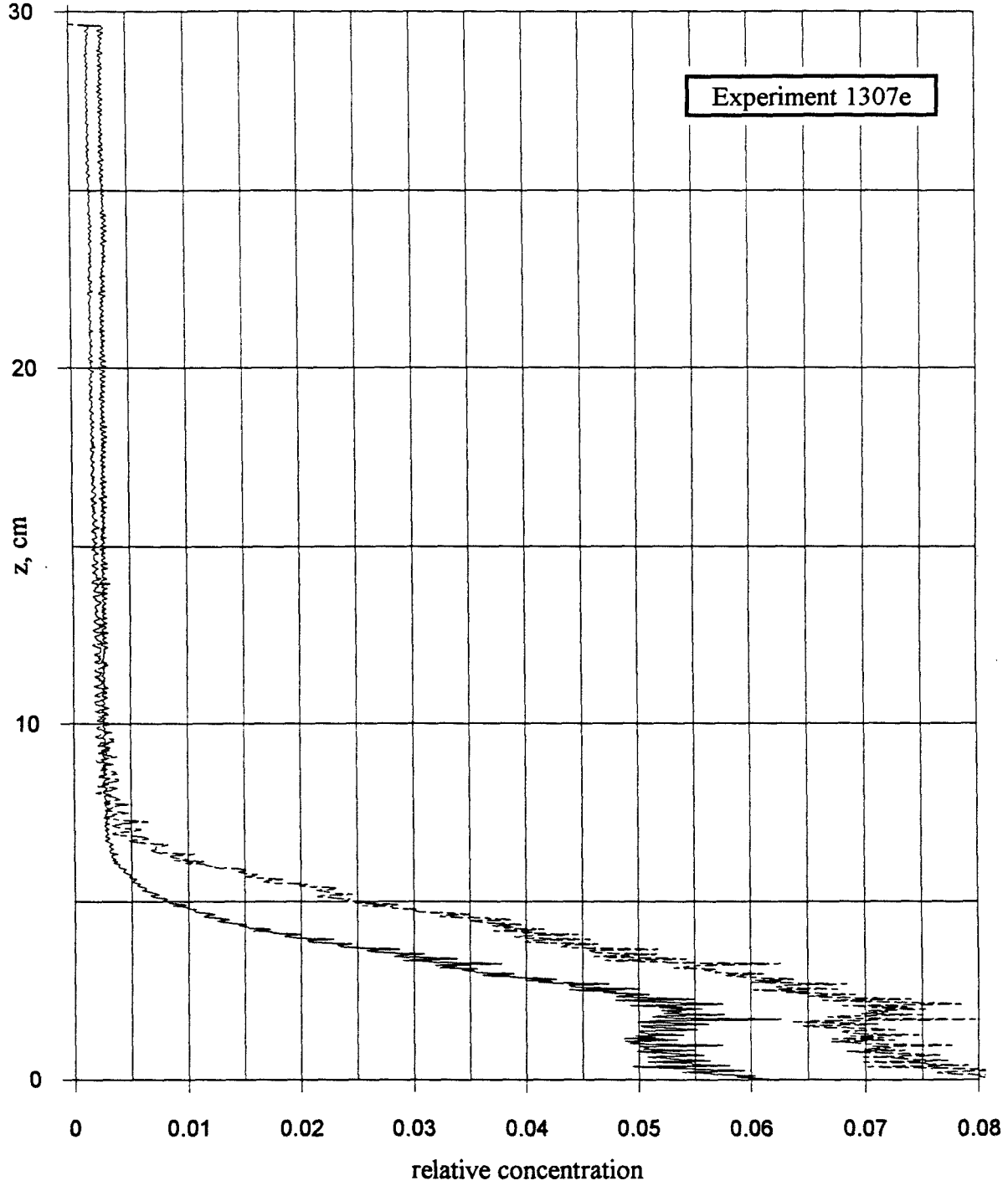

Figure 6.19 Average relative concentration and standard deviation for low flow rate case

6.2.1 Functional relationships

The dilution equations for the bent plume and the diffusive mixing regimes of flow were formulated in chapter 2. We based those formulations on dimensional arguments and assumed that in the diffusive mixing regime, the coefficient of diffusion was directly proportional to the shear velocity and the overall depth of flow. As we mentioned in chapter 5, this argument relies on the belief that upon reaching the diffusive mixing regime, the buoyant jet has had an opportunity to spread and hence sample from length scales of the order of the flow depth. If this is not the case, in other words, if the flow reaches the diffusive mixing regime earlier in the flow development, then the turbulent mixing coefficient must be proportional to the shear velocity and the elevation of the buoyant jet, as follows:

$$D \propto u_* z \tag{6.5}$$

In this case, the dilution cannot be written as a function of the horizontal location, x, unless the trajectory of the flow is known. If we assume for the sake of argument that the trajectory relations developed in chapter 5 for the jet, bent jet, and bent plume regimes are valid, then we can use these trajectory relations to write equations describing the dilution as a function of x in the region where the turbulent diffusion coefficient is proportional to the elevation, z. Of course, we do not know that the previously developed trajectory equations will be valid in a cross flow where the velocity profile is logarithmic. In fact, we have no reason to expect this to be true since in order to integrate the kinematic equation in chapter 5 we relied on a constant value of the cross-flow velocity, U. Clearly, in a boundary layer cross flow, this assumption would not be valid, and the trajectory is likely to be a more complex function of the flow parameters involved. Nonetheless, substitutions of the developed trajectory relations are simple to do and serve as first cut estimates of potential trajectories in the diffusive mixing region where the elevation is of importance.

The dilution equations for the remaining flow regimes particular to this study that might occur before the onset of diffusive mixing (jet and bent jet) were not discussed in chapter 2, however, can be obtained with dimensional analysis as was done for the bent plume dilution equation. Wright (1977) and Fischer (1979) used flux conservation techniques (conservation of momentum flux in the case of a jet and conservation of buoyancy flux in the case of a plume) combined with dimensional analysis to develop the appropriate equations.

A summary of the all the resulting dilution equations appears as Table 6.1. From these equations, it is possible to examine the effect of changes in various flow parameters on the dilution.

6.2.1.1 Effect of cross-flow velocity on the dilution

When we reasoned in chapter 1 that a transition from bent plume to diffusive mixing would occur, we utilized the functional relationship between the dilution, S, and the cross-flow velocity, U (or the shear velocity, u_*) to formulate our hypothesis. Therefore, we will first examine the effect of changing cross-flow velocity on the minimum average dilution, S, for a buoyant jet in a cross flow with shear.

The equations from Table 6.1 provide the basis for developing equations describing the effect of changing cross-flow velocity on the dilution. In Table 6.2, we assume that x, Q, M, and B are constant and summarize the resulting functional relationships between the dilution and the cross-flow velocity in each of the flow regimes. (Note: As a preliminary exercise, we have assumed that the shear velocity is directly proportional to the cross-flow velocity, U, instead of to the power of 7/8, as was shown in chapter 4 whenever both U and u_* appear in the equation. However, in cases not involving *both* the cross-flow velocity and the shear velocity, we replaced u_* with $U^{7/8}$.)

Table 6.1 Summary of dilution equations in various flow regimes

Regime	Dilution, z	Dilution, x
jet	$S \propto \frac{zM^{1/2}}{Q}$	$S \propto \frac{x^{1/2}M^{3/4}}{U^{1/2}Q}$
bent jet	$S \propto \frac{z^2U}{Q}$	$S \propto \frac{x^{2/3}M^{2/3}}{U^{1/3}Q}$
bent plume	$S \propto \frac{z^2U}{Q}$	$S \propto \frac{x^{4/3}B^{2/3}}{UQ}$
diffusion, h	$S \propto \frac{u_*h\{x(z)\}}{Q}$	$S \propto \frac{u_*hx}{Q}$
jet trajectory	$S \propto \frac{u_*hUz^2}{QM^{1/2}}$	$S \propto \frac{u_*hx}{Q}$
bent jet trajectory	$S \propto \frac{u_*hU^2z^3}{QM}$	$S \propto \frac{u_*hx}{Q}$
bent plume trajectory	$S \propto \frac{u_*hU^{3/2}z^{3/2}}{QB^{1/2}}$	$S \propto \frac{u_*hx}{Q}$
diffusion, z	$S \propto \frac{u_*z\{x(z)\}}{Q}$	$S \propto \frac{u_*\{z(x)\}x}{Q}$
jet trajectory	$S \propto \frac{u_*Uz^3}{QM^{1/2}}$	$S \propto \frac{u_*x^{3/2}M^{1/4}}{QU^{1/2}}$
bent jet trajectory	$S \propto \frac{u_*U^2z^4}{QM}$	$S \propto \frac{u_*x^{4/3}M^{1/3}}{QU^{2/3}}$
bent plume trajectory	$S \propto \frac{u_*U^{3/2}z^{5/2}}{QB^{1/2}}$	$S \propto \frac{u_*x^{5/3}B^{1/3}}{QU}$

Table 6.2 Summary of dilution as a function of cross-flow velocity

Regime	Dilution as a function of U
jet	$\propto U^{-1/2}$
bent jet	$\propto U^{-1/3}$
bent plume	$\propto U^{-1}$
diffusion, h	$\propto U^{7/8}$
jet trajectory	
bent jet trajectory	
bent plume trajectory	
diffusion, z	
jet trajectory	$\propto U^{1/2}$
bent jet trajectory	$\propto U^{1/3}$
bent plume trajectory	independent of U

Figures 6.20- 6.22 show the dilution versus cross-flow velocity U for different initial volumetric flow rates, Q, at fixed locations x = 25, 50, and 100 cm. In this study, these are the most accurate and repeatable experimental measurements where the effect of parameter changes can be observed. This is true predominantly because both the cross-flow velocity and the initial volumetric flow rate can be varied without recalibrating the LIF system and, since the calibration procedure is sensitive, recalibration increases potential error. As indicated in each of these figures, the dilution increases with increasing cross-flow velocity. The functional relationship is exactly as predicted in Table 6.1 for the case of diffusive mixing where the turbulent mixing coefficient is proportional to the overall depth.

Figure 6.23, where the dilution is plotted versus the cross-flow velocity U at a fixed initial volumetric flow rate and various locations, x, with the remaining flow parameters held constant, further reinforces this conclusion . (The slight changes in the relative density difference that exist are estimated to have minimal effect.) Examination of

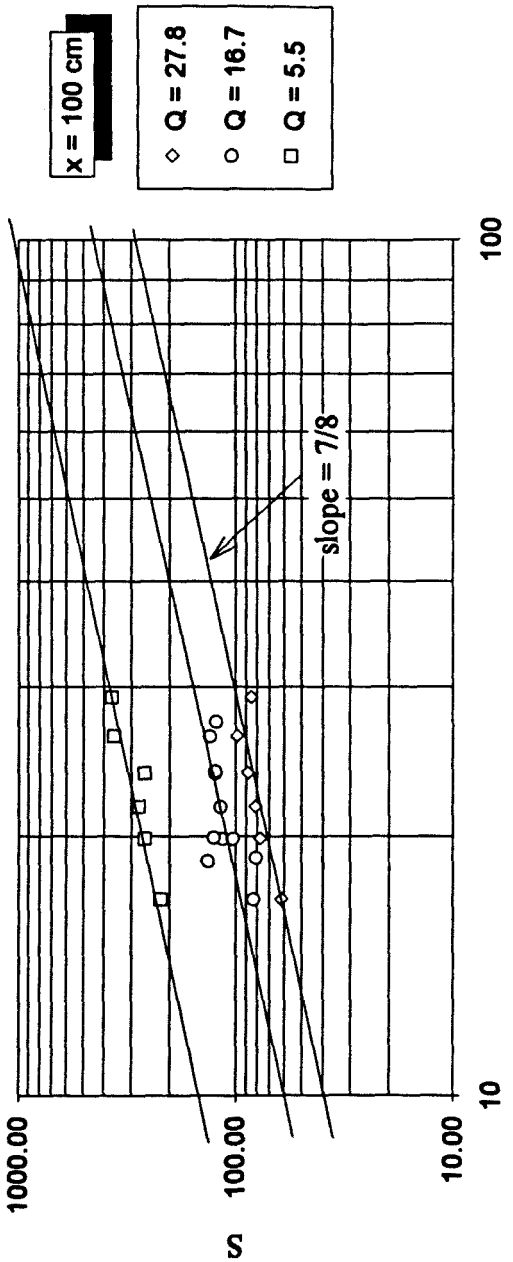

Figure 6.20 Dilution versus cross-flow velocity at various Q levels, x = 100 cm

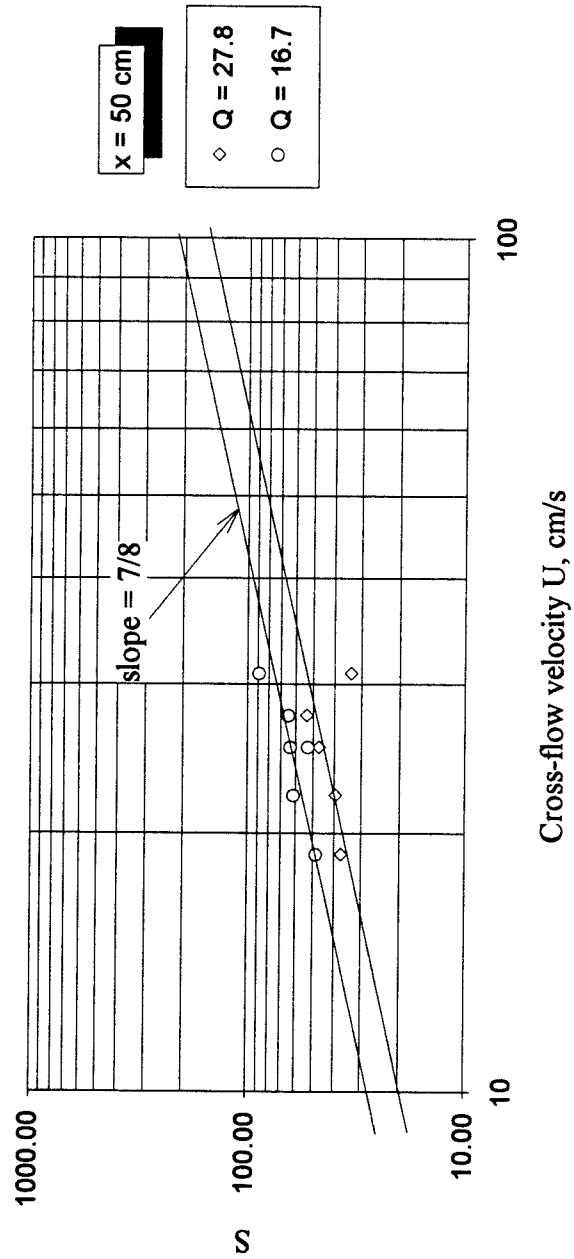

Figure 6.21 Dilution versus cross-flow velocity at various Q levels, x = 50 cm

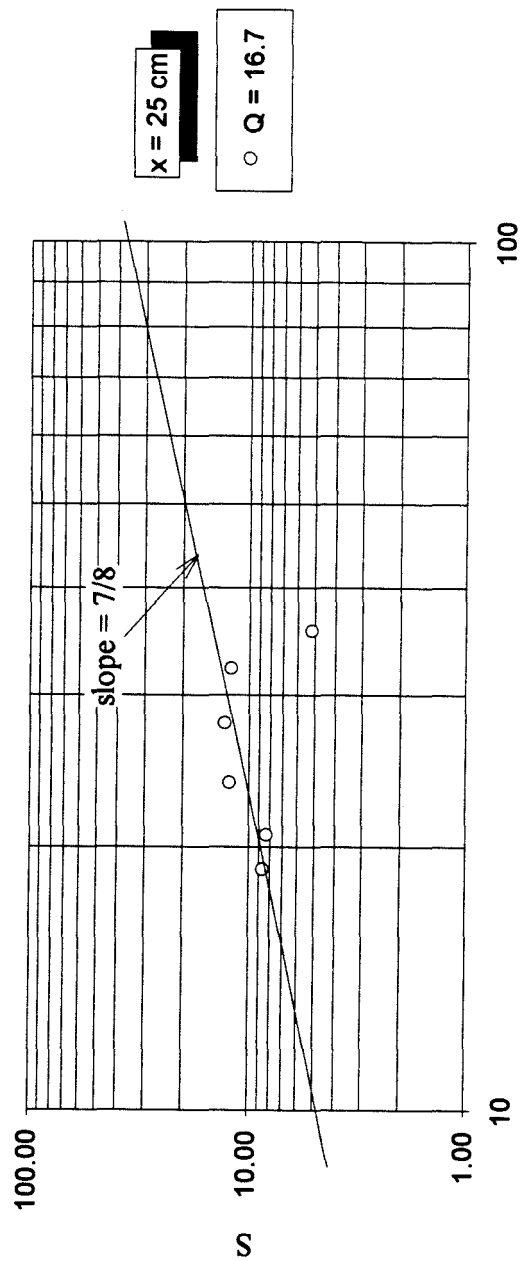

Figure 6.22 Dilution versus cross-flow velocity at various Q levels, x = 25 cm

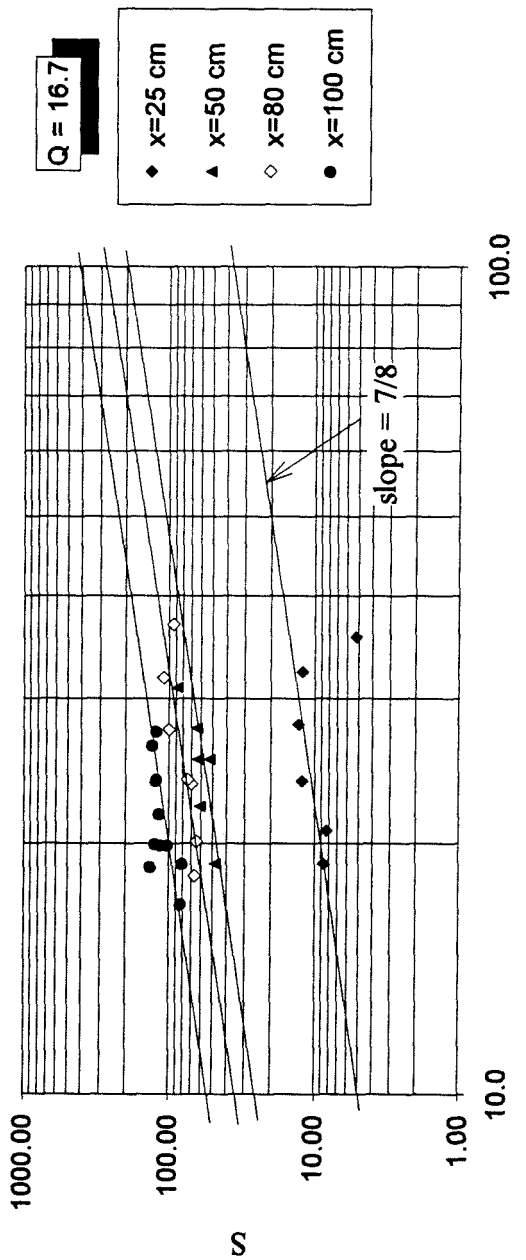

Figure 6.23 Dilution versus cross-flow velocity at various x-locations, Q = 16.7 cm^3/s

this figure shows again that the dilution is proportional to $U^{7/8}$ as predicted by diffusive mixing where the turbulent mixing coefficient is proportional to the overall depth of flow, h. Even as early as 25 cm from the point of release, the effect of increasing the cross-flow velocity is to increase strongly the dilution. As indicated in Table 6.2, this indicates that the flow is in the turbulent diffusive mixing regime.

Therefore, our first indication is that the flow is dominated by turbulent diffusive mixing even as early as 50 diameters from the point of release. We observe no region of jet or plume dominated mixing, at least as might be suggested by changes in the cross-flow velocity.

6.2.1.2 Effect of distance from the point of release on the dilution

If the above conclusion is accurate, then we would expect to observe a linear relationship between the dilution and the distance from the point of release, x. Figure 6.24 shows the dilution as a function of x at a constant initial volumetric flow rate of 16.7 cm^3/s and various cross-flow velocities corresponding to shear velocities of 0.98, 1.2, and 1.5 cm/s. (Note: Some of the values for the dilution shown in Figs. 6.24 and the subsequent 6.25 are interpolated between cross-flow velocities using $S \sim U^{7/8}$ to obtain a true plot of the dilution as a function of x under uniform experimental conditions.) In Figure 6.24*a* we observe that there does indeed exist a linear relationship between the dilution, S, and the horizontal distance, x, but that the onset of this behavior is preceded by some other type of relationship between S and x. Furthermore, Figs. 6.24*b* and *c* show that the effect of increasing the cross-flow velocity is to delay the onset of the linear relation between S and x. Whatever type of flow behavior exists prior to diffusion based on the overall depth of flow persists longer at higher cross-flow velocities.

Figure 6.25 shows the dilution as a function of x at a constant cross-flow velocity corresponding to a shear velocity of 1.2 cm/s and various initial volumetric flow rates of 27.8, 16.7, and 5.5 cm^3/s. From these plots, we observe that the relationship between the

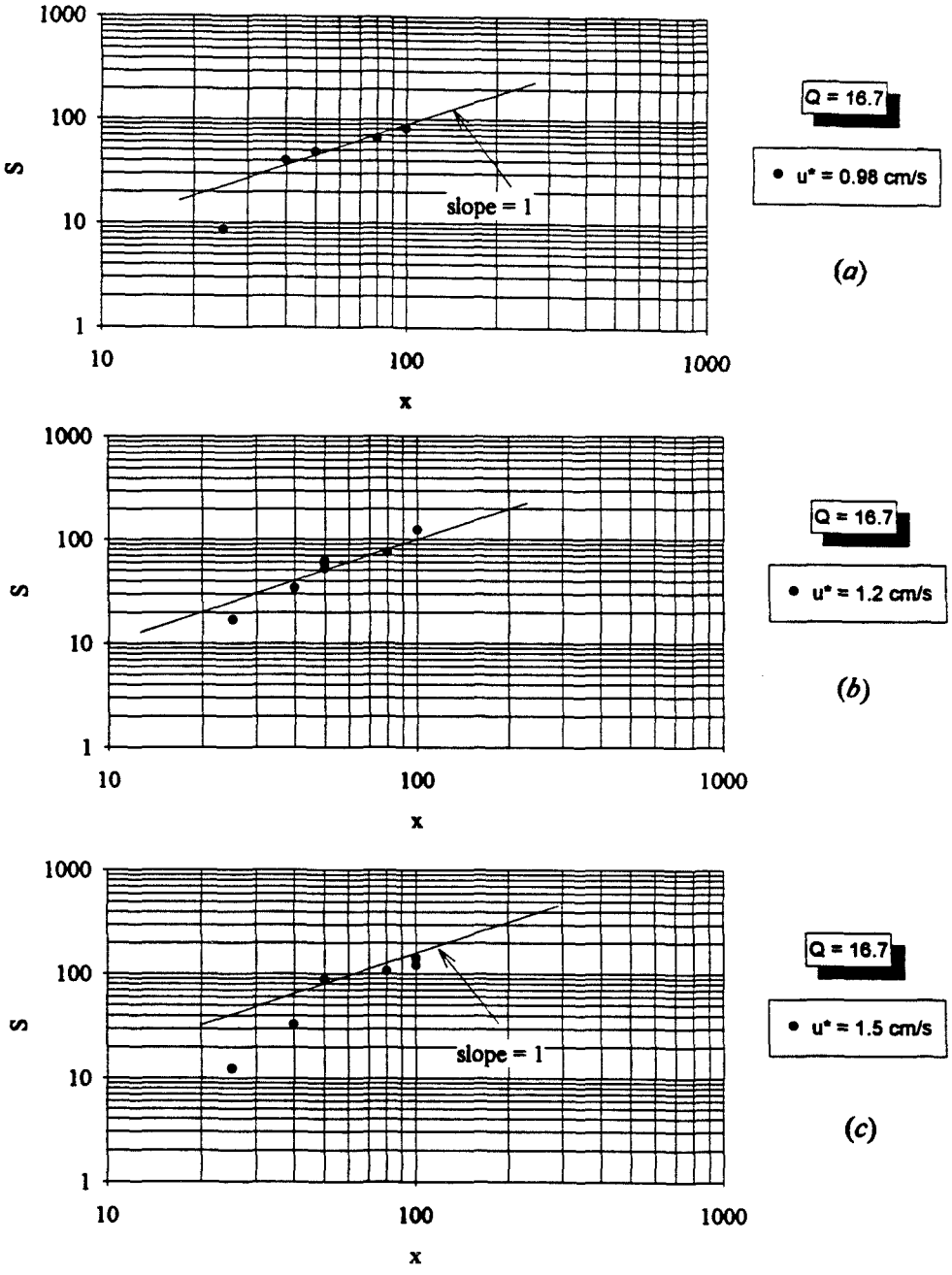

Figure 6.24 Dilution versus horizontal distance at various shear velocities, Q = 16.7 cm^3/s

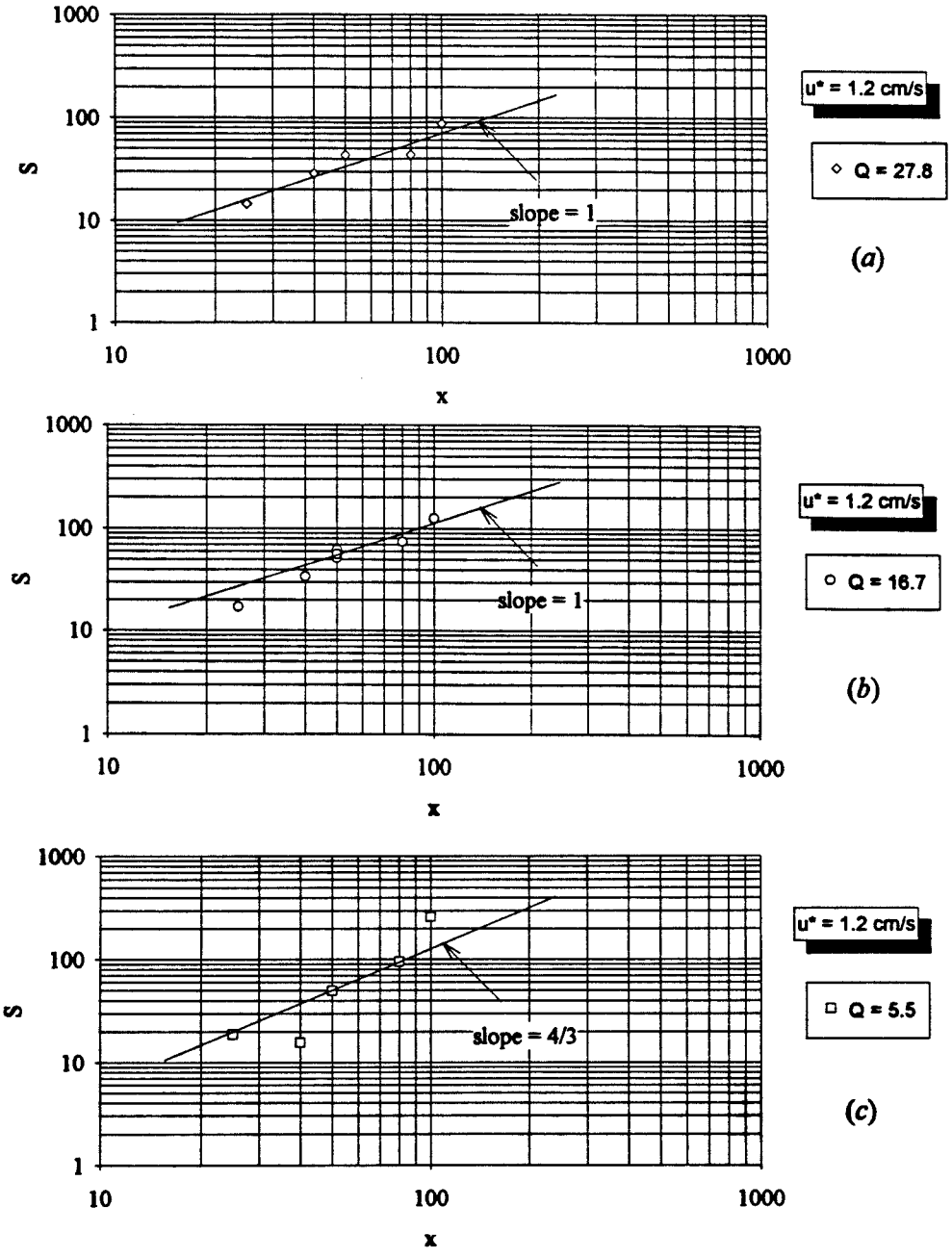

Figure 6.25 Dilution versus horizontal distance at various volumetric flow rates, $u^* = 1.2$ cm/s

S and x is linear over all values of x at the highest volumetric flow rate and that for the lowest, the relationship never achieves a linear trend. In fact, $S \sim x^{4/3}$ in this case which hints of diffusive mixing where the turbulent mixing coefficient is characterized by the local elevation, z, for a bent jet trajectory, as can be seen from the results shown in Table 6.1.

If this indication is correct, the data should show that at some elevation a transition from diffusive mixing based on the local elevation, z, to diffusive mixing based on the overall depth of flow occurs. As discussed in chapter 5, the vertical coordinate of this transition is determined from the following formula (refer to Table 5.2):

$$z_{bld-hd} = a_{hd} h$$

where we previously noted that the value of the constant a_{hd} must be determined from experiments. Since, the data shown in Figs. 6.24 and 6.25 indicates where this transition occurs in terms of the horizontal coordinate, x, we must first relate the x-coordinate of transition to the z-coordinate. This is done using trajectory data as shown in Fig. 6.26. Then, once we know the z-coordinate of transition, we can determine the value of a_{hd}.

As an example, consider the data shown in Figure 6.25*a*, where we find that $S \sim x$ as early as 25 cm from the point of release. Figure 6.26 indicates that for this set of experiments, $x = 25$ cm corresponds to a value of z greater than 8 cm. Similarly, in Figure 6.25*b* we observe that the onset of $S \sim x$ behavior occurs between $x = 40$ and $x = 50$ cm which, from Fig. 6.26, corresponds to z-coordinate values between 6 and 6.1 cm. We follow the same procedure for the remaining cases to obtain the following results:

Figure	Q, cm3/s	u^*, cm/s	x range of transition, cm	z range of transition, cm
6.24	16.7	0.98	$25 < x < 40$	$6 < z < 8.6$
6.25	16.7	1.2	$x \sim 50$	$z \sim 6$
6.26	16.7	1.5	$x \sim 50$	$z \sim 6$
6.27	27.8	1.2	$x < 25$	$z < 8.5$
6.28	16.7	1.2	$x \sim 50$	$z \sim 6$
6.29	5.5	1.2	$x > 100$	$z > 2.2$

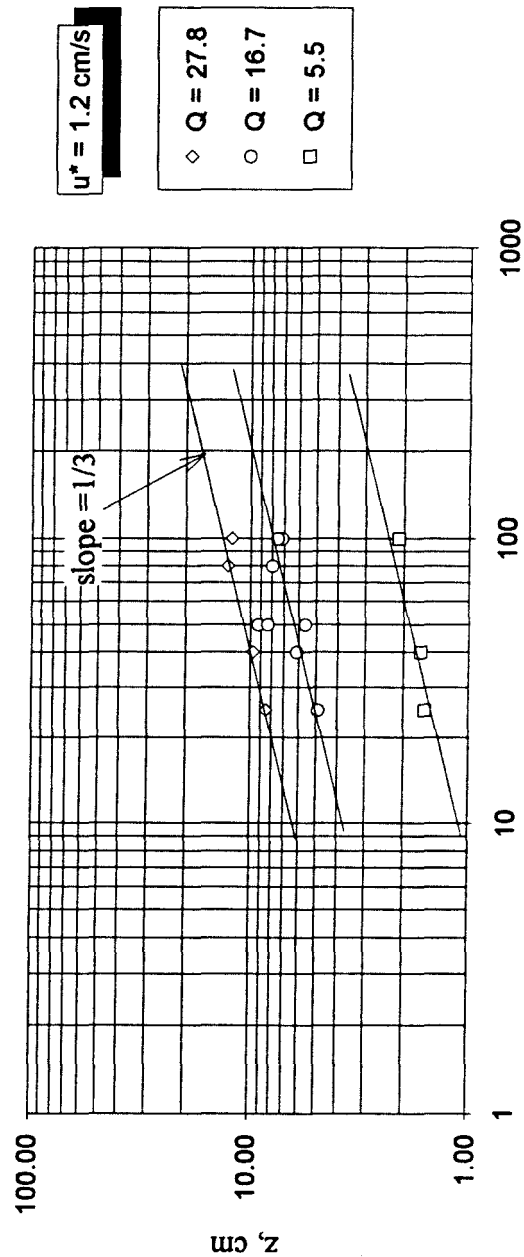

Figure 6.26 Trajectory data for shear velocity of 1.2 cm/s and various volumetric flow rates

This very rudimentary data suggests that the transition from diffusive mixing based on the elevation to diffusive mixing based on the overall depth occurs at an elevation of approximately 6 cm for a flow depth of 41.3 cm and a boundary layer thickness of 12.5 cm. This implies that a_{hd} equals roughly 0.14, or that $z_{bld\text{-}hd}$ is approximately equal to half of the boundary layer depth.

6.3 Intermediate dimensional presentation of data

If the above calculations are truly indicative of the transitional nature of this flow, we can use the value of $z_{bld\text{-}hd}$ to separate the data into two distinct regimes. For data points where the elevation is less than $z_{bld\text{-}hd}$ (6 cm in this case), or half of the boundary layer thickness, we expect to find that the dilution is described by

$$S \propto \frac{u_* zx}{Q} \qquad z < z_{bld-hd} \tag{6.6}$$

and thus a log-log plot of SQ/u_*z versus x should yield a slope equal to one. Figure 6.27 does not convincingly verify this behavior. However, there exists considerable scatter in the data. This is partly due to the fact that two experimentally determined values are required for the ordinate of this plot, thus compounding the associated error. If we replace the experimentally determined value of the elevation, z, with the theoretical value determined from the trajectory equation for a bent jet (the validity of this assumption is confirmed in Fig. 6.26) then we obtain the data shown in Fig. 6.28 which demonstrates the expected slope of one.

Similarly, for data points where the elevation is greater than $z_{bld\text{-}hd}$, we expect the following equation to be valid:

$$S \propto \frac{u_* hx}{Q} \qquad z > z_{bld-hd} \tag{6.7}$$

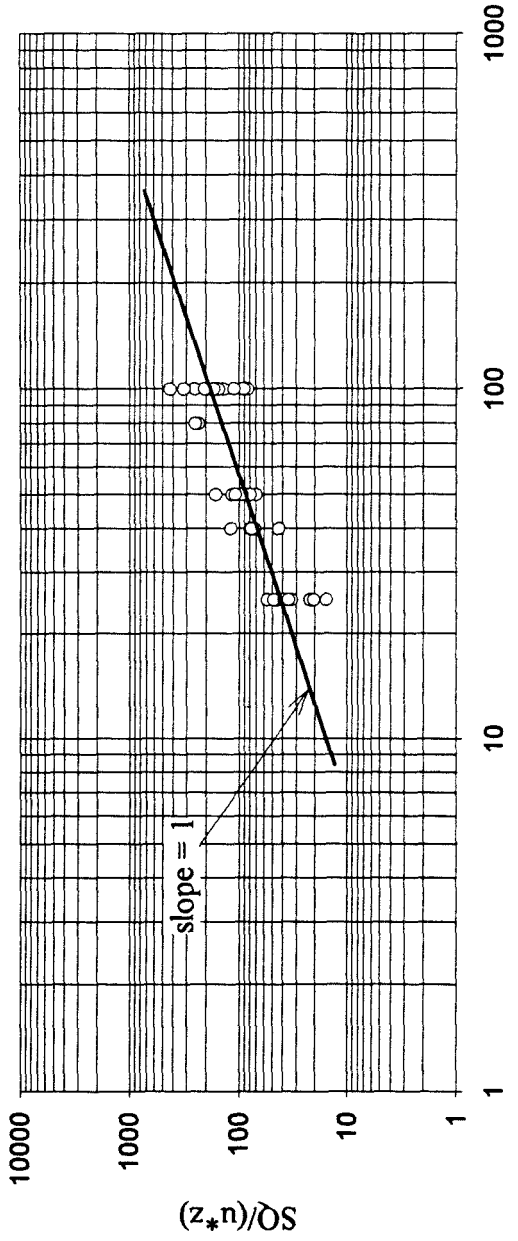

Figure 6.27 Dilution data for elevations below $z_{bld\text{-}hd}$.

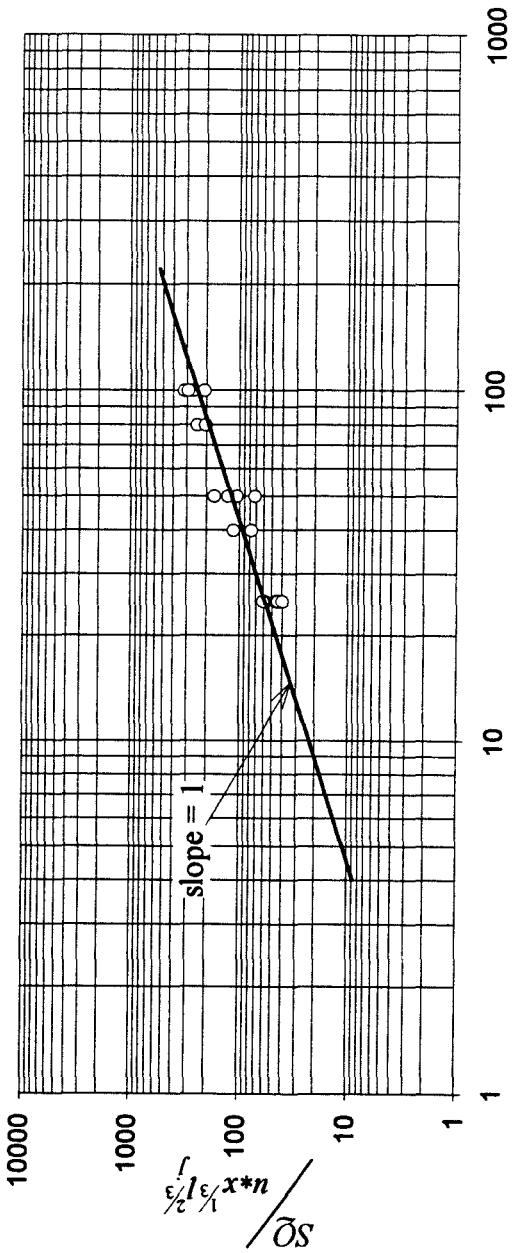

Figure 6.28 Dilution data for elevations below $z_{bld\text{-}hd}$ with experimental z replaced by theoretical

and again the slope of this data on a log-log plot of SQ/u_*h versus x should yield a slope of one. This is shown in Fig. 6.29.

6.4 Non-dimensional presentation of data

The above work suggests that the relevant transition of interest, under the flow conditions particular to this work, is the transition from diffusive mixing where the turbulent diffusion coefficient is based on the local elevation, z to diffusive mixing where the coefficient is based on the overall depth of flow, h. Therefore, now that we know in which regimes the flow exists, it is possible to elucidate this transition by presenting the data in nondimensional form. For this purpose, it is useful to define some nondimensional parameters as shown below.

In the region of flow dominated by mixing as described in Eq. 6.6, we can write that:

$$S_{bld} = \frac{SQ}{u_* zx} = c_{bld} \tag{6.8}$$

similarly, we can write for the region of flow described by Eq. 6.7:

$$S_{dh} = \frac{SQ}{u_* hx} = c_{dh} \tag{6.9}$$

We can, alternatively obtain Eq. 6.9 if we multiply Eq. 6.8 by z/h. Thus:

$$S_{dh} = S_{bld}\frac{z}{h}$$

Therefore, a log-log plot of S_{dh} versus z/h would exhibit a slope of one when S_{bld} tends to a constant (in regions of diffusive mixing based on the elevation, z) and change to a slope of zero when S_{dh} becomes equal to a constant indicating the onset of diffusive mixing based on the overall depth of flow, h. The value of z/h where this change in slope occurs indicates the transition location.

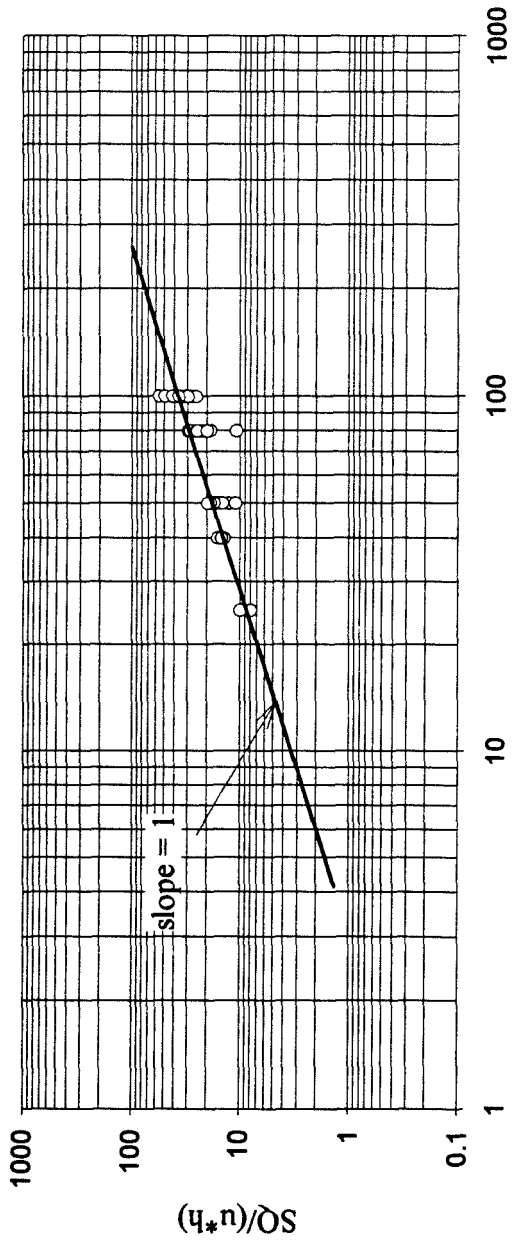

Figure 6.29 Dilution data for elevations above $z_{bld\text{-}hd}$.

Figure 6.30 is a plot of S_{dh} versus z/h where, as we did in Fig. 6.28, we have replaced the experimentally determined value of the elevation with the theoretical value. We can observe from this figure evidence of a slope change from one to zero at an approximate value of $z/h = 0.11$ which is close to the value suggested by the rudimentary data analysis shown above.

Finally, we conclude that over the range of flow parameters and observations in this study, the predominant mixing mechanism is entirely turbulent diffusion. Further, the flow undergoes a transition within the diffusive mixing regime from a region where the diffusion coefficient is proportional to the local elevation, z, *to a region where the diffusion coefficient is proportional to the overall depth of flow,* h. *This transition occurs at an elevation of approximately* z/h = 0.14, *or one half of the boundary layer depth.*

6.5 Checking the magnitude of the dilution

The value of the constant relating the absolute magnitude of the dilution to the other flow parameters need not be treated as an arbitrary constant since it can be determined based on previous work. The equation describing the dilution in the region dominated by diffusive mixing based on the depth of flow was derived in chapter 2 and is repeated below:

$$S = \frac{4\pi Dx}{Q}$$

and we found that the effective diffusion coefficient could be written as:

$$D = 0.082 u_* h$$

Thus, the dilution in this mixing regime could be written as:

$$S = mx \quad \text{where} \quad m = \frac{4\pi(0.082)u_* h}{Q}$$

Figure 6.31 shows a plot of S versus x for an initial volumetric flow rate of 16.7 cm^3/s, an average flow depth of 41.3 cm, and a cross-flow shear velocity of 0.98 cm/s. The slope

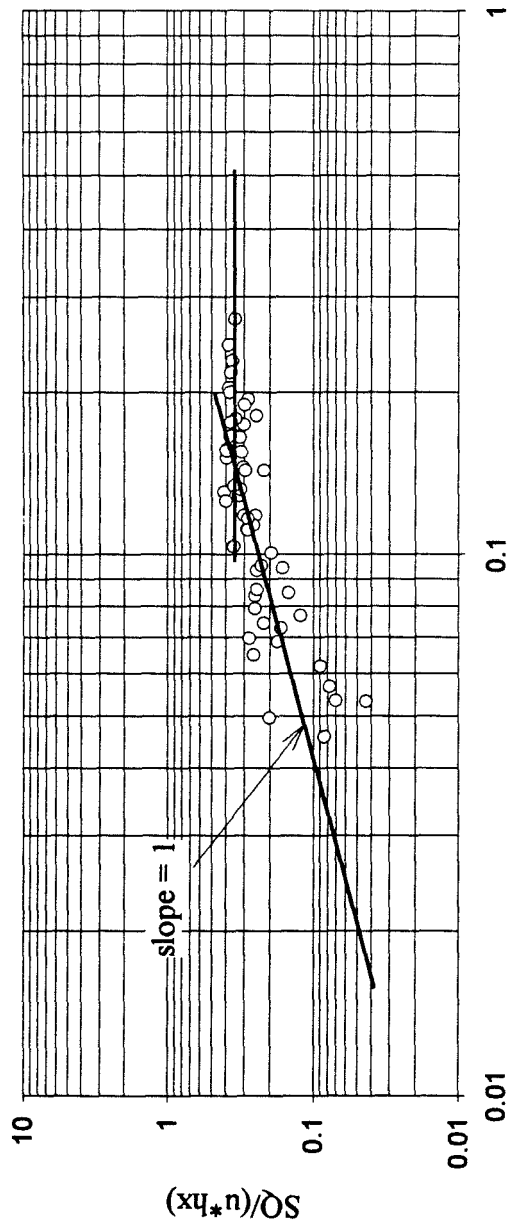

Figure 6.30 Nondimensional presentation of data

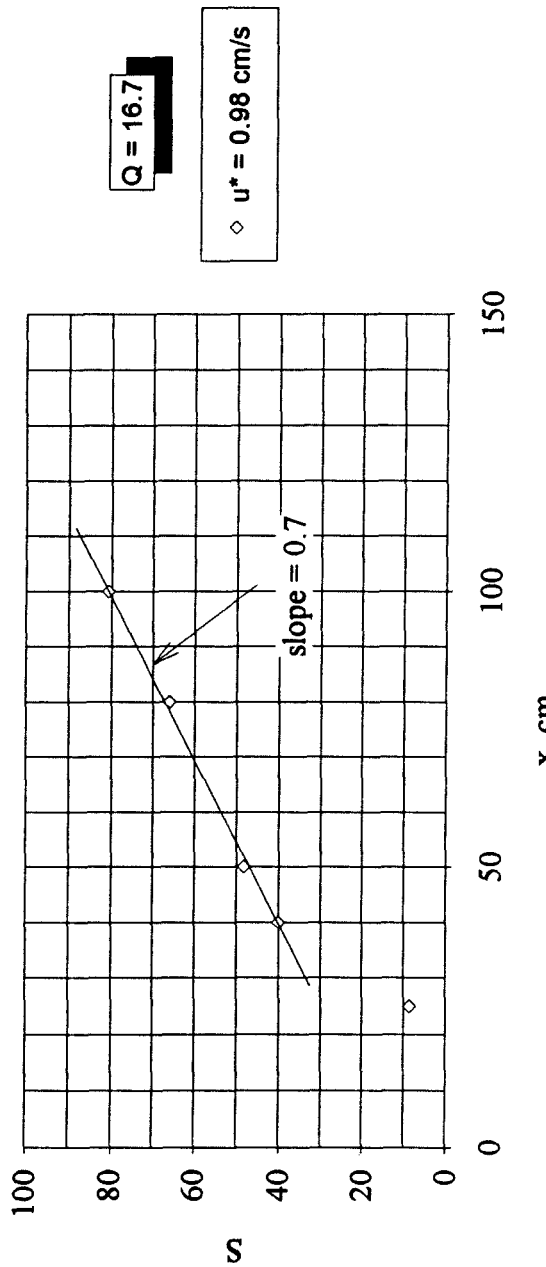

Figure 6.31 Absolute dilution values as a function of horizontal distance from the point of release

calculated from the above equation is equal to 2.5. The data indicates a slope of 0.7 which is substantially less than the predicted value. If, however, we use the boundary layer thickness (or $0.3h$)as the characteristic length scale, then the resulting slope is calculated to be 0.75. In this case, the data demonstrates a slope which is less than 7% different from the theoretical value. Given the reported inaccuracy in the transverse mixing coefficient ($\pm 50\%$, see chapter 2), this is a quite satisfying result.

This result suggests that the boundary layer thickness is the appropriate length scale governing diffusive mixing in the region where the turbulent mixing coefficient is constant.

6.6 The functional behavior of the flow trajectory

The question that remains unresolved is the effect of changing flow parameters on the trajectory of a buoyant jet in this boundary layer cross flow. In chapter 5, we derived trajectories relations for the jet, bent jet, and bent plume regimes of flow for a buoyant jet in a *uniform* cross-flow. As we did above for the dilution, we wish to examine the trajectory data in dimensional form in the hope of identifying the particular regimes of flow. For this purpose, we prepared Table 6.3.

Table 6.3 Summary of elevation z as a function of cross-flow velocity

Regime	Trajectory Equation	Elevation, z as a function of U
jet	$z \propto \frac{x^{1/2} M^{1/4}}{U^{1/2}}$	$z \propto U^{-1/2}$
bent jet	$z \propto \frac{x^{1/3} M^{1/3}}{U^{2/3}}$	$z \propto U^{-2/3}$
bent plume	$z \propto \frac{x^{2/3} B^{1/3}}{U}$	$z \propto U^{-1}$

The data in Fig. 6.26 shows the $z \sim x^{1/3}$ behavior indicative of bent jet flow; however, Fig. 6.32 which shows the effect of varying cross-flow velocity on the elevation z at different x-locations does not show the corresponding $z \sim U^{-2/3}$ relationship indicative of bent jet flow. In fact, Fig. 6.32 shows a complex functional relationship between the elevation and the cross-flow velocity that depends on the distance x from the point of release.

Figures 6.33, 6.34, and 6.35 show the elevation versus cross-flow velocity at various initial volumetric flow rates and x-locations of 100, 50, and 25 cm. These figures imply yet a more complex relationship between the elevation z and the cross-flow velocity U. We do not propose an explanation for this behavior; however, it seems likely that it is related to the fact that the local cross-flow velocity is a function of the elevation itself.

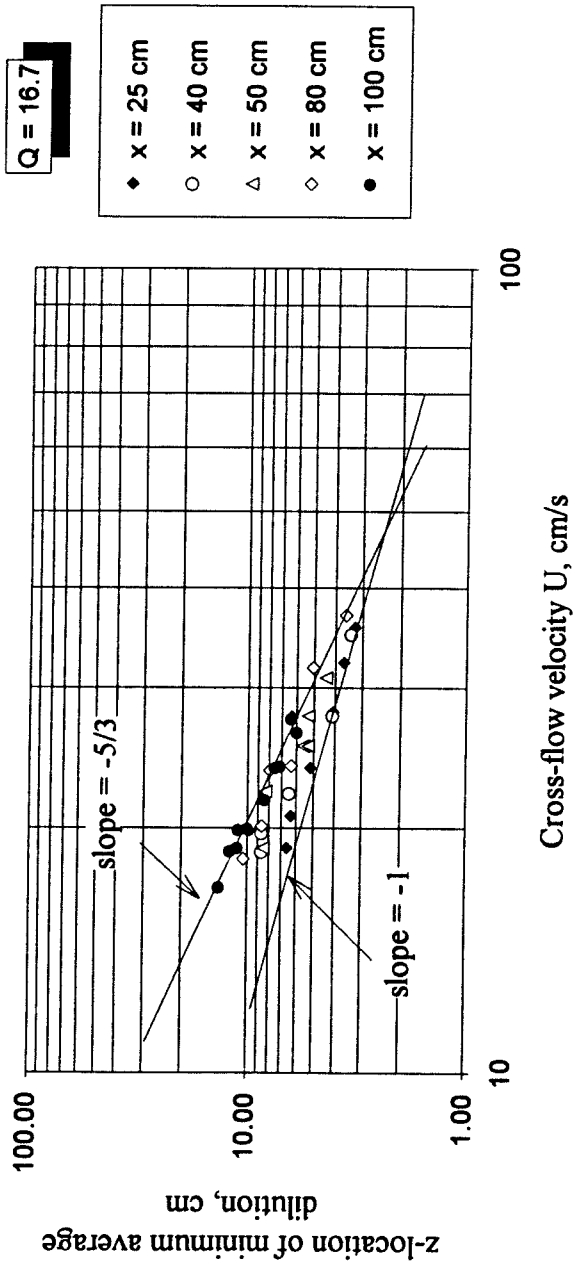

Figure 6.32 Effect of cross-flow velocity on the buoyant jet elevation

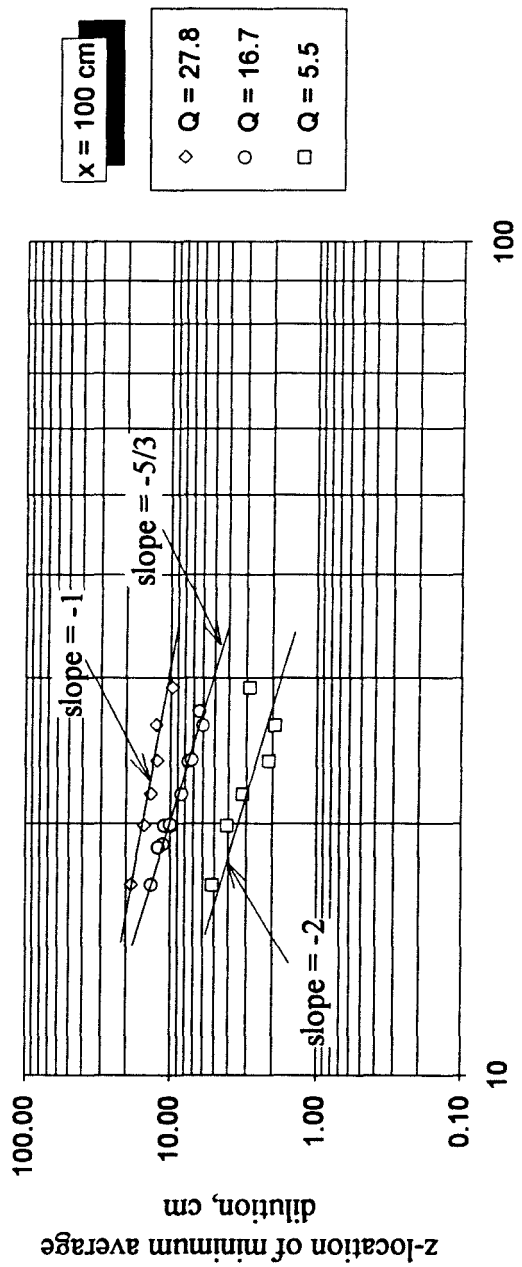

Figure 6.33 Effect of cross-flow velocity on the buoyant jet elevation at x = 100 cm

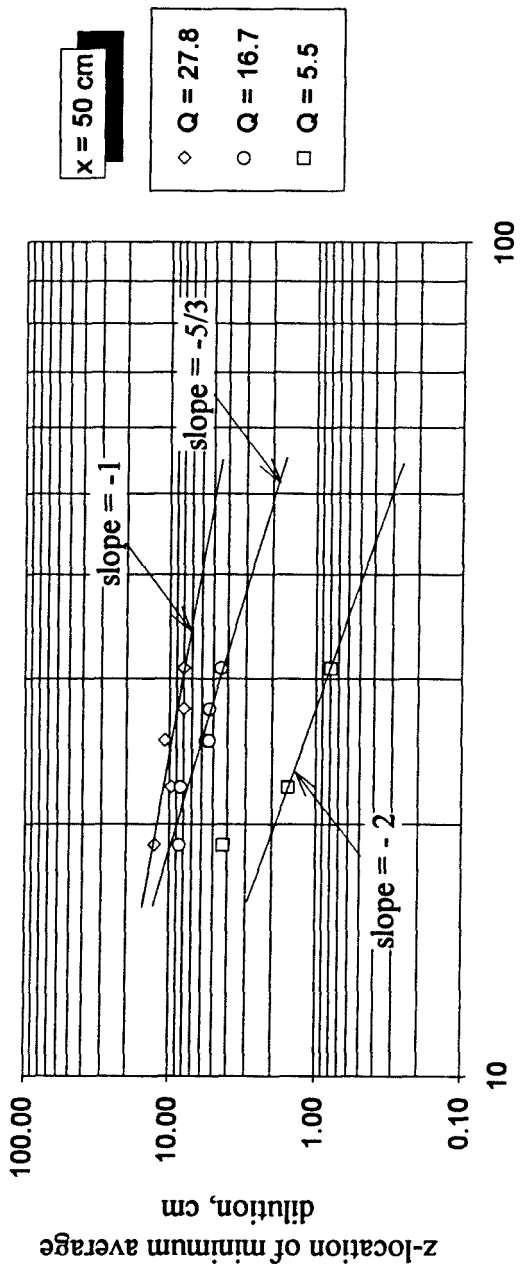

Figure 6.34 Effect of cross-flow velocity on the buoyant jet elevation at $x = 50$ cm

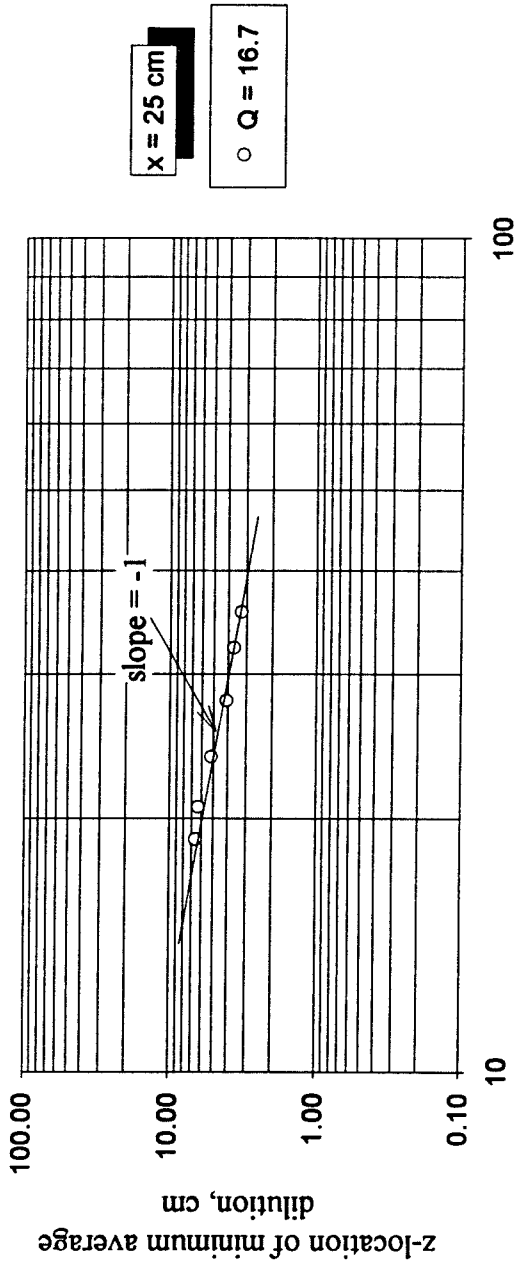

Figure 6.35 Effect of cross-flow velocity on the buoyant jet elevation at $x = 25$ cm

Chapter 7. Summary and Use of Results

The purpose of this study was to determine, using detailed experimental observations of the velocity and concentration fields, the predominant mixing mechanisms for a buoyant jet released into a cross flow with shear. We summarize our conclusions and discuss their usefulness below.

In highly complex flows, we seek to understand the flow behavior by "whittling away" at the problem through the study of simpler problems. In this spirit, we first addressed the transitional behavior of a buoyant jet in a *uniform* cross flow with shear. We discovered that a technique based on the definition of transition as the point of centerline velocity equivalence works reasonably well for predicting the relevant coordinates of transition for this simpler flow. The technique required the determination of leading constants, from previous experimental investigations, and relied on the development of virtual origins for the various asymptotic flow regimes. We presented this technique as a preliminary method for estimating the coordinate of transition as distinguished from the characteristic length scale of transition. This method, however, would require testing over extensive ranges of flow parameter values before we would be

able to use it with any degree of confidence. Nonetheless, it appears that this technique may be useful at least for the purpose of determining, more accurately than characteristic length scale arguments alone permit, the transition locations for a buoyant jet in a uniform cross flow.

In this study, we sought to understand the parameters affecting transition and mixing for the more complex flow of a buoyant jet released into a *cross flow with shear*. We proposed that an initial region of jet/plume dominated mixing would be followed by a region of mixing dominated by turbulent diffusion. Because of the high number of potential transitions in this complex flow, we first examined the data in dimensional form to elucidate the functional relationships between parameters. We found that for the experimental conditions of this study, there was no observable region of mixing dominated by initial jet/plume phenomena. Rather, over the range of horizontal distances in which experiments were conducted, the flow was dominated entirely by shear-flow induced mixing. Thus, we determined that the relevant transition for the experimental conditions of this investigation was from diffusive mixing, where the coefficient of mixing is proportional to the local elevation, z, to diffusive mixing, where the mixing coefficient is constant and proportional to the boundary layer thickness, δ. We found that this transition occurred at an elevation equal to one half of the boundary layer depth. To determine the horizontal location of this transition, the trajectory of the flow must be known.

Finally, through comparisons of the instantaneous relative concentration profiles, the time-averaged profile, and the standard deviation, we found that even well into the diffusive mixing regime, relative concentrations exceeding the average by a factor between two and three occur approximately 10% of the time. This suggests that in situations where peak concentrations are important, discharge regulations should perhaps be stated with peak concentrations in mind.

7.1 Use of experimental results - the design procedure

The ultimate purpose of an investigation such as this, is to provide the environmental engineer tasked with releasing an effluent into a cross flow with shear, guidelines for determining the onset of diffusive mixing. We cannot, from the results of this study, determine the point of *transition* between jet/plume mixing and diffusive mixing since such a transition was never observed. We cannot determine from the results presented here if buoyant jet mixing near the point of discharge exists; however, it seems unlikely that none occurs. Rather, we can only determine, a bound for the onset of diffusive mixing. It may in fact be true that the transition occurs sooner, however, we can not determine how much sooner from the available data.

In this investigation, the onset of diffusive mixing occurred in the region where the *trajectory* of the flow resembled that of a bent jet. If we assume that the bent jet relations are valid even within the boundary layer, we can write the appropriate length scales defining the transitions relevant for this study. There are four characteristic length scales in this case:

- the length scale defining transition between *jet* and *bent jet* behavior.
- the length scale defining transition between *bent jet* mixing and of *diffusive mixing based on the local elevation*.
- the length scale defining transition between *bent jet* mixing and *diffusive mixing based on* δ.
- the length scale defining transition within the diffusive mixing regime from a region where the diffusion coefficient is *based on the local elevation* to a region where the diffusion coefficeint is *based on* δ.

(Note: It is conceivable that for cross-flow velocities that are weak in relation to the initial jet volumetric flux, i.e., for l_j large, the relevant transitions would be between the near-field jet regime and the diffusive regimes. We have not considered this case above

since it complicates the discussion and further, seems unlikely in this experimental investigation, since the value of l_j achieved in these experiments never exceeded 3.7 cm and in most cases was approximately 1 cm.)

Thus, the procedure for determining the regimes of flow is as we discussed in chapter 5 - namely a rank-ordering of characteristic length scales. Table 7.1 shows the relevant transition length scales in the vertical and horizontal dimensions:

Table 7.1 Summary of characteristic length scales in horizontal and vertical dimensions

Transition	***Vertical* characteristic length scale**	***Horizontal* characteristic length scale**
jet - bent jet	$l_{j-bj,z} = l_j$	$l_{j-bj,x} = l_j$
bent jet - diffusion, *z*	$l_{bj-bld,z} = \left(\frac{M}{Uu_*}\right)^{1/2}$	$l_{bj-bld,x} = \left(\frac{MU}{u_*^3}\right)^{1/2}$
bent jet - diffusion, *h*	$l_{bj-hd,z} = \left(\frac{M}{Uu_*h}\right)$	$l_{bj-hd,x} = \left(\frac{M^2}{Uh^3u_*^3}\right)$
diffusion, *z* - diffusion, *h* *(bent jet trajectory)*	$l_{bld-hd,z} = \delta$	$l_{bld-hd,x} = \frac{\delta^3}{l_j^2}$

*Note: In the previous chapter we determined that the appropriate scaling length was the boundary layer thickness. δ represents the boundary layer thickness.

We reason that the order of transition is determined as follows. If $l_{bj\text{-}bld,x} < l_{bld\text{-}hd,x}$, then the transition will be from *bent jet* behavior to *diffusion based on z* to *diffusion based on* δ. We are not interested in the value of $l_{bj\text{-}hd,x}$ in this case, since mixing based on δ is not available until *after* the transition characterized by $l_{bld\text{-}hd,x}$. Thus, if $l_{bj\text{-}bld,x} < l_{bld\text{-}hd,x}$ then the transition from bent jet to diffusive mixing based on δ simply *cannot* occur before the onset of diffusive mixing based on *z*. By contrast, if $l_{bj\text{-}bld,x} > l_{bld\text{-}hd,x}$ then the relevant transition from bent jet mixing would be to diffusive mixing based on δ which is, of course, determined by the characteristic length scale, $l_{bj\text{-}hd,x}$.

In what follows, we demonstrate this method of determining the order of transition from the characteristic length scales. Further, since we are interested in the *coordinate* of transition, we show how the experimental data can be utilized to obtain bounds on the leading coefficients.

7.2 Predicting the order of transition and determining the leading constants

Consider as an example the flow depicted in Fig. 6.25*c*. For this flow, we calculate the relevant characteristic length scales to be as follows:

Characteristic length scale	Value, cm
$l_{bj\text{-}bld,x}$	46.6
$l_{bld\text{-}hd,x}$	7115
$l_{bj\text{-}hd,x}$	0.30

These values suggest that the flow will transition from bent jet to diffusion based on the local elevation, z, since diffusion based on the boundary layer thickness is not available until 71 meters from the point of release. Under these conditions, we would expect therefore, to observe a flow that is initially in the bent jet regime and then in the boundary layer diffusion regime. In Fig. 6.25*c* we observe only boundary layer diffusion regime over the entire range of experiments. The flow does not exhibit bent jet behavior in the range of x-values considered. Therefore, we may use this result to obtain a bound on the *coordinate* of the horizontal transition between the bent jet to boundary layer diffusion regimes: we can ascertain a rough estimate of the characteristic length scale fraction at which transition must have *already* occurred. (Keep in mind that the transition may, in fact, have occurred sooner, we are simply not able to determine from the available experimental data, how much sooner.) We repeat a similar procedure for other data sets to find:

$$x_{bj-bld} \leq 0.15\left(\frac{MU}{u_*^3}\right)^{1/2} \tag{7.1}$$

Similarly we can determine an upper bound on the transition from bent jet to diffusion based on the boundary layer thickness. For the data shown in Fig. 6.25*a*, we find that:

Characteristic length scale	Value, cm
$l_{bj\text{-}bld,x}$	233
$l_{bld\text{-}hd,x}$	283
$l_{bj\text{-}hd,x}$	192

where here $l_{bj\text{-}bld,x}$ and $l_{bld\text{-}hd,x}$ are close in magnitude. Therefore, we reason that diffusion based on δ is possible and that, in this case, the appropriate transition will be from bent jet to diffusion based on δ. Figure 6.25*a* shows that the flow exhibits the behavior of diffusion based on δ as early as 25 cm from the source release point. As above, we can use this result to obtain an upper bound on the leading coefficient defining this transition. This procedure yields:

$$x_{bj-hd} \leq 0.13\left(\frac{M^2}{Uh^3u_*^3}\right) \tag{7.2}$$

Finally, the x-coordinate of the transition from diffusion based on z to diffusion based on δ, can be analogously determined from the comparison of characteristic length scales and experimental data to obtain:

$$x_{bld-hd} = (0.06)\left(\frac{\delta^3}{l_j^2}\right) \tag{7.3}$$

7.3 Use of the results for design

If we consider, as an example, the experimental results presented in Fig. 6.24*b*, we calculate using the experimental parameters below (which are average values over all the experiments depicted in Fig. 6.24*b*):

Q, cm^3/s	16.7
M, cm^4/s^2	1414.8
U, cm/s	23.9
u^*, cm/s	1.2
h, cm	41.3

the following values of the characteristic length scales:

Characteristic length scale	Value, cm
$l_{bj\text{-}bld,x}$	140
$l_{bld\text{-}hd,x}$	789
$l_{bj\text{-}hd,x}$	24.8

This implies that the flow will first undergo transition from bent jet to boundary layer diffusion and then to diffusion based on δ. Further, if we calculate, using the above coordinate estimates, the coordinates of those transitions are estimated to be:

Coordinate of transition	Value, cm
$x_{bj\text{-}bld}$	21
$x_{bld\text{-}hd}$	47

As predicted above, we observe no bent jet behavior past 25 cm in Fig. 6.24*b*. Further, the onset of diffusive mixing based on δ occurs at a value roughly between 40 and 50 cm which further confirms the above approximations.

7.4 The bottom line - using the results to determine dilutions

As we discussed earlier, what we actually desire as engineers, is knowledge about the dilution. Therefore, we next examine how the results of this study affect how dilutions are calculated.

As an example consider the experiment discussed above where the flow parameters are repeated here for convenience:

Q, cm^3/s	16.7
M, cm^4/s^2	1414.8
U, cm/s	23.9
u^*, cm/s	1.2
h, cm	41.3

We can easily show (using the results in Table 5.9, of chapter 5) that this flow will transition from jet to bent jet behavior at an $x_{j\text{-}bj} = 0.6$ cm, and further that the transition from bent jet to bent plume behavior occurs at an $x_{bj\text{-}bp} = 241$ cm. Therefore, the buoyant jet exhibits bent-jet behavior almost exclusively between $x = 0$ and $x = 100$ cm.

Prior to the results of this investigation, the dilution would thus have been calculated from the equation for a bent jet. As was shown above, however, the dilution should actually follow the bent jet equation only up to an $x_{bj\text{-}bld} = 21$ cm. The dilution would then be as described by the diffusion regime equation where the diffusion coefficient is proportional to the local elevation, z. This would be valid until the transition from diffusion based on z to diffusion based on δ, which occurs at an $x_{bld\text{-}hd} = 47$ cm.

We can determine the dilutions from the following equations:

Regime	Dilution equation
bent jet	$S = 2.1\frac{x^{2/3}M^{2/3}}{QU^{1/3}}$
diffusion, z - bent jet	$S = 2.4\frac{u_* x^{4/3}M^{1/3}}{QU^{2/3}}$
diffusion, h	$S = 12.9\frac{u_* x}{Q}$

Figure 7.1 shows a comparison between the dilution as calculated from the bent jet equation alone, and the dilution as calculated including diffusive-type mixing. In Fig. 7.1 we show two cases. First, we assume that mixing up until $x_{bj\text{-}bld}$ is dominated by bent jet flow although we have not explicitly demonstrated this behavior. Second, we assume that that the flow is dominated by diffusive mixing immediately after release with no bent jet mixing whatsoever. The experimental data plotted on Fig. 7.1 suggest that the transition occurs somewhere between these two cases.

From these figures, we can conclude that the magnitude of the dilution at 100 cm under these flow conditions is not strongly a function of which method we choose to utilize. In either case, the maximum deviation of the computed dilution from the actual value is less than 20%. However, under different flow conditions, the difference between the methods might be greater.

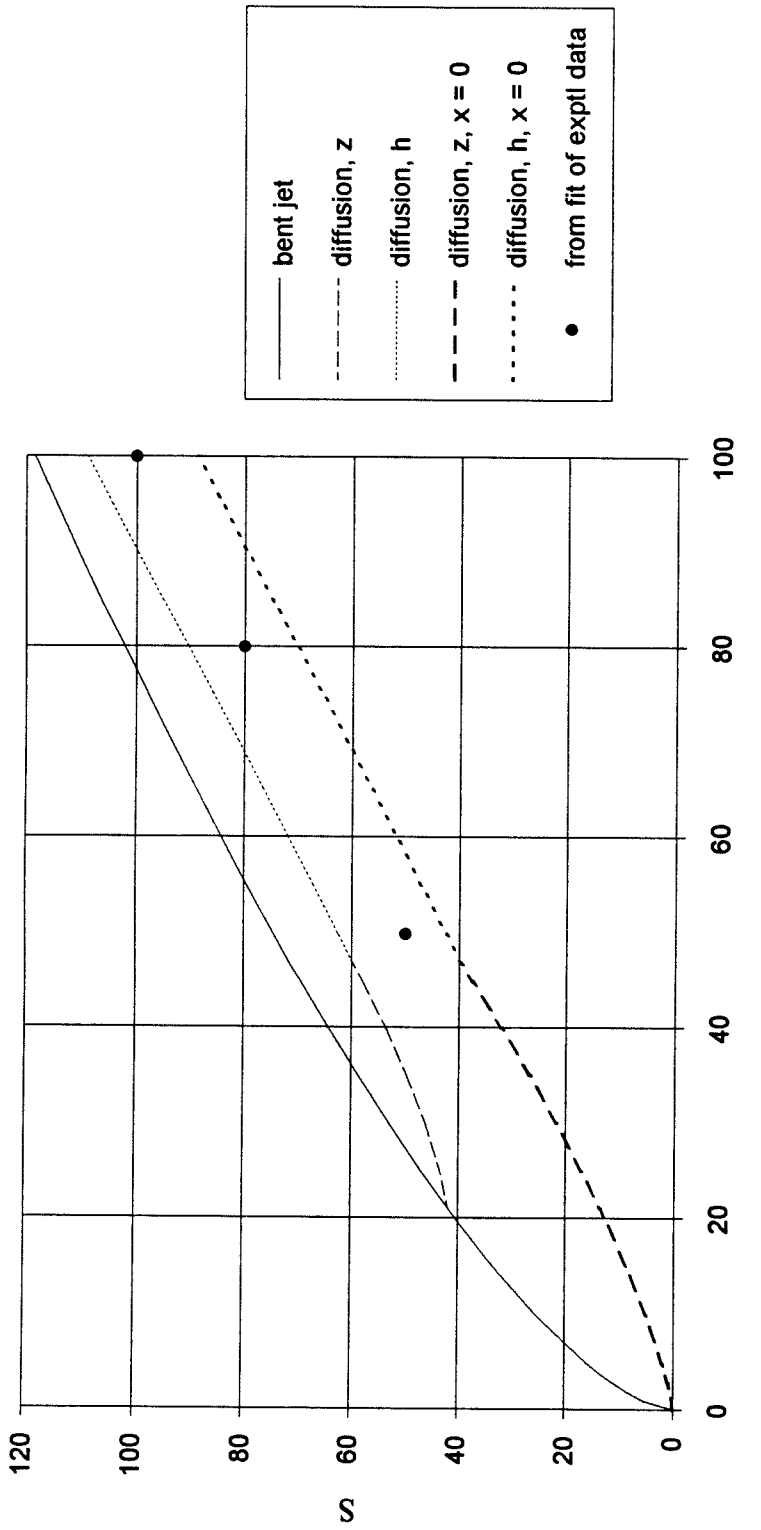

Figure 7.1 Comparison of dilution prediction methods

7.5 Conclusion

In this investigation, we demonstrated that the long-held regulatory practice of utilizing jet or plume mixing equations, and neglecting the effects of turbulent diffusive mixing, to predict dilutions near the point of release is ill-founded. The experimental evidence of this study indicates that, over the range of experimental parameters tested, turbulent diffusive mixing dominates the flow even near the point of release. Further, within the diffusive mixing regime, we observed a transition from a region of mixing where the turbulent diffusion coefficient was proportional to the local elevation, to a region of mixing where the turbulent diffusion coefficient was constant and proportional to the boundary layer depth.

7.6 Limitations of the experimental conclusions and recommendations for future work

It is worthy of mention that the conclusions reached above with regard to the dominant mixing mechanism may not be universal. For the experiments relevant to this investigation, the requirement that the indices of refraction of the release and ambient fluids match, limits the potential density difference achievable in the experiments. For this

reason, all of the flows in this study are "weakly" buoyant. We cannot therefore conclude that in flow situations where buoyancy-generated momentum dominates the flow closer to the point of release, the same conclusions would be valid. Experiments substantially past the transition from bent jet to bent plume behavior are required to determine the nature of the flow under such circumstances.

We suggest such a caveat based on the fact that a bent plume is a stronger function of the horizontal distance from the point of release than is a bent jet and hence may be more able to delay the onset of diffusive mixing. In other words, for a bent jet, the *rate* of dilution *decreases* with horizontal distance in a buoyancy driven flow:

$$\left.\frac{\partial S}{\partial x}\right|_{bj} \propto \frac{x^{-1/3} M^{2/3}}{U^{1/3} Q}$$

whereas for a bent plume, the *rate* of dilution *increases* with horizontal distance:

$$\left.\frac{\partial S}{\partial x}\right|_{bp} \propto \frac{x^{1/3} B^{2/3}}{UQ}$$

Thus, in the case of bent plume mixing, even if the flow has transitioned into the diffusive mixing regime where the mixing coefficient is based on the overall depth of flow, it is conceivable that when the effects of buoyancy become significant, the flow would experience yet another transition to bent plume mixing. This point amounts to a questioning of the definition of transition since it suggests that perhaps it is the rate of dilution that is important in determining transition. This point warrants further investigation.

Additionally, we mentioned above that for the case where the cross flow is weak in relation to the buoyant jet initial momentum flux, the characteristic length scales describing transition would be different from those relevant to the present study. We might use the same length scale arguments to estimate the order of transition, however

experiments would be required to confirm the transitional behavior of a near-field jet in a cross flow with shear.

However, with regard to more fully understanding the nature of a buoyant jet in a cross flow with shear, experiments conducted over the *entire* range of flow regimes are needed. Namely, it would be useful to conduct experiments closer to the point of discharge to determine if buoyant jet mixing ever dominates the flow, and if so, for how long.

Lastly, the scatter in the data shown in Fig. 6.30 is believed to be the result of the inherent sensitivity of the LIF calibration procedure. In particular, we suggest that a system for more reliably determining the source fluid dye concentration (or εC_o) would greatly enhance the technique.

Appendices

Appendix A. Ramp Design

The program shown below was used to design the fitted cubic spline ramp for the flume.

The final design is shown in Figure A.1.

This program was used for the design of the ramp contour

```
c
c
c       This program determines the contour of a cubically matched nozzle
c       of length L, inflection point xm at half L, inlet radius ri, exit re.
c
c       The contour is Rx
c
c
        Real Ri,Re,De,L,x
        Ri=5.0
        Re=0.0
        De=2.0*Re
        Di=2.0*Ri
        L=72.0
        xstep=L/24.0
        x=0.0
        do 100 i=1,24
        x=x+xstep
        Rx=Di/2.0 - 3.0*(Di-De)*x**2.0/(2.0*L**2.0) + (Di-De)*x**3.0/L**3.0
        write(10,1000)x,Rx
1000    format(1x,2(f6.2,2x))
100     continue
        end
```

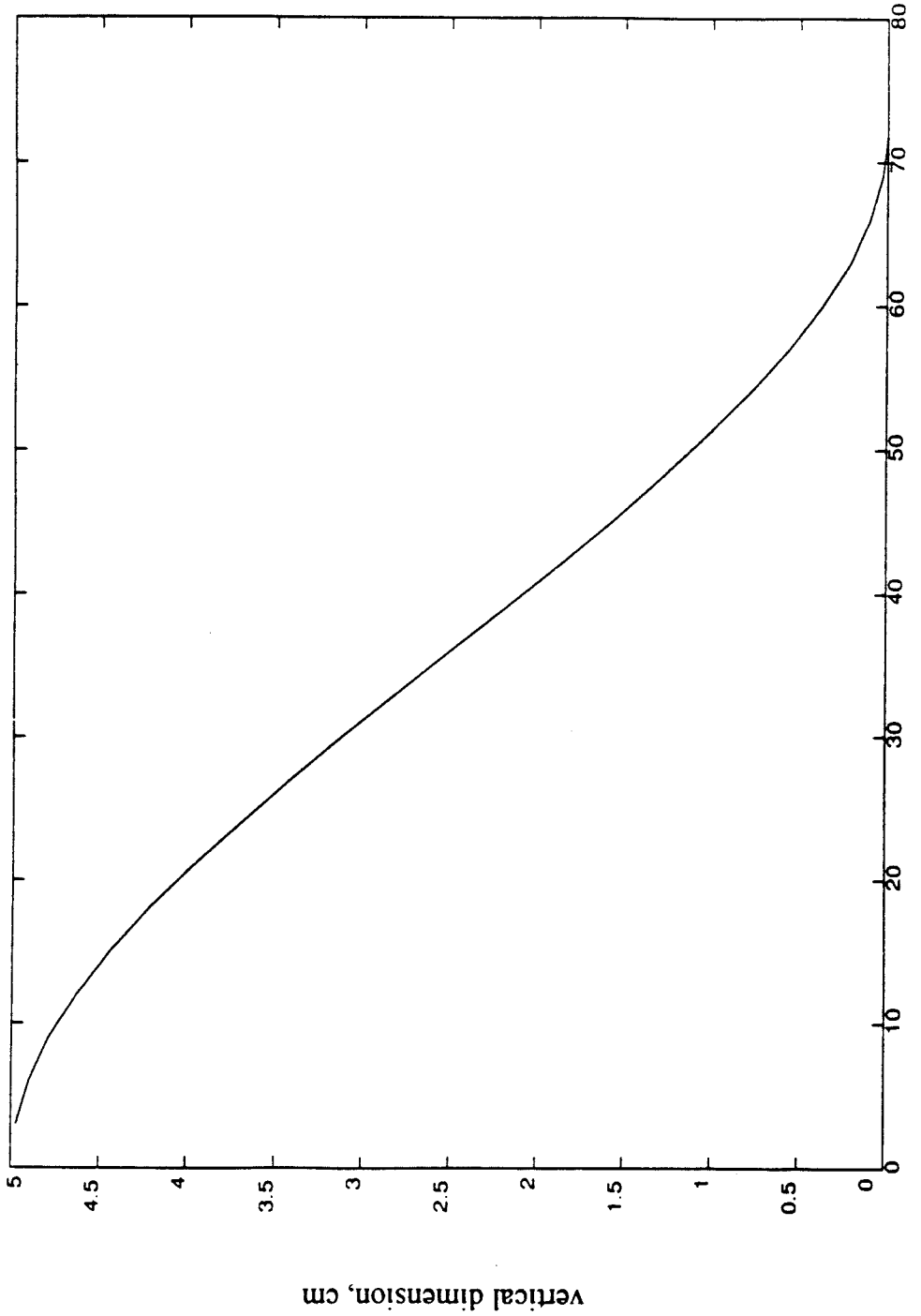

Figure A.1 Ramp final design

Appendix B. Flow meter calibration

The following is the calibration data for the buoyant jet flow meter used in this study. A large box (13,630 ml) was placed to catch the output of the flow through the flow meter. The flow was stopped after a time, t, recorded using a stop watch, and the volume, V, was measured using a 1000 ml graduated cylinder. The volumetric flow rate is then calculated as:

$$Q = \frac{V}{t}$$

The calibration was done in situ.

Percent reading on flowmeter, x_{fm}	Volumetric flow rate = V/t (ml/min)	Time for collection t (min)
0.0	0.0	0.0
30.0	959.5	14.2046
66.5	2160.6	6.3084
89.0	3024.0	4.5073

This results in a linear relationship (correlation coefficient = 1.00) between the flow rate Q, and the flow meter reading, x_{fm}:

$$Q = -0.5727 + 33.3534 \cdot x_{fm}$$

where Q is measured in ml/min and x_{fm} is measured in percent of flow meter capacity. (Note: the zero point was padded with extra data points in order to reduce the constant in the above equation. Because of the inherent experimental error associated with this technique, the unpadded calibration curve puts the zero flow condition at about a 1% reading of the flow meter.)

Appendix C. Investigation of Flume Salt Mixing Rates using Conductivity Probe

A conductivity probe was used to obtain a correlation between salinity and output voltage. First, the probe was calibrated for unsalinated laboratory water and three different saline solutions, as detailed in Table C.1.

Table C.1 Solutions for conductivity probe calibration

	density, kg/m^3	index of refraction
Lab Water, W	0.9943	1.3330
Solution A	0.9954	1.3337
Solution B	0.9968	1.3343
Solution C	1.0001	1.3351

The output voltage of the probe (obtained using the data acquisition system described in section 3.2.1 with an amplification of 10) was sampled continuously at 140 Hz for the probe in lab water, in each of the saline solutions, and in lab water again. As Figure C.1 shows the results of this test. This figure indicates that the probe has a virtually instantantaneous response at a sampling frequency of 140 Hz. Further, the output voltage is linear with the salinity.

The probe was subsequently installed in the flume along the centerline at a location approximately 5 m from the upstream (south) hopper of the flume. Both the 30 hp pump and the 10 hp pumps operating at 30% were used to mix 27 kg of salt added at the downstream (north) hopper of the flume. The output voltage of the conductivity probe was then recorded at various times after salt addition. It was observed that the output voltage reaches an equilibrium value in approximately 10 minutes for a salt addition of 27 kg. Of course, the amount of time required for mixing depends on the total amount of salt added. Figure C.2 shows the output voltage with time for salt additions of 27 kg and 55 kg. It was noted that visible index of refraction variations were gone at roughly the same time that the conductivity probe voltage stabilized. Therefore, it was concluded that 30 minutes of mixing past the point of observable optical homogeneity was sufficient for the salt to be well mixed.

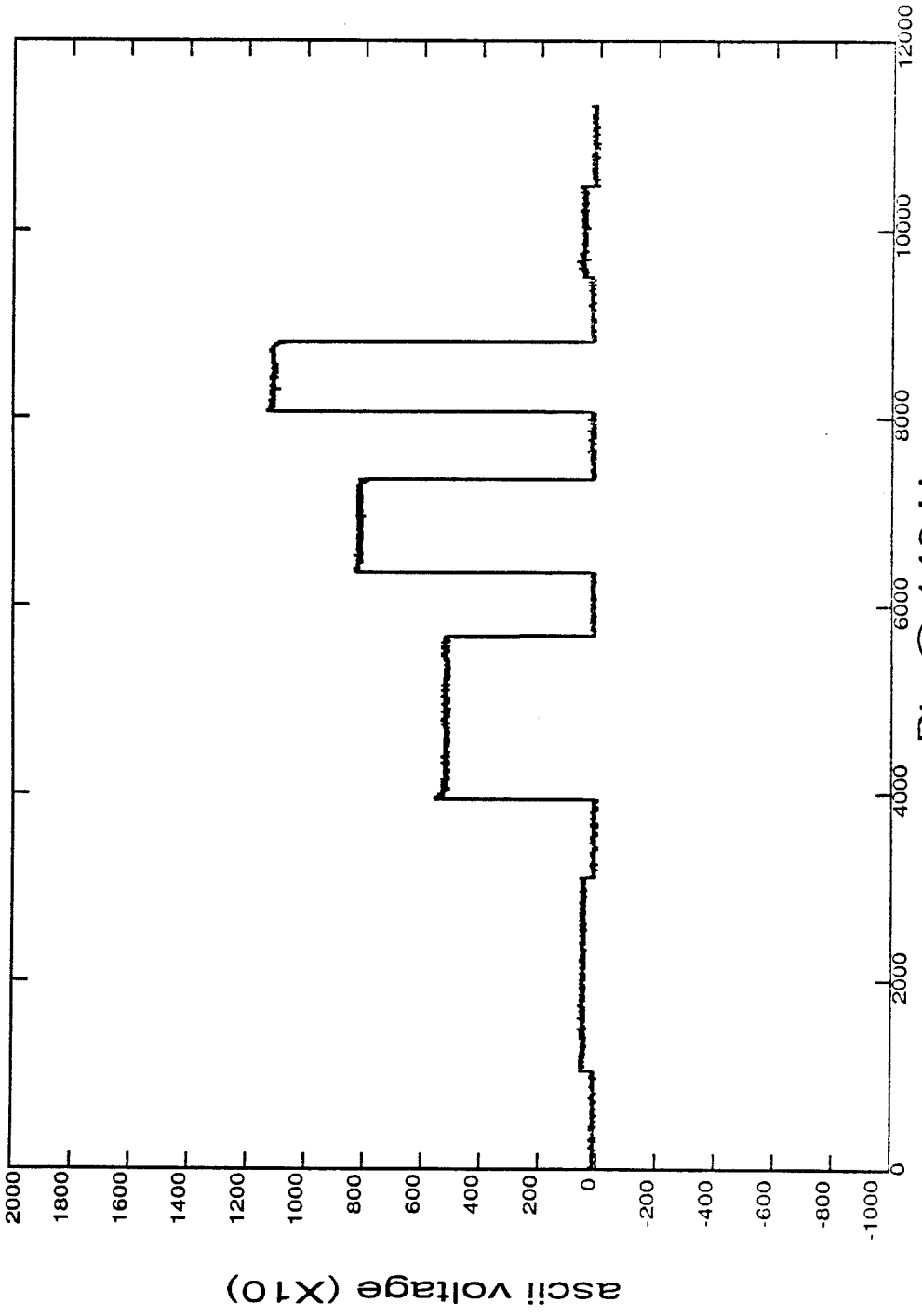

Figure C.1 Calibration of conductivity probe for salinity tests

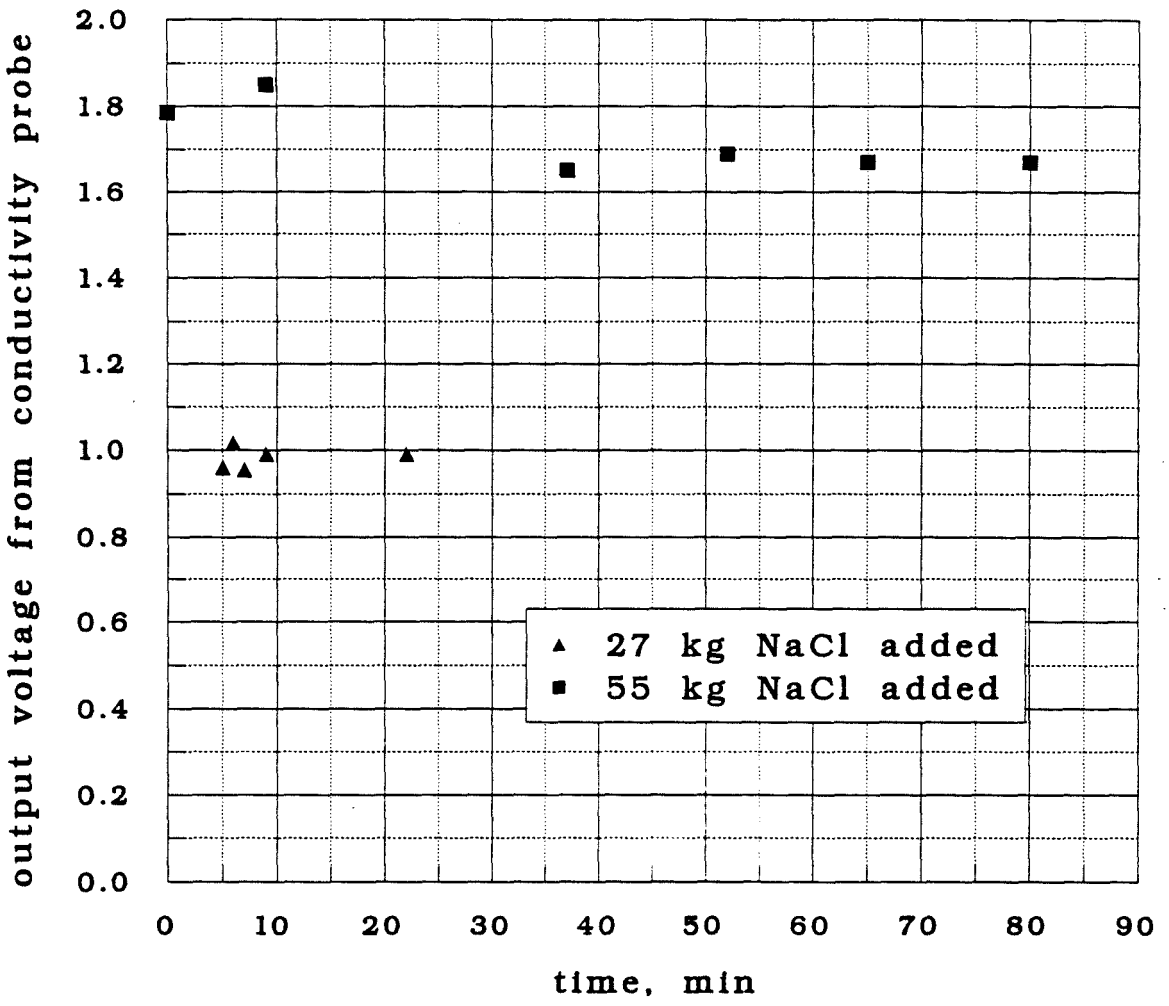

Figure C.2 Investigation of salt mixing in flume using conductivity probe

Appendix D. Effect of temperature on the index of refraction of an ethanol-water mixture

Early in this experimental investigation, concern was registered regarding the corrosive effects of salt-water on the precision-tilting flume. Therefore, a series of experiments were conducted to investigate the option of creating a density difference by heating the water, which decreases the index of refraction (see Weast), and compensating for the decrease by adding ethanol to the heated water. The heated water was placed in a wedge-shaped container and the exit angle-change was measured as a function of temperature and mole fraction of alcohol, mf_a. Figure D.1 shows the experimental configuration. This technique is necessitated because the refractometer is temperature-compensating and as such, is not capable of measuring the effect of temperature.

From this figure, the index of refraction is determined as:

$$n_1 \sin\alpha_1 = n_2 \sin\alpha_2$$

$$n_1 = \frac{n_2 \sin\alpha_2}{\sin\alpha_1} = \frac{\sin\alpha_2}{\sin\alpha_1}$$

since n_2 is the index of refraction of air and thus is unity. The $\sin\alpha_2$ is determined by the ratio of d/x as shown in Figure D.1. The temperature and ethanol-mole fraction dependence on d are thus found to be:

$$d = (9.62 - 0.53 \cdot T) + 195.4 \cdot mf_a$$

for a distance x of 27 m. Thus, for two mixtures with no ethanol, the distance d at T = 20°C is -0.98 cm and at 25°C is -3.63cm. Thus:

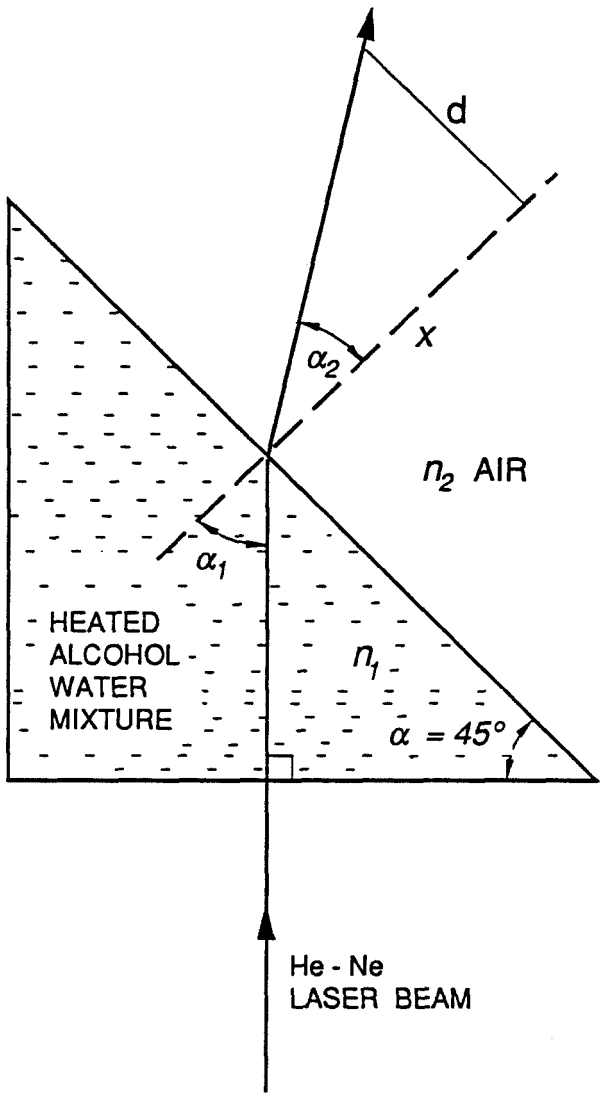

Figure D.1 Geometry of temperature effect on index of refraction of ethanol-water mixture

$$\sin\alpha_2\big|_{T=20°C} = \frac{d\big|_{T=20°C}}{2700\text{ cm}} = \frac{-0.98}{2700} = -0.00036$$

$$n_1 = \frac{\sin\alpha_2\big|_{T=20°C}}{\sin\alpha_1} = \frac{\sin\alpha_2\big|_{T=20°C}}{\sin 45°}$$

$$= \frac{-0.00036}{0.7071} = -0.000509$$

These experiments were conducted such that for $n = 1.3330$, the index of refraction of pure water at $T = 18°C$; $d = 0$. Thus, n_1, as calculated above is the change from 1.3330 induced by temperature. (This only works because the angles are small and hence sin α is approximately α.) Finally, this means that $T = 20°C$ is 1.3330-0.000509 = 1.3326. Similarly, at $T = 25°C$, n_1 = 1.3330-0.001344 = 1.3343. This amounts to an error of 0.1% for a temperature difference of 5°C. This data suggests a larger error than the temperature dependence data of Weast (1967) suggests. According to Weast, the error over this temperature range would be more like 0.05%.

The concept of using heat and alcohol to obtain an optically homogeneous fluids of differing densities was abandoned since mixing changes the temperature of the fluid continually and hence the index of refraction varies continuously. This is clearly unacceptable in a flow where there are many interfaces. It would perhaps be much more attractive in a flow such as that observed by Gartrell (1979). In fact, Gartrell was able to obtain LDV measurements with a tolerable level of signal dropout even using temperature to adjust the relative density of the two fluids under study. It is noted, however, that it is not possible using the LIF technique to distinguish signal dropout that is an artifact of the index of refraction variation from a zero signal caused by flow variations.

Appendix E. LDV Calibration results

The results of a typical LDV calibration procedure are shown below in Table E.1.

Table E.1 LDV calibration results

Channel A		Channel B	
frequency, f (kHz)	Voltage, V	frequency, f (kHz)	Voltage, V
599.49	2.998050	601.88	2.758790
549.47	1.572270	554.64	1.586910
526.10	0.817871	526.34	0.786133
502.91	0.002441	504.52	0.112305
476.19	-1.032710	473.37	-0.964355
449.57	-2.185060	449.15	-1.904300
400.17	-4.736330	406.24	-3.847660

The coefficients for this data along with the correlation coefficient of the fit to $V = A+B/f$ appears below:

Channel A:

A	18.500668
B	-9300.113630
r	-0.9999

Channel B:

A	16.468808
B	-8252.924016
r	-1.0000

Appendix F. LDV geometry and coordinate transformation

As was shown in Fig. 3.13, the geometry of the LDV system was fixed for all experiments. For the system used here, taking into account the index of refraction changes between the glass walls of the flume and the water of the flume, and utilizing the distances given in Fig. 3.13 and other physical experimental measurements (i.e. glass wall width and flume width), we can determine the angle each reference beam makes with the scattering beam. Then, using the theory developed in chapter 3, we find for each of the coordinate directions, the relationship between the frequency shift and the velocity:

$$\Delta f = \frac{2n}{\lambda_s}(u\cos\alpha)\sin\alpha_{r-s}$$

where $\alpha_{r\text{-}s}$ refers to the angle of the reference beam to the scattering beam. Then, for $u\cos\alpha \sim u$, we find (Petroff(1990)):

Direction*	$\alpha_{r\text{-}s}$	$\Delta f/u$
1	3.04°	1117.54
2	3.09°	1135.91
3	3.015°	1108.35
4	2.995°	1101

*Note: These numbers refer to the directions shown in Fig. 3.13.

The coordinate system for LDV measurements is different than the *x-z* coordinate system used for the buoyant jet reference system. Therefore, the LDV measurement coordinate frame must be rotated. Since the measurement system is not orthogonal, it is not possible to perform a simple rigid rotation to obtain the buoyant jet reference coordinate system. However, the fact that the original system is not orthogonal introduces some error if it is rotated to an orthogonal system without taking into account the overlap in measurement caused by nonorthogonality. It was determined that this error exceeds the error in measurement associated with utilizing the original coordinate system as if it were

orthogonal and rotating it rigidly. Therefore an angle of rotation of 45° was used as the average angle necessary for rotation, as can be determined from the coordinates shown in Fig. 3.13. Thus, the velocity in the *x-z* coordinate frame of the buoyant jet is found from the following transformation, where we have rotated only the 3-4 pair of velocities pertinent to the downward-looking mode of the LDV:

$$\begin{bmatrix} u \\ w \end{bmatrix} = \begin{bmatrix} -\cos 45^\circ & \cos 45^\circ \\ -\cos 45^\circ & -\cos 45^\circ \end{bmatrix} \begin{bmatrix} u_3 \\ u_4 \end{bmatrix}$$

Appendix G. Attenuation parameter

The attenuation parameter is defined by the following equation:

$$I_e = I_o e^{-\varepsilon C \xi}$$

where ε is the attenuation parameter, I_O is the incident laser beam power, I_e is the exit laser beam power, C is the concentration of dye in the fluid, and ξ is the distance over which the laser beam attenuates, in this case the vessel is 29.6 cm long. This is shown schematically in Fig G.1. Upon rearrangement, we have the following result:

$$\varepsilon C = -\frac{1}{\xi} ln\left(\frac{I_e}{I_o}\right)$$

Experiments were conducted wherein the concentration of Rhodamine 6-G in the fluid was known, and the incident and exit laser beam powers were measured using a power meter. (Newport, Digital Power Meter, 815 Series with 883-SL Filter) Specifically, a 1 x 10^{-3} M (g/mol) solution of Rhodamine 6-G and water was made. Then, small amounts of this solution were injected using a pipette accurate to 0.002 ml into a vessel with a known volume of water. The vessel used in this determination of the attenuation parameter was the same vessel used for calibration of all LIF experiments. To minimize the effect of attenuation by the Lucite on the top and on the bottom of the vessel, 1/8 in. Lucite was used for these surfaces. Table G.1 shows the results of these experiments.

Next, a plot of εC versus C was produced and a second-degree polynomial fit was made. The plot along with the polynomial fit is shown in Fig. G.2. The higher-order fit is necessary since over the range of concentrations observed in this experimental investigation, the attenuation parameter is not linear. This results in part from the high dilution rates observed in the experiments. The relationship is as follows:

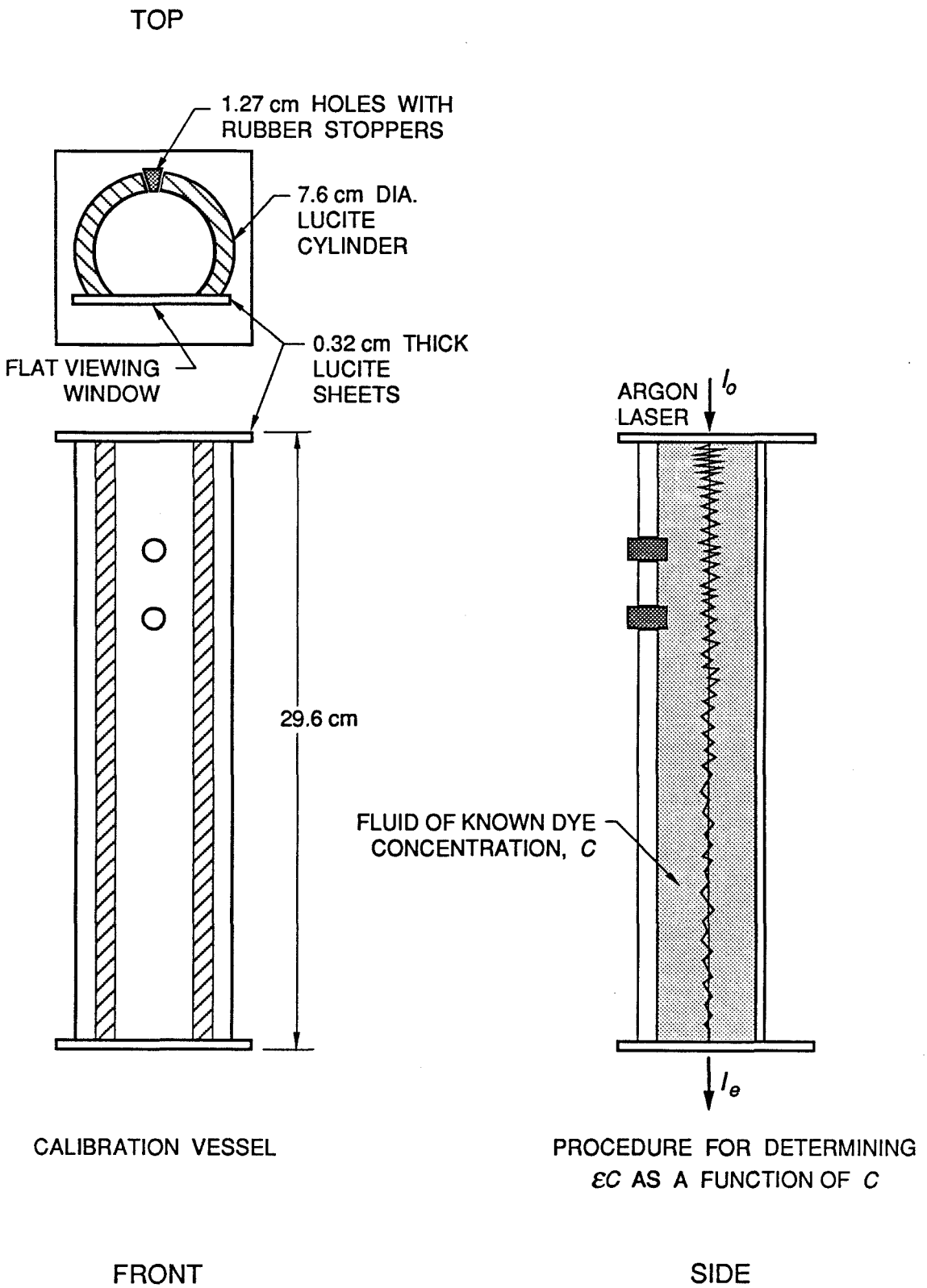

Figure G.1 Configuration for experimental determination of attenuation parameter

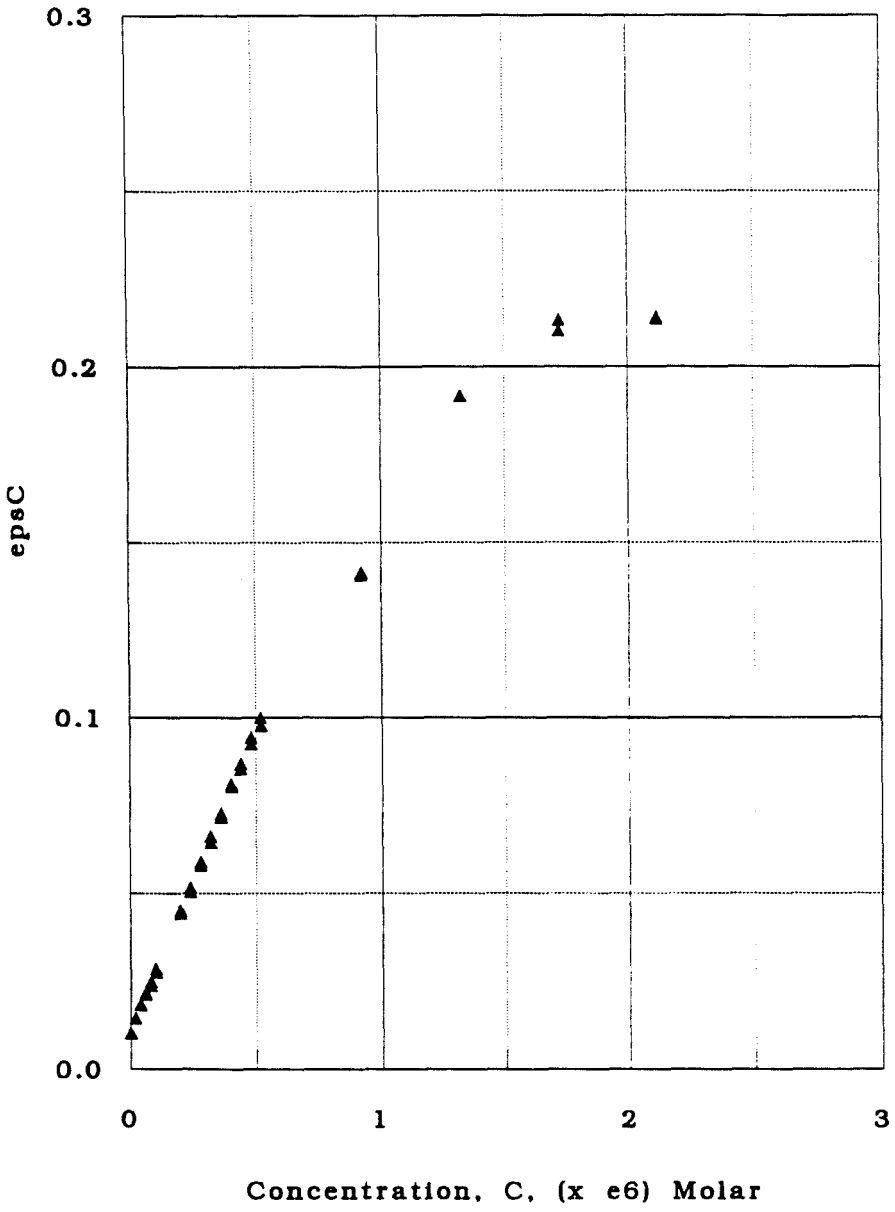

Figure G.2 Attenuation parameter as function of dye concentration for Rhodamine 6G

$$\varepsilon C = 9.4198\times10^{-3} + 0.19298\cdot C - (4.4853\times10^{-2})C^2$$

$$0 = C^2 - 4.3025\cdot C + \left(\frac{\varepsilon C}{4.4853\times10^{-2}}\right) - 2.10015$$

where C is in M x 10^6 and εC is in (M/cm) x 10^6 as indicated in the above table. If we then use the quadratic equation, we find:

$$C = \frac{4.3025 \pm \sqrt{(4.3025)^2 - 4\left(\frac{\varepsilon C}{4.4853\times10^{-2}} - 0.210015\right)}}{2}$$

The negative sign is always used so as to obtain the left-side of the parabolic fit. For concentrations exceeding 1.72 x 10^{-6} M, the equation for the tangent of this curve at 1.72 x 10^{-6} M is used.

$$\left[\frac{d(\varepsilon C)}{dC}\right]_{C=1.72} = 0.19298 - 2(4.4853\times10^{-2})C = 0.03869$$

Therefore,

$$\varepsilon C = 0.03869C + 0.142113$$

In summary,

For C ≤ 1.72 x 10^{-6} M:

$$\varepsilon C = 9.4198\times10^{-3} + 0.19298\cdot C - (4.4853\times10^{-2})C^2$$

For C > 1.72 x 10^{-6} M:

$$\varepsilon C = 0.03869\cdot C + 0.142113$$

While this second equation may not be accurate at large concentrations, it is difficult to obtain experimental data for high concentrations since the laser beam is attenuated rapidly and the exit laser intensity is hence not detectable.

Table G.1 Experimental Results for Attenuation Parameter Determination

C (M) x10^6	I_o (mW)	$I_{e,1}$ (mW)	$I_{e,2}$ (mW)	$\varepsilon C_{,1}$ (M/cm) x 10^6	$\varepsilon C_{,2}$ (M/cm) x 10^6
0.00	58.0	43.0	42.7	0.0101	0.0103
0.02	57.8	37.6	42.7	0.0145	0.0145
0.04	58.1	33.8	33.7	0.0183	0.0184
0.06	58.1	30.9	30.4	0.0213	0.0219
0.08	57.0	27.2	28.1	0.0250	0.0239
0.10	57.0	24.3	25.0	0.0288	0.0278
0.20	57.0	14.9	15.3	0.0453	0.0444
0.24	57.3	12.4	12.8	0.0517	0.0506
0.28	57.0	9.9	10.2	0.0591	0.0581
0.32	56.9	8.0	8.4	0.0663	0.0646
0.36	57.0	6.6	6.8	0.0728	0.0718
0.40	57.4	5.3	5.2	0.0805	0.0811
0.44	56.2	4.3	4.5	0.0868	0.0853
0.48	57.1	3.5	3.7	0.0943	0.0924
0.52	55.8	2.9	3.1	0.0999	0.0976
0.92	56.2	0.850	0.870	0.1416	0.1408
1.32	55.7	0.191	0.192	0.1917	0.1916
1.72	57.0	0.103	0.113	0.2134	0.2103
2.12	56.1	0.100	0.099	0.2138	0.2142

Appendix H. External data aquisition box - electrical diagram

Figure H.1 shows the electrical diagram for the external data acquisition box constructed to allow sampling of three channels at two different sampling rates and determination of valid data start.

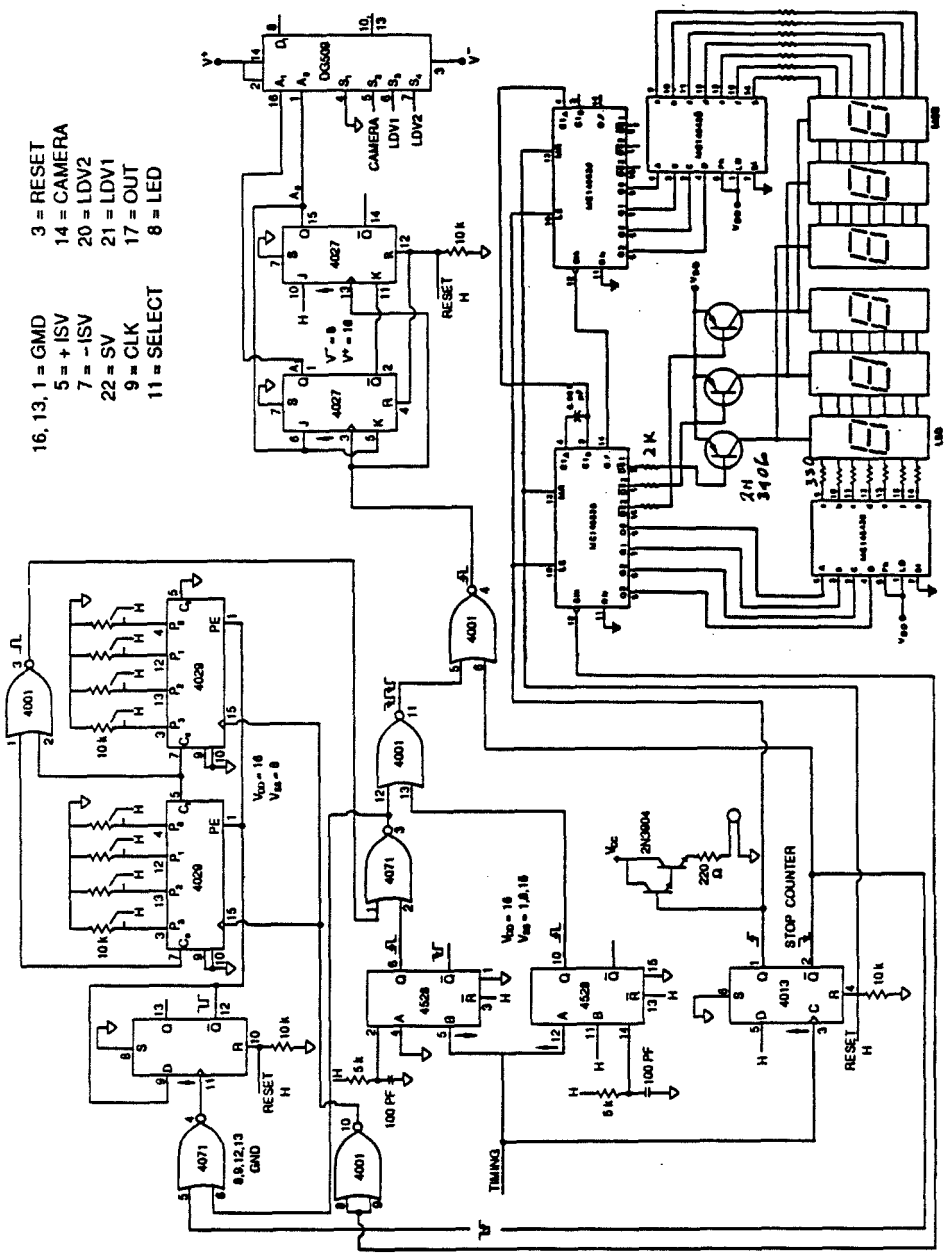

Figure H.1 Electrical diagram for external data acquisition box

Appendix I. Static and dynamic resolution of LIF experiments

The following discussion is provided as a guide for determining the spatial and temporal resolution of the LIF system.

Spatial resolution

The spatial resolution of the LIF system is determined by two components – the static and the dynamic resolution. The static resolution is found by multiplying the effective aperture area by the magnification ratio. A typical value for the static resolution is as follows:

$$\Delta x = 25\mu m \cdot (mr) = 25\mu m \cdot (18) = 450\mu m$$
$$\Delta z = 26\mu m \cdot (mr) = 26\mu m \cdot (18) = 470\mu m$$

The resolution in the y-direction (spanwise) direction is determined by the laser beam width, which in these experiments is approximately 450-500μm. Therefore, for these experiments, the static resolution of the probe volume is roughly a cube with sides of length 500μm. In a flowing system, however, Koochesfahani(1984) argued that the spatial resolution would be made up of static and dynamic components. The dynamic component is equal to the average distance the flow moves during the sample time. It is calculated below using the high-end *cross-flow* velocities used in this study:

$$\Delta x = U \cdot (\text{scantime}) = 23.9\text{cm/s} \cdot 0.0052\text{s/scan}$$
$$= 0.123\text{cm}$$

Papantoniou(1984) suggested that the actual spatial resolution in the flow direction is not an additive effect, but rather determined by the greater of the static and the dynamic resolution. Thus, in these experiments, clearly it is the dynamic component that limits the spatial resolution of the probe.

Temporal resolution

The temporal resolution is determined solely by the rate at which the LIF photo-diode array is sampled. For all of the experiments conducted in this study, the pixel-to-pixel sampling rate was 200kHz, which, for the 1024 element array plus 8 down counts, amounts to a scan rate of approximately 194 scans/s.

The physics of the flow:

The minimum spatial and temporal resolution in the probe volume necessary to capture the Kolmogorov time and length scales are determined by the following parameters which are related to the *local* small time scale:

$$t_\nu = \left(\frac{\nu}{\varepsilon}\right)^{1/2} = \text{Kolmogorov time scale}$$

$$l_\nu = \left(\frac{\nu^{3/4}}{\varepsilon^{1/4}}\right) = \text{Kolmogorov length scale}$$

Further, we can approximate $\varepsilon \sim w^3/L$, where w is the centerline velocity of the buoyant jet flow. Then, we can write the Kolmogorov scales as:

$$t_\nu \cong \frac{T}{\mathrm{Re}^{1/2}}$$

$$l_\nu \cong \left(\frac{L}{\mathrm{Re}^{3/4}}\right)$$

where t_ν is indicative of the fastest variations in a turbulent flow as they are related to the random "jittery" motions of the smallest eddies, and T refers to the large scale passage of time, or the integral time scale, $T = L/w$. For the flows considered in this study, the relevant length scale is the elevation, z, therefore, this becomes $T = z/w$, and if we substitute the equation for a bent jet, we find:

$$T = \frac{z}{w_m(z)} \propto \frac{z}{\left(\frac{M}{Uz^2}\right)} = \frac{Uz^3}{M}$$

For large values of the Schmidt number (which relates the diffusion of momentum measured by the viscosity, to molecular diffusion, measured by the diffusion coefficient), the molecules are not mixing. In other words, molecular mixing does not occur until the smaller Batchelor (or diffusion) length scale defined by:

$$l_d = \frac{l_\nu}{\mathrm{Sc}^{1/2}}$$

In water, the Schmidt number is approximately equal to 600 which means that the Batchelor and the Kolmogorov scales are different by a factor of roughly 25.

The desirable *local* temporal resolution of the sample probe can be calculated from typical values of the experimental parameters as shown below:

$$\begin{aligned} t_\nu &= \frac{T}{\mathrm{Re}^{1/2}} = \frac{z\nu^{1/2}}{w^{3/2}d^{1/2}} = \frac{z^4\nu^{1/2}U^{3/2}}{(11.0)^{3/2}M^{3/2}d^{1/2}} \\ &= \frac{10^4(1e-2)^{1/2}(23.9)^{3/2}}{(11.0)^{3/2}(1414.8)^{3/2}(0.5)^{1/2}} = 0.085\,\mathrm{sec} \\ &\Rightarrow 12\,\mathrm{Hz} \end{aligned}$$

and the desired *local* spatial resolution is:

$$\begin{aligned} l_\nu &= \frac{L}{\mathrm{Re}^{3/4}} = \frac{t_\nu w}{\mathrm{Re}^{3/4}} = \frac{t_\nu w^{1/4}\nu^{3/4}}{d^{3/4}} = \frac{t_\nu \nu^{3/4}}{d^{3/4}}\left(\frac{11.0M}{Uz^2}\right)^{1/4} \\ &= \frac{0.085}{0.5^{3/4}}\left(\frac{11.0\cdot 1414.8}{23.9\cdot 10^2}\right)^{1/4}(1e-2)^{3/4} \\ &= 0.0072\,\mathrm{cm} \\ &\Rightarrow 72\,\mu\mathrm{m} \end{aligned}$$

If we use the advective velocity, U, instead of the centerline velocity we find:

$$t_v = 0.012\,\text{sec}$$
$$\Rightarrow 83\text{Hz}$$

and the desired spatial resolution to be:

$$l_v = 0.0014e-2\text{cm}$$
$$\Rightarrow 14\mu\text{m}$$

Clearly, the limitation of this technique lies in its spatial resolution. These calculations indicate that we may fail to capture the Kolmogorov scale, therefore, our results can only provide an upper limit on the amount of mixing. We do not even approach the Batchelor scale.

Appendix J. Computer program listings

The following program listings are provided to facilitate continuation of the work. In particular, the LIF processing programs are time-consuming to generate. However, it should be noted that each of the following programs was written for data specifically formatted by either the Masscomp system or Caltech computer system. Thus, each should be used only for guidance with different systems.

Program for calculating background noise — LIF system calibration

```
      integer*2 vb(1032),dummy
      real va(1032),vtot(1032),bno(1032)
      character*15 INP,OUTP
      type 5
 5    format(///,18x,'What are you kidding me?  The only'
     $       /,18x,'background noise we should have is',
     $       /,18x,'reggae, man....')
      type 10
10    format(///,5x,'Input number of scans -  ',$)
      accept *,nscns
      type 15
15    format(///,5x,'Input ithrow -  ',$)
      accept *,ithrow
      type 20
20    format(/,5x,'Name of background noise input file? -')
      read 25, INP
25    format (a15)
      type 30
30    format(/,5x,'Name of output file? -')
      read 25, OUTP
      open(unit=1,file=INP,status='old',access='sequential',
     $       form='unformatted',recl=2064)
      open(unit=2,file=OUTP,status='new',access='sequential',
     $       form='formatted')
c
c                          zero parameters
c
      do 50 i=1,1032
            vtot(i) = 0.0
50    continue
      do 60 i=1,ithrow
            read(1) dummy
60    continue
c
c                                  calculate average over scans
c
      do 100 j=1,nscns
        do 200 i=1,1032
          read(1) vb(i)
          va(i)=vb(i)
          vtot(i)=vtot(i)+va(i)
          if (j.eq.nscns) then
            bno(i)=vtot(i)/float(nscns)
                if(i.ge.1025)then
                      bno(i)=0.0
                end if
            write(2,1000) bno(i)
1000      format(1x,f7.2)
          end if
200     continue
100   continue
      close(unit=1)
      close(unit=2)
      end
```

Program for calculating transfer function and magnification ratio — LIF calibration

```
      integer*2 fb(1032),dummy
      integer ithrow,ibegpx,iendpx
      real thres,thresb,mr
      character*15 BNOINP,INP,OUTP
      real f(1032),favg(1032),bno(1032),h(1032),ftot(1032)
      type 5
5     format(///,18x,'TRANSFER FUNCTION PROGRAM',
     $          /,18x,'And away we go...')
      type 10
10    format(///,5x,'Input number of scans - ',$)
      accept *, nscns
      type 9
9     format(/,5x,'Input ithrow - ',$)
      accept *, ithrow
      nscns=nscns-int(ithrow/1032+1)
      type 11
11    format(/,5x,'Input mag ratio - ',$)
      accept *, mr
      print *,mr
      type 12
12    format(/,5x,'Input Cotf, M e6 - ',$)
      accept *, Cotf
      if(Cotf.lt.0.10)then
      eps=0.3934
      else
      eps=0.195
      end if
      type 15
15    format(/,5x,'Input ibegpx - ',$)
      accept *,ibegpx
      type 16
16    format(/,5x,'Input iendpx - ',$)
      accept *,iendpx
      epsCotf=eps*Cotf
      print *,epsCotf
      type 20
20    format(/,5x,'Name of averaged background noise file? -')
      read 25, BNOINP
25    format(a15)
      type 30
30    format(/,5x,'Name of input file? -')
      read 25, INP
      type 40
40    format(/,5x,'Name of output file? -')
      read 25, OUTP
      open(unit=1,file=INP,status='old',access='sequential',
     $          form='unformatted',recl=2064)
      open(unit=2,file=OUTP,status='new',access='sequential',
     $          form='formatted')
      open(unit=3,file=BNOINP,status='old',access='sequential',
     $          form='formatted')
      write(2,1003) epsCotf
1003  format(1x,f10.6)
      write(2,1030) Cotf
1030  format(1x,f7.4)
      write(2,1066) ibegpx,iendpx
1066  format(1x,i4)
      print *,epsCotf
      do 60 i=1,ithrow
          read(1)dummy
60    continue
      do 100 i=1,1032
          ftot(i)=0.0
100   continue
      do 200 j=1,nscns
```

```
          do 300 i=1,1032
            if (j.eq.1) then
                  read(3,1001) bno(i)
1001              format(1x,f7.2)
            end if
            read(1) fb(i)
            f(i)=fb(i)-bno(i)
            ftot(i)=ftot(i)+f(i)
                  if (j.eq.nscns) then
                        favg(i)=ftot(i)/float(nscns)
                  end if
300       continue
200        continue
          do 550 i=1,1032
                  if ((i.lt.ibegpx).or.(i.gt.iendpx)) then
                        h(i)=0.0
                        go to 1005
                  end if
                        h(i)=favg(i)*exp(epsCotf*(i-ibegpx)*25e-4*mr)
1005                    write(2,1002) h(i)
1002                    format(1x,f7.3)
 550      continue
          close(unit=1)
          close(unit=2)
          close(unit=3)
          end
```

This program calculates the concentration values from a data set

(Note: for noisy data - the final dilution number must by multiplied by the following number: (number of scans/ (number of scans-spikes)) because the program replaces spike concentration values with zeros

```
c
c
c
c
      character*15 BNOINP,TRFINP
      character*20 RINP
      integer*2 fb(512,1024),dummy(256)
      real f(512,1024),bno(1024),denom(1024),crel(512,1024)
      real cavg(1024),cstnd(1024),ctot(1024),ctot2(1024),ccum,dilution,factor
      real cavgmax,crelmax(1024),cinstmax,fminb(512,1024)
      real integr,integr2,lovalue,mininstdil,minavgdil,lofactor,lofactorb
      real crelavgfilter(1024),crelthres(1024),cfilter1(1024),cfilavg(1024)
      real cfilter2(1024),mr,epscosf,epscotf
      integer value,ipchoice,middle(3)
      character*1 t,chtrf
      integer*2 buffer(256),itmp1,itmptmp,a(-255:530000)
      byte bbuffer(512),tmp,image(512,512),imageB(512,512)
      equivalence (bbuffer,buffer)
      character*5 outroot
      character*4 chavgs
      character*2 chnumber
      character*10 outsa
      character*10 outsaT,outsaB
      character*11 outavgs,outconv,outprof,outdil
      character*12 outconv1,outconv2,outconv3
      character*1 LIN,chbnotrf,chframes
      real bkgd(1024),b1,b2,crelminb(512,1024),cfilstnd(1024)
      real cfiltot(1024),cfiltot2(1024)
      chavgs='avgs'
      t=char(9)
      ccum=0.0
      middle(1)=0
      middle(2)=0
      middle(3)=0
      cinstmax=0.0
      cavgmax=0.0
      do 600 i=1,1024
        crelmax(i)=0.0
600   continue
      type 5
 5    format(///,18x,'CONCENTRATION PROGRAM',
     $          /,18x,'This is it, all the money...')
      type 9
 9    format(5x,'Input ithrow - ',$)
      accept *, ithrow
      type 8
 8    format(5x,'Input crelmax to adjust ct (this should be 0-1) - ',$)
      accept *, cmax
      type 10
 10   format(5x,'Input number of scans -  ',$)
      accept *, nscns
      nopts=nscns*1032-ithrow
      nopics=int((nopts/1032)/512)
      type 15
 15   format(5x,'Input mag ratio -  ',$)
      accept *, mr
      type 41
 41   format(5x,'Enter ratio of ff/sf for trf fluid -  ',$)
```

```
      accept *,factor
      realfactor=factor+1.0
      type 52
 52   format(5x,'Enter flume Co(M*e6), for Io adj -  ',$)
      accept *,Coflume
      type 578
 578  format(5x,'Enter background rel conc - ',$)
      accept *,bkgdCrel
 567  type 53
 53   format(5x,'Enter depth of flow (cm) -  ',$)
      accept *,depth
      delh=depth-29.6
      type 5112
5112  format(5x,'Enter fraction of laser power from first exp -  ',$)
      accept *,pwrfraction
      Iofactorb=1.0/pwrfraction
c
c     Note: epsCoflume doesn't have initial constant, because for Co
c        equal to zero, the calibration and the data have the same
c        Io.  In other words, the beam is attenuated by plain water
c        for the cal just as it is for the data, thus Iofactor=1 when
c        Coflume=0.0
c
c
c     epsCoflume=0.19925*Coflume-1.7516e-2*Coflume**2.0
      epsCoflume=0.19298*Coflume-4.4853e-2*Coflume**2.0
      Iofactor=exp(epsCoflume*delh)
c     Iofactor=1.0
      type *,delh,epsCoflume,Iofactor,Iofactorb
      type 46
 46   format(5x,'Do you have bno and trf data (y/n)? -')
      read 43,chbnotrf
      if((chbnotrf.eq.'y').or.(chbnotrf.eq.'Y'))then
      type 20
 20   format(5x,'Name of averaged background noise file? -  ')
      read 25, BNOINP
 25   format(a15)
      open(unit=3,file=BNOINP,status='old',access='sequential',
     $          form='formatted')
      type 30
 30   format(5x,'Name of transfer fn file? -  ')
      read 25, TRFINP
      open(unit=1,file=TRFINP,status='old',access='sequential',
     $          form='formatted')
      read(1,1003) epsCotf
      read(1,1300) Cotfold
      Cotf=(4.3025-sqrt(4.3025**2.0-4*(epsCotf/4.4853e-2-0.210015)))/2.0
      type *,Cotfold,Cotf
1003  format(1x,f10.6)
1300  format(1x,f7.4)
      read(1,1330)itrfbegpx,itrfendpx
1330  format(1x,i4)
      else
      LIN='n'
      go to 67
      end if
      type 1121
1121  format(5x,'Use trf or const for trf (t/c)? - ')
      read 43,chtrf
            if(chtrf.eq.'t')then
                  go to 5645
            else
                  type 657
657               format(5x,'enter constant trf value - ',$)
                  accept *,trfconst
            end if
5645  type 42
 42   format(5x,'Adjust epsCo from trf fluid (y/n)? -')
      read 43,LIN
```

```
 43     format(a1)
 67     if((LIN.eq.'y').or.(LIN.eq.'Y'))then
                Cosf=Cotf*realfactor*1e-6
                type *,'Cosf=',Cosf,'Cotf=',Cotf
        else
        type 44
 44     format(5x,'Enter Co for source fluid (x e6 Molar)-  ',$)
        accept *,Cosf
        end if
        type *,'bgdCrel=',bkgdCrel
        type 64
 64     format(5x,'Do you want pictures? - ')
        read 43,chframes
        if((chframes.eq.'n').or.(chframes.eq.'N'))then
        ipchoice=0
        go to 65
        end if
        type 17
 17     format(5x,'You have 3 choices for image processing:  ',/,
  $             15x,'1 - One picture per 512 scans, avgs over 2 pixels',/,
  $             15x,'2 - Two pictures 512 pixels each, top and bottom',/,
  $             15x,'3 - One picture with a chosen range of 512 pixels',/,
  $             25x,'Enter 1,2,or 3 -   ',$)
        accept *,ipchoice
        if(ipchoice.eq.3)then
 21     type 13
 13     format(5x,'Input ibegpx -  ',$)
        accept *, ibegpx
        if(ibegpx.gt.512)then
                type 14
 14             format(/,5x,'Value must be less than 512!')
                go to 21
        end if
        iendpx=ibegpx+512
        end if
 65     type 22
 22     format(5x,'How many pixels for convergence data (3 max)-  ',$)
        accept *,iconv
        do 23 i=1,iconv
        type 16
 16     format(5x,'Input pixel # for convergence - ',$)
        accept *,middle(i)
 23     continue
        type 35
 35     format(5x,'Name of run data file? -  ')
        read 37, RINP
 37     format(a30)
        type 40
 40     format(5x,'Root Name of output file? -  ')
        read 25, OUTROOT
c
c
        open(unit=2,file=RINP,status='old',recordtype='fixed',
  $             recordsize=128,form='unformatted',readonly)
        OUTPROF=OUTROOT//'prof'
        OUTDIL=OUTROOT//'dilu'
        open(unit=7,file=OUTPROF,status='new',access='sequential',
  $             form='formatted')
        open(unit=12,file=OUTDIL,status='new',access='sequential',
  $             form='formatted')
        outavgs=outroot//chavgs
        open(unit=6,file=outavgs,status='new',access='sequential',
  $             form='formatted')
        if(iconv.gt.1)then
                outconv1=outroot//'conv'//'1'
                outconv2=outroot//'conv'//'2'
        open(unit=8,file=OUTCONV1,status='new',access='sequential',
  $             form='formatted')
        open(unit=10,file=OUTCONV2,status='new',access='sequential',
```

```
     $              form='formatted')
                    if(iconv.lt.3)then
                    go to 1055
                    end if
               end if
               if(iconv.gt.2)then
                    outconv3=outroot//'conv'//'3'
               open(unit=11,file=OUTCONV3,status='new',access='sequential',
     $              form='formatted')
               go to 1055
               end if
               OUTCONV=OUTROOT//'conv'
               open(unit=8,file=OUTCONV,status='new',access='sequential',
     $              form='formatted')
    1055       ithrowrecords=int(ithrow/256)
               iplus=ithrowrecords+129
               type *,'ithrowrecords,iplus = ',ithrowrecords,iplus
               do 50 i=1,iplus
                    read(2) dummy
    50         continue
               ithrowoffset=ithrow-ithrowrecords*256
               type *,ithrowoffset
               do 100 i2=1,nopics
                    if (i2.gt.9)then
                         iten=i2-10
                         chnumber=char(49)//char(iten+48)
                              if(i2.gt.19)then
                              chnumber=char(50)//char(48)
                              end if
                         go to 77
                    end if
                    chnumber=char(i2+48)
    77              type *,chnumber
                    if(ipchoice.eq.2)then
                      outsaT=outroot//chnumber//'T'
                      outsaB=outroot//chnumber//'B'
               if((i2.gt.1).and.(i2.lt.9))then
               open(unit=5,file=OUTSAT,status='new',form='unformatted',recl=
     $              128,recordtype='fixed',defaultfile='.pv')
               open(unit=9,file=OUTSAB,status='new',form='unformatted',recl=
     $              128,recordtype='fixed',defaultfile='.pv')
               end if
                      go to 1000
                 end if
                    outsa=outroot//chnumber
    1002            type *,outsa
                    if((chframes.eq.'n').or.(chframes.eq.'N'))then
                go to 1000
                    end if
               if((i2.gt.1).and.(i2.lt.9))then
               open(unit=5,type='new',form='unformatted',recl=128,
     $              name=OUTSA,recordtype='fixed',defaultfile='.pv')
               end if
               type *,itrfbegpx,itrfendpx
    c
    c
    c                    Here's where I read in and convert data ...
    c
    c
    1000       if((i2.eq.1).and.(ithrowoffset.ne.0))then
                 icount=-1.0*ithrowoffset
               else
                 itmp0=imax*256-256
                 icount=256-ithrowoffset
                 do itmp=1,icount
                   a(itmp)=a(itmp0+itmp)
                 enddo
               end if
               imax=2064
```

```
      if((i2.eq.1).and.(ithrowoffset.ne.0))then
        imax=imax+1
      end if
      do i=1,imax
        read(2,end=3939)buffer
c
c               i is block number,so this reads 2064 blocks
c               which is int*2=2bytes=1point, 512scans*1032pts*2bytes=#bytes
c               per point, but 512 scans is one picture, so
c               since 512 bytes is one block, one picture of
c               512 scans is 1032*2=2064 blocks
c
c
c               Now swap in 16 bit words
c
        do j=1,512,2
               tmp=bbuffer(j)
               bbuffer(j)=bbuffer(j+1)
               bbuffer(j+1)=tmp
        enddo
c
c               Put file in array
c
        do j=1,256
               jj=j+icount
               a(jj)=buffer(j)
        enddo
        icount=icount+256
      enddo
      do 200 j=1,512
        do 300 i=1,1024
          if ((j.eq.1).and.(i2.eq.1)) then
                        ctot(i)=0.0
                        ctot2(i)=0.0
               if((chbnotrf.eq.'n').or.(chbnotrf.eq.'N'))then
                        bno(i)=0.0
                        denom(i)=50.0
                        go to 1066
               end if
                        read(3,1001) bno(i)
               if(chtrf.eq.'t')then
                        read(1,1033) denom(i)
                        denom(i)=denom(i)*realfactor
               else
                        denom(i)=trfconst*realfactor
1001                    format(1x,f7.2)
1033                    format(1x,f9.4)
               end if
                if((i.lt.itrfbegpx).or.(i.gt.itrfendpx))then
                        bkgd(i)=0.0
                else
                        bkgd(i)=bkgdCrel
                end if
1066      end if
          jj=(j-1)*1032+i
          fb(j,i)=a(jj)
          f(j,i)=fb(j,i)
          fminb(j,i)=f(j,i)-bno(i)
               if (fminb(j,i).lt.0.0) then
                        fminb(j,i)=0.0
               end if
          if (i.eq.1) then
               integr=1.0
               go to 310
          end if
               if((i.ge.itrfbegpx).and.(i.le.itrfendpx))then
                        if(j.eq.jbad)then
                          crel(j,i)=bkgd(i)
                          crelminb(j,i)=0.0
```

```
                        go to 5555
                    end if
                    clast=crel(j,i-1)*Cosf*1.0e6
                    epsclast=9.4198e-3+0.19298*clast-4.4853e-2*clast**2.0
                    if(clast.ge.1.72)then
                        epsclast=0.03869*clast+0.142113
                    end if
                end if
            integr=integr*exp(epsclast*25e-4*mr*1.0)
c
c       The intensity, Io, falls out of the equations since
c       when h(i) is calculated, it is divided by Io.  Then
c       in the calcs for conc, we multiply by Io again.
c
310     if ((i.lt.itrfbegpx).or.(i.gt.itrfendpx))then
            crel(j,i)=0.0
            crelminb(j,i)=0.0
            go to 311
        end if
        crel(j,i)=Iofactor*Iofactorb*(fminb(j,i)*integr)/denom(i)
        if(crel(j,i).gt.1.0)then
            crel(j,i)=cfilavg(i)
        end if
        crelminb(j,i)=crel(j,i)-bkgd(i)
            if(crelminb(j,i).lt.0.0)then
                crelminb(j,i)=0.0
            end if
            if(((i2.gt.1).and.(j.gt.1)).and.((i.ge.itrfbegpx)
     $          .and.(i.le.itrfendpx)))then
                cfilter1(i)=cfilavg(i)*10.0
                cfilter2(i)=crelminb(j-1,i)+cfilstnd(i)*6.0
                if(cfilter1(i).gt.0.8)then
                    cfilter1(i)=0.8
                end if
                if(cfilter2(i).gt.0.8)then
                    cfilter2(i)=0.8
                end if
            else
                cfilter1(i)=0.8
                cfilter2(i)=0.8
            end if
            diff=abs(crelminb(j,i)-cfilter1(i))
            diff2=abs(crelminb(j,i)-cfilter2(i))
            if(diff2.gt.diff)then
                diff=diff2
            end if
        if((i.ge.itrfbegpx).and.(i.lt.(itrfbegpx+50)))then
            if((diff.gt.0.001).and.((crelminb(j,i).gt.cfilter1(i)).or.
     $          (crelminb(j,i).gt.cfilter2(i)))) then
                if(j.ne.jbad1)then
                    nospikes=nospikes+1
                    if(nospikes.gt.250)then
                        go to 999
                    end if
                    type *,'nospikes,j,i=',nospikes,j,i
                    type *,'crelminb(j,i),cfilter1(i),cfilavg(i),',
     $                  'cfilter2(i),cfilstnd(i)=',
     $                  crelminb(j,i),cfilter1(i),
     $                  cfilavg(i),cfilter2(i),cfilstnd(i)
                end if
                jbad1=j
                jbad=j
                    crelminb(j,i)=0.0
                    crel(j,i)=bkgd(i)
            end if
        end if
5555        if((i2.gt.1).and.(crelminb(j,i).gt.crelmax(i)))then
                crelmax(i)=crelminb(j,i)
            end if
```

```
                if((chframes.eq.'n').or.(chframes.eq.'N'))then
                        go to 1023
                end if
311                     itmp1=int(crelminb(j,i)/cmax*242.)
                if(ipchoice.eq.1)then
                        iby2=int(i/2)*2
                        if(iby2.ne.i)then
                          itmptmp=itmp1
                        end if
                        if(iby2.eq.i)then
                          itmpavg=(itmptmp+itmp1)/2
                if(itmpavg.gt.242) then
                        itmpavg=242
                end if
                if(itmpavg.gt.127) then
                        itmpavg=itmpavg-256
                end if
                        istore=int(iby2/2)
                        image(j,istore)=itmpavg
                        end if
                        go to 1023
                end if
                if(itmp1.gt.242) then
                        itmp1=242
                end if
                if(itmp1.gt.127) then
                        itmp1=itmp1-256
                end if
                if(ipchoice.eq.2)then
                        if(i.lt.513)then
                                image(j,i)=itmp1
                        end if
                        if(i.gt.512)then
                                inew=i-512
                                imageB(j,inew)=itmp1
                        end if
                        go to 1023
                end if
                if(ipchoice.eq.3)then
                        if((i.gt.ibegpx).and.(i.le.iendpx))then
                        i3=i-ibegpx
                        image(j,i3)=itmp1
                        end if
                end if
1023            if(i2.le.2)then
                        cfiltot(i)=cfiltot(i)+crelminb(j,i)
                        cfiltot2(i)=cfiltot2(i)+crelminb(j,i)**2.0
                        cfilavg(i)=cfiltot(i)/float((i2-1)*512+j)
                                if(cfilavg(i).gt.0.3)then
                                        type *, 'cfilavg(i) gt 0.3',cfilavg(i)
                                        cfilavg(i)=0.3
                                end if
                        cfilstnd(i)=(abs(cfiltot2(i)/
     $                                 float((i2-1)*512+j)-cfilavg(i)**2.0))**0.5
                end if
              ctot(i)=ctot(i)+crelminb(j,i)
              ctot2(i)=ctot2(i)+crelminb(j,i)**2.0
                if((j.eq.512).and.(i2.eq.nopics)) then
                        cavg(i)=ctot(i)/float(i2*512)
                          if((i.gt.1):and.(cavg(i).gt.cavgmax))then
                                cavgmax=cavg(i)
                                icavgmax=i
                          end if
                          if((i.gt.1).and.(crelmax(i).gt.cinstmax))then
                                cinstmax=crelmax(i)
                                icinstmax=i
                          end if
                        cstnd(i)=(abs(ctot2(i)/float(i2*512)-cavg(i)**
     $                       2.0))**0.5
```

```
                        write(6,1006) cavg(i),cstnd(i),crelmax(i)
1006                    format(1x,f8.5,2x,f8.5,2x,f8.5)
                end if
                if(j.eq.256)then
                        write(7,1007)crelminb(j,i)
1007                    format(1x,f8.5)
                end if
        if((i.eq.middle(1)).or.(i.eq.middle(2)).or.(i.eq.middle(3)))then
                        cavg(i)=ctot(i)/float((i2-1)*512+j)
                        cstnd(i)=(abs(ctot2(i)/float((i2-1)*512+j)-cavg(i)**
     $                      2.0))**0.5
                if(i.eq.middle(1))then
                write(8,1008) j,i,crelminb(j,i),cavg(i),cstnd(i)
1008            format(1x,2(i4,1x),3(f9.5,2x))
                end if
                if(i.eq.middle(2))then
                write(10,1008) j,i,crelminb(j,i),cavg(i),cstnd(i)
                end if
                if(i.eq.middle(3))then
                write(11,1008) j,i,crelminb(j,i),cavg(i),cstnd(i)
                end if
        end if
 300      continue
 200     continue
        if((chframes.eq.'n').or.(chframes.eq.'N'))then
          go to 100
        end if
        if((ipchoice.eq.2).and.((i2.gt.1).and.(i2.lt.8)))then
                do i=512,1,-1
                        write(5) (image(j,i),j=1,512)
                        write(9) (imageB(j,i),j=1,512)
                end do
                go to 100
        end if
        if((i2.gt.1).and.(i2.lt.8))then
                do i=512,1,-1
                        write(5) (image(j,i),j=1,512)
                end do
        end if
 100    continue
        write(12,1999)nospikes
1999    format(1x,'nospikes = ',i4)
        minavgdil=1.0/cavgmax
        write(12,1009)minavgdil,icavgmax
1009    format(1x,'minimum avg dilution = ',f8.2,2x,i4)
        mininstdil=1.0/cinstmax
        write(12,1099)mininstdil,icinstmax
1099    format(1x,'minimum inst dilution = ',f8.2,2x,i4)
        go to 333
 999    type 99
  99    format(1x,'You have more than 20 pics worth of data...')
        go to 333
3939    type*, 'you just ran out of data'
 333    close(unit=1)
        close(unit=2)
        close(unit=3)
        close(unit=4)
        close(unit=5)
        close(unit=6)
        close(unit=7)
        close(unit=8)
        close(unit=10)
        close(unit=11)
        end
```

This program is used for processing LDV data

```
c
c
C
C       THIS PROGRAM CALCULATES THE VERTICAL AND HORIZONTAL VELOCITY
C       AS A FUNCTION OF TIME. THE MEAN AND RMS VELOCITIES THE CROSS
C       -CORRELATION.
C       THE USER IS ASKED TO INPUT THE NAME OF THE SOURCE FILE CONTAIN-
C       ING THE NAME OF THE CALIBRATION FILES AND THE FILES AT EACH HT
C
        INTEGER*2  V1,V2,MULTI
        REAL RV1,RV2,U,V,RU,RV,ZU,ZV,USUM,VSUM,URMSSUM,VRMSSUM
        REAL UAVG,VAVG,URMS,VRMS,USHEAR
        REAL FU,FV,RI,RR,USHEARSUM
        REAL*8 A1,B1,A2,B2
        INTEGER NUMPTS, NOSPIKES
        INTEGER I,J,K,JREC,MULTIPTS
        REAL HT,BASE,TOP,THRESU,DIFFU
        CHARACTER*15 INPFILE,INPFILE0
        CHARACTER*15 OUTU,OUTV
        CHARACTER*15 OUTCC,OUTP,OUTCONV
        CHARACTER*1 t,chu,chv,chp,chdata,chrecord
        CHARACTER*4 chuavg,chvavg,churms,chvrms,chconv
        CHARACTER*2 chcc,ptno
        CHARACTER*6 noinfo
        CHARACTER*20 cmmnt1,cmmnt2
        PARAMETER (RIR=1.333)
        PARAMETER (ALAMDA=632.8e-7)
        PARAMETER (PI=3.14159265)
        INTEGER IOCHECK,IOSTAT
        t=char(9)
        chu='u'
        chv='V'
        chp='p'
        chuavg='uavg'
        chvavg='vavg'
        churms='urms'
        chvrms='vrms'
        chcc='cc'
        chconv='conv'
C
C
C
C
C       TYPE HEADER
C
        TYPE 10
10      FORMAT(////,20X,'PROGRAM RLDV',///)
        TYPE 20
20      FORMAT(5X,'THIS PROGRAM CALCULATES VELOs AND RMS STATS')
C
C
C       READ IN PARAMETERS
C
C
        TYPE 30
30      FORMAT(///,5X,'WHAT IS THE INPUT FILENAME ? :')
        READ 35,INPFILE0
35      FORMAT (a15)
        noinfo=INPFILE0
        outp=chp//noinfo
21      TYPE 25
25      FORMAT(5X,'Type A for all data, S for a subset thereof - ')
        READ 26,CHDATA
26      FORMAT(A1)
        IF((CHDATA.NE.'A').AND.(CHDATA.NE.'S')) THEN
```

```
                GO TO 21
        END IF
        IF(CHDATA.EQ.'S') THEN
         TYPE 31
31       FORMAT(5X,'Enter n, for n * 1024 = no. data pts. - ')
         READ 32,MULTI
32       FORMAT(I2)
        ENDIF
27      TYPE 28
28      FORMAT(5X,'Would you like to record each data point? - ')
        READ 26,CHRECORD
        IF((CHRECORD.NE.'N').AND.(CHRECORD.NE.'Y')) THEN
        GO TO 27
        END IF
C
C       OPEN FILES
C
        OPEN(UNIT=4,FILE=INPFILE0,STATUS='OLD',ACCESS='SEQUENTIAL',
     $          FORM='FORMATTED')
      OPEN(UNIT=5,FILE=outp,STATUS='NEW',ACCESS='SEQUENTIAL',
     $          FORM='FORMATTED')
        read(4,44) cmmnt1
        read(4,44) cmmnt2
44      format(1x,a20)
        read(4,42) A1,B1
        read(4,42) A2,B2
42      format(1x,f10.7,2x,f12.5)
        read(4,*) F
        read(4,*) FDATA
        read(4,*) JREC
        read(4,*) BASE,TOP
        type 49,BASE,TOP
49      format (1x,2(f6.3,2x))
909     read(4,50) HT,INPFILE
        if(INPFILE.eq.'99.D')then
                go to 999
        end if
50      format(1x,f6.3,2x,a5)
        ht=base-ht
        OPEN(UNIT=1,FILE=INPFILE,STATUS='OLD',ACCESS='SEQUENTIAL',
     $          FORM='UNFORMATTED',RECL=JREC)
        ptno=INPFILE
        outu=chu//ptno
        outv=chv//ptno
        outcc=chcc//ptno
        outconv=chconv//ptno
        type 44,outp
c       OPEN(UNIT=10,FILE=outu,STATUS='NEW',ACCESS='SEQUENTIAL',
c    $          FORM='FORMATTED')
c       OPEN(UNIT=11,FILE=outv,STATUS='NEW',ACCESS='SEQUENTIAL',
c    $          FORM='FORMATTED')
c       OPEN(UNIT=12,FILE=outcc,STATUS='NEW',ACCESS='SEQUENTIAL',
c    $          FORM='FORMATTED')
        OPEN(UNIT=13,FILE=outconv,STATUS='NEW',ACCESS='SEQUENTIAL',
     $          FORM='FORMATTED')
C
C
C
C       READ IN BINARY NUMBERS CORRESPONDING TO VOLTAGES
C
C
C
        NOSPIKES=0
        NUMPTS=1
        USUM=0.
        VSUM=0.
        URMSSUM=0.
        VRMSSUM=0.
        USHEARSUM=0.
```

```
      MULTIPTS=MULTI*1024
      zu=1./1.10835
      zv=1./1.101
      DO WHILE (.TRUE.)
        RI=float(NUMPTS)
        READ(1,IOSTAT=IOCHECK,END=130) v1,v2
        RV1=V1*.00244141
        RV2=V2*.00244141
        FU=B1/(RV1-A1)
        FV=B2/(RV2-A2)
        RU=(F-FU)*ZU
        RV=(F-FV)*ZV
C
C       Regina's geom.:
C
        U=0.7071*ru-0.7071*rv
        V=-0.7071*ru-0.7071*rv
        USUM=USUM+U
        VSUM=VSUM+V
        UAVG=USUM/RI
        VAVG=VSUM/RI
        THRESU=ABS(0.5*UAVG)
        DIFFU=ABS(U-UAVG)
      IF(DIFFU.GE.THRESU)THEN
              USUM=USUM-U+UAVG
              U=UAVG
              VSUM=VSUM-V+VAVG
              V=VAVG
              NOSPIKES=NOSPIKES+1
      END IF
        URMSSUM=URMSSUM+U*U
        VRMSSUM=VRMSSUM+V*V
        USHEARSUM=USHEARSUM+U*V
      IF(CHRECORD.EQ.'Y')THEN
              URMS=SQRT(ABS(URMSSUM-RI*UAVG**2.0)/(RI))
              VRMS=SQRT(ABS(VRMSSUM-RI*VAVG**2.0)/(RI))
              USHEAR=(USHEARSUM-RI*UAVG*VAVG)/(RI)
              WRITE(10,1007)NUMPTS,U,UAVG,URMS
              WRITE(11,1007)NUMPTS,V,VAVG,VRMS
              WRITE(12,1008)NUMPTS,USHEAR
1007          FORMAT(1X,I10,3(F8.3))
1008          FORMAT(1X,I10,F8.3)
      END IF
        RR=RI/1024.
        IF((RR-FLOAT(INT(RR))).LT.0.00001) THEN
          IF(CHRECORD.EQ.'N')THEN
              URMS=SQRT(ABS(URMSSUM-RI*UAVG**2.0)/(RI-1.))
              VRMS=SQRT(ABS(VRMSSUM-RI*VAVG**2.0)/(RI-1.))
              USHEAR=(USHEARSUM-RI*UAVG*VAVG)/(RI-1.)
          ENDIF
          WRITE(13,1014)NUMPTS,UAVG,VAVG,URMS,VRMS,USHEAR
1014      FORMAT(1X,I6,2X,5(F8.3))
        ENDIF
        NUMPTS=NUMPTS+1
        IF((CHDATA.EQ.'S').AND.(NUMPTS.GT.MULTIPTS)) THEN
          GO TO 130
        END IF
      END DO
C
C
C       PRINT RESULTS IN THE  PROFILE(data file #6)

C
130   IF(CHRECORD.EQ.'Y')THEN
              GO TO 135
      ENDIF
      URMS=SQRT(ABS(URMSSUM-RI*UAVG**2.0)/(RI-1.))
      VRMS=SQRT(ABS(VRMSSUM-RI*VAVG**2.0)/(RI-1.))
      USHEAR=(USHEARSUM-RI*UAVG*VAVG)/(RI-1.)
```

```
135     WRITE(5,1011)ht,UAVG,URMS,VAVG,VRMS,USHEAR,NOSPIKES
1011    FORMAT(1X,6(F7.3,2x),i5)
        go to 909
999     continue
C
C
        CLOSE(UNIT=1)
        CLOSE(UNIT=4)
        CLOSE(UNIT=5)
        CLOSE(UNIT=10)
        CLOSE(UNIT=11)
        CLOSE(UNIT=12)
        CLOSE(UNIT=13)
        END
```

This program calculates the average velocity in the flume

```
      Program veloavg
c
c
c     This program calculates the average velocity
c     in the flume for a given velo profile along with other
c     important parameters.
c
c     22 January 1991/1 September 1991
c
c
      character*3  EXPTID
      character*15 INFILE,OUTFILE1,OUTFILE2
      integer*2 npts,i,nspikes,iter
      real mano,depth,urmssum,vrmssum,area,usurf,delu,knu,knucm,Q,Re
      real sigurms,sigvrms,uavg,vavg,Dh,m,width,uguess,ustartot,ustaravg
      real fuguess,fprime,unew,kappa,A,ratio
      real ht(15),u(15),urms(15),v(15),vrms(15),ubar(15),hbar(15)
      real cc(15),ustar(15),ucross(15),urmscross(15),vrmscross(15)
      real ycross(15),Restress(15)
c
c
      knu=0.9055e-6
      knucm=0.9055e-2
      gcm=981.0
      width=110.0
      kappa=0.412
      A=5.29
      type 10
10    format(1x,'Input filename - ')
      read 1030,INFILE
1030  format (a15)
      type 20
20    format(1x,'Experiment ID - ')
      read 1031,EXPTID
1031  format (a3)
      OUTFILE1=EXPTID//'smry'
      OUTFILE2=EXPTID//'nond'
      open(unit=4,file=INFILE,status='old',access='sequential',
     $           form='formatted')
      open(unit=5,file=OUTFILE1,status='new',access='sequential',
     $           form='formatted')
      open(unit=6,file=OUTFILE2,status='new',access='sequential',
     $           form='formatted')
      read(4,1000)npts
      read(4,1011)depth
      read(4,1012)mano
1000  format(1x,i2)
1011  format(1x,f5.2)
1012  format(1x,f6.3)
      urmssum=0.
      vrmssum=0.
      area=0.
      do 100 i=1,npts
            read(4,1010)ht(i),u(i),urms(i),v(i),vrms(i),cc(i),nspikes
1010        format(1x,6(f7.3,2x),i5)
            lht(i)=log(ht(i))
c
c
c     Here is the set-up for the least squares fit for u vs lny
c     For the subroutine mentioned later, require:
c           data(1,i)=x(i).
c           data(2,i)=y(i).
c           data(3,i)=standard error in y(i).
c
c
```

```
                data(1,i)=lht(i)
                data(2,i)=u(i)
                data(3,i)=1.
c
c       End of array set-up
c
c
                urmssum=urmssum+urms(i)
                vrmssum=vrmssum+vrms(i)
                if(i.eq.1)then
                        area=0.5*ht(i)*u(i)
                        go to 100
                end if
                area=area+(ht(i)-ht(i-1))*(u(i)+u(i-1))/2.0
100     continue
c
c       Here is where the CIT library subroutine is called, lsquar.
c       To use, must link prgrmname, 'CIT lib'.
c       npts = number of data points
c       adata is the array containing the coefficients of the fit.
c       2 = linear fit.
c       chisq = sum of the residuals.
c       stor = working storage
c
c
        call lsquar(data,npts,2,adata,chisq,stor)
        mfit=adata(2)
        bfit=adata(1)

        m=(u(npts)-u(npts-1))/(ht(npts)-ht(npts-1))
        delu=m*(depth-ht(npts))
        usurf=u(npts)+delu
        area=area+(depth-ht(npts))*(usurf+u(npts))/2.0
        uavg=area/depth
        aspratio=width/depth
        Fr=uavg/(gcm*depth)**0.5
        Q=uavg*depth*width/(100.**3.0)
        Dh=(4*depth*width/(2*depth+width))
        Re=2.0*uavg*Dh/knucm
        urmsavg=urmssum/npts
        vrmsavg=vrmssum/npts
        do 200 i=1,npts
                ubar(i)=u(i)/uavg
                hbar(i)=ht(i)/depth
                sigurms=abs(urms(i)-urmsavg)
                sigvrms=abs(vrms(i)-vrmsavg)
c
c
c               Here's the iterative scheme for u*.  It is Newton's method.
c
c
                iter=0
                uguess=urms(i)
                go to 223
222             uguess=unew
223             iter=iter+1
                if(iter.gt.100)then
                        type *,'iter gt 100'
                        stop
                end if
                type *,iter
                fuguess=(knucm/ht(i))*exp(kappa*(u(i)/uguess-A))-uguess
                fprime=(fuguess+uguess)*(-1.0*u(i)*kappa/(uguess**2.0))-1.0
                unew=uguess-0.5*fuguess/fprime
                diffu=abs(unew-uguess)
                type *,uguess,unew,diffu
                if(diffu.lt.0.001)then
                        ustar(i)=unew
                        ucross(i)=ustar(i)/u(i)
```

```
                        urmscross(i)=urms(i)/ustar(i)
                        vrmscross(i)=vrms(i)/ustar(i)
                        Restress(i)=-1.0*cc(i)/ustar(i)**2.0
                        ycross(i)=ht(i)*ustar(i)/knucm
                        write(6,1021)ht(i),ycross(i),ubar(i),ustar(i)
1021                    format(1x,f5.2,2x,f6.1,2x,f6.4,2x,f6.4)
                        ustartot=ustartot+ustar(i)
                        if(i.eq.npts)then
                                ustaravg=ustartot/npts
                                Restar=depth*ustaravg/knucm
                                ratio=ustaravg/urmsavg
                                sigurms=sigurms/npts
                                sigvrms=sigvrms/npts
                        end if
                        go to 200
                end if
        go to 222
 200    continue
        write(5,1020)uavg,urmsavg,sigurms,vrmsavg,sigvrms,ustaravg,ratio,Q
        write(5,1022)Re,Fr,Restar
1020    format(1x,f6.3)
1022    format(1x,f10.2)
        close (unit=4)
        close (unit=5)
        close (unit=6)
        end
```

Appendix K. List of all experimental conditions

date	expt	x, cm	fm%	mano	Δρ/ρ, %	h,cm	M,p	B,p	Q,p	U, cm/s	u*, cm/s	S, avg	pixel Savg	ibegpx	iendpx	at S,avg z,cm	mr
5-Jun-92	q	100	10	0.197	1.10	40.55	156.8	59.9	5.5	16.9	0.893	218.54	787	229	905	5.17	17.5
	b	100	10	0.349	1.10	40.55	156.8	59.9	5.5	19.9	1.029	259.26	812	229	905	4.07	17.5
	f	100	10	0.436	1.10	40.55	156.8	59.9	5.5	21.7	1.105	276.71	832	229	905	3.20	17.5
	j	100	10	0.544	1.10	40.55	156.8	59.9	5.5	23.8	1.199	260.29	857	229	905	2.10	17.5
	k	100	10	0.668	1.10	40.55	156.8	59.9	5.5	26.3	1.306	358.94	861	229	905	1.93	17.5
	p	100	10	0.819	1.10	40.55	156.8	59.9	5.5	29.2	1.433	368.36	839	229	905	2.89	17.5
	r	100	30	0.197	1.10	40.55	1414.8	179.9	16.7	16.9	0.893	82.51	597	229	905	13.49	17.5
	t	100	30	0.294	1.10	40.55	1414.8	179.9	16.7	18.9	0.980	80.71	650	229	905	11.17	17.5
	a	100	30	0.349	1.10	40.55	1414.8	179.9	16.7	19.9	1.029	114.26	680	229	905	9.85	17.5
	d	100	30.05	0.349	1.10	40.55	1419.5	180.2	16.7	19.9	1.029	102.66	653	229	905	11.03	17.5
	e	100	30	0.436	1.10	40.55	1414.8	179.9	16.7	21.7	1.105	116.92	713	229	905	8.41	17.5
	i	100	30	0.544	1.10	40.55	1414.8	179.9	16.7	23.8	1.199	124.70	733	229	905	7.53	17.5
	l	100	30	0.668	1.10	40.55	1414.8	179.9	16.7	26.3	1.306	131.04	768	229	905	6.00	17.5
	s	100	50	0.197	1.10	40.55	3931.8	299.8	27.8	16.9	0.893	61.77	483	229	905	18.48	17.5
	c	100	50	0.349	1.10	40.55	3931.8	299.8	27.8	19.9	1.029	77.32	561	229	905	15.06	17.5
	g	100	49	0.436	1.10	40.55	3776.0	293.8	27.2	21.7	1.105	81.09	593	229	905	13.66	17.5
	h	100	50	0.544	1.10	40.55	3931.8	299.8	27.8	23.8	1.199	87.73	624	229	905	12.30	17.5
	m	100	50	0.668	1.10	40.55	3931.8	299.8	27.8	26.3	1.306	98.70	617	229	905	12.61	17.5
	n	100	50	0.819	1.10	40.55	3931.8	299.8	27.8	29.2	1.433	85.06	681	229	905	9.81	17.5
date	expt	x, cm	fm%	mano	Δρ/ρ, %	h,cm	M,p	B,p	Q,p	U, cm/s	u*, cm/s	S,avg	pixel, Savg	ibegpx	iendpx	at S,avg z,cm	mr
19-Jun-92	a	50	10	0.297	1.10	40.55	156.8	59.9	5.5	18.9	0.983	87.20	833	162	946	4.27	15.1
	f	50	10	0.464	1.10	40.55	156.8	59.9	5.5	22.2	1.130	50.32	905	162	946	1.55	15.1
	h	50	10	0.62	1.10	40.55	156.8	59.9	5.5	25.3	1.265	48.87	945	162	946	0.04	15.1
	o	50	10	0.738	1.10	40.55	156.8	59.9	5.5	27.6	1.365	47.72	945	162	946	0.04	15.1
	n	50	10	0.903	1.10	40.55	156.8	59.9	5.5	30.9	1.504	150.84	925	162	946	0.79	15.1
	b	50	30	0.297	1.10	40.55	1414.8	179.9	16.7	18.9	0.983	48.26	721	162	946	8.49	15.1
	e	50	30	0.464	1.10	40.55	1414.8	179.9	16.7	22.2	1.130	61.23	725	162	946	8.34	15.1
	i	50	30	0.62	1.10	40.55	1414.8	179.9	16.7	25.3	1.265	63.40	797	162	946	5.63	15.1
	k	50	30	0.62	1.10	40.55	1414.8	179.9	16.7	25.3	1.265	52.63	805	162	946	5.32	15.1
	p	50	30	0.735	1.10	40.55	1414.8	179.9	16.7	27.6	1.362	64.76	805	162	946	5.32	15.1
	l	50	30	0.903	1.10	40.55	1414.8	179.9	16.7	30.9	1.504	88.74	829	162	946	4.42	15.1
	c	50	49.5	0.297	1.10	40.55	3853.5	296.8	27.5	18.9	0.983	37.02	609	162	946	12.72	15.1
	d	50	49	0.464	1.10	40.55	3776.0	293.8	27.2	22.2	1.130	39.45	689	162	946	9.70	15.1
	j	50	50	0.62	1.10	40.55	3931.8	299.8	27.8	25.3	1.265	46.91	661	162	946	10.76	15.1
	q	50	50	0.735	1.10	40.55	3931.8	299.8	27.8	27.6	1.362	53.48	733	162	946	8.04	15.1
	m	50	49	0.903	1.10	40.55	3776.0	293.8	27.2	30.9	1.504	33.50	733	162	946	8.04	15.1

																at S,avg	
date	expt	x, cm	fm%	mano	Δρ/ρ, %	h,cm	M,p	B,p	Q,p	U, cm/s	u*, cm/s	S, avg	pixel, Savg	ibegpx	iendpx	z, cm	mr
5-Jul-92	a	25	10	0.549	0.96	41.4	156.8	52.26	5.5	23.9	1.204	18.79	925	144	969	1.58	14.4
	b	25	20.05	0.549	0.96	41.4	631.6	104.9	11.1	23.9	1.204	18.59	861	144	969	3.87	14.4
	c	25	30	0.549	0.96	41.4	1414.8	157	16.7	23.9	1.204	17.02	833	144	969	4.88	14.4
	d	25	39	0.549	0.96	41.4	2391.6	204.1	21.7	23.9	1.204	14.87	777	144	969	6.89	14.4
	e	25	49	0.549	0.96	41.4	3776.0	256.4	27.2	23.9	1.204	14.47	733	144	969	8.47	14.4
	f	25	60	0.551	0.96	41.4	5662.4	314	33.3	23.9	1.205	14.88	705	144	969	9.47	14.4
																at S,avg	
date	expt	x, cm	fm%	mano	Δρ/ρ, %	h,cm	M,p	B,p	Q,p	U, cm/s	u*, cm/s	S, avg	pixel, Savg	ibegpx	iendpx	z, cm	mr
10-Jul-92	e	25	30	0.296	1.10	41.99	1414.8	179.9	16.7	18.9	0.982	8.61	799	156	984	6.61	14.3
	d	25	30	0.389	1.10	41.99	1414.8	179.9	16.7	20.7	1.064	8.31	806	156	984	6.36	14.3
	c	25	30	0.545	1.10	41.99	1414.8	179.9	16.7	23.8	1.200	12.26	839	156	984	5.18	14.3
	b	25	30	0.75	1.10	41.99	1414.8	179.9	16.7	27.9	1.375	12.94	870	156	984	4.08	14.3
	a	25	30	0.976	1.10	41.99	1414.8	179.9	16.7	32.3	1.564	12.07	882	156	984	3.65	14.3
	f	25	30	1.144	1.10	41.99	1414.8	179.9	16.7	35.7	1.703	5.17	893	156	984	3.25	14.3
																at S,avg	
date	expt	x, cm	fm%	mano	Δρ/ρ, %	h,cm	M,p	B,p	Q,p	U, cm/s	u*, cm/s	S, avg	pixel, Savg	ibegpx	iendpx	z, cm	mr
12-Jul-92	b	40	30	0.284	1.20	41.69	1414.8	196.2	16.7	18.7	0.971	39.61	733	134	978	8.59	14
	c	40	30	0.338	1.20	41.69	1414.8	196.2	16.7	19.7	1.019	40.92	733	134	978	8.59	14
	a	40	30	0.459	1.20	41.69	1414.8	196.2	16.7	22.1	1.126	31.86	793	134	978	6.49	14
	d	40	30	0.734	1.20	41.69	1414.8	196.2	16.7	27.6	1.362	26.61	861	134	978	4.10	14
	e	40	30	1.11	1.20	41.69	1414.8	196.2	16.7	35.0	1.675	40.92	881	134	978	3.40	14
																at S,avg	
date	expt	x,cm	fm%	mano	Δρ/ρ, %	h,cm	M,p	B,p	Q,p	U,cm/s	u*,cm/s	S,avg	pixel, Savg	ibegpx	iendpx	z,cm	mr
13-Jul-92	e	40	10	0.545	1.20	41.68	156.8	65.33	5.5	23.8	1.200	15.67	925	135	972	1.66	14.2
	a	40	30	0.545	1.20	41.68	1414.8	196.2	16.7	23.8	1.200	33.98	799	135	972	6.12	14.2
	b	40	40	0.545	1.20	41.68	2515.9	261.6	22.2	23.8	1.200	31.44	757	135	972	7.60	14.2
	c	40	50	0.545	1.20	41.68	3931.8	327.1	27.8	23.8	1.200	28.54	697	135	972	9.73	14.2
	d	40	60	0.543	1.20	41.68	5662.4	392.5	33.3	23.8	1.198	22.01	661	135	972	11.00	14.2

																at S,avg	
date	expt	x,cm	fm%	mano	Δρ/ρ, %	h,cm	M,p	B,p	Q,p	U,cm/s	u*,cm/s	S,avg	pixel, Savg	ibegpx	iendpx	z,cm	mr
15-Jul-92	e	80	30	0.264	1.20	41.66	1414.8	196.2	16.7	18.3	0.953	66.50	674	80	997	10.43	12.9
	f	80	30	0.358	1.20	41.66	1414.8	196.2	16.7	20.1	1.037	64.50	730	80	997	8.62	12.9
	g	80	30	0.535	1.20	41.66	1414.8	196.2	16.7	23.6	1.191	70.46	750	80	997	7.97	12.9
	a	80	30	0.549	1.20	41.66	1414.8	196.2	16.7	23.9	1.204	74.82	800	80	997	6.36	12.9
	b	80	30	0.731	1.20	41.66	1414.8	196.2	16.7	27.5	1.359	100.05	800	80	997	6.36	12.9
	c	80	30	0.95	1.20	41.66	1414.8	196.2	16.7	31.8	1.543	108.87	840	80	997	5.07	12.9
	d	80	30	1.209	1.20	41.66	1414.8	196.2	16.7	37.0	1.756	93.61	886	80	997	3.58	12.9
	i	80	10	0.535	1.20	41.66	156.8	65.33	5.5	23.6	1.191	95.37	990	80	997	0.23	12.9
	j	80	40	0.535	1.20	41.66	2515.9	261.6	22.2	23.6	1.191	54.83	686	80	997	10.04	12.9
	k	80	50	0.532	1.20	41.66	3931.8	327.1	27.8	23.6	1.189	43.23	602	80	997	12.75	12.9
	l	80	52	0.532	1.20	41.66	4252.7	340.2	28.9	23.6	1.189	31.64	602	80	997	12.75	12.9
	m	80	60	0.531	1.20	41.66	5662.4	392.5	33.3	23.5	1.188	29.55	602	80	997	12.75	12.9
																at S,avg	
date	expt	x,cm	fm%	mano	Δρ/ρ, %	h,cm	M,p	B,p	Q,p	U,cm/s	u*,cm/s	S,avg	pixel, Savg	ibegpx	iendpx	z,cm	mr
16-Jul-92	b	100	30	0.288	1.11	41.73	1414.8	181.5	16.7	18.7	0.975	134.46	622	143	949	12.01	14.7
	a	100	30	0.35	1.11	41.73	1414.8	181.5	16.7	20.0	1.030	126.00	677	143	949	9.99	14.7
	c	100	30	0.548	1.11	41.73	1414.8	181.5	16.7	23.9	1.203	123.54	754	143	949	7.16	14.7
	d	100	30	0.724	1.11	41.73	1414.8	181.5	16.7	27.4	1.353	122.39	775	143	949	6.39	14.7

date	expt	Re,p	Re,f	Fr,f	urms,cm/s	uratio	lj,cm	lb,cm	lq,cm	lm,cm	Ri,lq/lm
5-Jun-92	q	1383	174656	0.085	0.663	0.743	0.739	1.23E-02	0.44	5.73	0.077
	b	1383	205657	0.100	0.766	0.745	0.628	7.55E-03	0.44	5.73	0.077
	f	1383	223401	0.109	0.824	0.746	0.578	5.89E-03	0.44	5.73	0.077
	j	1383	245429	0.119	0.896	0.747	0.526	4.44E-03	0.44	5.73	0.077
	k	1383	270720	0.132	0.976	0.748	0.477	3.31E-03	0.44	5.73	0.077
	p	1383	301517	0.147	1.073	0.749	0.428	2.39E-03	0.44	5.73	0.077
	r	4154	174656	0.085	0.663	0.743	2.221	3.70E-02	0.44	17.20	0.026
	t	4154	194440	0.095	0.729	0.744	1.995	2.68E-02	0.44	17.20	0.026
	a	4154	205657	0.100	0.766	0.745	1.886	2.27E-02	0.44	17.20	0.026
	d	4161	205657	0.100	0.766	0.745	1.889	2.27E-02	0.44	17.23	0.026
	e	4154	223401	0.109	0.824	0.746	1.736	1.77E-02	0.44	17.20	0.026
	i	4154	245429	0.119	0.896	0.747	1.580	1.33E-02	0.44	17.20	0.026
	l	4154	270720	0.132	0.976	0.748	1.433	9.94E-03	0.44	17.20	0.026
	s	6925	174656	0.085	0.663	0.743	3.702	6.17E-02	0.44	28.68	0.015
	c	6925	205657	0.100	0.766	0.745	3.144	3.78E-02	0.44	28.68	0.015
	g	6786	223401	0.109	0.824	0.746	2.836	2.89E-02	0.44	28.10	0.016
	h	6925	245429	0.119	0.896	0.747	2.634	2.22E-02	0.44	28.68	0.015
	m	6925	270720	0.132	0.976	0.748	2.388	1.66E-02	0.44	28.68	0.015
	n	6925	301517	0.147	1.073	0.749	2.144	1.20E-02	0.44	28.68	0.015
date	expt	Re,p	Re,f	Fr,f	urms,cm/s	uratio	lj,cm	lb,cm	lq,cm	lm,cm	Ri,lq/lm
19-Jun-92	a	1383	195051	0.095	0.731	0.744	0.662	8.85E-03	0.44	5.73	0.077
	f	1383	229112	0.111	0.843	0.746	0.564	5.46E-03	0.44	5.73	0.077
	h	1383	260930	0.127	0.945	0.747	0.495	3.70E-03	0.44	5.73	0.077
	o	1383	284997	0.139	1.021	0.748	0.453	2.84E-03	0.44	5.73	0.077
	n	1383	318650	0.155	1.126	0.749	0.405	2.03E-03	0.44	5.73	0.077
	b	4154	195051	0.095	0.731	0.744	1.988	2.66E-02	0.44	17.20	0.026
	e	4154	229112	0.111	0.843	0.746	1.693	1.64E-02	0.44	17.20	0.026
	i	4154	260930	0.127	0.945	0.747	1.486	1.11E-02	0.44	17.20	0.026
	k	4154	260930	0.127	0.945	0.747	1.486	1.11E-02	0.44	17.20	0.026
	p	4154	284385	0.138	1.019	0.748	1.364	8.57E-03	0.44	17.20	0.026
	l	4154	318650	0.155	1.126	0.749	1.217	6.09E-03	0.44	17.20	0.026
	c	6856	195051	0.095	0.731	0.744	3.282	4.38E-02	0.44	28.39	0.016
	d	6786	229112	0.111	0.843	0.746	2.765	2.68E-02	0.44	28.10	0.016
	j	6925	260930	0.127	0.945	0.747	2.478	1.85E-02	0.44	28.68	0.015
	q	6925	284385	0.138	1.019	0.748	2.273	1.43E-02	0.44	28.68	0.015
	m	6786	318650	0.155	1.126	0.749	1.988	9.95E-03	0.44	28.10	0.016

date	expt	Re,p	Re,f	Fr,f	urms,cm/s	uratio	lj,cm	lb,cm	lq,cm	lm,cm	Ri,lq/lm
5-Jul-92	a	1383	249396	0.119	0.899	0.747	0.524	3.83E-03	0.44	6.13	0.072
	b	2775	249396	0.119	0.899	0.747	1.051	7.68E-03	0.44	12.30	0.036
	c	4154	249396	0.119	0.899	0.747	1.574	1.15E-02	0.44	18.41	0.024
	d	5401	249396	0.119	0.899	0.747	2.046	1.49E-02	0.44	23.94	0.019
	e	6786	249396	0.119	0.899	0.747	2.571	1.88E-02	0.44	30.08	0.015
	f	8310	249809	0.119	0.900	0.747	3.143	2.29E-02	0.44	36.84	0.012
date	expt	Re,p	Re,f	Fr,f	urms,cm/s	uratio	lj,cm	lb,cm	lq,cm	lm,cm	Ri,lq/lm
10-Jul-92	e	4154	198771	0.093	0.731	0.744	1.990	2.67E-02	0.44	17.20	0.026
	d	4154	218121	0.102	0.793	0.745	1.814	2.02E-02	0.44	17.20	0.026
	c	4154	250579	0.117	0.896	0.747	1.579	1.33E-02	0.44	17.20	0.026
	b	4154	293233	0.137	1.029	0.748	1.349	8.30E-03	0.44	17.20	0.026
	a	4154	340255	0.159	1.172	0.75	1.163	5.31E-03	0.44	17.20	0.026
	f	4154	375210	0.176	1.277	0.75	1.054	3.96E-03	0.44	17.20	0.026
date	expt	Re,p	Re,f	Fr,f	urms,cm/s	uratio	lj,cm	lb,cm	lq,cm	lm,cm	Ri,lq/lm
12-Jul-92	b	4154	195477	0.092	0.723	0.744	2.016	3.02E-02	0.44	16.47	0.027
	c	4154	206667	0.098	0.759	0.745	1.907	2.56E-02	0.44	16.47	0.027
	a	4154	231740	0.109	0.840	0.746	1.700	1.81E-02	0.44	16.47	0.027
	d	4154	288725	0.136	1.019	0.748	1.365	9.37E-03	0.44	16.47	0.027
	e	4154	366640	0.173	1.256	0.75	1.075	4.58E-03	0.44	16.47	0.027
date	expt	Re,p	Re,f	Fr,f	urms,cm/s	uratio	lj,cm	lb,cm	lq,cm	lm,cm	Ri,lq/lm
13-Jul-92	e	1383	249527	0.118	0.896	0.747	0.526	4.83E-03	0.44	5.48	0.081
	a	4154	249527	0.118	0.896	0.747	1.579	1.45E-02	0.44	16.47	0.027
	b	5539	249527	0.118	0.896	0.747	2.105	1.94E-02	0.44	21.96	0.020
	c	6925	249527	0.118	0.896	0.747	2.632	2.42E-02	0.44	27.45	0.016
	d	8310	249112	0.118	0.895	0.747	3.164	2.92E-02	0.44	32.95	0.013

date	expt	Re,p	Re,f	Fr,f	urms,cm/s	uratio	lj,cm	lb,cm	lq,cm	lm,cm	Ri,lq/lm
15-Jul-92	e	4154	191254	0.090	0.709	0.744	2.059	3.22E-02	0.44	16.47	0.027
	f	4154	210725	0.100	0.772	0.745	1.869	2.41E-02	0.44	16.47	0.027
	g	4154	247387	0.117	0.890	0.747	1.592	1.49E-02	0.44	16.47	0.027
	a	4154	250287	0.118	0.899	0.747	1.574	1.44E-02	0.44	16.47	0.027
	b	4154	287986	0.136	1.017	0.748	1.368	9.43E-03	0.44	16.47	0.027
	c	4154	333348	0.157	1.156	0.749	1.182	6.08E-03	0.44	16.47	0.027
	d	4154	386996	0.183	1.318	0.751	1.018	3.89E-03	0.44	16.47	0.027
	i	1383	247387	0.117	0.890	0.747	0.530	4.95E-03	0.44	5.48	0.081
	j	5539	247387	0.117	0.890	0.747	2.123	1.98E-02	0.44	21.96	0.020
	k	6925	246766	0.117	0.888	0.747	2.661	2.50E-02	0.44	27.45	0.016
	l	7202	246766	0.117	0.888	0.747	2.767	2.60E-02	0.44	28.55	0.016
	m	8310	246559	0.116	0.887	0.747	3.196	3.01E-02	0.44	32.95	0.013
date	expt	Re,p	Re,f	Fr,f	urms,cm/s	uratio	lj,cm	lb,cm	lq,cm	lm,cm	Ri,lq/lm
16-Jul-92	b	4154	196413	0.093	0.725	0.744	2.007	2.76E-02	0.44	17.12	0.026
	a	4154	209267	0.099	0.767	0.745	1.884	2.28E-02	0.44	17.12	0.026
	c	4154	250319	0.118	0.898	0.747	1.575	1.33E-02	0.44	17.12	0.026
	d	4154	286809	0.135	1.012	0.748	1.375	8.86E-03	0.44	17.12	0.026

References

ANDREWS, K A (1988) Orifice coefficients for an asymmetrical flow into a slot. Engineer's Degree Thesis, California Institute of Technology, Pasadena, CA.

BRIGGS, G A (1975) Plume rise predictions. In Lectures on Air Pollution and Environmental Impact Analyses, D A Haugen, ed, Am Met Soc, Boston, pp 59-111.

CHOW, V T (1959) Open-Channel Hydraulics. McGraw-Hill. 680p.

CHU, V H, and GOLDBERG, M B (1974) Buoyant forced-plumes in cross flow. J Hydr Div, ASCE, 100, HY9: 1203-1213.

CLAUSER, F H (1956) The turbulent boundary layer. Adv in Appl Mech, IV: 2-51.

COLES, D (1956) The law of the wake in the turbulent boundary layer, J Fluid Mech, 1: 191-226.

CORBETT, D M *et. al.* (1943) Stream-gagin procedure, U.S. Geological Survey, Water Supply Paper 888.

CORRSIN, S, and UBEROI, M S (1950) Further experiments on the flow and heat transfer in a heated turbulent air jet. NACA Rep 998.

CROW, S C and CHAMPAGNE, F H (1971) Orderly structure in jet turbulence. J Fluid Mech, 48: 547-596.

DEAN, R B (1978) Reynolds number dependence of skin friction and other bulk flow variables in two-dimensional rectangular duct flow. J of Fluids Eng, 100: 215-223.

DEARDORFF, J W and WILLIS, G E (1984) Ground level concentration fluctuations from a buoyant and non-buoyant source within a laboratory convectively mixed layer. Atmos Environ, 18(7):1297-1309.

DRAIN, L E (1990) The Laser-Doppler Technique. John Wiley & Sons.

DURST, F, MELLING, A, and WHITELAW, J H. (1981) Principles and Practices of Laser-Doppler Anemometry, 2nd ed. Academic Press.

FISCHER, H B, LIST, E J, KOH, R C Y, IMBERGER, J, and BROOKS, N H. (1979) Mixing in Inland and Coastal Waters, Academic Press, 483p.

FRIC, T F (1989) Structure in the near field of the transverse jet. 7th Symposium on Turbulent Shear Flows at Stanford University, August 21-23, 1989.

GARTRELL, G (1979) Studies on the mixing in a density-stratified shear flow. PhD Thesis, California Institute of Technology, Pasadena, CA.

GARTRELL G (1978) A signal processor for a laser-Doppler velocimeter. Technical Memo. 78-5 W.M.Keck Laboratory of Hydraulics and Water Resources, California Institute of Technology, Pasadena, CA.

GUDIKSEN, P H et al., (1984) Field studies of transport and dispersion of atmospheric tracers in nocturnal drainage flows. Atmos Environ, 18(4):713-731.

HANNA, S R, BRIGGS, G A, and HOSKER, R P (1982) Handbook on Atmospheric Diffusion, U S Dept of Energy Report DOE/TIC - 11223, 102p.

HANNOUN, I A (1985) Matching the refractive index in density-stratified flows. Tech Memo. 85-1, W.M. Keck Laboratory of Hydraulics and Water Resources, California Institute of Technology, Pasadena, CA.

HINZE, J O (1959) Turbulence. McGraw-Hill. 586p.

HIRST, E A (1971) "Analysis of round, turbulent, buoyant jets discharged to flowing stratified ambients," Oak Ridge National Laboratory, Report No. ORNL-4685.

HUFFMAN, G D, and BRADSHAW, P (1972) A note on von Karman's constant in low Reynolds number turbulent flows. J Fluid Mech, 53: 45-60.

KOLMOGOROV, A N (1941a) Compt. rend. acad. sci. URSS, 30: 301.

KOLMOGOROV, A N (1941b) Compt. rend. acad. sci. URSS, 32: 16.

KOOCHESFAHANI, M M (1984) Experiments on turbulent mixing and chemical reaction in a liquid mixing layer. PhD Thesis, California Institute of Technology, Pasadena, CA.

LABUS, T L, and SYMONS, E P (1972) Experimental investigation of an axisymmetric free jet with an initially uniform velocity profile. NASA TN D-6783.

LAMB, R G (1978) A numerical simulation of dispersion from an elevated point source in the convective boundary layer. Atmos Environ, 12:1297-1304.

LAU, Y L and KRISHNAPPAN, B G (1977) Transverse dispersion in rectangular channels. J Hydraul Div Proc Am Soc Civ Eng, 103: 1173-1189.

LEGG, B J and RAUPACH, M R (1982) Markov-chain simulation of particle dispersion in inhomogeneous flows: The mean drift velocity induced by a gradient in Eulerian velocity variance. Boundary-layer Meteorology 24:3-13.

LIST, E J (1982a) Turbulent jets and plumes. Ann Rev Fluid Mech 14:189-212.

LIST, E J (1982b) Mechanics of turbulent jets and plumes pp 1-68 in Turbulent Buoyant Jets and Plumes, W Rodi ed, Pergammon.

LYN, D A (1986) Turbulence and turbulent transport in sediment-laden open-channel flows. PhD Thesis, California Institute of Technology, Pasadena, CA.

McDOUGALL, T J On the elimination of the refractive index variations in turbulent density-stratified liquid flows. J Fluid Mech, 93:83-96.

MILLS, A F (1992) Heat Transfer. Irwin. 888 p.

MUELLENHOF, W P *et al.* (1985) Initial mixing characteristics of municipal ocean discharges. Vol. 1, Procedures and Applications. EPA/600/3-85/073a, November.

NEZU, I and RODI, W (1986) Open-channel flow measurements with a laser Doppler anemometer. J Hyd Eng, ASCE, 112:335-355.

NOKES, R I, MCNULTY, A J and WOOD, I R (1984) Turbulent dispersion from a steady two-dimensional horizontal source. J Fluid Mech, 149:147-159.

NOKES, R I, and WOOD, I R (1988) Vertical and lateral turbulent dispersion some experimental results. J Fluid Mech, 187:373-394.

OKOYE, J K (1970) Characteristics of transverse mixing in open-channel flows. Keck Laboratory of Hydraulics and Water Resources, Report KH-R-23, California Institute of Technology, Pasadena, CA.

PAPANICOLAOU, P A and LIST, E J (1988) Investigations of round turbulent buoyant jets. J Fluid Mech, 195:341-391.

PAPANICOLAOU, P A and LIST, E J (1987) Statistical and spectral properties of tracer concentration in round buoyant jets. Intl J Heat and Mass Trans, 30:2059-2071.

PAPANTONIOU, D and LIST, E J (1989) Large-scale structure in the far field of buoyant jets. J Fluid Mech, 209:151-190.

PEARSON, H J, PUTTOCK, J S, and HUNT, J C R (1983) A statistical model of fluid element motions and vertical diffusion in a homogeneous stratified turbulent flow. J Fluid Mech, 129:219-249.

PETROFF, C (1990) Personal communication.

PRIESTLEY, C H B (1956) "A working theory of the bent-over plume of hot gas," Quarterly J Roy Metero Soc, 81: 165-176.

RAUPACH, M R and LEGG, B J (1983) Turbulent dispersion from an elevated line sources: Measurements of wind concentration moments and budgets. J Fluid Mech, 136:111-137.

RAUPACH , M R (1983) Near-field dispersion from instantaneous sources in the surface layer. Boundary-layer Meteorology, 27:105-113.

RETICON (1981) LC 300A Camera Manual. EG&G Reticon.

ROSLER, R S and BANKOFF, S G (1963) Large scale turbulence characteristics of a submerged water jet. AIChE J, 9(5): 672-676

SABERSKY, R H, ACOSTA, A J, and HAUPTMAN, E (1964) Fluid Flow. Macmillan.

SAMI, S, CARMODY, T, and ROUSE, H (1967) Jet diffusion in the region of flow establishment. J Fluid Mech, 27: 231-252.

SAWFORD, B L (1985a) Lagrangian statistical simulation of concentration mean and fluctuation fields. J of Climate and Appl Met, 24(11):1152-1166.

SAWFORD, B L (1985b) Concentration statistics for surface plumes in the atmospheric boundary layer. Proc 7th Symp on Turb and Diff AMX, Boulder, CO, Nov 12-15.

SAWFORD, B L, FROST, C C and ALLAN, T C (1985) Atmospheric boundary layer measurements of concentration statistics from isolated and multiple sources. Boundary-layer Meteorology, 31:249-268.

SCHATZMANN, M. (1979) An integral model of plume rise. Atmos Environ, 13:721-731.

SKJELBREIA, J E (1987) Observations of breaking waves on sloping bottoms by use of laser-Doppler velocimetry. PhD Thesis, California Institute of Technology, Pasadena, CA.

STEFFLER, P M, RAJARATNAM, N, and PETERSON, A W (1983) LDA measurements of mean velocity and turbulence distribution in a smooth rectangular open channel. Water Res Eng, Report 83-4, Dept of Civil Eng, University of Alberta, Canada.

SULLIVAN, G D (1992) An investigation of mixing and transport at a sheared density interface. PhD Thesis, California Institute of Technology, Pasadena, CA.

TAYLOR, G I (1921) Diffusion by continuous movements. Proc Lond Math Soc, A20:196-211.

VANONI, V A, BROOKS, N H and RAICHLEN, F (1967) "A 40-meter precision tilting flume," Tech Memo 67-3, W. M. Keck Lab of Hyd and Water Res, California Institute of Technology, Pasadena, CA.

WEAST, R C (1967) Handbook of Chemistry and Physics College Edition, 47th edition, Chemical Rubber Corporation, Cleveland, OH.

WRIGHT, S J (1977) Effects of ambient cross flows and density stratification on the characteristic behavior of round, turbulent buoyant jets. PhD Thesis, California Institute of Technology, Pasadena, CA.